2014

Investigation of superconducting thin films and multilayered structures for electronic applications

Sergey Fedoseev
University of Wollongong

UNIVERSITY OF WOLLONGONG

Institute for Superconducting and Electronic Materials

Investigation of superconducting thin films and multilayered structures for electronic applications

Sergey Fedoseev

"This thesis is presented as part of the requirements for the award of the Degree of

Doctor of Philosophy

from

University of Wollongong"

August 2014

ABSTRACT

The grand challenge in twenty-first-century physical and material sciences is related to enabling continued advances in information processing and data storage beyond conventional silicon based electronics. Recent researches in oxide electronics suggest that it may be plausible to implement complex systems at the device level, thereby drastically increasing computational density and power efficiency. High temperature superconducting (HTS) ceramics $YBa_2Cu_3O_{7-\delta}$ (YBCO) is currently one of the most promising candidates for the creation of sophisticated cryo-electronic devices such as: Josephson junctions, microwave filters, single photon detectors, and etc. One of the important problems in YBCO thin film technology is an enhancement of superconducting properties of epitaxial films which allows the creation of reliable cryo-electronic devices with high performances. Heteroepitaxial structures consisting, for example, of YBCO layers and layers of different superconducting cuprates having a very similar crystal lattice are likely to have enhanced microstructural properties and possibly better performances of Josephson junctions. The same multilayering approach can be successfully implemented for the fabrication of superconducting single photon detectors on the base of extremely thin heteroepitaxial structures grown on monocrystalline substrates.

The doped perovskite manganite $La_{1-x}Ca_xMnO_3$ (LCMO) is one of most extensively studied material for future oxide electronics due to the interactions between the electronic, magnetic and crystal lattices, and the wide range of phases that can coexist. This is very attractive ferromagnetic oxide because of its colossal magnetoresistance (CMR) and so the great application potential for magnetic memory and spintronics devices. Due to increasing demands for high quality manganite thin films with good electrical and magnetic properties, there is an important issue to grow epitaxial films of LCMO on conventional substrates as well as the creation of multilayered heterostructures and superlattices.

The interplay between superconductivity (S) and ferromagnetism (F) in hybrid structures is one of the fascinating fields of modern research. Such artificially made bilayers, multilayers, and superlattices could have clear advantage over naturally grown layered crystals due to the fact that the thickness of magnetic and

superconducting components can be tailored individually. The oxide based doped Mott insulators, like high temperature superconductor (YBCO) and ferromagnetic manganite (LCMO) are of particular interest for making S/F hybrids.

This thesis is focused on fundamental studies of both the fabrication by Pulsed Laser Deposition (PLD) and characterization of: YBCO based multilayered device structures for practical applications, LCMO thin films and LCMO/STO superlattices, as well as YBCO/LCMO hybrid structures and superlattices with thin insulating interlayer.

During this work, a few additional related research and technical problems have been addressed. An emphasis was made onto automation and optimization of PLD technique (to prepare thin films of the highest quality especially for longue size samples l = 8 cm). Optimal deposition conditions for thin films of YBCO, LCMO and their hybrids were defined that has significantly increased the productivity of PLD system and the samples reproducibility.

Multilayered approach has been employed for fabrication of step-edge YBCO/NdBCO multilayered Josephson junction. The results demonstrate significant enhancement of the tunnelling current in the multilayered junctions compared to the single layered ones. We attribute the result observed to the formation of a more suitable microstructure in YBCO/NdBCO multilayered films, which reveals (i) smoother surfaces, (ii) fewer and shallower voids, (iii) a larger density of extended defects that provide stronger pinning, (iv) a smaller number of facets at the boundary, and (v) thinner and more uniform barrier at the junction boundary, providing more homogeneous tunnelling properties across the junction. As a result, the multilayered junctions show higher I_c and I_cR_n values, and an uniform distribution of the Josephson current.

The properties of multilayered YBCO/SmBCO/YBCO thin films structures with reduced thicknesses (< 90 nm) were investigated. It was found that as the film's thickness decreased there was a decrease in superconducting characteristics (T_c, J_c) of the structure. The properties obtained were rationalized using SEM and MOI visualization techniques. It was demonstrated that the thinner samples had very poor structural homogeneity, and thus magnetic flux could easily penetrate the sample along many defects. If an epitaxial growth of initial layers of YBCO and SmBCO is

improved, the multilayering approach may enhance structural and electromagnetic properties of the films at very thin (tens of nm) thickness.

High quality epitaxial LCMO films on different substrates were manufactured by PLD method and their magnetic and transport properties were investigated. It was shown that the Curie temperature for LCMO samples is strongly dependent on film thickness and substrate type having the trend of significant reduction as the film thickness decreases. LCMO films thicker than 150 nm have demonstrtated bulk-like behaviour with metal-insulator transition at $T_p \approx 250$ K. All LCMO thin film samples demonstrated CMR with negative magnetoresistance minimum in the vicinity of metal-insulator transition temperature.

Magnetic and transport properties of multilayered hybrid structures based on YBCO/STO/LCMO multilayers with thin insulating interlayer were investigated. Although measurements show the coexistence of ferromagnetism at high temperatures ($T > T_c$) and superconductivity at low temperatures ($T < T_c$) in hybrid structures, they demonstrate no enhancement in the critical current compared to single YBCO films, but hybrids with YBCO as the first grown layer always have better superconducting properties. In the hybrid structure of S/I/F type (YBCO micro-bridge on top of buffered LCMO film) the possibility to control the micro-bridge resistance by injection of an in plane current through LCMO layer was demonstrated. The application of injection current dramatically changes the shape of $R(T)$ curve, it leads to the decreasing in T_c, demonstrate the drop in resistance before T_p, and the reduction in resistance at room temperature. The tri-layers hybrid structure of F/I/S type (LCMO on top of buffered YBCO micro-bridge) also demonstrated the unusual $R(T)$ behaviour, with a sharp dip in resistance below T_c. It was also found that electroresistance and magnetoresistance around T_{Rmin} can be tuned by electric current, which may have applications in controlling the properties of such YBCO/LCMO hybrid based devices.

We have managed to establish an acceptable technology for combination of manganite films exhibiting the CMR effect with HTS (YBCO) films for novel hybrid functionalities and devices, so that the relevant magnetic properties of ferromagnetic layer would be exhibited below the superconducting transition temperature. So the LCMO/STO superlattices with very thin sub-layers (~3-7 nm) were grown by PLD

on different substrates and their properties were investigated by means of magnetic and transport measurements. We have obtained $T_{Curie} \approx 75$ K which is even below liquid nitrogen temperature (and $T_c = 91$ K for YBCO films). Importantly, the resistivity vs temperature curves of superlattices below the metal-insulator temperature have remarkable sharp features exhibiting about two order of magnitude drops of resistivity, which result in the positive peak of magnetoresistance in excess of 1800% at 75 K. This behaviour was explained in the framework of the phase separation theory for manganites for the well-organized 3D structures, which experience dimensional transitions of their spin-charge transport properties. The significant result is that because the structure of the superlattices can be easily controlled, it can enable the prescribed tuning of the magnetoresistance properties required for applications.

Four series of cuprate/insulator/manganite superlattices with STO, PBCO, and CeO_2 as insulating layer between YBCO and LCMO sub-layers were fabricated by PLD. It was shown that superconducting properties of such superlatices may be significantly improved to be compared with single layer YBCO film by the introduction of an STO insulator with thickness $d_i > 1$ nm. All samples (even with thinnest LCMO sub-layer) demonstrated the suppression of superconductivity by means of critical temperature and critical current. Superlattices of type $(YBCO/PBCO/LCMO)_{20}$ have a quite different shape of resistance vs temperature *R(T)* curves for two mirror samples depending on LCMO or YBCO was the first grown layer. If the LCMO layer was grown first the superconductivity is depressed significantly and ferromagnetic properties (LCMO-like behaviour) become more pronaunced. The similar behaviour of the mirror sample with LCMO as a first grown layer and even well-defined re-entrant resistance peak at $T_{re} \approx 46$ K (for the current $I = 10$ μA) was observed in the superlattices of type $(YBCO/CeO_2/LCMO)_{20}$. It was shown that the re-entrant resistance is stable and it can be controlled by the external magnetic field and applied current which is interesting for possible practical applications.

ACKNOWLEDGEMENTS

I would like to express my deepest sincere appreciation my supervisor Professor Alexey Pan for his valuable advices, suggestions, guidance, patience and constructive critics through the completion of my thesis work.

I also would like to thank all Thin Films Team members especially Dr. Olga Shcherbakova and Igor Golovchanskiy, as well as the other ISEM staff. It had been a pleasure working with all of you. My sincerest thanks are extended to all my friends in our group. Thanks for your constant support and contributions.

TABLE OF CONTENTS

LIST OF FIGURES

LIST OF TABLE

Chapter 1
Superconductivity and Magnetism

The interplay between competing superconductivity and magnetism in hybrid heterostructures attracts much attention, which gives opportunity to study fundamental problems in physics and open the door for possible applications such as: magnetic sensors, magnetic recording and spintronic devices. In this thesis, I chose multilayered heterostructures and superlattices based on thin films of $YBa_2Cu_3O_7$ (YBCO) and $La_{0.7}Ca_{0.3}MnO_3$ (LCMO) as candidates to study some of novel physical phenomena. In the following pages, I present some basic introduction about superconductivity, magnetism and the interaction between high temperature superconducting and ferromagnetic oxides. The properties of LCMO and YBCO thin films, as well as YBCO/LCMO hybrid structures are also discussed.

1.1 Superconductivity: $YBa_2Cu_3O_{7-\delta}$

Superconductivity is characterized by zero resistance and perfect diamagnetism. It is a macroscopic quantum mechanical phenomenon. Superconductivity appears below a transition temperature T_c, when the conduction electrons form Cooper pairs. In 1911, superconductivity was first discovered by H. Kamerlingh Onnes in mercury. It was found that the resistivity of Hg suddenly dropped to zero at 4.2 K. For the introduction to superconductivity one can refer to the books written by Tinkham [1] and Schmidt [2]. According to the Bardeen-Cooper-Schrieffer theory (BCS) [3] the mechanism of superconductivity is related to the attraction between electrons with energies close to Fermi surface. The attractive potential is believed to come from electron-phonon interactions. The range of the interaction is equivalent to the coherence length ξ, which varies from a material to a material over a wide range. A consequence of this attraction of two electrons is a formation of Cooper pairs. At normal conditions electrons occupy all levels from the bottom of a conductivity band to the Fermi surface because of the Fermi distribution. Electrons making the Cooper pair have spins directed antiparallel. When some physical interaction changes the spins direction from antiparallel to parallel the Cooper pairs will be destroyed killing

the superconductivity. Superconductivity disappears under the influence of following factors:

1) rise of temperature above critical value, T_c;

2) application of a strong magnetic field;

3) high density of electrical current which is bigger than the critical value, J_c.

According to the different behaviours in magnetic field, superconductors are classified into two groups: Type I and Type II superconductors. When a type I superconductor is exposed to a low applied magnetic field *H*, it penetrates the superconductor only a small distance λ, (London penetration depth) and λ decays exponentially to zero. This is called the Meissner effect. The phenomenon of repulsion of the magnetic field is produced by a thin screening current that flows around the edge of the superconducting sample and is known as the Meissner current.

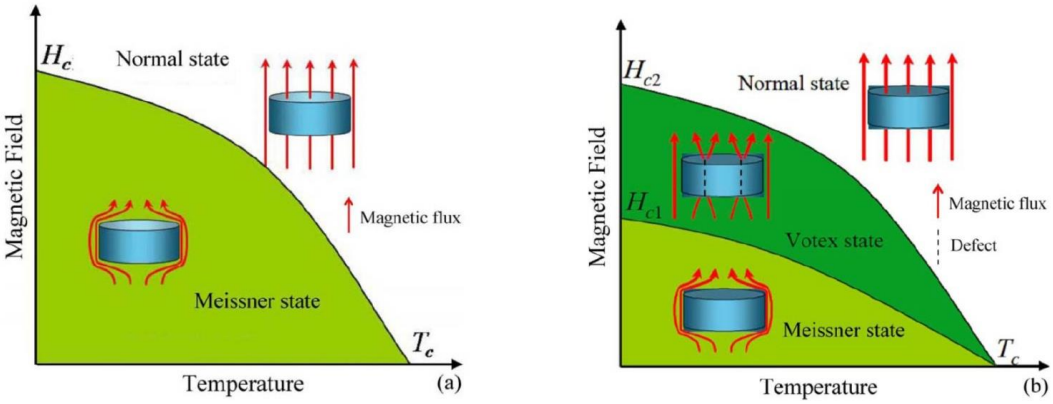

Figure 1.1 Phase diagrams of Type–I (a) and Type–II (b) superconductors.

Figure 1.1 illustrates how all superconductors are divided into two families: Type–I and Type–II superconductors. The response to an applied magnetic field is quite different in the two cases. In a Type–I superconductor, there is an exact cancellation of an applied magnetic field H by an equal and opposite magnetization (M) up to so called critical magnetic field H_c. Above the critical field superconductivity vanishes. Type–II superconductor demonstrates its basic feature compared to Type-I superconductor when the magnetic field reaches the critical value H_{c1} (see Figure 1.1). The magnetic field starts to penetrate into the superconducting material and creates superconducting current *vortices*. This state is

called mixed (or *vortex*) state. As long as vortices are stationary (pinned) the magnetic fields can penetrate while still maintaining zero electric resistivity paths through the material. As the temperature or the external magnetic field is increased, the normal regions are packed closer together. The penetration increases until the upper critical field H_{c2} is reached. At this stage the superconductor is fully penetrated by magnetic field and the normal state is restored.

The vortices interact with each other and arrange themselves in a regular structure known as vortex lattice (Abrikosov vortex lattice) [1]. The vortex matter can also interact with the defects of the material. These Abrikosov vortices can be pinned by the defects. Vortices trapped in these pinning sites are effective for blocking the motion of the whole flux line lattice due to the vortex interaction [4]. However, an applied current gives a Lorentz force F_L which drives the flux vortices and produces dissipation. The Lorentz force on each vortex per unit length is given by

$$F_L = J\varphi_0/c \tag{1.1}$$

where, φ_0 is the magnetic flux quantum, J is the current density, and c is the speed of light.

When the Lorentz force F_L exceeds the pinning force F_P , the flux lines start a viscous flow:

$$\eta v_L = F_L - F_P \tag{1.2}$$

Here, v_L is the velocity of the vortex and η is the viscosity coefficient of the vortex matter. The vortices move perpendicular to the current direction and an electric field E_0 is induced in the direction of applied current J, that is

$$E_0 = (v_L/c)B \tag{1.3}$$

Then, the flux flow resistivity ρ_f can be written as

$$\rho_f = dE_0/dJ = \varphi_0 B/\eta c^2 \tag{1.4}$$

It is found that ρ_f is independent of the critical current of the sample, or the pinning force F_p. Furthermore, ρ_f is closely associated with the normal core resistivity ρ_n using the Bardeen and Stephen expression [3]:

$$\rho_f = \rho_n H/H_{c2} \tag{1.5}$$

The understanding of how the flux moves and penetrates a superconducting material under an applied field and in the presence of a current is useful for practical application of superconductors.

The discovery of High Temperature Superconductivity (HTS) by Bednorz and Müller at the IBM laboratory in Switzerland in 1986 [5] has opened a new era of superconductor research. HTS cuprates based on $YBa_2Cu_3O_{7-\delta}$ (commonly named as YBCO) are very practical for potential applications at liquid nitrogen temperatures (77 K), which will dramatically improve performance while also lowering costs. The oxidised compound YBCO, which is superconductive around 92 K, has a layered perovskite orthorhombic unit cell, as seen in Figure 1.2, with the lattice parameter of a = 3.82 Å, b = 3.89 Å and c = 11.68 Å [6]. Both *a*-axis and *b*-axis films are referred to as *a*-axis since *a* and *b* sub-lattice constants are so close that it is difficult to distinguish between the two. Growth of YBCO thin films is often classified as *c*-axis or *a*-axis. Since the cuprate superconductors exhibit strong anisotropy in the normal and superconducting properties, this anisotropy can produce significant differences in properties along the *a*-*b* plane and *c*-axis. C-axis refers to films grown with the *c*-axis vector parallel to the normal vector of the substrate. Practically, to get a higher quality for superconducting films the *c*-axis has to be oriented perpendicular to the substrate, so that current can be applied easily along the *a*-*b* plane [7]. The YBCO structure consists of two CuO_2 planes separated by a Y atom. The Yttrium atom's primary role is simply to hold the CuO_2 planes apart and does little electrically. Outside the CuO_2-Y-CuO_2 sandwich, the BaO plane and Cu-O chains are placed. The superconductivity in this material is determined by electrons moving within the copper-oxide (CuO_2) layers. The neighbouring layers act to stabilize the structure and provide electrons/holes into the copper-oxide layers. The oxygen content in YBCO directly influences the quality of the material very much. When δ is smaller

than 0.7, the crystal structure of YBCO exist in orthorhombic phase, whereas, if δ is greater than 0.7, YBCO is more deoxygenated and exists in its non-superconducting tetragonal phase. Hence, growth in low O_2 partial pressures result in the tetragonal system with $a = b$. Evidently, YBCO, like all cuprates, is very sensitive to carrier doping and is only superconducting for a particular range of doping levels.

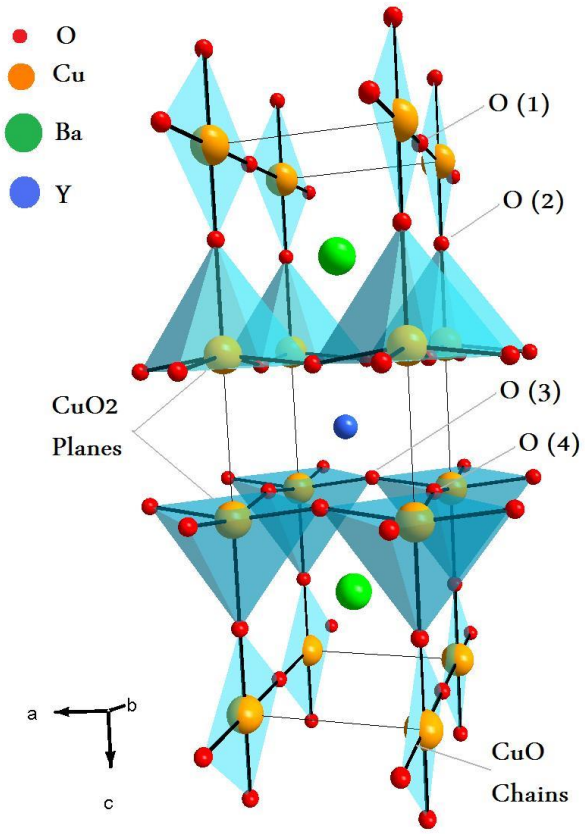

Figure 1.2 Crystallographic structure of YBCO.

A summary of the optimal doping YBCO ($YBa_2Cu_3O_{6.93}$) properties is shown in Table 1.1 including the superconducting transition temperature T_c, coherence length, penetration depth, the resistivity in the normal state (at 100 and 290 K) and so on, taken from Ref. [8]. Compared with the conventional superconductors, YBCO has a higher superconducting transition temperature, a very small coherence length ξ, and a large anisotropy in the transport properties of the normal state and in the penetration and coherence lengths. YBCO is a Type II superconductor. It displays a *d*-wave pairing symmetry but the possible mechanisms responsible for superconductivity in YBCO are not so clear and additional study is needed.

Table 1.1 Properties of optimal doped YBCO [8].

Properties	Symbol	Values along the a-b plane	Values along the c direction	General values %
Critical Temperature	T_c			92K
Resistivity at 100K	ρ(100K)	70 - 250 μΩ·cm	9 - 18 mΩ·cm	
Resistivity at 290K	ρ(290K)	180 - 550 μΩ·cm	11 - 21 mΩ·cm	
Critical density of current at 77K	J_c (77K)			5×10^6 A/cm^2
Critical density of current at 4.2K	J_c (4.2K)			6×10^7 A/cm^2
Penetration Depth	λ	26 - 260 nm	125 - 550 nm	
Coherence Length	ξ	1.2 - 4.3 nm	0.2 - 0.8 nm	
Lower Critical Field	H_{c1}	5 - 18 mT	53 - 520 mT	
Upper Critical Field	H_{c2}	110 - 240 T	29 - 40 T	

Epitaxial films of YBCO have much higher J_c values than it was reported for the bulk samples [9]. These high values are elated to the high density of defects that are presented in YBCO films and acted as pinning centres [10, 11]. For practical applications the strong pinning is very important because it reduces the dependence of critical current on the applied magnetic field and the temperature. There are many different types of defects found in YBCO films: stacking faults in the *ab*-plane, lattice mismatch edge dislocations, twin boundaries, antiphase boundaries, low- and high-angle grain boundaries, etc. [12]. These defects are mostly formed during the process of the film growth, and their density depends on the substrate structure, the quality of its surface, and the depositions conditions. The investigation of superconducting properties of YBCO epitaxial thin films is presented in more details in Chapter 3.

1.2 Ferromagnetic Manganites: $La_{2/3}Ca_{1/3}MnO_3$

Rare earth manganites are oxide compounds with interesting structural and physical properties, like doping dependent electric conductivity, ferromagnetism and large magnetoresistance values. Thin films can even exhibit a colossal magnetoresistance

(CMR) which means the change in resistivity for many orders of magnitude upon application of small magnetic fields [13]. Magnetoresistance (*MR*) is a change in resistance of the material under the application of external magnetic field, *B*. The *MR* can be defined as:

$$MR = [(\rho_B - \rho_0)] / \rho_0] \times 100\% \qquad (1.6)$$

where ρ_B and ρ_0 are resistivities in presence and absence of magnetic field *B* respectively. The enhancement in the resistivity under applied field is known as positive *MR* while the suppression in resistivity under applied field is named as negative *MR*. Manganites exhibit large negative *MR* under the application of magnetic field.

LaMnO3 is the parent compound of the rare earth manganites. It is an antiferromagnetic insulator. The crystal lattice of most manganites is nearly cubic and perovskite-like (see Fig.1.3) which is similar to the oxide high temperature superconductors [14]. Chemical substitution in LaMnO3 is possible at all lattice sites. La^{3+} can be replaced by the rare earth elements, Y and Bi, as well as by divalent (Sr, Ca, Ba, Pb), tetravalent (Ce, Te, Sn) and monovalent (K, Na) elements. Non-trivalent substitutions act as dopants: they induce a mixed Mn valence and, thereby, charge carriers.

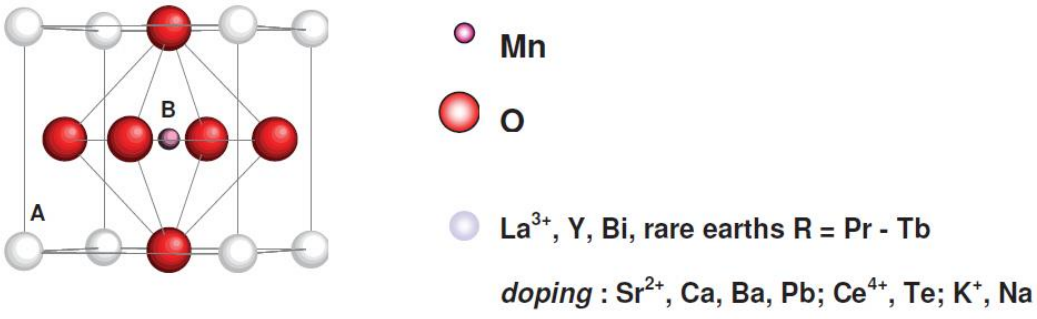

Figure 1.3 Schematic of the unit cell of the perovskite-type lattice of doped $LaMnO_3$. Mn on the lattice B site is centred in an oxygen octahedron. La on the lattice A site can be replaced or partially substituted by several metal ions of appropriate ionic radius. Non-trivalent metals act as dopants [15].

We will discuss only the doped $LaMnO_3$. Depending on temperature and carrier concentration, it can be a ferromagnetic metal, ferromagnetic insulator, or antiferromagnet. The phase diagram of the Ca-doped $LaMnO_3$, which is $La_{1-x}Ca_xMnO_3$ is presented in Fig. 1.4. When doped with 1/3 Ca which is located at the La sites, the obtained phase is a ferromagnetic metal $La_{2/3}Ca_{1/3}MnO_3$ (LCMO) with a bulk metal/insulator transition (MIT) temperature of 275 K. Above this temperature it is a paramagnetic insulator.

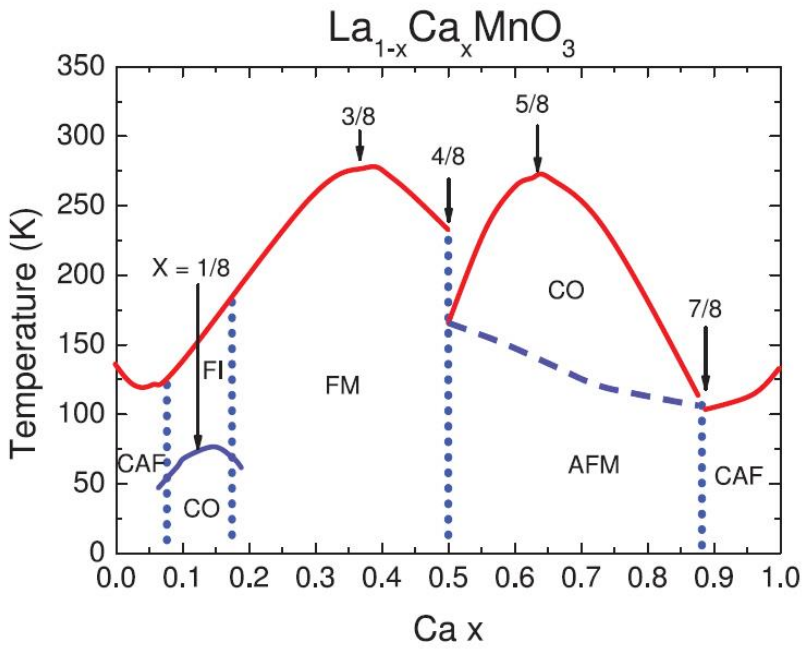

Figure 1.4 Phase diagram of $La_{1-x}Ca_xMnO_3$. FM: Ferromagnetic Metal, FI: Ferromagnetic Insulator, AF: Antiferromagnet, CAF: Canted Ferromagnet, and CO: Charge/Orbital Ordering [16].

This metal-semiconductor phenomenon was early explained by *double exchange* model theory [17]. In case of Mn^{+3}-O-Mn^{+4}, Mn ions can exchange their valence between Mn^{+3} and Mn^{+4} with simultaneous jumping of e_g electrons in the 3d shell from Mn^{+3} to Mn^{+4} ions (see Figure 1.5). However, anti-ferromagnetic behavior occurs for Mn^{+3}-O-Mn^{+3} whereas antiferro/ferromagnetic interaction is observed for Mn^{+4}-O-Mn^{+4}. Referring to Figure 1.5, the crystal field splitting Δ ~1.5 eV is lower than the exchange energy J_H ~ 2 eV so that, on a Mn^{3+} site, three electrons occupy the three $t_{2g}\uparrow$ levels, and the remaining electron lies on the first $e_g\uparrow$ level. The introduction of Mn^{4+} thus represents a form of hole doping of the e_g subband. Then, the double exchange mechanism, proposed by Zener [17] takes place between Mn

mixed-valence sites across O and contributes to the effective delocalization of these $e_g \uparrow$ electrons among all Mn sites. These exchange interactions require that the initial and final states be degenerate in energy.

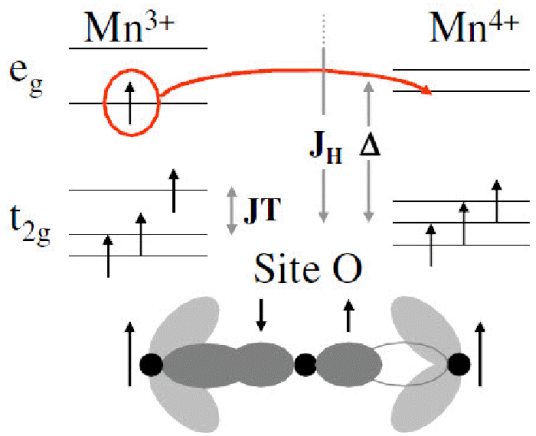

Figure 1.5 Schematic of the double exchange mechanism in manganite between the σ orbitals of Mn^{3+} and Mn^{4+} sites across the oxygen 2p orbitals. For Mn^{3+}, the lifting of degeneracy between the two e_g levels, and between the top two t_{2g} levels, reflects the Jahn–Teller (JT) distortion of the oxygen octahedra around this site [18].

The temperature dependence of the resistivity of single-crystal $La_{0.7}Ca_{0.3}MnO_3$ is presented in Figure 1.6. It is seen that there are three regions with substantially different $\rho(T)$ dependences: the region of a ferromagnetic metallic phase below 220 K; the region of the magnetic phase transition in the range 220 - 250 K; and the region of the paramagnetic semiconductor phase at $T > 250$ K. Near the Curie point, a weakly pronounced temperature hysteresis was observed [19]. At $T <$ 150 K, the resistivity is described satisfactorily by the expression $\rho(T) = \rho(0) + AT^2$, where $\rho(0) = 0.13$ mΩ-cm and $A = 2.3 \times 10^{-5}$ mΩ·cm/K^2. At $150 < T < 220$ K, the resistivity grows somewhat more rapidly, reaching the value of 1.87 mΩ·cm at $T =$ 220 K. In the ferromagnetic region, the dependence of the magnetoresistance on the magnetic field is as follows: under weak fields, $\Delta\rho/\rho > 0$; with increasing field, the magnetoresistance first grows, then diminishes, and changes its sign at a certain value of B. The reason for the change in the sign of $\Delta\rho/\rho$ is that in weak fields, the dominant role is played by the anisotropy, and in the paramagnetic semiconductor region, by the suppression of spin fluctuations. The detailed discussion of magnetic and transport properties of LCMO epitaxial thin films van be found in Chapter 5.

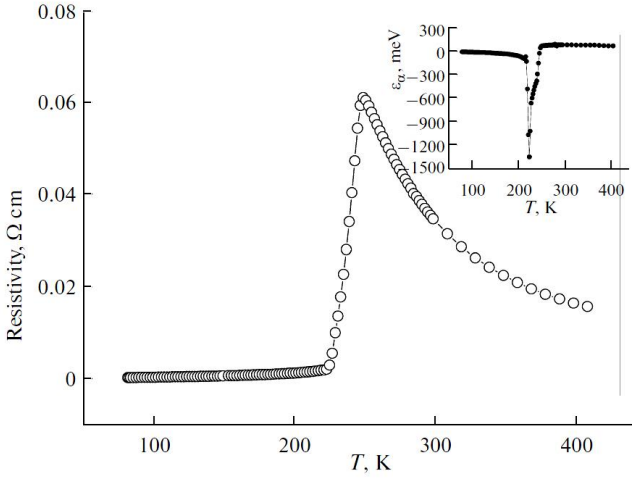

Figure 1.6 Temperature dependence of resistivity for the single crystal LCMO [19]. In the inset: the temperature dependence of the local activation energy.

1.3 Interplay between superconductivity and magnetism in artificial heterostructures

The study of the interaction between ferromagnetism and superconductivity in superconductor/ ferromagnet heterostructures received increased interest in the late 1990s. This research activity was motivated by realizing that LCMO was a half-metal with a fully spin polarised conduction band and thus ideally suited for an efficient spin injection into adjacent materials, while YBCO was known as a superconductor with a complex *d*-wave symmetry order parameter and very high superconducting transition temperature. YBCO/LCMO heterostructures were expected to be suitable candidates for the creation of *spintronic* devices [21]. At the same time there was technologically possible to realize the high quality heteroepitaxial thin films of YBCO and LCMO as their lattice parameters were very close to each other [22]. Despite of generally incompatible phenomena, ferromagnetism and superconductivity can really coexist in YBCO/LCMO hybrid structures. The suppression of the superconductivity in such hybrids is a consequence of the Pauli principle. In superconductors the electrons of a Cooper pair have opposite spins. In other words, both electrons are not in the same state, which would happen if they had the same spin direction. When the exchange field of the ferromagnet is strong enough, it tries to align the spins of electrons in a Cooper pair parallel to each other which destroys the superconductivity. As concerns the

superconductor/ferromagnet interfaces, this *proximity effect* means that the superconducting condensate decays fast in the region of the ferromagnet.

The coexistence of superconductivity and ferromagnetism in cuprate/manganite hybrid structures was investigated by many research groups. Ferromagnet/superconductor bilayers [23-27] usually demonstrate features related to both materials with mutual suppression of superconductivity and magnetism. Figure 1.7 shows the typical plot of magnetization as a function of temperature for such bilayered hybrid. It can be clearly seen, that the sample orders ferromagnetically at $T \approx 145$ K and has a superconducting transition at $T_c \approx 87$ K. There is a diamagnetic signal occurring below T_c in the zero field cooled measurement. This demonstrates that below this temperature both superconducting and magnetic ordering appears in the same sample.

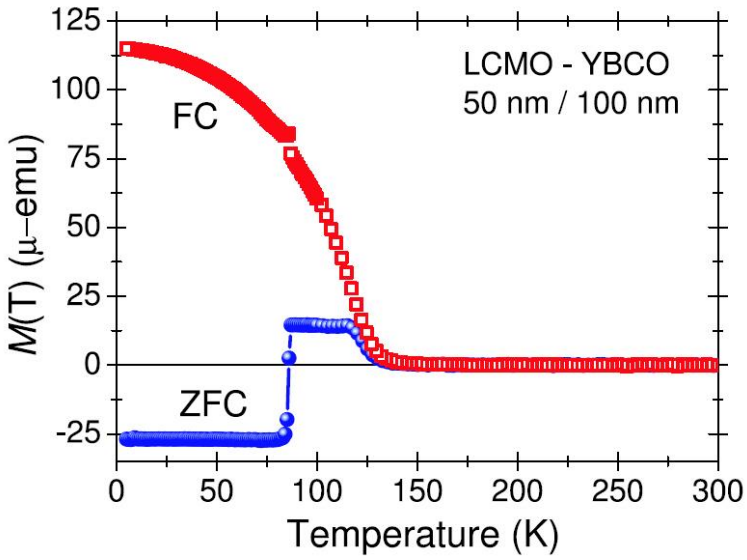

Figure 1.7 Temperature dependence of the magnetization in a bilayer consisting of 50 nm LCMO and 100 nm YBCO [23].

It was found [28] that the T_c depression at the interface of hybrid structure might be related to proximity effect (for short length scale) but the depression mechanism occurring at longer scale (with YBCO layer thickness > 5 unit cells) is most likely due to pair breaking by spin-polarized carriers entering the superconductor. The clear evidence for long-range proximity effect was found in YBCO/LCMO bilayers [29] and trilayers [30]. This effect survived for LCMO film thicknesses of up to ~ 30 nm which is an order of magnitude larger than the

coherence length in LCMO. On the other hand in [31] was shown that the increase of LCMO layers conductance in LCMO/YBCO/LCMO trilayers is associated with the induction of the triplet correlation to LCMO over an effective penetration depth ξ_F. However in very resent publication [32] with help of the sophisticated XSTS and EELS/STEM technics it was found that although proximity effects based solely on charge transfer can be excluded, it is possible that mechanisms involving coupling between charge and other degrees of freedom with longer length scale could have an important role in explaining the long-range proximity effect in YBCO/LCMO systems. Possible mechanisms are, for examples, strain fields or long-range electron–phonon coupling which is a consequence of long-range Coulomb forces in conjunction with a short-range orbital reconstruction at the interface. For a detailed discussion of the interaction between superconductivity and magnetism in LCMO/YBCO heterostructures, see Chapters 6 and 8.

References

[1] M. Tinkham. *Introduction to superconductivity*, 2 ed. Dover Publications, New York, (2004)

[2] V. V. Schmidt. *The Physics of Superconductors*, Springer-Verlag, (1997)

[3] J. Bardeen, L. N. Cooper, and J. R. Schrieffer, Phys. Rev. **108**, 1175, (1957)

[4] F.Owens and C. Pool. *The new superconductors, Selected topics in superconductivity*. New York, Plenum Press, (1996)

[5] J.G. Bednorz and K.A. Muller, Possible High Tc Superconductivity in the Ba-La-Cu-O System. Z. *Phys. B. Condens. Matter*, **64, (**1986)

[6] D. Larbalestier. A. Gurevich, D. Matthew Feldmann and A. Polyanskii, "High-T_c superconducting materials for electric power applications", *Nature* **414**, 15, November, (2001)

[7] D.P. Norton. *Annual Review of Materials Science*, **28**, 299-347, (1998)

[8] C. Poole, H. Farach, and R. Creswich, *Superconductivity*, 1st ed. (Academic Press Inc., London, U. K., (1995)

[9] M. McElfresh, T.G. Miller, D.M. Schaefer, R. Reifenberger, R.E. Muenchausen, M. Hawley, S.R. Foltyn, X.D. Wu, *J. Appl. Phys.* **71**(10), 5099,(1992)

[10] Ch. Jooss, R. Warthmann and H. Kronmuller, *Phys. Rev. B* **61**(18), 12433, (2000)

[11] F. Laviano, D. Botta, R. Gerbaldo, G. Ghigo, L. Gozzelino. L. Gianni, S. Zannella, E. Mezzetti, *Physica C* **404**, 220, (2004)

[12] S.R.Foltyn, L. Civale, J.L. MacManus-Driscoll, Q.X. Jia, B. Maiorov, H. Wang, M. Maley, *Nat. Mater.* **6**, 631, (2007)

[13] R.von Helmolt, J. Wecker, B. Holzapfel, L. Schultz, and K. Samwer. *Phys. Rev. Lett*., **71**, 2331, (1993)

[14] T. Venkatesan and R.P. Sharma. *Mater. Sci. Eng. B*, **41**, 30, (1996)

[15] Kathrin Dörr *J. Phys.D:Apple.Phys.* **39**, 125-150, (2005)

[16] A. J. Millis *Nature* **392**, 147-150, (1998)

[17] Clarence Zener *Phys. Rev.* **82**(3), 403, (1951)

[18] MBowen, J-LMaurice, A Barthelemy, M Bibes, D Imhoff, V Bellini *at all*. *J. Phys.: Condens. Matter* **19,** 315208, (2007)

[19] N. G. Bebenin, R. I. Zainullina, N. S. Bannikova, and V. V. Ustinov. *Phys. Rev. B: Condens. Matter Mater. Phys.***78**, 064415, (2008)

[20] N. G. Bebenin. ISSN 0031_918X, *The Physics of Metals and Metallography*,**111**, 3, 236–252, (2011)

[21] A.M.Goldman, V.Vas'ko, P.Kraus, K.Nikolaev and V.A. Larkin. *Journal of Magnetism and Magnetic Materials.* **200**, 69, (1999)

[22] G. Jakob, V.V.Moshchalkov and Y.Bruynseraede. *Applied Physics Letters*, **66**, 2564, (1995)

[23] Soltan S. Interaction of superconductivity and ferromagnetism in ybco/lcmo heterostructures, Universität Stuttgart, http://elib.unistuttgart.de/opus/volltexte/2005/2194/. Dissertation, (2005)

1.1 [24] M. Djupmyr, S. Soltan, H.-U. Habermeier, and J. Albrecht. *Phys. Rev. B* **80**, 184507, (2009)

[25] Z. L. Zhang, U. Kaiser, S. Soltan, H.-U. Habermeier and B. Keimer. *Appl. Phys. Lett*. **95**, 242505, (2009)

[26]R. Werner,C. Raisch, A. Ruosi, B. A. Davidson, P. Nagel, M. Merz at all. *Physical Review B* **82**, 224509, (2010)

[27]Piano S, De Santis A, Bobba F, Giubileo F, Longobardi M, Di Bartolomeo A. at all. *J Phys Condens Matter.* **21**(25), 254205, (2009)

[28] Pena, V; Visani, C; Garcia-Barriocanal, J; Arias, D; Sefrioui, Z. at all. *Physical Review B,* 7**3**, 10, p. 7, (2006)

[29]Yoav Kalcheim, Tal Kirzhner, Gad Koren, and Oded Millo *Physical Review B,* 8**3**, 064510 (2011)

[30] Pena, V; Sefrioui, Z; Arias, D; Leon, C; Santamaria, J; Varela, M; Pennycook, SJ; Martinez, JL. *Physical Review B*, 69, 224502, (2004)

[31] Hu, T; Xiao, H; Visani, C; Sefrioui, Z; Santamaria, J; Almasan, CC. *Physical Review B,* **80**, 6, p. 4, (2009)

[32] Te Yu Chien, Lena F. Kourkoutis, Jak Chakhalian, Benjamin Gray, Michael Kareev, Nathan P. Guisinger at all. *Nature Communications*. **4**, 2336, (2013)

Chapter 2
Samples Preparation and Characterization

2.1 Photolithography with Mask Aligner

Optical lithography comprises the formation of images with visible radiation in a photo resist using proximity or projection printing. These methods rely upon a mask to form the beam for the necessary image to be formed on the resist. The basic setup for optical lithography is shown in Figure 2.1. Optical lithography, in its current form, is bound by some key parameters – numerical aperture, depth of field, and resolution. The unexposed parts of the resist gradually receive radiation because of diffraction in the system and scattering in the resist and substrate layers, and hence, this affects the resolution of the system [1].

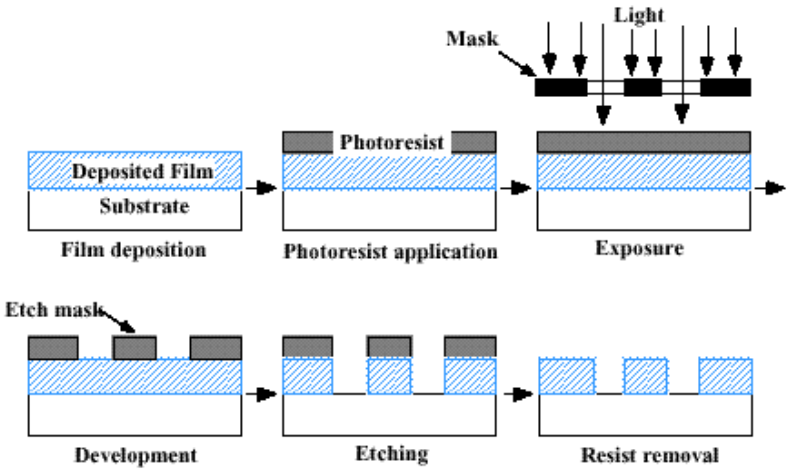

Figure 2.1 Basic outline of optical lithography processes. The diagram shows the optical radiation entering the system, which is then filtered by the chromium mask. The image is then projected on to the resist, and any non-exposed material removed during development. The sample then must be etched and after resist removal it contains necessary pattern [1].

Modern optical lithography offers higher resolution than proximity and contact printing, and resolutions of 0.35μm have been reported. Projection printing

relies on an image formation system between the mask and the resist. Because the beam is focused between the mask and the resist (wafer in Figure 2.2), the resolution of the system is very good. We can also see that the projection system consists of several sub-systems, each of which can be manipulated to improve the overall resolution of the system. The numerical apertures of the lenses can be increased up to around 1.6. However, a greater improvement in resolution will be given by decreasing the wavelength of the exposing radiation (as we want to make the resolution as better as possible). Therefore, we must look at going beyond optical wavelengths with a view to using ultra-violet radiation in lithographical systems.

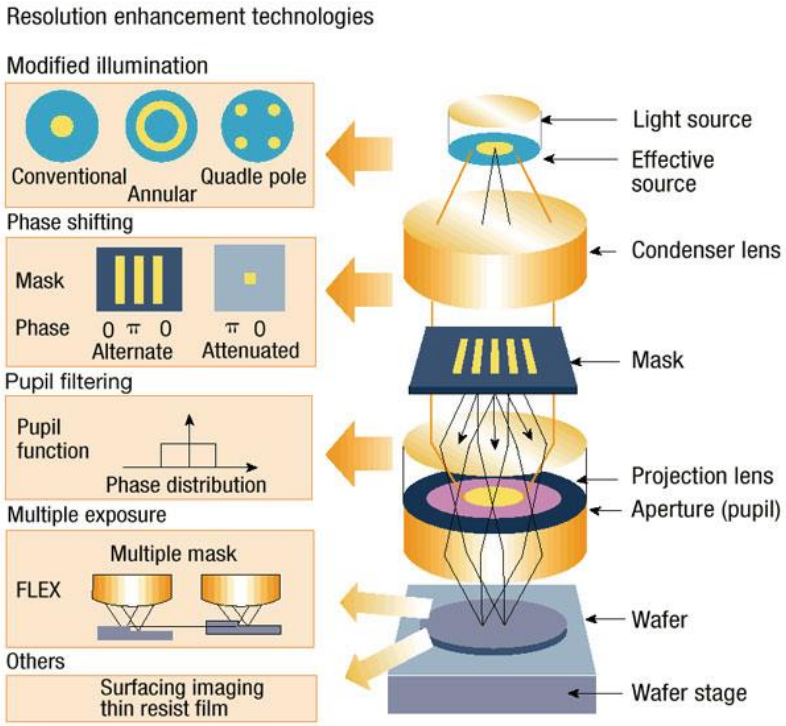

Figure 2.2 Schematic view of the exposure system in proximity optical lithography with mask aligner. Resolution enhancements can be applied at various stages [1].

Modern photolithography is based on implementation of mask aligners for samples patterning. These are machines which actually transfer the pattern onto the wafer. A mask is placed above the wafer (see Figure 2.2). The mask has the desired pattern on it. A high intensity ultraviolet light is placed over the mask. The light only transmits through the openings in the pattern allowing the pattern is burned into the photoresist on the wafer. In this work the Suss MJB3 Mask Aligner (see Figure 2.3) was used

mostly for all samples patterning. It allows the creation of samples with the resolution pattern around few micrometers.

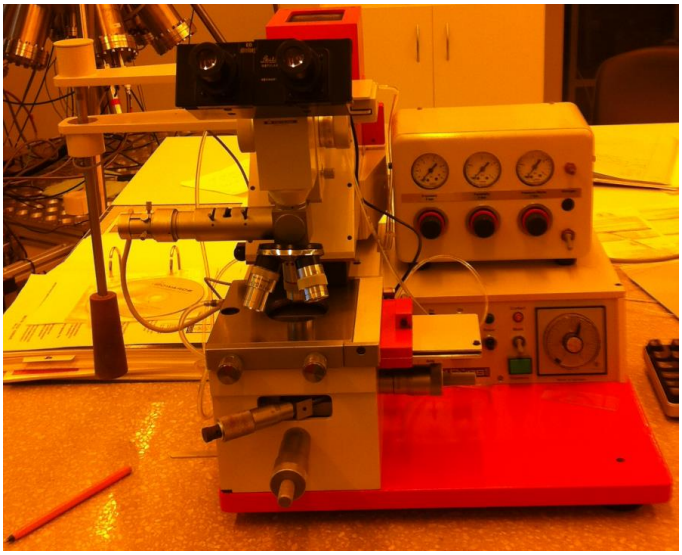

Figure 2.3 Suss MJB3 Mask Aligner at the Clean Room of ISEM used for sample patterning in this work.

2.2 Ion Beam Milling

Ion milling is a mechanical process which makes use of noble gases, most commonly, argon [2]. Unlike chemical etching, it involves no chemical reactions with the etch species. In simple terms ion beam milling can be viewed as an atomic sand blaster. In place of actual grains of sand, submicron ion particles are accelerated and bombard the surface of the target work while it is mounted on a rotating table inside a vacuum chamber. The target work is typically a wafer, substrate, or element that requires material removal by atomic sandblasting or dry ion etching.

As with any etching process, a selectively applied protectant – a photo sensitive resist (photoresist), is applied to the work element prior to its introduction into the ion miller. The resist protects the underlying material during the etching process (which may be up to four hours or longer, depending upon the amount of material to be removed and the etch rate of the materials). Everything that is exposed to the collimated 5 inch diameter ion beam etches during the process cycle, even the photoresist. The key however is that the photoresist's etch rate is lower than that of

the material that is being etched (generally the target metal etches at a rate 3 to 10 times faster than the photoresist), so while everything etches to some degree, when the process is complete, the metallization that defines the circuit remains. Different formulations of photoresist can be used depending on the type of metal and the amount of material to be removed.

Argon ions strike the target materials while they rotate. This ensures uniform removal of waste material resulting in straight side walls in all features with zero undercutting. This leads to a perfectly repeatable circuit time after time.

This precision and its attendant repeatability is ultimately the key strength of the wide collimated ion beam milling process. Other methods of etching or cutting such as the chemical process or laser simply do not deliver the same level of precision that an ion beam etch can. Furthermore, some materials such as Platinum cannot be etched effectively using a chemical process while other materials are not as suited to other methods of etching or cutting. The Ion Beam Milling process comes as close as possible to a universal etching solution. The diagram in Fig. 2.4 shows a simplified view of the function of the ion beam miller.

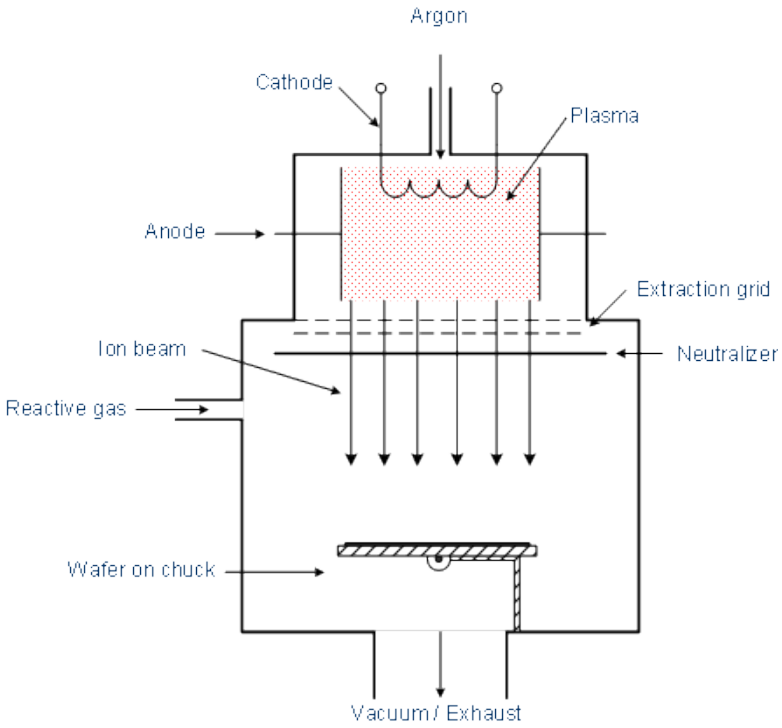

Figure 2.4 Ion beam miller operation [2].

Argon ions contained within plasma formed by an electrical discharge are accelerated by a pair of optically aligned grids. The highly collimated beam is focused on a tilted work plate that rotates during the milling operation. A neutralization filament prevents the build-up of positive charge on the work plate. As noted in the picture, the work plate is cooled and rotates so as to ensure uniformity of the ion beam bombardment. The work plate can be angled to address specific requirements, but it usually sits at an 8° to 10° angle to the ion beam.

The ion beam sputtered away the surface of the film at a rate which varies with material on the surface. The rate of surface particle loss depends on the momentum transfer, which depends also on the mass of the surface particle in relation to that of Ar^{+}, and the bonding energy of the surface particles. In this way, the carbon-based photoresist milled away at a slower rate than the thin film.

The milling chamber is pumped down to below 2×10^{-6} mbar before introducing a small amount of Ar gas. During the milling process, the chamber is kept at a pressure of 10^{-3} mbar. The good vacuum will minimize collisions between the Ar^{+} ions and the residual gas molecules, allowing the ejected ions to travel in straight lines towards the target electrode with maximum energies. The higher vacuum also reduces possible reactions between the film surface and gaseous impurities during the milling process.

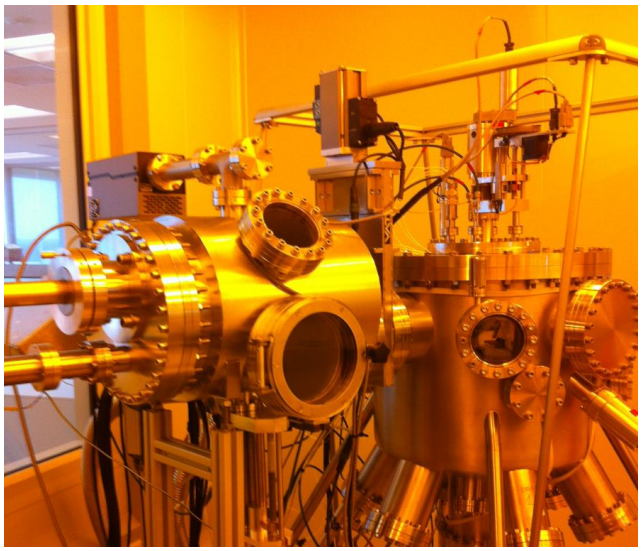

Figure 2.5 "Mantis" chamber at the Clean Room of ISEM for Ion Beam Milling of thin films.

In this work the Ion beam milling with “Mantis” equipment (see Fig.2.5) was used for micro-bridges fabrication (especially for our superlattices) because it has several significant advantages over chemical etching [3]. Ions in the beam, are accelerated by a strongly vertical electric field, and with a low chamber pressure, impinge almost completely vertically on the film surface. It can be used to pattern a wide variety of materials, including ternary and quaternary compounds, such as YBCO and LCMO.

2.3 Scanning Electron Microscopy

The scanning electron microscope (SEM) is one of the most versatile instruments available for the examination and analysis of the microstructural characteristics of solid objects [4]. The primary reason for the SEM’s usefulness is the high resolution that can be obtained when bulk objects are examined; values on the order of few nanometers are now usually quoted for commercial instruments, while advanced research instruments are available with achieved resolutions of better than 1 nm. The basic components of the SEM are the lens system, electron gun, electron collector, visual and recording cathode ray tubes (CRTs), and the electronics associated with them. In the SEM a fine electron probe is produced which rapidly scans (rasters) across the area of interest. The signals generated in the latter case are detected and converted to CRT electronic signals, which are then fed to a cathode ray tube (CRT). The CRT and the scanning coils are linked through the same scan generator, so that the image appearing on the CRT corresponds spatially to the area of the sample scanned (see Fig.2.6).

The interaction of the electron beam with the specimen produces a variety of signals that are used for imaging and spectroscopy. These signals are not generated at a point, but rather within a volume known as the *interaction volume*.

The incident (primary) electrons lose energy as they penetrate the sample, giving rise to an X-ray continuum, which consists of all possible wavelengths corresponding to the range of energies of the incident beam. The high-energy primary electrons may penetrate some distance into the sample before being scattered outside of the sample again by the Coulombic repulsion of the electron cloud in the solid. It has been experimentally determined that a significant fraction of the

incident electrons that strike a flat, bulk target placed normal to the probe subsequently escape through the same surface that they entered. The re-emergent beam electrons are called *backscattered electrons* (BSE). The strength of the scattering will depend on the atomic number of the scattering atom, so that *atomic number contrasts.* Backscattered electrons provide an extremely useful signal for imaging in scanning electron microscopy. Backscattered electrons respond to composition (atomic number or compositional contrast), crystallography (electron channelling), and internal magnitude fields (magnetic contrast).

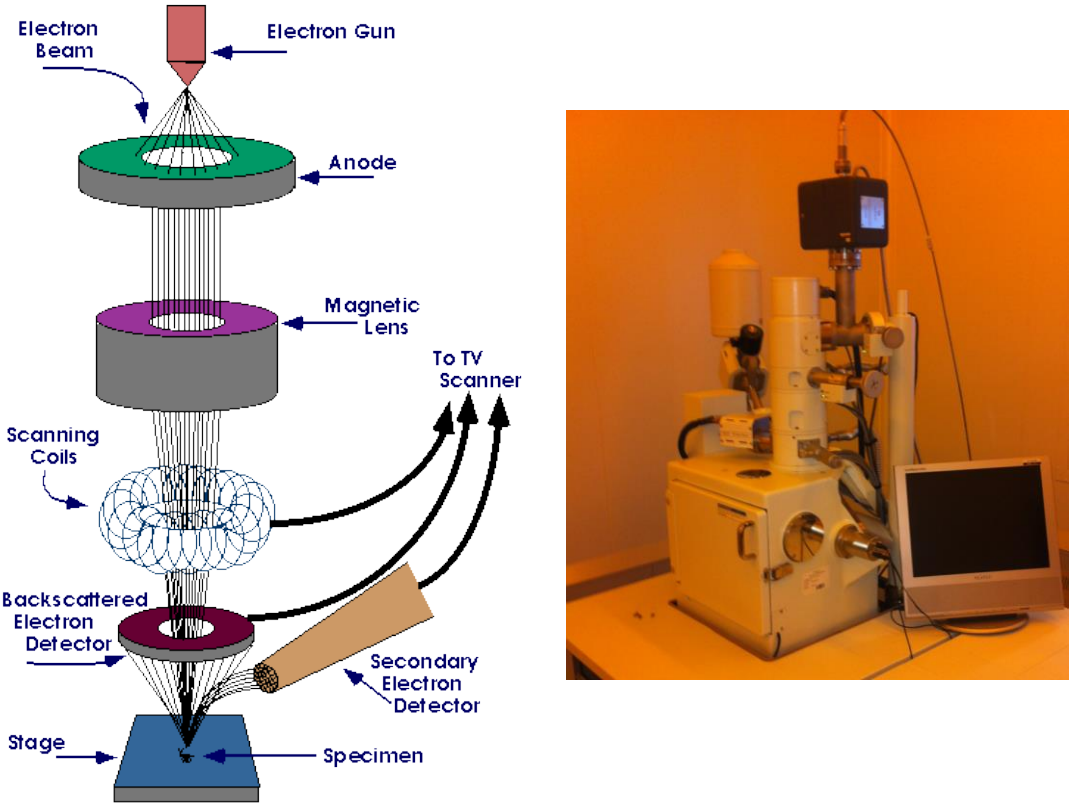

(a) **(b)**

Figure 2.6 (a) Scanning electron microscope schematic diagram [5]. (b)Scanning electron microscope at the Clean Room of ISEM used for the investigation of thin films and hybrid structures.

The primary or backscattered electrons may knock electrons out of the conduction band of the solid. These secondary electrons are relatively low in energy, and so can only escape from a region near the surface of the sample. This signal is thus often

used for generating topographic information. The electron probe and the CRT are linked through the same scan generator, so that both sample and screen are scanned in the same X-Y grid pattern. The intensity of the signal reaching the detector from a given point on the sample is used to adjust the brightness of the CRT at the corresponding point. The result is the construction of a map of the sample [6]. Figure 2.6 shows a scanning electron microscope and an image analyser used in this work.

2.4 Measurements of magnetic and transport properties

The most sensitive way to measure small magnetic fields employs a SQUID, or Superconducting Quantum Interference Device. This is based on flux quantization within a superconducting loop containing two Josephson Junctions (see Fig.2.7). Magnetic flux through the loop changes the relation between the phase difference across the two junctions.The phase difference of two current paths around a loop is based on the flux through the loop:

$$\Delta\varphi = \frac{q\Phi}{\hbar}$$

In order to avoid scattering of these two paths, this phase difference must be a multiple of 2π, thus limiting the flux allowed within the superconducting loop to multiples of Φ_0:

$$\Phi_0 = \frac{nh}{q} = \frac{nh}{2e} = n\Phi_0 = 2\times10^{12} \text{ Weber}$$

If a magnetic field B is applied such that given the area of the loop A, the flux contained should be $\Phi = BA$. For a general B, this would not be a multiple of Φ_0, but rather we could write it as $n\Phi_0 + \delta\Phi$. Therefore, a screening current I_s induces in the superconductor to cancel out this additional $\delta\Phi$ component of flux, keeping the flux in the loop strictly to $n\Phi_0$.

If we pass a current through the loop, this would split equally between the two arms in the absence of a field, as shown in Figure 2.7. If a magnetic field is

applied, the screening current I_s adds/subtracts to the two arms, such that the current in one arm is enhanced, and in the other, decreased. If $\delta\Phi$ is sufficiently large such that the enhanced current exceeds the critical current, the material will go into the normal state and a voltage can be measured across the device. Once $\delta\Phi$ exceeds $\Phi_0/2$, the screening current is reversed as it now becomes more favourable to generate an additional flux to bring the flux enclosed to $(n + 1)\Phi_0$. As the applied field increases further, the screening current now falls back towards zero, as would any measured voltage caused by driving the material into the normal state. Thus, oscillations in the measured voltage are seen for each multiple of Φ_0. It is worth pointing out that the flux quantum Φ_0 is tiny - performing this measurement with a loop of 1 mm radius would yield voltage oscillations for every nanotesla of applied field. Consider also that it is possible to measure voltage on a much finer scale than one complete oscillation: typical measurements give a sensitivity of $1{:}10^4$ of an oscillation, or 10^{-13} T.

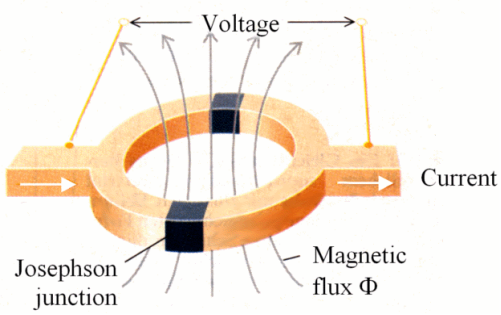

Figure 2.7 SQUID, or Superconducting Quantum Interference Device.

The SQUID is the most sensitive device available for measuring magnetic fields: although it does not detect directly a magnetic field from the sample, instead it drives the sample through a system of superconducting coils to convert the current from the coils to an output voltage which is strictly proportional to the current flowing in the SQUID coil.

The measurements were done by using a Quantum Design's Magnetic Property Measurement System MPMS *XL* at ISEM. This measurement system comprises:

- Temperature control system which gives a precise control of the sample temperature in the range 2K to 400K;

- Magnet control system: the current from a power supply provides magnetic fields from -5 to 5 T;

- Superconducting SQUID amplifier system detecting magnetic moments of a sample which is used for the determination of magnetization.

The apparatus functions as a highly linear current to voltage convertor and the variations in the current in the detection coils produce corresponding variations in the SQUID output voltage which are proportional to the magnetic moment of the sample. We get accurate measurement of the sample magnetic moment by measuring the voltage variations from the SQUID detector as the sample is moved through the detection coils. Figure 2.8 shows the MPMS setup at ISEM used in this work.

Figure 2.8 MPMS setup at ISEM.

The measurement procedure

The sample is mounted in a sample holder that is attached to a rigid rod. This rod will be put inside the MPMS and a stepper motor will make the sample go through the detection coil in a series of discrete steps.

Magnetic measurements of critical temperatures

In this work, the critical temperature T_c of superconducting samples was determined via magnetic measurements conducted on the same MPMS equipment used for the determination of J_c. Meissner current flows in a superconducting material at low temperature in a weak applied magnetic field. This Meissner current shields the superconductor from the magnetic field. It creates a magnetic moment, which has a direction opposite to the direction of the applied magnetic field. When the temperature is increased close to T_c, magnetic flux begins to penetrate the sample, and the magnetic moment decreases. Above T_c the Meissner current completely disappears, and thus, the magnetic moment vanishes. The MPMS allows the measurement of the magnetic moment and its variation during the temperature changes from below T_c to above T_c in a small applied magnetic field. In practice, the sample is cooled in zero fields (ZFC) to the temperature of about 10 K. Then a weak magnetic field (typically 25 Oe) is applied and the temperature is progressively ramped to 95 K. Around T_c the magnitude of the negative magnetic moment decreases dramatically until it becomes zero when the sample reaches its normal state. In some cases (especially for hybrid structures) it may reach positive values after crossing the zero level line and it drops back to zero value.

The MPMS allows the measurement of the magnetic moment and its variation during the temperature changes from below T_c to above T_c in a small applied magnetic field. Then a weak magnetic field (typically 25 Oe) is applied and the temperature is progressively ramped to 95 K. Around T_c the magnitude of the negative magnetic moment decreases dramatically until it becomes zero when the sample reaches its normal state. The typical *m(T)* curve is shown in Figures 2.9. The point where the magnetic moment reaches the zero level is identified as T_c. In this work, the value of the transition width ΔT_c is defined from the *m(T)* curve measured in the (ZFC) regime (see Figure 2.9). This value is extracted from the difference

between the two temperatures which correspond to m = - 0.1 and m = -0.5 in the *m(T)* curve, with m being normalized to the value of the magnetic moment at 10 K. The transition width is very important characteristics, because it shows the quality of the samples and together with the critical temperature reflects the fraction of non-superconducting phase in the material.

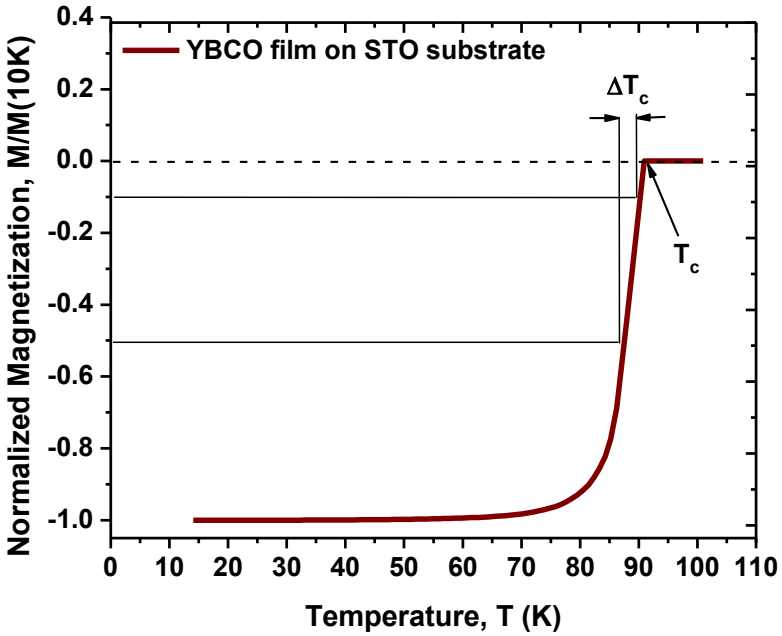

Figure 2.9 Temperature dependence of normalized magnetic moment m = M/M(at 10K) measured in typical YBCO film for the determination of critical temperature T_c and transition width ΔT_c.

Critical current J_c calculation

Current density indicates the amount of current a superconductor is able to carry and it is one of the most important characteristics of superconductors. To obtain J_c from the magnetization against the applied field data we use the relation between M and J_c given by the Bean model for a parallelepiped like sample

$$Jc = \frac{\Delta M * 12 * b}{d(3b - d)}$$

where $\Delta M = M_+ - M_-$ represents the irreversible part of the magnetization, while *b* is the length of the sample, and *d* is its width. Since we work with data that result from the screening of a volume we have to calculate the volume of the parallelepiped:

$$V = b * d * h$$

where *h* is a thickness of the film.

Now we use the volume to get the magnetization value per volume unit:

$$\frac{\Delta M}{V} = \frac{\Delta M}{3 * 10^{-6}}$$

and finally:

$$Jc = \frac{\Delta M}{V} * 2 * 10^{6} \qquad (\mathrm{A/cm^2})$$

Transport measurements

The standard method of determination of the superconductor critical temperature T_c comprises a conventional four–probe technique of measurement of *R* vs. *T* dependency, where *R* is the electrical resistance and *T* is the temperature of the sample [10]. This method requires the formation of electrical contacts on the sample surface by soldering, vacuum deposition, pressuring etc. Generally, contacting is a large disadvantage of this technique. In some cases, the electrical contacting can cause a change of the chemical properties of the samples, mainly in the vicinity of the electrodes. It is significant particularly for the thin film superconducting samples [11]. To prevent such troubles, the method of ohmic contacts formation on the surface of complex oxides was proposed. It consists of metallization by pulsed laser deposition of Pd/Au, Cr/Au, or Pt/Au films in vacuum at the room temperature and shortest distance between the target and substrate. The metallization at the room temperature prevents possible de-oxidation and even decomposition of the sample surface, and the high energy of particles in the laser plume provides their partial implantation into sample surface which ensures a good adhesion of the metal layer.

During four-probe measurements the current I was provided by a programmable *Keithley* 6221 current source and the voltage V was recorded by a *Keithley* 2182A nano–voltmeter. For the measured values the average between measured voltages was taken. The bridge resistance (when the lithography was used before the metallization) or sheet resistance of a hybrid structure were calculated as $R = V/I$. Knowing the real voltage values the resistivity of the film ρ can be determined; $\rho = R \times A/L$; where the film area $A = h \times W$; h is the film thickness, W is the film width, and L is the distance between the voltage contacts, as shown in Figure 2.10.

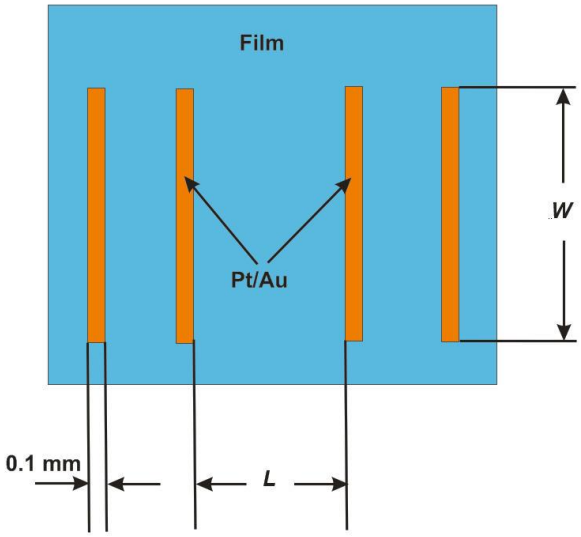

Figure 2.10 Sketch of the sample geometry for four–probe measurements. The multilayered structure was grown by pulsed laser deposition onto 5×5 mm^2 $LaAlO_3$ (100) single crystalline substrates. Afterwards, 100 nm/50 nm Pt/Au are deposited by laser ablation on top of the film as contacts for the attachment of Au wires.

2.5 Magneto-Optical Imaging

Magneto-Optical Imaging (MOI) of flux structures is based on the magneto-optical Faraday effect which describes empirically the rotation, α_F , of the vector of linearly polarized light propagating parallel to the magnetic field direction over a distance, through a medium with longitudinal optical birefringence in a magnetic field, B_z

[12], where V is a Verdet constant dependent on a light frequency. This is the origin of a Faraday effect, which is represented schematically in Figure 2.11.

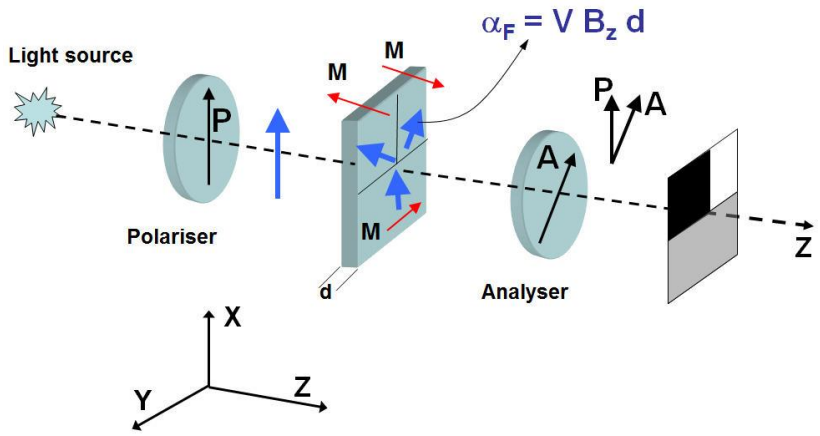

Figure 2.11 Faraday effect: The linearly polarized light sees its direction of polarization shifted by an angle α_F when going through a magneto-optically active crystal under an external magnetic field B_z [13].

The eigenmodes of light propagation (left and right circular polarized) have a different index of refraction directly proportional to the expectation value of the magnetic moment along the propagation axis. This rotation of the polarization plane in conjunction with polarization optics is used in MOI.

In a typical geometry for MOI the light passes through MO layer (MOL), is reflected at the sample surface and passes a second time through the MOL, thus doubling the rotation angle (see Fig.2.12). The measurement of α_F can be made by placing a crossed polarizer and analyser on the light path, before and after the double crossing of the MOL. When a magnetic field is applied on a superconducting sample covered by a MOL, the direction of polarization of the light focused on areas with high flux density will be rotated, and the analyser will let some light through. On the contrary, if the light beam is reflected above a flux free area, α_F will stay constant and equal to 0, and thus the analyser will block all the light. Therefore, on typical MO images, the bright areas indicate regions in the mixed state whereas dark areas correspond to flux free regions.

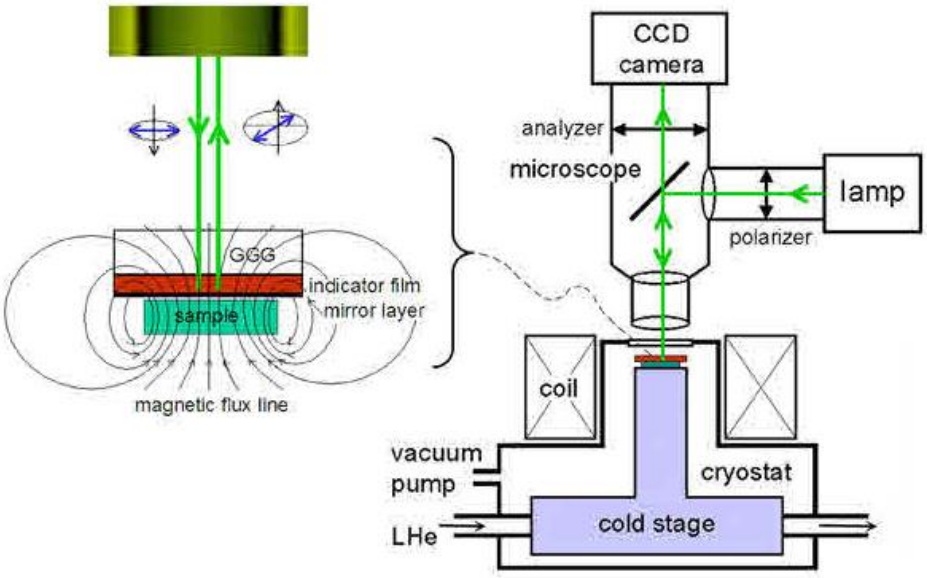

Figure 2.12 Diagram of Magneto-Optical Imaging setup built and used in this work [14].

The magneto-optical (MO) imaging technique has been used to study the local magnetic flux penetration in the YBCO films. When the external field exceeds the first critical field H_{c1}, the magnetic flux can penetrate Type-II superconductor in form of Abrikosov vortices (flux lines), each carrying one quantum of magnetic flux, *h/2e*. The flux penetration is hindered by microscopic inhomogeneities which pin (trap) vortices. As a result, a critical state is formed with some gradient of flux density determined by the critical current [15]. The MO image shows flux penetration in a zero-field-cooled film placed in a perpendicular magnetic field. Similar to the Meissner state, the brightest areas are found at the edges where the expelled flux concentrates. At the same time, the flux already penetrated deep inside the superconductor from the sides of the square. Only the corners and the central part remain flux free (completely black) [16, 17].

In this work, we used a home-built MOI set-up for the characterization of the samples. The MOI set-up was constructed by Assoc. Prof. Alexey V. Pan at ISEM (see Figure 2.13). The system can reach temperatures down to 1.9 K, owing to liquid helium cooling, and an external magnetic field of up to 0.1 T can be applied. Presented work used indicator (MOL) is ferromagnetic YIG film with in-plane magnetization. During the measurements, the MOI indicator was placed in the path

of the light beam between the polarizer and the analyser, which are positioned at 90 degrees to each other. In order tocapture magnetic features of the superconductors the fast digital camera was attached to the microscope setup.

Figure 2.16 View of Magneto-Optical Imaging setup at ISEM.

References

[1] http://www.caiciss.co.uk/lithography.pdf

[2]http://www.halbleiter.org/en/dryetching/etchprocesses/

[3] http://www.mantisdeposition.com/?url=ionsources

[4] http://faculty.washington.edu/nemati/chapter3.pdf

[5] http://www.purdue.edu/rem/rs/sem.htm

[6] Joseph I. Goldstein, Dale E. Newbury, Patrick Echlin, David C. Joy, Charles E. Lyman, Eric Lifshin, Linda Sawyer, Joseph R. Michael Scanning Electron Microscopy and X-ray Microanalysis SBN: 978-1-4613-4969-3

[7]www.jeolusa.com/DesktopModules/Bring2mind/DMX/Download.aspx?EntryId=760&Command=Core_Download&PortalId=2&TabId=344

[8] Werner Grogger, Maria Varela, Roger Ristau, Bernhard Schaffer, Ferdinand Hofer, Kannan M. Krishnan. Energy-filtering transmission electron microscopy on the nanometer length scale *Journal of Electron Spectroscopy and Related Phenomena* **143,** 139–147, (2005)

[9] www.casaxps.com

[10]A. Koňakovsky, A. Cigaň, J. Maňka, S. Buchta. *Measurement Science Review*, **1**, Number 1, (2001)

[11]V. Pan, Y. Cherpak, V. Komashko, S. Pozigun, C. Tretiatchenko, A. Semenov, E. Pashitskii, and A. V. Pan. *Physical Review B* **73**, 054508, (2006)

[12] http://arxiv.org/ftp/cond-mat/papers/0401/0401032.pdf - Habermeier

[13] http://www.tifr.res.in/~ivw10/Presentations/Tutorials/7jan/Satyajit.ppt

[14] http://www.bnl.gov/cmpmsd/moi/facility.asp

[15]http://www.mn.uio.no/fysikk/english/research/groups/amks/superconductivity/mo/#mo

[16] Alexey V. Pan, Serhiy V. Pysarenko, and Shi X. Dou. *IEEE Transaction on Applied Superconductivity*, **19**, 3, (2009)

[17] J. I. Vestgården; D. V. Shantsev; Y. M. Galperin; T. H. Johansen. Lightning in superconductors *Scientific Reports* Vol: **2**:-. DOI: 10.1038/srep00886, (2012)

Chapter 3

Development and optimization of Pulsed Laser Deposition process for the epitaxy of complex oxide thin films and heterostructures

3.1 Introduction to Pulsed Laser Deposition Technique

The method of thin films deposition by evaporation of initial targets using the laser radiation was developed very soon after the creation of powerful lasers in 1960's. Progress in laser technology, the understanding of processes of the interaction of laser radiation with materials, and the condensation of the formed plasma plume have created a basis for the further development of Pulsed Laser Deposition (PLD). However, for a long period of time PLD was used only for the deposition of some semiconductors compounds and for the spectral analysis of various materials. The interest in PLD technology increased dramatically when it was found one of the most suitable techniques for the epitaxial growth of high-temperature superconducting thin films. PLD has following attractive advantages:

1. Moving of the evaporating component (laser) outside the vacuum chamber will reduce the risk of contamination for growing thin films;
2. Extremely high power density of laser radiation (~10^9 W/cm^2) on the target allows the evaporation and deposition of any possible materials;
3. Very short laser pulse duration (~ 10 - 20 ns) allows the creation of the stoichiometric condensate close to the substrate;
4. Relatively high deposition rates, typically ~ 1 Å/s, can be achieved at moderate laser fluencies, with film thickness controlled in real time by simply turning the laser on and off;
5. High energy laser plasma make possible the reduction of the temperature for the epitaxial growth and then it allows the formation of very sophisticated hetero-structures;
6. The use of a carousel, housing a number of target materials, enables multilayer films to be deposited without the need to break vacuum when changing between materials.

The basic idea of PLD is to exploit high-power laser pulses, e.g., from an excimer laser (or 4-th harmonic of a Nd:YAG laser), in order to evaporate a small amount of a solid target. The focused laser pulses are absorbed on the target surface in very small volume. As a result, the supersonic jet of particles (laser plasma plume) is ejected normal to the target surface (see Fig. 3.1). According to the evaporation model the dynamics of these processes is defined by absorption of laser radiation by resulting plasma plume. Increase of plume temperature leads to an essential role of the radiant heat conductivity along with the electronic heat conductivity. Therefore the depth of a layer heated by the laser pulse under the target surface could exceed the depth of penetration of the laser radiation. During very short time the ions in this layer receive a considerable energy which is much more than evaporation warmth of a material. Then this overheated layer operates as explosive. The shock wave with considerable energy penetrates the target which leads to the substance evaporation in the returning wave [1].

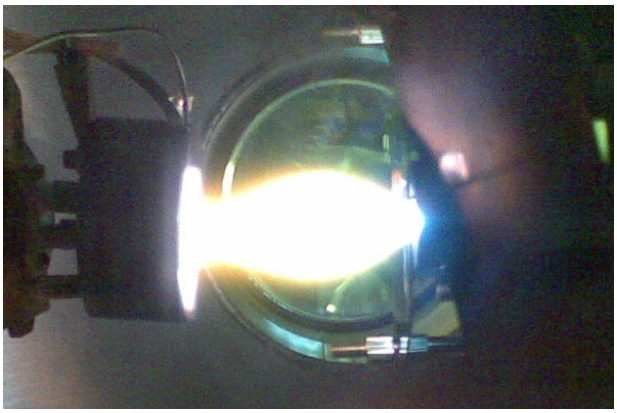

Figure 3.1 Laser plasma plume from the target (on the right) directed to the heated substrate (on the left).

The structure, composition, and parameters of plasma plume particles propagating through the deposition chamber represent the big interest as they basically define epitaxial process. The great part of plume ions possesses energy in the range of 50 - 1000 eV. The power spectrum of neutral particles was defined by registration of atoms emission, by resonant absorption, and by others methods.

According to data received during experiments in spectral diagnostics of laser plume with high time resolution, it may be concluded that the difference in scattering speeds of ions and neutral particles was insignificant [2]. Hence, the real power spectrum of particles which compose the laser plume has a wide strip with the maximum around 100 eV.

The processes arising at the interaction of products of laser erosion with a substrate surface have a great interest. It is well known, that high energy ions (E > 10 eV) can sputter the surface of a substrate. Depending on parameters of incident and sputtered streams their interaction will vary.

According to experimental PLD data, the following mechanism of epitaxial film formation was suggested. First, high energy ions arrive on a substrate and sputter a part of superficial atoms. As a result of interaction of the incident plume with the atoms which have been sputtered out from a surface, the impact area with the raised temperature and the high concentration of particles can be formed. This area will block for a while the direct penetration of an incident plume on a substrate.

In this case the film growth begins after formation of the thermalised region which will be a source of condensed particles. Condensation rate will increase with time and since the moment, when it will exceed the rate of incident plume the thermalised region will start to break up. After its definitive decomposition the film growth occurs from the direct plume only in which the particles energy decreases by approximately to 10 eV. In the case of less dense or shorter incident plasma plume the thermalised region probably is not formed. Processes of condensation and defect formation in the growing film run in parallel until the particles energy will not become less than the defect formation threshold. Thus, in the case of thermalised region formation over substrate surface the film growth occurs from particles with smaller energy and corresponds to more equilibrium conditions.

The explanation of epitaxy mechanisms in PLD is a most important and difficult problem. It is known, that the most perfect epitaxial films turn out at the step-layer mode of growth [3]. Realization of three-dimensional and island-based mechanisms of growth in PLD can sharply worsen its advantages in comparison with other epitaxial methods. The possible reasons leading to the transition from step-layer mechanism to growth from the separate centres could be: residual pollution of

substrate surfaces, mobility restriction of *adatoms* on a surface, influence of lattices parameters mismatch in the hetero-epitaxy.

PLD can take place both in vacuum and in the presence of some dilute background gas which is used to influence the composition of the film. In the case of oxide films, oxygen is the most common background gas. Under proper process parameters (e.g., the background gas pressure, the substrate temperature, the target to substrate distance, and the laser fluence), the film grows epitaxially and the stoichiometry of the film is a replica of that of the target. Process parameters have also an effect on the growth rate of the film but if the fluence and the target-substrate distance have been optimized, the rate remains nearly constant (approximately 1 Å/pulse for oxides, such as YBCO) [4]. The basic experimental setup for oxide thin films deposition using PLD includes: laser, vacuum chamber, substrate holder with precise temperature control, and source materials (targets) mounted on a target carousel. Figure 3.2 shows a schematic diagram of a typical PLD system with all components listed above.

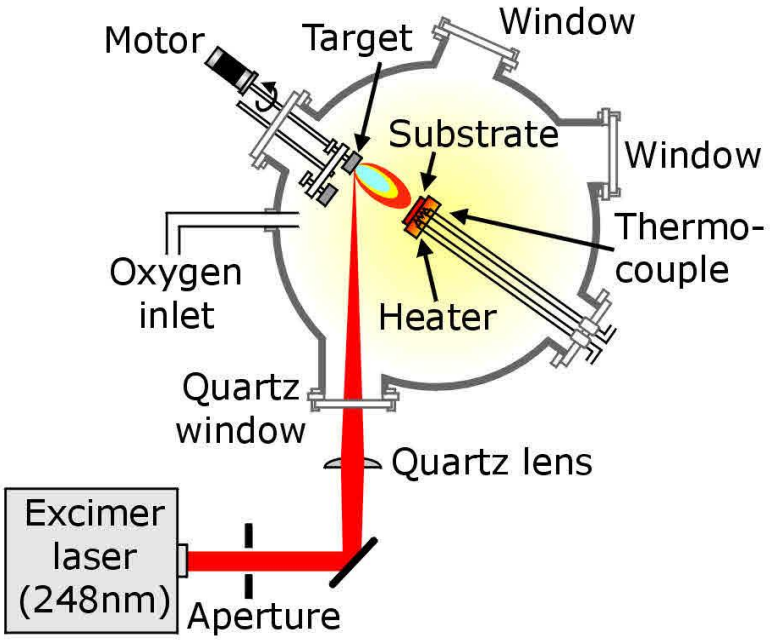

Figure 3.2 Typical PLD system setup [5].

3.2 PLD process automation with LabView

PLD system used for a deposition of all oxide thin films and oxide multilayered heterostructures, described in this thesis, includes following components (see Fig. 3.3 and 3.4):

1) Compex 301 KrF excimer laser with: wavelength λ = 248 nm, pulse duration τ = 25 ns, and fluence f = 1-10 Hz.

2) Spherical vacuum chamber with the turbo molecular pump allowing maximum vacuum level of ~10^{-7} Torr.

3) EXCEL INSTRUMENTS programmable target carousel with six target holders, controlled by firmware for multi-layer deposition.

4) Substrate heater up to 900^{o} C, controlled by EUROTHERM digital controller.

5) Two vacuum gauges for the pressure measuring from 1 atm to 10^{-8} Torr.

6) Analogue oxygen flow controller MKS Type 247.

Figure 3.3 General view of a PLD System at developed by TFT group (ISEM) showing: vacuum chamber with a target carousel and excimer Laser Compex 301.

PLD parameters usually used for complex oxides deposition are presented in the following table.

Table 3.1 Requirements for PLD process of complex oxides [6].

Average deposition time, min	Laser fluence, Hz	Laser energy, mJ	Substrate heater temperature, ^{o}C	Distance between target and substrate, mm	Oxygen pressure, mTorr	Annealing temperature and time, ^{o}C/min
10	1-5	430-450	780-800	60-80	300	400 /60

Manufacturing of a single sample usually takes a few hours. It needs the presence of an operator at each stage of PLD process. At the beginning it's necessary to pump out the chamber, then to heat the substrate, next to fill the chamber with oxygen, and as a final step it's necessary to switch on the laser and start the deposition itself. As usual all samples need to be post annealed for about one hour after the deposition.

In order to optimize the PLD process, to make it simpler, and more controllable I performed the automation of PLD system using computer interfaces and LabView software. The block diagram of PLD automation is presented in Fig.3.5. It demonstrates three independent modules designed for the remote virtual control of three main components of PLD system.

Figure 3.4 PLD System hardware front panel showing (from left to right): Oxygen flow controller, pyrometer, vacuum gauges, substrate temperature controller, and turbo molecular pump controller.

Temperature control module was designed for the precise remote control of a substrate temperature during deposition and post annealing operations. Based on RS232 interface and et3500 series LabView programs, this module gives the possibility to choose and start the predesigned heating programs. It also displays the actual substrate temperature, and keeps this temperature at the necessary level during both the deposition and the annealing operations. The heating component of this

software module was placed in the top central part of a LabView front panel (see Fig. 3.6) and it can be switched on by pushing “HEATING ON” knob. When the substrate temperature reaches the necessary level the module may be switched out using the knob “Heating Control OFF”.

The oxygen flow control module is placed in the right top part of virtual front panel. This software module receives data from vacuum gauge via RS232 interface, analyzes it, and decides whether the oxygen flow must be adjusted (see the flowchart in Fig. 3.7). If the oxygen pressure is in the range (usually around 300 mTorr) then the program terminates. When the oxygen flow isn’t in the range the virtual proportional-integral-derivative (PID) controller starts to adjust the signal and submits it for the digital-to-analogue conversion. NI_PID.vi from LabView files library was used in this design. Because the gas flow controller installed in given PLD system has only analogue input/output the USB-1208FS DAQ device was used for signal conversion and interfacing. The virtual control of a gas flow can be switched from the automatic mode to the manual one, as it may be seen from Fig.3.5 and Fig.3.6.

Laser control module is based on RS232 interface, which allows the real time exchange of data between computer and laser Communication Unit in order to display all possible laser parameters, as well as to control the laser fluence (repetition rate) and the laser energy by tuning the applied high voltage. Laser software module is placed in the centre of LabView front panel (see Fig. 3.6) and its operation can be better understood by examining the flow chart presented in Fig. 3.8. Laser module starts if the knob “Laser Control” is pushed. Then laser starts by pushing the knob “LASER ON” and the program analyzes the information received from laser Communication Unit and display all laser parameters. These are: high voltage, laser energy, repetition rate, and laser gas pressure. If the laser gas pressure is not enough for its operation the program is terminated and the announcement “Refill Laser” appears on the front panel. The applied high voltage, which directly corresponds to the output laser energy, and the repetition rate can be chosen and setting up very easy from LabView front panel. The laser energy monitor visualizes each separate laser pulse which allows the collection of information about laser energy fluctuation during the deposition. In order to make deposition process more precise and simpler the simple software timer is implemented to counts elapsed seconds and it

automatically stops the laser operation if the time is out. The timer is setting up before the deposition starts but it may be also switched off if necessary. In this case the laser operation can be terminated by pushing the knob “LASER OFF”.

After completing the deposition the annealing software module can be running if necessary. This module is placed at the bottom of a LabView front panel and its operation obeys the same algorithm as was described for the substrate heating software module. The annealing program starts if the knob “Annealing ON” is clicked and stops after clicking on “Annealing Control OFF”. When all necessary PLD operations are completed, all virtual instruments can be terminated by single click on “PLD Control OFF” in the left bottom part of LabView front panel.

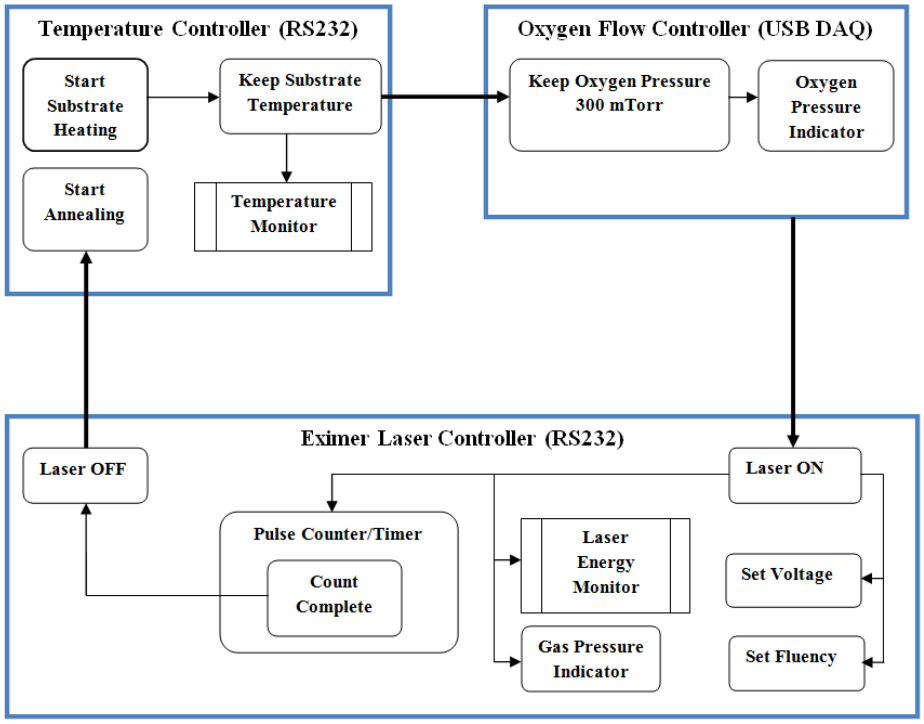

Figure 3.5 Block diagram of PLD process automation with LabView.

The programmable target carousel from EXCEL INSTRUMENTS (see Fig. 3.9) was used in all PLD processes. The carrousel was controlled independently via RS232 interface. It allowed the fast and flexible tuning of each of six possible targets before the deposition and provided the rotation and switching between targets during the PLD process according to the preinstalled target sequence program.

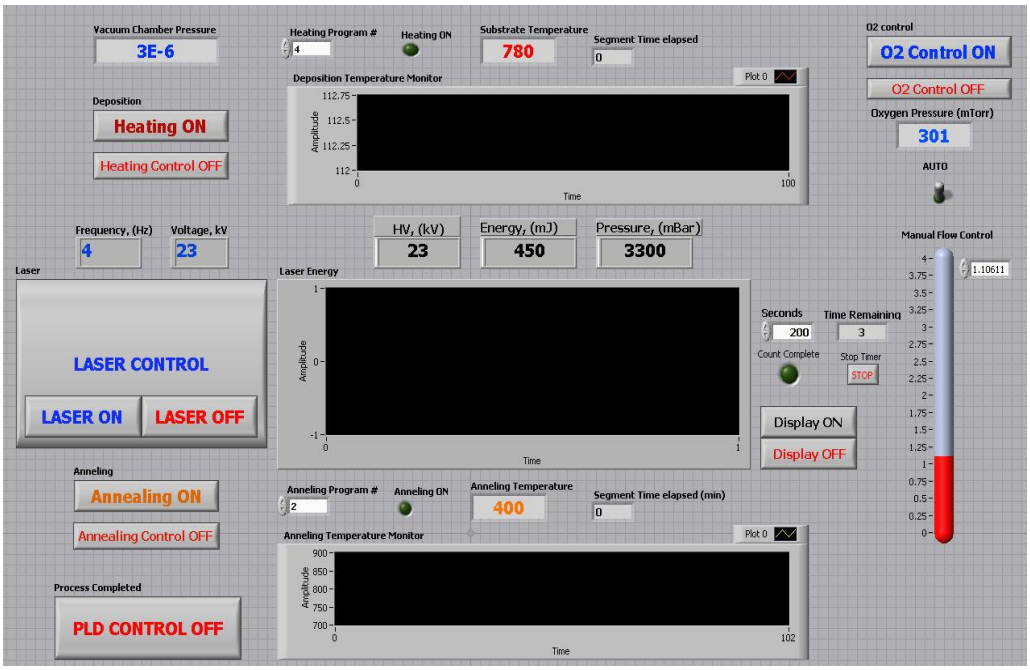

Figure 3.6 Screen shot of a LabView front panel for PLD process automation.

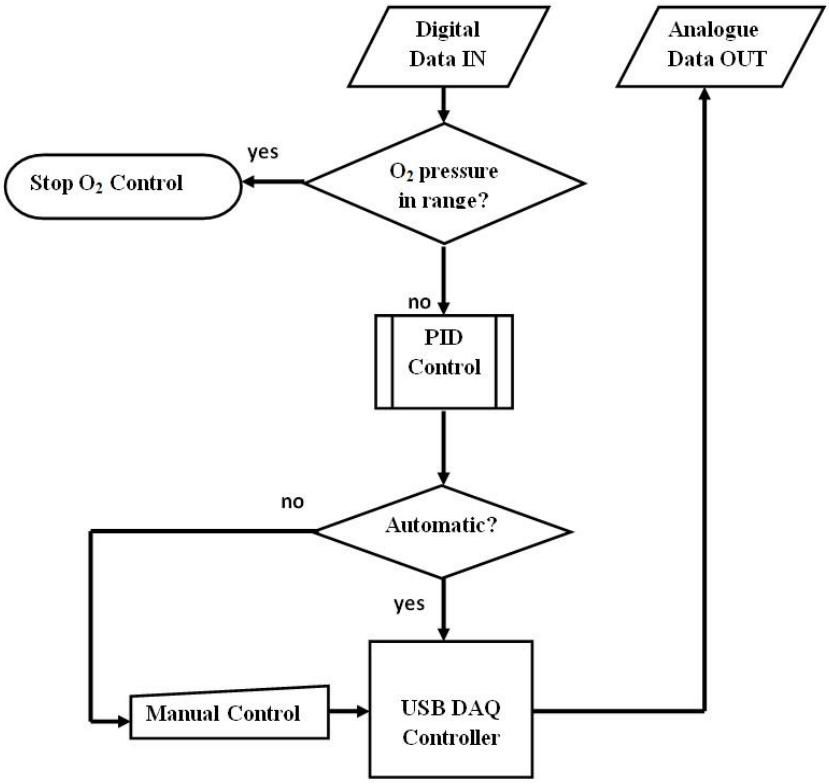

Figure 3.7 Flowchart of the oxygen pressure software module.

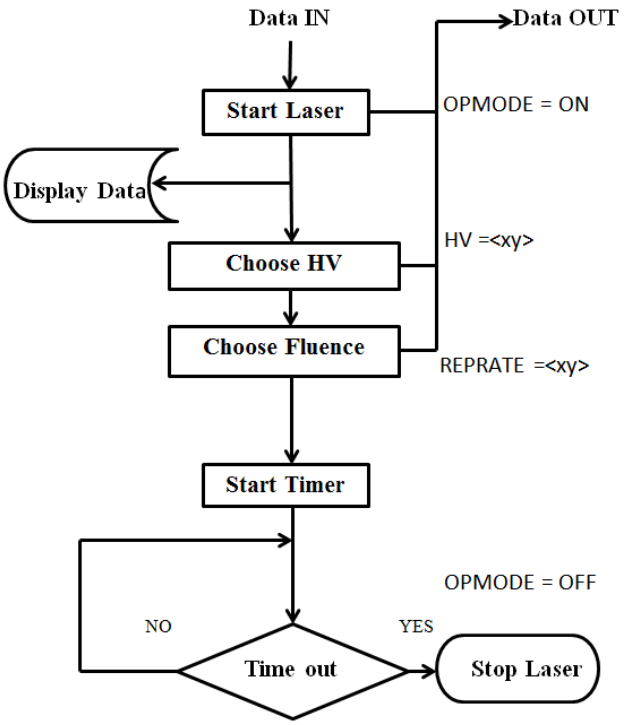

Figure 3.8 Flowchart of the laser virtual controller.

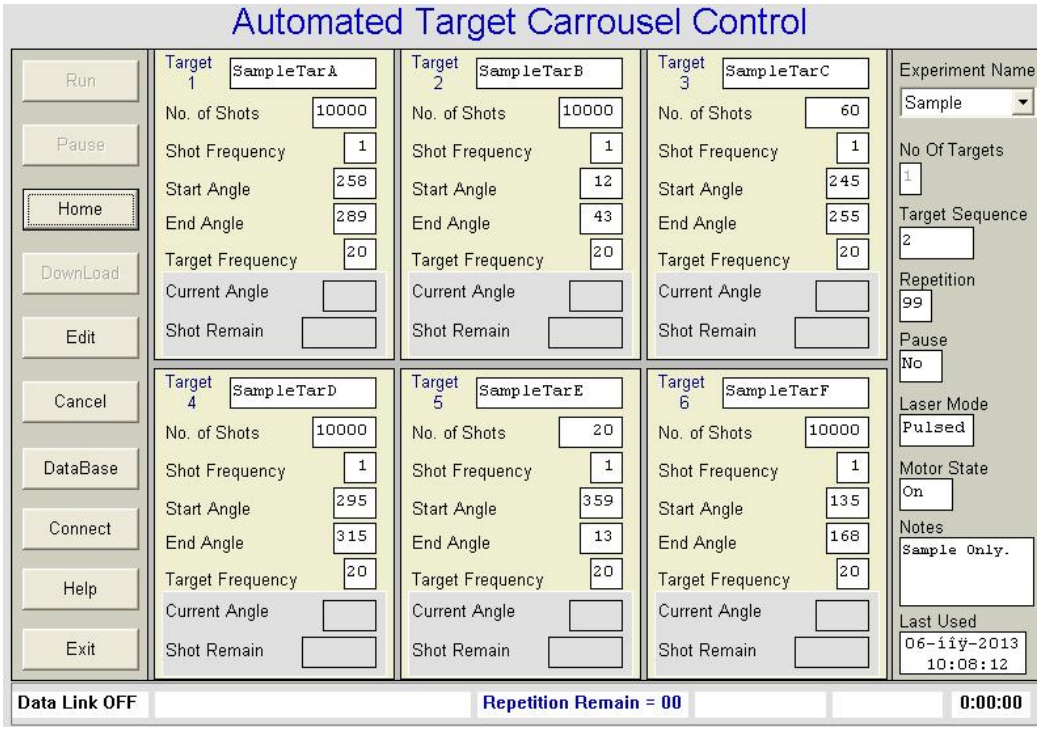

Figure 3.9 Screen shot of a front panel of the Automated Target Carrousel.

3.3 Chemical composition and surface quality of YBCO thin films manufactured in automated PLD system

The surface chemical state of YBCO films was analysed by x-ray photoelectron spectroscopy (XPS). The measurements were collected at room temperature by standard dedicated laboratory equipment using non-monochromatised Al Kα x-ray radiation (1486.6 eV) and a hemispherical electron energy analyser. Spectra were recorded for both the surface as deposited film and the same film after sputtering of about 30 nm of YBCO. The chemical quality of YBCO surfaces can be readily assessed from the details of core level photoemission signals, which is very sensitive probe of the surface quality.

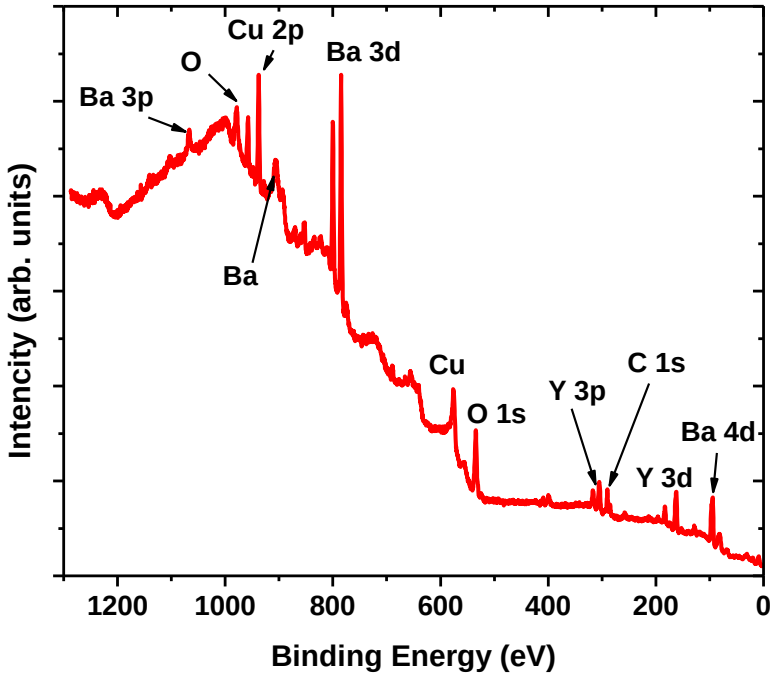

Figure 3.10 XPS survey spectra of the surface of YBCO film grown on YSZ substrate showing the core level signals identified and labeled.

Figure 3.10 shows XPS survey spectra of a surface of YBCO as deposited by PLD film with thickness $h \approx 200$ nm grown on YSZ substrate. Recording this spectra in high sensitivity mode allows to consider the main lines of all elements presented in the surface layer of the material in amounts greater than 0.3 at. %. As could be expected, there are peaks of the electronic levels of yttrium, barium, copper, and oxygen contained in the composition of the YBCO film under study. The C 1s peak

includes a signal from the carbon contamination of the random nature and it almost completely vanished after sputtering of a film surface. Few YBCO samples demonstrated some traces of Ni which could be the result of re-evaporation from vacuum chamber walls. However this did not affect the superconducting properties of such YBCO films.

The energy distribution curves for the core levels O 1s, Cu $2p_{3/2}$, Ba $3d_{3/2,5/2}$, Y 3d are reported in Figure 3.11. All the spectra were energy referenced to the C 1s peak binding energy (BE) at 284.7 eV. The sputtered surface spectrum (labelled as bulk material) usually demonstrates more narrow peaks in comparison with as deposited surface. XPS signals from this sample (see Table 3.2) are in general agreement with data reported in the literature for superconducting YBCO films deposited with different techniques [7].

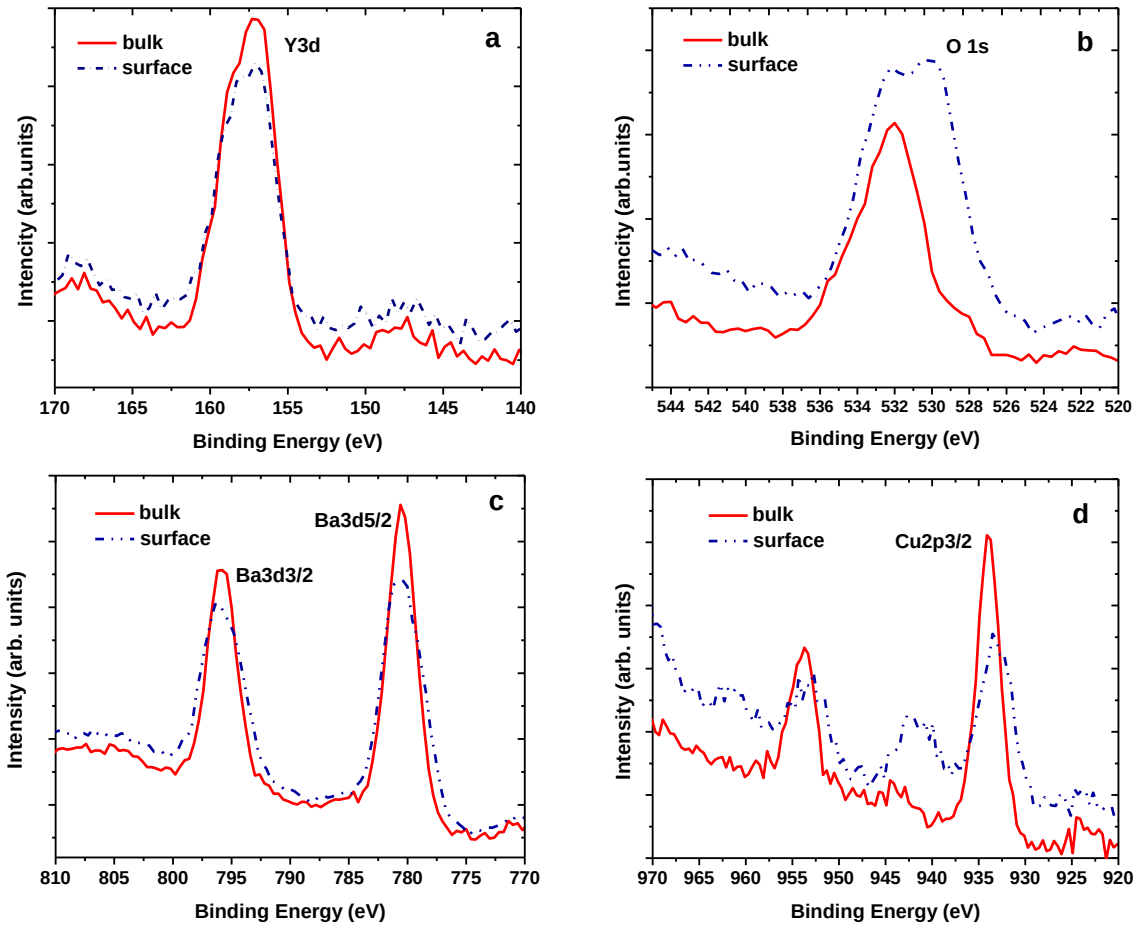

Figure 3.11 XPS spectra of the monitored emission lines of YBCO thin film grown on YSZ substrate: (a) Y 3d; (b) O 1s; (c) Ba $3d_{5/2;3/2}$; (d) Cu $2p_{3/2;1/2}$. The individual core level spectra well agree well with those shown in [7, 8].

Table 3.2 Positions of characteristic XPS lines for YBCO film grown on YSZ substrate.

Electron orbital	Peak Position, eV	Reference Peak, eV [8]
Y $3d_{5/2}$	156.8	156.3
O 1s	532.0	531.4
Ba $3d_{5/2}$	780.6	780
Cu $2p_{3/2}$	933.9	933.3

Figure 3.12 shows typical SEM surface morphologies of the two YBCO films with the same thickness ($h \approx 200$ nm) grown on YSZ and STO substrates with optimal PLD parameters. It can be seen that both films have dense, crack-free surfaces with evenly distributed pores. The average grain size was found to be of about 200-500 nm which is typical for YBCO films deposited by PLD [6].

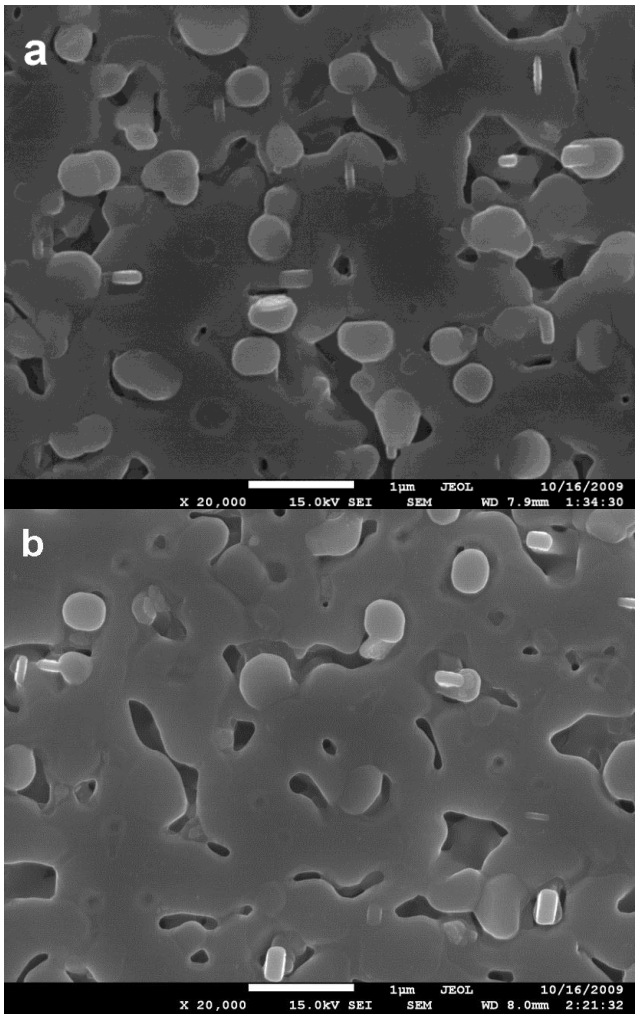

Figure 3.12 SEM image of surface morphology of YBCO film grown on YSZ substrate (a) and STO substrate (b).

To further investigate the chemical composition of observed YBCO films, the *Energy Dispersive Spectroscopy* (EDS) analysis has been performed on various areas of a surface in the positions as seen in Figure 3.13a. Table 3.3 shows quantitative data of EDS. The EDS results (see Fig. 3.13b) show the elemental composition ratio of the YBCO in atomic percentage which is very close to the composition ratio of the bulk $YBa_2Cu_3O_{7-x}$. From the EDS analysis it can be concluded that there is no evidence of impurity traces (except carbon) on as deposited YBCO film. It also reconfirms the result of XPS analysis that all elemental compositions are in a good ratio.

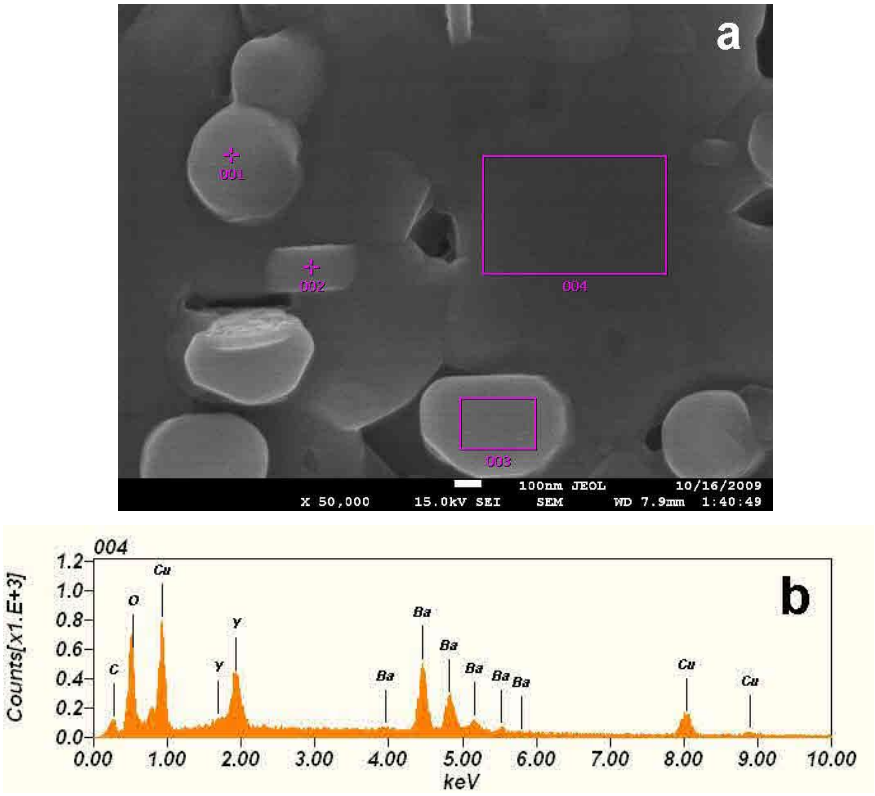

Figure 3.13 SEM image of YBCO film grown on YSZ substrate (a), and EDS spectra of this film (scanned area '004") (b).

Table 3.3 Quantitative elemental analysis of YBCO/YSZ film obtained from SEM-EDS spectrum as seen in Figure 3.3.4.

Chemical	O	C	Cu	Y	Ba
Mass% Area 001	14.66	5.93	24.65	17.93	36.83
Mass% Area 002	10.02	4.66	28.52	15.71	41.09
Mass% Area 003	11.90	4.00	26.89	16.85	40.36
Mass% Area 004	11.10	4.05	27.45	15.91	41.49
Average Mass	11.92	4.66	26.88	16.60	39.94

3.4 Optimization of PLD process for YBCO films by target-substrate distance adjustment

3.4.1 Substrates used for HTS films deposition

Regardless of the details of the film to be deposited, a number of issues are critical in substrate selection for HTS thin film growth. The best HTS films grown to date as determined by critical current density, morphology, and stability over time are epitaxial on their substrates. Epitaxial growth requires the controlled crystallographic orientation of the film with respect to the substrate. In general, this necessitates matching the film and substrate with respect to lattice parameters, atomic positions, crystallographic orientation, etc. The better the match of all these parameters, the more likely high the quality epitaxial growth is to occur. Table 3.4 summarizes main characteristics of widely used substrate for the epitaxy of YBCO thin films.

Table 3.4 Monocrystalline substrates widely used for YBCO films deposition [10].

Substrate	**Structure/ Lattice Constant (A)**	**Melting Temperature (^oC)**	**Thermal Expansion Coefficient ($\times 10^6/^oC$)**	**Dielectric Constant**	**Lattice Mismatch to YBCO (%)**
$SrTiO_3$	Cubic, a = 3.905	2080	10.4	300	0.12
$LaAlO_3$	Rhombo, a = 3.790, c =13	2100	9.2	24.5	2.8
YSZ	Cubic, a = 5.125	~2500	10.3	27	31
MgO	Cubic, a = 4.21	2852	12.8	9.8	7.9

After the simple analysis of the above table $SrTiO_3$ (STO) can be chosen as the best substrate for YBCO deposition because of the smallest lattice mismatch with YBCO. That's why this substrate became very popular for all cuprate thin film deposition. However, STO is may be rejected because of its large dielectric constant if high frequency properties of deposited superconducting film are predominant. The best choice of substrate in this case may be MgO. The superconducting properties of YBCO films grown on substrates with high lattice mismatches (as YSZ or MgO) can be dramatically improved by depositing of a thin STO buffer layer (h ~ 20-30 nm) directly on the substrate surface just before superconducting film deposition [9].

Superconducting properties of YBCO films epitaxially grown on different substrates were investigating. The deposition parameters for all substrate types were fixed as it was shown in Table 3.2. All substrates had an identical size 5×5 mm^2 and the standard cleaning procedure was performed before PLD. In the case of YSZ and

MgO substrates, a thin STO buffer layer was deposited on their surface just before YBCO. The results of this investigation are presented in Fig.3.14 and Table 3.5. They demonstrate one of the most important characteristics of HTS epitaxial film, the critical temperature of superconducting transition T_c, as a function of a substrate type. It can be seen that the best superconducting film with higher superconducting transition temperature and lowest transition width was grown on STO substrate, but superconducting properties of YBCO films deposited on YSZ and MgO substrate buffered with STO are also good enough which makes them promising for future high frequency applications.

Table 3.5 Deposition parameters and properties of YBCO films grown by PLD on different substrates.

Substrate	**YBCO film thickness, nm**	**STO Buffer Layer Thickness, nm**	**Distance substrate-target, mm**	**Critical Temperature T_c, K**	**ΔT_c, K**
$SrTiO_3$	~250	-	75	90	1.2
$LaAlO_3$	~250	-	75	88	2
YSZ	~250	30	75	89	1.8
MgO	~250	30	75	88	1.9

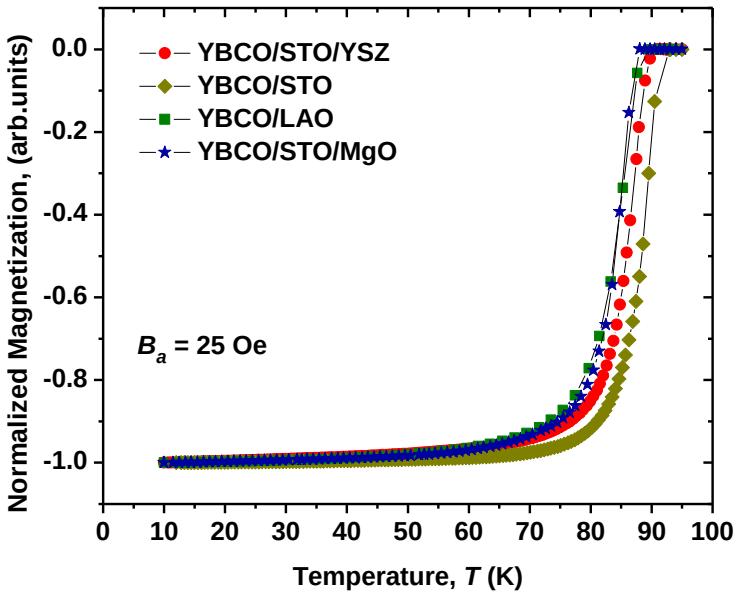

Figure 3.14 Temperature dependence of normalized magnetization M/M(at 10K) for YBCO thin films ($h \approx 250$ nm) grown on different substrates.

3.4.2 Investigation of the influence of substrate-target distance on YBCO thin films quality.

The quality of YBCO thin films grown by PLD technique is very sensitive to deposition parameters such as: oxygen pressure, deposition temperature, annealing temperature, laser fluence, laser energy, and distance between target and substrate. It's necessary to carry out a large number of experiments setting various deposition conditions in order to find the best combination of parameters mentioned above.

In the Table 3.1 main PLD process parameters used by many research groups were already listed. However few characteristics are still individual for each separated PLD setup and vacuum chamber in use. This is the case of the distance between the target and the substrate in PLD chamber which appreciably exerts influence over the superconducting properties of deposited films. In order to find the optimal target-substrate distance the surface morphology, critical temperature of superconducting transition, and critical current density of YBCO films were systematically studied. Three samples YSd1, YSd2, YSd3 were manufactured for three different target-substrate distances d = 65, 75, and 85 mm with the condition that all other PLD parameters were kept unchanged (see Table 3.6).

Magnetic measurements were made using the MPMS. Figure 3.15 shows the temperature dependence of magnetization for different distances d which allows the direct determination of critical temperature T_c and ΔT_c. The critical current density (J_c) of films was deduced from the dependence of magnetization as function of external field at 10 K and 77 K as it was described in Chapter 2.

Table 3.6 PLD process parameters used for YSd samples deposition.

Target	YBCO
Substrate	STO
Laser fluence	5 Hz
Laser beam energy	430 mJ
Substrate temperature	780^{o}C
Background oxygen pressure	300 mTorr

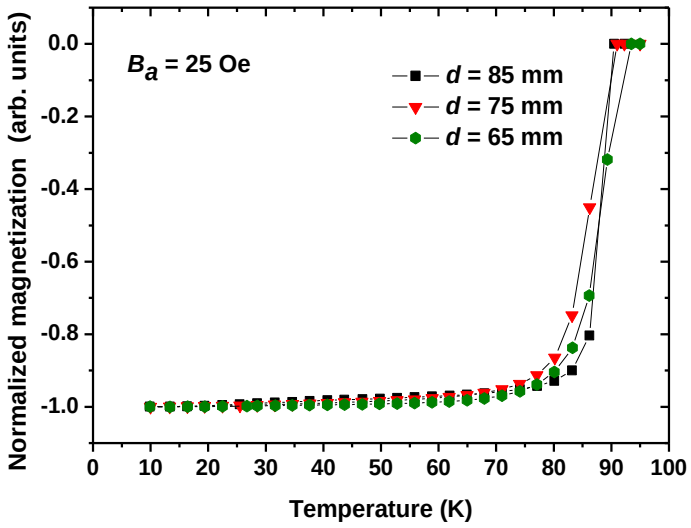

Figure 3.15 Normalized magnetization curves for YBCO/STO films with 200 nm thickness deposited at three different target-substrate distances.

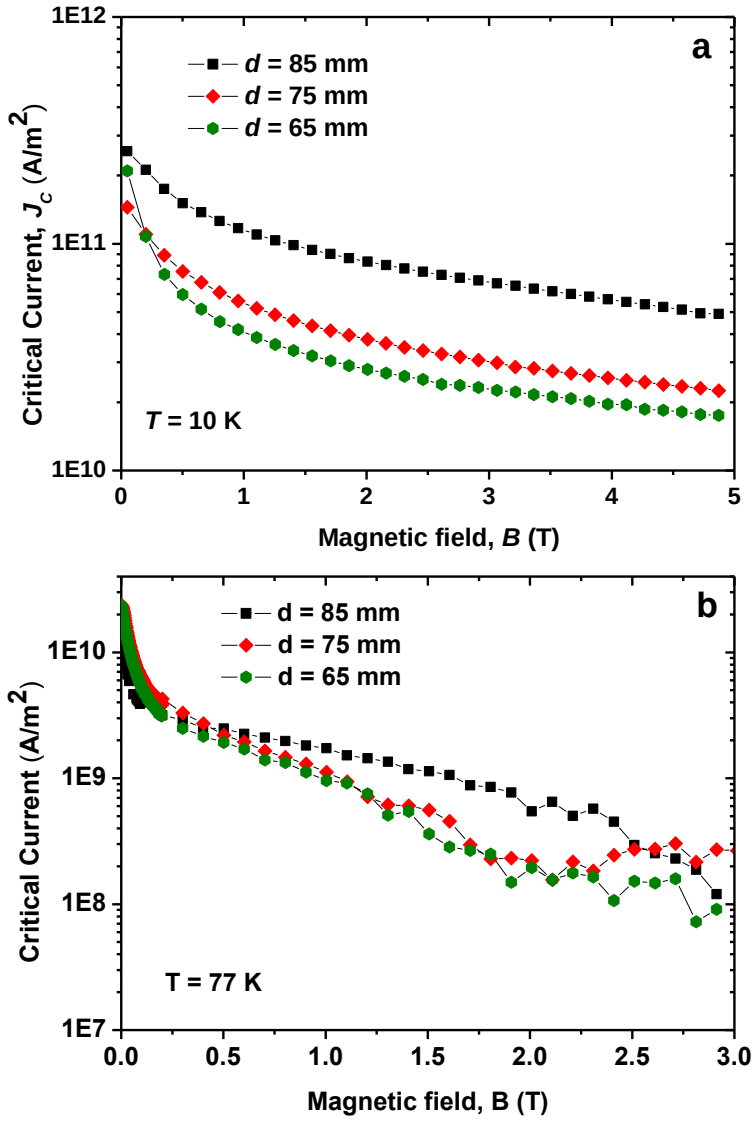

Figure 3.16 Critical current density (J_c) as a function of applied magnetic field for three YBCO films grown on STO substrate with different distances *d*. (a) at T = 10 K, (b) at T = 77K.

Measurements of a critical current density for all samples manufactured in the same PLD conditions except the target-substrate distance *d* are shown in Figure 3.16 and in Table 3.7. All films demonstrate a good quality and there is no any significant difference between their superconducting parameters. For all films, J_c monotonically decreases with increasing applied field.

Table 3.7 Superconducting properties of YBCO/STO samples deposited at different target-substrate distances.

Sample	**YBCO film thickness, nm**	**Distance substrate-target, mm**	**Critical Temperature T_C, K**	**ΔT_C, K**	**J_C(10K) A/m^2**	**J_C(77K) A/m^2**
YSd1	~200	65	91	1.8	2.1×10^{11}	2.4×10^{10}
YSd2	~200	75	91	1.5	2.8×10^{11}	2.4×10^{10}
YSd3	~200	85	91	1.2	2.6×10^{11}	2.2×10^{10}

Although the values of critical current density at zero field as their behavior of all J_c curves at low magnetic fields are almost similar, the decline in J_c for d = 75 mm is somewhat less than that of the other target-substrate distances, which implies that for this distance YBCO film may have stronger flux pinning which is a positive factor for superconductors film quality.

Figure 3.17 shows the SEM surface morphologies of the same three samples YSd1, YSd2, and YSd3 deposited with various distances *d*. Analysis of all SEM images shows that the surface roughness and the density of pores are target-substrate distance dependent. The YBCO film surface morphology can be characterized by the density and shape of existing voids. Their density is a largest for the sample YSd1 deposited at d = 65 mm (see Fig. 3.17 c). The density of voids for the sample YSd3 deposited at d = 85 mm (Fig.3.17 a) is a smallest but their size is much bigger (~300-400 nm) then for the sample YSd1. In contrast, the density of voids is seemingly lower and their size is much smaller for the sample YSd2 obtained at d = 75 mm (Fig.3.17 b). Such morphological evolution has explanation in the frame of the film growth model [11, 12]. In this model the degree of nucleus coalescence depends on the kinetic energy of adatoms on the surface. All particles (ions, atoms, clysters) coming from the plasma plume become the adatoms on the film surface. The shorter the target-substrate distance, the greater is the kinetic energy of coming particles and the bigger is their mobility. The result of this adatoms behavior is an incomplete

coalescence and the formation of voids (pores) between grains. For bigger target-substrate distances the adatomes have lower kinetic energy and they probably fill holes and voids.

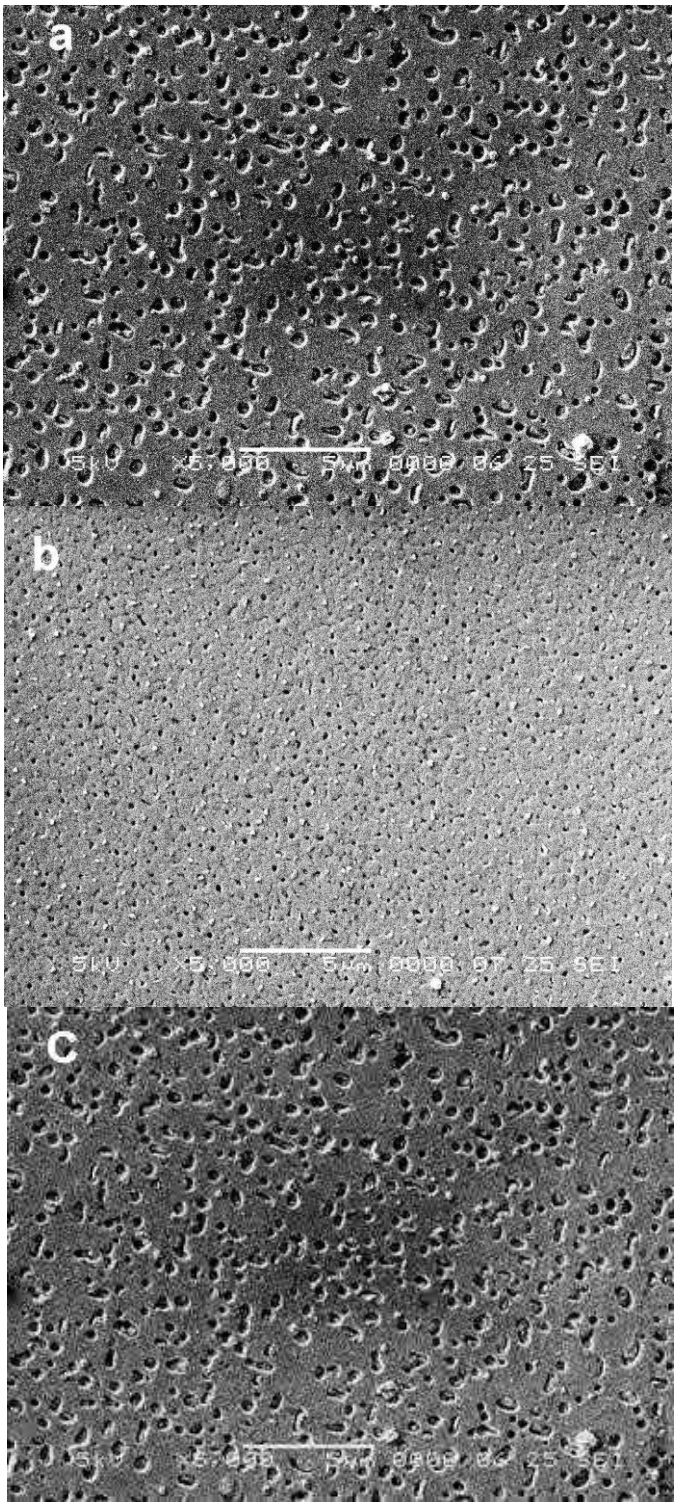

Figure 3.17 SEM images of the surface morphology for YBCO films deposited at substrate-target distances: d = 85 mm (a), d = 75 mm (b), and d = 65 mm (c).

Taking into account the examined superconducting properties and the surface morphology of YBCO/STO films deposited at different target-surface distances we may conclude that the optimal target-substrate distance *d* for given PLD setup must be chosen between 70 and 80 mm. Here we do not concentrate in the influence of surface roughness and porosity of our films on their properties as it was already described in details and particularly discussed in [6, 13] for YBCO films manufactured with help of the same experimental setup.

3.5 Summary

The pulsed laser deposition technique for manufacturing of complex oxide thin films used in this work has been described. Significant modification of existing PLD setup was conducted and the system was completely automated using serial interfaces and LabView software in order to simplify and optimize the process of multilayered films deposition and annealing. Clear and friendly LabView virtual instrumentation was designed. Chemical composition and surface morphology of superconducting films were investigated. It was shown that the modified and automated PLD system allows the deposition of high quality superconducting films on different substrates. In the last section of this Chapter the systematic study of YBCO film quality dependence on the target-substrate distance was performed. The optimal distance for given setup was found to be d = 75 mm. YBCO thin films deposited with this optimal distance have smooth surface morphology and best superconducting properties.

References

[1] http://tfy.tkk.fi/aes/AES/projects/prlaser/thesis/node4.html

[2] Fedoseev S.A., Giannini G., Lagomarsino S., Pyskin S.L. *Applied Surface Science*, **58,** 56, (1992)

[3] Aziz, Michael J. *Applied Physics A: Materials Science & Processing* 93(3): 579-587, (2008)

[4] M. Strikovski and J. H. Miller. *Appl. Phys. Lett.* 73, 1733, (1998)

[5] http://www2.physics.colostate.edu/groups/PattonGroup/systems/pld_desc.html

[6] Pysarenko, S.V; Pan, A.V.; Dou, S.X. *IEEE Transaction on Applied Superconductivity*. **21**, 3, (2011)

[7] A Angrisani Armeni, A Augieri, L Ciontea, G Contin, I Davoli, V Galluzzi, at all. *Supercond. Sci. Technol.* **21,** 125015, (2008)

[8] C. R. Brundle and D. E. Fowler *Surf. Sci. Rep*. 19, 143, (1993)

[9] V. Boffa, T. Petrisor, L. Ciontea, U. Gambardella, S. Barbanera *Physica C*, 260(1):111-116, (1996)

[10] [http://www.mtixtl.com/superconductfilmsubstrates.aspx]

[11] P.E. Dyer, A. Issa and P.H. Key, *Appl. Surf. Sci.* **46** 89, (1990)

[12] P.E. Dyer, at al. *Appl. Phys. Lett.* **57**, 186, (1990)

[13] Serhiy Pysarenko. Multilayering approach to enhance current carrying capability of YBa2Cu3O7 films. Manuscript of PhD Thesis, University of Wollongong, (2010).

Chapter 4

Investigation of HTS multilayered device structures for practical applications

4.1 Step-Edge Josephson Junctions based on multilayered High Temperature Superconducting thin film

4.1.1 Introduction to Josephson Junctions Technology

Josephson junctions based on high temperature superconducting (HTS) thin films are an important component of superconducting electronic devices (SQUID-based magnetic sensors [1–4], THz imaging application [5], qubit implementation [6], etc.) working at 77 K. These applications requires the technology of reproducible HTS-based Josephson junctions (JJs) with minimum spread of junction parameters. To satisfy this, different types of JJs, such as bicrystal [7], bi-epitaxial [8], [9], narrow constriction [10], ramp-type [11], step-edge [12] had been engineered. Among them, the step-edge JJ distinguishes itself by a remarkable simplicity of fabrication and low cost as well as the flexibility of positioning the JJs anywhere on the substrate. In order to fabricate HTS JJs with similar electrical parameters, researchers need to stick with a particular process as the junction's electrical properties largely depend on the fabricating parameters such as HTS film thickness, step angle and HTS film deposition technique.

The important aspects of the JJs for electronic applications are non-hysteretic $I - V$ characteristics, reproducible junctions parameters (critical current, I_c , and normal resistance, R_n), and a high I_cR_n product, which sets the upper limit for device operation [13]. These issues are well established in the JJs made of low temperature superconducting materials, but less mature for HTS Josephson junctions. It is mainly due to the small coherence length, unconventional symmetry of the order parameter and the complexity of structural characteristics peculiar to HTS materials, which lead to strong influence of the microstructure on the transport properties of HTS [7].

In order to fabricate robust high-T_c JJs, HTS thin films with high critical current, good crystallinity and smooth surface are required. Among the techniques developed for thin film deposition: DC and RF sputtering, Molecular Beam Epitaxy,

Electron Beam Evaporation (EBE), and Pulsed Laser Deposition (PLD), PLD produces (YBCO) thin films with the highest critical current densities [16]. The additional benefit of the PLD technique is that it allows growth of heteroepitaxial multilayers. However, YBCO films grown by laser ablation show a certain level of porosity and outgrowths. Poor surface quality is mainly due to an island growth mode [16], [17] of YBCO on most of the substrates.

To improve the morphology of the YBCO epitaxial film grown by PLD, Marre *et al.* [18] lowered the deposition oxygen pressure down to 5×10^{3} mbar (reaching the so-called MBE conditions [19]) and fabricated atomically smooth YBCO films of 20–100 nm thick on $SrTiO_3$ substrates. They claimed a transition temperature for their films of 88 K and critical current density, J_c, of 8×10^{10} A/m^2 at 4.2 K.

However *Pan at al.* [15], have demonstrated the improving of the surface quality and the enhancing of superconducting properties for thick (~1μm) YBCO thin films by the introduction of an intermediate NdBCO superconducting layer. This multilayered approach improves the film morphology, creates additional defects and enhances the critical current density of thick YBCO films. Critical temperatures of monolayer YBCO and multilayer YBCO/NdBCO/YBCO films deposited on substrates $SrTiO_3$ were around 91 K, and J_c values observed for 1 μm thick films were 3×10^{10} A/m^2 and 5.5×10^{10} A/m^2 at 77 K and 10 K, respectively. In this section, we present results of a multilayered approach for the fabrication of YBCO-based step-edge Josephson junctions, and discuss its impact on electric and microstructural properties of fabricated step-edge junctions.

4.1.2 Details of the Experimental Procedure

Step edges were made on 10 ×10 mm^2 MgO (100) substrates using the techniques described in [14]. The step angle and height were around 35^o and 400 nm, respectively. The *single layer* YBCO (MN) and *multilayer* YBCO/NdBCO/YBCO (ML) thin films both have thickness of 210 nm (85 nm/40 nm/85 nm for ML sample) were deposited at a temperature of 780^o by PLD technique and annealed at an oxygen atmosphere at 400^o [15]. Step-edge superconducting junctions were patterned

using a standard photolithographic process and ion beam milling. Each sample contains four junctions with width of 3 μm patterned over a step-edge on MgO substrate, and a 50 μm micro-bridge for measuring superconducting transport properties of the thin film. Figure 4.1.1 shows typical image of samples after photolithographic patterning. The gold pads, shown as bright squares in Fig.4.1, were deposited in order to assure good electric contact between the sample and a testing probe.

Microstructure was studied by Field Emission gun Scanning Electron Microscope (FESEM). Current-voltage characteristics at 77 K and 4.3 K were measured by a four-point technique. Critical current and normal resistance values were determined from I –V curves. I_c corresponds to the onset of voltage at 5 μV; R_n was defined from the resistive part of the I –V curve using linear fitting in the region, where $I >> I_c$.

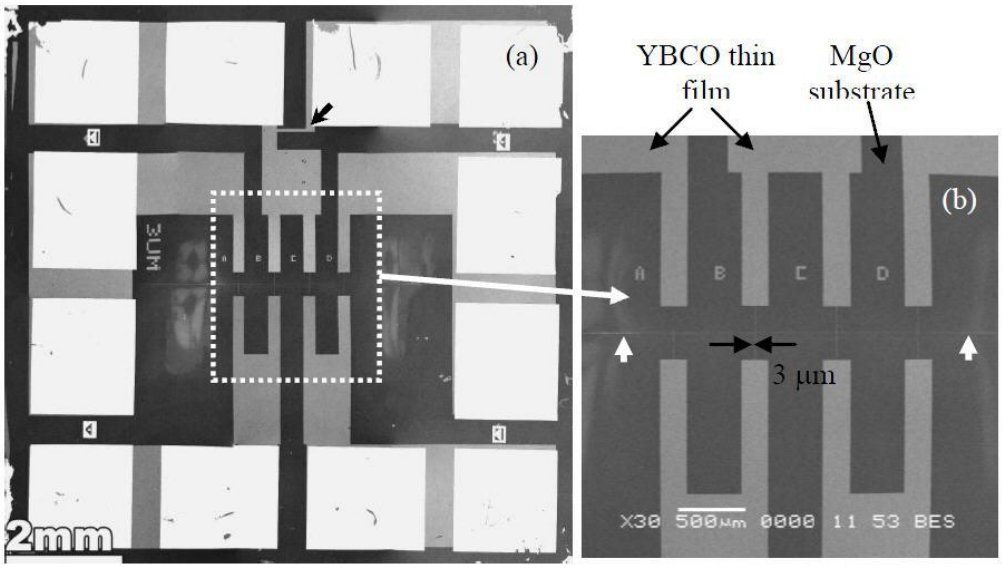

Figure 4.1 (a) SEM image of the superconducting chip after patterning. The black arrow indicates location of the 50 μm micro bridge. (b) Sample contains 4 junctions (A-D) crossing the step-edge on MgO substrate marked by white arrows.

4.1.3 Properties of single layered and multilayered Josephson Junctions

The critical temperature of about 88 K was obtained for both single - YBCO and multilayered Y/Nd/YBCO films after deposition. This is slightly lower than values reported in [15]. It is due to larger mismatch of lattice parameters between MgO substrate and YBCO film (9% [20]) compared to 1.4% misfit for YBCO film and STO substrate, used in [15]. Table 4.1 summarized the electrical parameters of the measurements. Transport critical currents of 155 and 255 mA were measured at 77 K in MN and ML 50 μm wide bridges (denoted as "mb" in the table), respectively. These values correspond to critical current densities of 1.47×10^{10} A/m^2 for YBCO and 2.43×10^{10} A/m^2 for Y/Nd/YBCO samples. In [15] it was demonstrated that the introduction of multilayer Y/Nd/YBCO film structures results in the enhancement of magnetic J_c value [J_c(0 T,77K) = 2.9×10^{10} A/m^2] compared to J_c of the single layer YBCO film [J_c(0 T,77K) = 2.0×10^{10} A/m^2], both having a large thickness of 1μm. Thus, there is a good correlation between the magnetic and transport J_c values for single layer and multilayer samples (taking into account different measurement techniques and the substrates used).

Transport I –V characteristics of 3 junctions (namely A, B, C for SL and B, C, D for ML) on each sample were measured at 77 K and 4.3 K and presented in Figs. 4.2 and 4.3. Although the critical current of the single layer YBCO film is sufficiently high, the critical current of the junctions is very small and could not be detected at 77 K [Fig. 4.2 (a)]. All junctions made on the single layer YBCO film have value in the range of 240–300 Ω. In contrast, the 77 K I –V curve for the ML junctions shows a well-defined Josephson junction-like behaviour [Fig. 4.1.2 (b)]. The I –V characteristics fit very well with the resistively shunted junction (RSJ) model [21]. The I_c values of 22 – 8 μA are measured, whereas R_n values obtained from the fit vary from 6 to 8.8 Ω. Significant excess current is commonly observed in HTS junctions [7]. Here we estimate the excess current (I_{exc}) of ML_B junction of 0.015 mA from the curve and the calculated value of I_cR_n is 0.038 mV after subtracting the excess current from the measured I_c.

TABLE 4.1 Electric properties of single layer (MN) and multilayered (ML) junctions

Sample	I_c, mA 4.3 K	$J_c \times 10^8$, A/m^2 4.3K	I_cR_n, mV 4.3 K	I_c, mA 77 K	$J_c \times 10^8$, A/m^2 77K	I_cR_n, mV 77 K
MN_A	0.012	0.21	2.08	0	-	-
MN_B	0.013	0.23	2.08	0	-	-
MN_C	0.013	0.23	2.08	0	-	-
MNmb	-	-	-	155	147	-
ML_B	0.85	15	5.50	0.022	0.32	0.120
ML_C	0.57	10	6.80	0.010	0.16	0.075
ML_D	-	-	-	0.008	0.13	0.064
MLmb	-	-	-	255	243	-

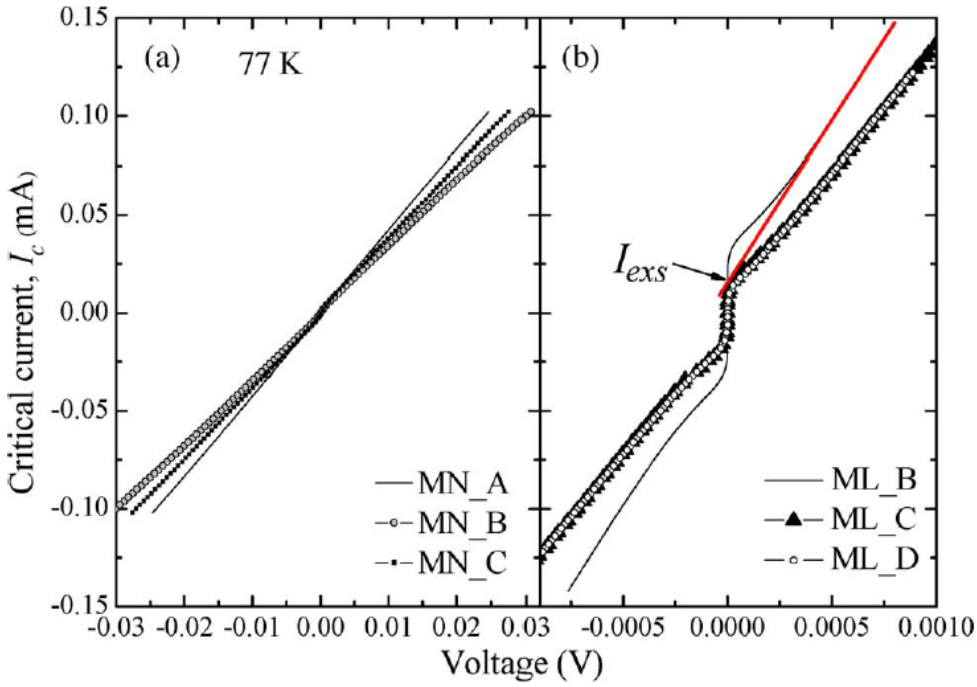

Figure 4.2 *I –V* curves of 3 μm bridges at temperature of 77 K for single layer (MN) YBCO (a) and multilayered (ML) Y/Nd/YBCO (b) thin films. Straight line in (b) is used for extrapolation of excess current I_{exc} for ML_B junction.

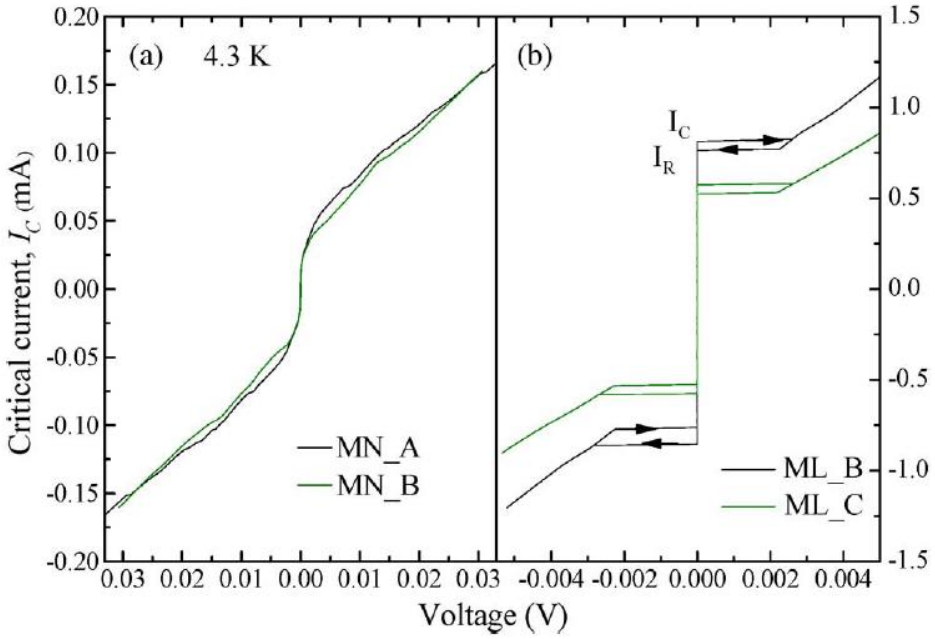

Figure 4.3 *I –V* curves of 3 μm bridges at temperature of 4.3 K for single layer YBCO (a) and multilayered Y/Nd/YBCO (b) thin films.

The measurements at 4.3 K reveal the existence of the Josephson effect in junctions made on the single layer YBCO sample [Fig. 4.3(a)]. However, I_c values are very small, about 0.012 mA (Table 4.1). The normal resistance of these junctions is 173 Ω, resulting in an I_cR_n value of 2.08 mV. For the ML junctions at 4.3 K, I_c increased dramatically from its 77 K value [Fig. 4.3(b)]. Hysteretic *I –V* curves were obtained suggesting that these junctions are underdamped with the Stewart-McCumber parameter [$\beta_c = (4I_c/\pi I_R)^2$] [22] of 1.85 and 1.94. The R_n value of these junctions is 6–12 Ω. The junction capacitance, C_j, of 5–7.6 fF is estimated from the equation $\beta_c = 2eI_cR_n^2C_j/h$ [21]. It is worth noting that the I_cR_n values of 5.5–6.8 mV (at 4.3 K) and 0.06–0.12 mV (at 77 K) observed in multilayered Y/Nd/YBCO sample (Table 4.1) are suitable for the fabrication of SQUIDs [2], [13] and other JJ based electronic devices. This value is comparable to step-edge junctions in which the YBCO films were deposited by the EBE technique [12].

The microstructure of both MN and ML junctions has been investigated and their FESEM images are presented in Fig. 4.4. As can be seen, both types of film have voids on the surface, but their sizes are different in these films. The single layer YBCO film has larger holes [up to 1 μm, Fig. 4.4(a)] than the multilayer sample [up to ~ 0.4 μm, Fig. 4.4(b)]. This porous morphology of YBCO film surface is due to

spiral growth of YBCO compound [16], [17]. This is consistent with previous observations, where it was demonstrated that multilayer approach for film fabrication enables improved conditions for film growth and relaxation of strain in the YBCO crystal lattice. This resulted in the formation of YBCO-based films with improved surface roughness and critical current density. However, it is very likely that the surface can be further improved as the substrate and thickness of these films are different than those showing smooth, dense surface in [15].

It is remarkable, that the step-edge junctions fabricated on the two types of YBCO-based superconducting films of similar thickness demonstrate strikingly different electrical characteristics (Figs. 4.2 and 4.3). Although there is a difference of 40% in the film J_c value, it cannot account for the large discrepancies on the junction parameters with a difference in J_c of ~2 orders of magnitude. In addition, the characteristic grain boundary resistivity, R_nA (A is the junction area) of junctions in MN and ML sample are of the order of 1×10^{-10} and 4×10^{-12} $\Omega\cdot$m, respectively. The R_nA value of the ML junctions is similar to the value of junctions fabricated by EBE technique, but the R_nA value of the SL junctions is 15 times larger.

TEM images of the EBE step-edge junction showed that a grain boundary junction of 1–2 nm thick is formed in the YBCO film on the top of the step [12]. The question is that if there is any difference on the thickness of the boundary or its properties which affect the J_c and R_nA values of single- and multilayered samples. Possible reasons for the much lower in the SL junctions are formation of many parallel small junctions and the faceted-microstructure of thin film along grain boundary [7], [23]. In combination with the *d*-wave symmetry, the Josephson current will flow in opposite direction in parallel small junctions with additional π phase shift, resulting in a large reduction of the net Josephson current across the width of the junction [23], [24].

There is a distribution on the size and angle of the faceting effect on the crystal orientation and hence, the Josephson current distribution is highly non-uniform. The critical current-magnetic field dependence becomes anomalous with a maximum critical current at non-zero magnetic field.

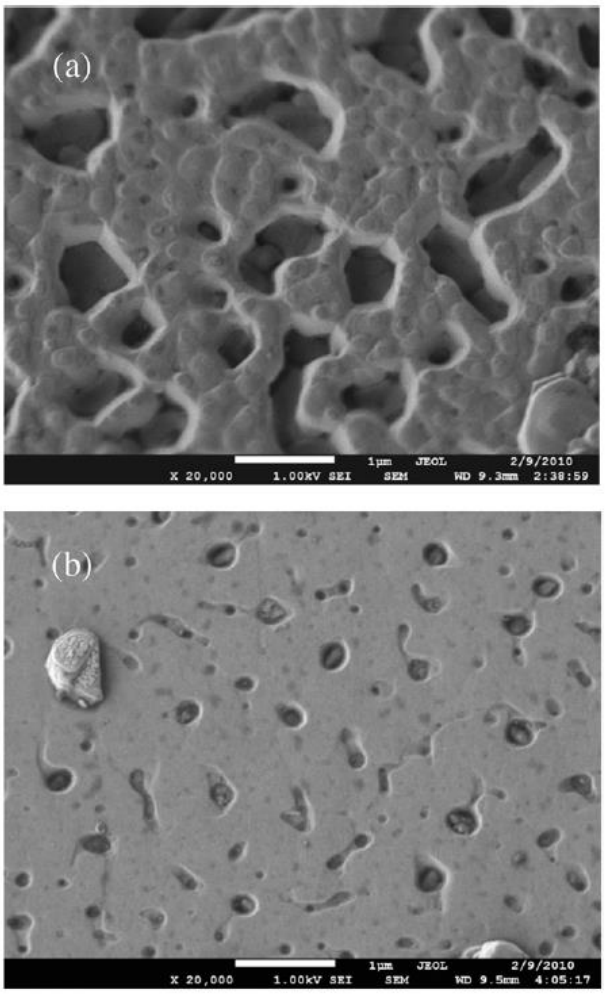

Figure 4.4 SEM images of the surface morphology of single-YBCO (a) and multilayered Y/Nd/YBCO (b) thin films.

This is found in the SL junctions as shown in Fig. 4.5, in contrast with the ML junctions. The maximum I_c peak for ML_B junction is also slightly shifted from zero magnetic fields, however, this shift is attributed to magnetic flux trapped in the junction during I_c (B_a) measurements. The results observed suggest that there may be a difference on the crystal growth orientation near the grain boundary between the single layer and multilayers samples.

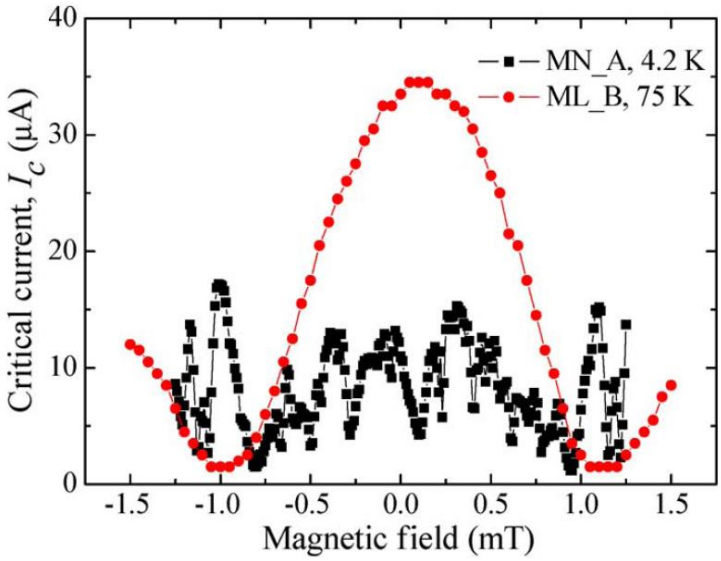

Figure 4.5 A plot of the critical current dependence on the magnetic field of the step-edge junction MN_A (single layer YBCO) and ML_B (multilayered Y/Nd/YBCO).

4.2 Development of Energy-Efficient Cryogenic Leads with High Temperature Superconducting Films on Ceramic Substrates

4.2.1 Introduction

Energy efficiency has become the dominant parameter for the design and implementation of the next generation of computing and communication systems. The next generation of supercomputers, the Exascale supercomputers, will not be feasible unless the energy-efficiency of the core digital and memory technologies and overall computing system are radically increased [25]. Cryogenic superconductor single flux quantum technology (SFQ) is viewed as a technology capable of drastically higher energy efficiencies than other technologies [26]. For any cryogenic electronics, an energy-efficiency of the integrated system is very critical. Power savings obtained by using energy-efficient electronic technologies will be wasted, if the system design is not optimized for low power. Achieving high overall systems efficiency involves optimizing power delivery to cryogenic electronics modules, input/output data interconnect, efficient cryopackage and cryocooler designs. The optimum placement of various system elements and technologies at different

temperature stages following the hybrid temperatures, hybrid technologies (ht2 or HTHT) integration principle [27] can be used to achieve the lowest overall heat load and overall power consumption for the cryocooler [26]. One of the significant heat loads for the cryocooler is related to the heat generation and conduction from higher-temperature to the lower-temperature stages via the network of cables required to deliver power to run cryogenic electronics. For normal metal cables, the minimum heat load Q_{bmin} for a particular value of the bias current I_b delivered between two different temperatures can be obtained by following the Wiedemann-Franz (WF) law connecting Joule heating and thermal conduction by electrons [28]. For a typical two-stage cryocooler, the WF-optimised specific heat load for delivery of bias current from the 50 K stage to the 4 K stage will be Q_{bmin} /I_b = 7.8 mW/A [29, 30]. This is too high to be acceptable for the energy-efficient optimised cryogenic systems. A YSZ substrate has the additional advantage that it can be used for high frequency RF applications unlike the prohibitively lossy conducting Hastelloy used in previous DC lead work.

Fortunately, the WF is not applicable to superconductors. High temperature superconductors (HTS) can significantly lower the overall heat loads at the 4 K stage that houses Nb-based superconductor integrated circuits due to their low thermal conductivity and resistance-free DC current transport. A multi-line flexible HTS cable made using a commercially-available YBCO coated tape on Hastelloy substrate was successfully demonstrated [29]. For this cable, the heat leak measured per YBCO line was 1/10th of that for optimised leads made from normal metals for the typical values of bias currents used for the RSFQ integrated circuits. In order to achieve this low heat conduction, a silver coating was removed from the commercial tape, so the heat was conducted through the unpatterned Hastelloy substrate. Recently, a different method was used in order to reduce heat transport via the substrate. The Hastelloy substrate was cut into strips by dicing [30]. This allowed the reduction of heat load. For further reduction of parasitic heat flow to the 4 K thermal stage, it is necessary to use a less heat conductive substrate. The natural choice for such substrates is flexible yttria-stabilized zirconia (YSZ). Such substrate was successfully used to fabricate flexible multi-line cable using medium-temperature superconductor material MgB_2 [31]. However, its lower operation temperature (< 30 to 35 K) limits the applicability of such cable to practical 4 K electronics systems. In

this section, we describe design, fabrication process, and measurements of YBCO cables made on low heat conductive flexible YSZ substrate. These cables capable of operating at temperatures up to 70 K can match the needs of energy-efficient superconductive system integration.

4.2.2 Experimental details

In Chapter 3, it was demonstrated our ability to grow high quality YBCO films and REBCO multilayers by pulsed-laser deposition with the help of KrF Excimer Laser (248 nm) on (100) $SrTiO_3$ (STO) or similar substrates in oxygen atmosphere of 300 mTorr in a quite standard 45 cm diameter vacuum chamber equipped with a three dimensional sample heater manipulator [32]. The distance between REBCO target and substrates was about 75 mm, although depending on substrate employed and the distance *d* the electromagnetic and structural properties of the films can substantially be changed [33]. The optimal deposition temperature (at which the highest J_c(0; 77 K), highest critical temperature (T_c) and the sharpest superconducting transitions are obtained for the YBCO films was found to be 780^o C. The critical temperature T_c = 90 ± 1 K is typical for so-deposited YBCO films and REBCO multilayers. The typical J_c values at T = 77 K are of about 2.5×10^{10} A/m^2. These values form our standard. The optimal thickness (with the same criterion as for deposition temperature) was found to vary from 0.1 to 0.4 μm. However, the criteria of the optimal thickness are quite different for microwave applications and determined by the penetration depth (λ).

To characterise films obtained in this work, we employ Quantum Design Magnetic Property Measurement System (MPMS) 5XL which has allowed us to measure magnetization (M) curves as a function of temperature (T) and applied magnetic field (B_a). In addition, the transport current measurement insert has been developed which allows us to directly measure critical current and T_c by means of the standard four terminal techniques. The limitation of this method is the current which can be flown through the current leads, which should not be higher than 0.1 A. As a consequence, it is impossible to measure critical currents at temperatures much lower than about 80 K, even after patterning the films by optical lithography into the narrow bridges of 50 to 200 μm wide. A standard criterion of 10^{-6} V/cm has been

used for determining the transport critical current, which can now be changed to match the results obtained by different techniques (for example, magnetisation measurements and transport measurements) [34].

4.2.3 Development of long sample deposition and measurement techniques

The existing PLD chamber has allowed us to deposit only rather small thin films of about 1×1 cm^2 without a strong change in superconducting properties and thickness towards the edges of the films. Hence, in order to obtain a long (7 cm to 10 cm) YBCO films a considerable modification of the deposition process has been undertaken. Fig. 4.6 shows the schematics of the modified PLD chamber which shows the long substrate attached to the special gearing mechanism driven by a stepping motor, which is controlled through a computer interface with variable speed and motion patterns. An optimisation process has determined that the sample drive speed of 5 mm/min provides films with the properties similar to those obtained with the fixed heater stage. Here we report the results obtained for the films deposited directly on 8 cm to 10 cm long YSZ single crystal substrates of 10 mm wide and 0.5 mm thick. The most challenging part of the design was the sample heater which would allow us to control the deposition temperature with high accuracy and reproducibility. A few designs is been trialled which included single and multiple halogen lamp radiation heaters, as well as resistive heaters with different number of heating elements. The resistive heater with two and three heating elements turned out to be the most successful, accurate, homogeneous, and reproducible. The problem of the homogeneous heating arose due to the fact that with the resistive heating elements the contact between the substrate to the heater surface determines the actual deposition temperature. Hence, substrates have to be well attached to the heater surface. However, this leads to a possibility of breaking the long sample upon removal them from the heater. The special clamping mechanism on the H-shape heater design with the heating elements on the sides of the substrates has satisfied all the requirements to the setup. A typical deposition run for about 45 min to 60 min with the pulsed laser frequency from 5 Hz to 10 Hz with a growth rate of about 40 nm/min results in a 200 to 400 nm thick YBCO films.

The patterning of 1 to 100 μm wide stripes for multichannel signal transmission has been created by optical lithography (Fig. 4.7). Both wet (chemical) etching and dry (ion) etching of the YBCO films have been attempted. Wet etching is rather simple procedure, so it is tempting to employ it in the first instance. However, as can be seen in the images taken with the help of an optical microscope shown in Figure 4.7, the quality of the film edges in the wet etching procedure is considerably rougher than those obtained by dry etching. In fact, the roughness of the wet etched edges is of the same magnitude (~2 - 4 μm) as the line width (3μm) obtained by the dry etching process. Using wet etching, it is difficult to obtain a reasonable quality pattern features with dimensions < 25 μm. Gold pads on the stripes for connectorizing the signal leads has also been deposited by PLD in vacuum of about 10^{-6} Torr at temperature 200^{o} C employing lift-off lithography procedure. A typical thickness of the gold pads is of 100 to 200 nm thick. In order to measure the properties of the films obtained over the entire deposited length, a special insert into a continuous flow cryostat has been designed which enables critical temperature and critical current measurements of long samples by means of the four terminal transport technique at a certain temperature.

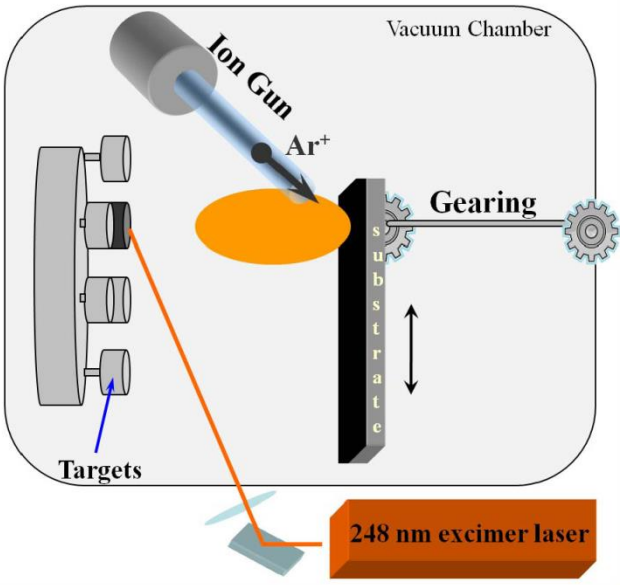

Figure 4.6 Pulsed laser deposition technique modified to produce films of up to 10 cm long.

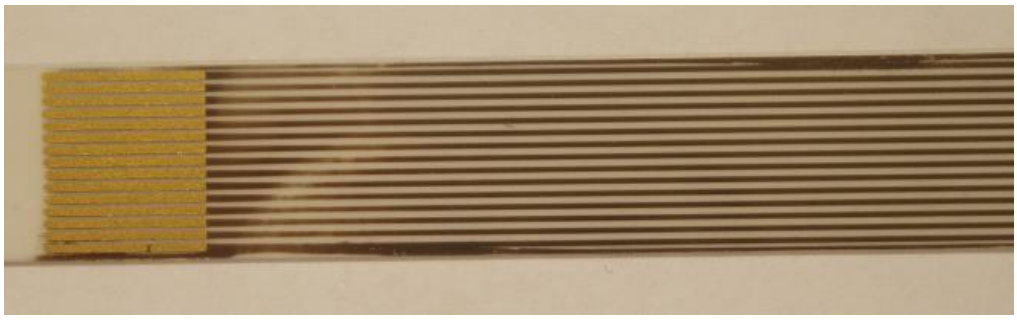

Figure 4.7 A long sample obtained in the modified PLD chamber with patterned stripe features of 100 μm wide. The gold padding on the left hand side of the sample is clearly seen.

4.2.4 Results and discussion

As long substrates (including YSZ) are rather expensive to use for optimization procedures, we have used small YSZ substrates of 3×3 mm^2 or 5×5 mm^2 during the optimization process. Fig. 4.8(a) shows the results of the final optimization stage with the small samples, which were mounted with silver paste on the long heater at three different positions (in the middle, at the upper end, and the lower end) and deposited simultaneously with the oscillating heater at 780^o C driven by the stepping motor. All three samples shows very similar onset of the critical temperature T_c = 90.0±0:6 K, while the width of the superconducting transition is broader for the sample situated at the ends. Because of the similarity of the broadening, we attribute it to the changes in temperature homogeneity of the long heater due to the edge effects.

Heat transfer is likely to be different in the centre of the heater and its ends. However, the problem with this optimization procedure based on the deposition of individual small samples is the mounting procedure. The small substrates were attached to the heater surface by the silver past providing strong heat exchange, while the long substrate is mounted by the end clamping, so that the contact heat exchanged is considerably reduced. This leads to the temperature difference between the heater surface and the substrate surface of up to 100^o C to 200^o C. Hence, a further corresponding optimization was necessary. The result of the resistivity measurement of the superconducting transition in a long sample over its nearly entire length is shown in Fig. 4.8(b).

A typical small piece of the long sample taken from about ±3.5 cm from the middle point shows the critical current density (J_c) dependence on the applied magnetic field (B_a) which is similar to the best available YBCO films with J_c(77K; 0) ≈ 2.4×10^{10} A/m^2 [Fig. 4.9(a)]. This value entirely satisfies the application demand of the heat switch link for DC signals and digital electronics. Moreover, the surface resistance of different films have been measured to ensure their characteristics for data transfer at Gigahertz frequencies. A 2×2 cm^2 films of 420 nm thick exhibited the surface resistance R_s = 4.3 μOhm at 1 GHz and 77 K. The temperate dependence of the surface resistance for a smaller film of 1×1 mm^2 and 500 nm thick measured at the resonance frequency of 25 GHz is shown in Fig. 4.9(b). However, this film might be exposed to some degree of degradation during measurement handling, which may be seen in a steep rise of the surface resistance at relatively low temperatures.

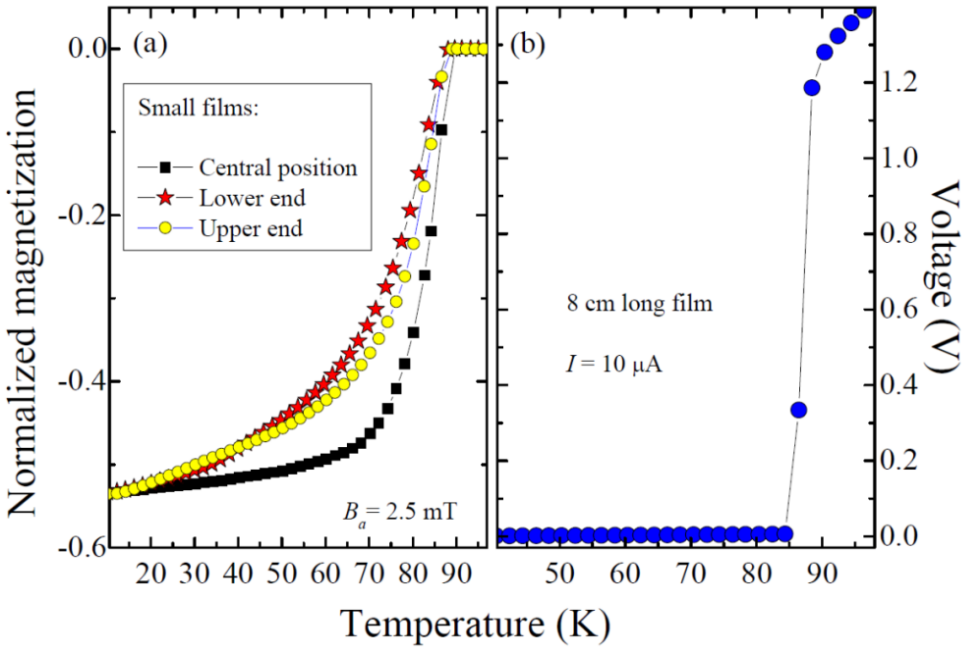

Fig.4.8 Superconducting transitions measured by (a) magnetization dependence on temperature for three different positions on the long heater: in the centre of the heater and at the two opposite (upper and lower) ends of the heater, (b) voltage dependence on temperature over the entire length of 8 cm long YBCO film.

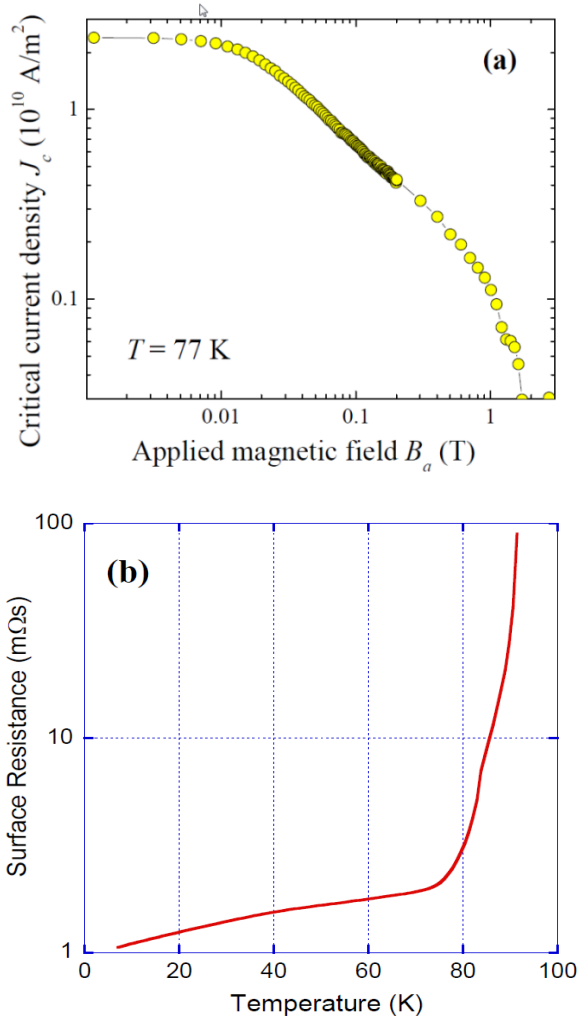

Figure 4.9(a) Critical current density as a function of applied field for a piece of the film cut from the long sample measured at 77 K. (b) Surface resistance measurement as a function of temperature at 25 GHz for a 500 nm thick 1×1 cm^2 YBCO film.

4.3 Investigation of possible application of multilayered HTS films with reduced thickness for Superconducting Single Photon Detector

4.3.1 Introduction

Recently, the ultimate sensitivity for low light level systems has been provided by a new class of nanowire Superconducting Single Photon Detector (SSPD) [35, 36].

These devices outperform other superconducting photon counters and are significantly better than commercially available semiconducting Si and InGaAs avalanche photodiodes [37]. To date, single photon sensitive detectors have been based on Nb and NbN superconducting thin films operating at 2.6 K or 4 K [38, 39]. There would be operational advantages in utilizing $YBa_2Cu_3O_7$ (YBCO) superconducting thin films operating up to 77 K, which would allow substantially relaxed (by modern cryocoolers) cooling requirements. However, for the potential to be realized, there is a need to develop methods of preparing nanoscale YBCO structures with a high degree of structural perfection. YBCO films of various thicknesses have been previously extensively investigated [40–43]. Superconductivity in the ultrathin films has shown to be present for thicknesses as small as 1 unit cell [41], but with the critical parameters which are much less than those on thicker (up to micrometer size) films [43]. However, several previous study demonstrated that multilayering approach (i.e. alternation of YBCO layers with other superconducting $NdBa_2Cu_3O_7$ [44–46]) or non-superconducting ($PrBa_2Cu_3O_7$ [41], Nd_2CuO_4 [43], CeO_2 [47]) materials drastically improve superconducting properties and morphology of final YBCO film. In spite of relatively thick (up to 1 μm) samples investigated, this approach may be viable for improving superconducting properties of YBCO films at smaller (a few nm) thickness [48]. Being attracted by the idea of possible fabrication of SSPD from YBCO films [49, 50], we have initiated study of structural and electromagnetic functionalities of laser ablated YBCO thin films with reduced (from optimal 250–300 nm for our technological process down to 28 nm) thickness. We have also investigated effect of multilayering approach on properties of YBCO films at the thickness down to 44 nm.

4.3.2 Experimental details

The epitaxial, *c*-axis oriented monolayer YBCO and multilayered YBCO/SmBCO/YBCO (where SmBCO denotes $SmBa_2Cu_3O_7$) thin films were made by pulsed laser deposition using the procedure described in Chapter 3. Bulk superconducting targets (YBCO or SmBCO) were ablated for different lengths of

time in order to fabricate films with different thicknesses (Table 4.2). The laser pulse repetition rate was fixed to 1 Hz for all samples. After deposition, films were annealed at 400^{o}C for 1 h at 1 atm of oxygen. The multilayered films were deposited with equal thickness layers of YBCO, SmBCO, and YBCO in this particular order.

Superconducting properties (critical temperature, magnetic moment) of the films were investigated in the Magnetic Property Measurement System (MPMS, Quantum Design). Distribution of magnetic flux in the films was studied by Magneto-Optical Imaging (MOI) at a temperature of 10 K. Images were acquired by a computer- controlled CCD camera with the magnetic field applied perpendicular to the sample surface. The morphology of the films was studied with the help of the Scanning Electron Microscope (SEM). The thickness measurements were carried out using a Dektak 6 M Stylus Profiler. The errors given in Table 2 are the 95% confidence limits (determined by twice the standard deviation) of the 5 measurements taken for each sample.

Table 4.2 Samples investigated.

Composition	Deposition time (s)	Film thickness, nm	Abbreviation
YBCO	500	90 ± 14	Y90
YBCO	350	60 ± 13	Y60
YBCO	250	28 ± 8	Y28
YBCO/SmBCO/YBCO	500	90 ± 15	Y/Sm90
YBCO/SmBCO/YBCO	350	58 ± 7	Y/Sm58
YBCO/SmBCO/YBCO	250	44 ± 7	Y/Sm44

4.3.3 Results and discussion

The surface morphology of the films studied is presented in Fig. 4.10. As can be seen, the Y28 sample has large cavities on the surface of the film (shown by arrows in Fig. 4.10a). This implies that the amount of ablated particles was insufficient to achieve full covering of the substrate area (5×5 mm^2). As the deposition time (and thus the thickness of the film) increases, more material arrives; thus, the film continuously covers the surface of the substrate, and becomes notably smoother (Fig. 4.10b and c).

The Y/Sm44 sample shows the most inhomogeneous morphology among all samples studied (Fig. 4.10d). Note that the thickness of each layer in this sample is as thin as ~14 nm. We speculate that the first YBCO layer at this thickness consists of many separated islands. This growth mode likely affects growth of the following SmBCO and YBCO layers, and results in observed high level of inhomogeneity and roughness of the final film. However, as the thickness of each individual layer increases, the morphology of the films improves (Fig. 4.10e and f). This is consistent with data presented in [15] for YNBO/NdBCO miltilayered structures. It was shown there that the proposed multilayerd approach may significantly improve smoothness of the film surface, which is likely to be the result of the defect formation and corresponding strain release of the entire crystal structure in the multilayers.

There are no large voids on the surface of ≤ 90 nm thick films in contrast to thicker (≥ 250 nm) YBCO films [10]. Indeed, initially strong adatom-substrate bonding results in layer-by-layer growth of the YBCO film on STO substrate up to the thickness of a few unit cells (~ 6 nm), as confirmed by the Reflection High Energy Electron Diffraction studies [40]. With increasing film thickness up to ~9-19 nm, adatom-adatom bonding prevails leading to the switch from two-dimensional (or layer-by-layer) to three-dimensional (or island) growth occurs [42]. Thus, all samples studied (having thickness in the range 28–90 nm) are grown in a three-dimensional mode, i.e. with increasing the film thickness YBCO islands become large in size and coalesce. The latter results are in appearance of voids in YBCO samples. Note that no voids formed in Y28 sample. They are started to be seen at the thickness of 60 nm and have the size of about 10 nm (shown by arrows in Fig. 4.10b). When the thickness of YBCO film reaches 90 nm, the voids have size in the range from 10 nm to 350 nm (Fig. 4.10c).

In contrast, there were no voids obtained in the multilayered films at any thicknesses (Fig. 4.10d–f). It is likely due to interrupted growth of island's height caused by multilayering. The improved surface morphology of Y/Sm58 and Y/Sm90 films is well suited for structuring a continuous meander line required for fabrication of SSPD device.

Fig. 4.11a shows magnetic moment of the films as a function of temperature, from which the onset critical temperature values (T_c) are determined and plotted against the film thickness in Fig. 4.11b. Thinner samples (Y28 and Y/Sm44) have

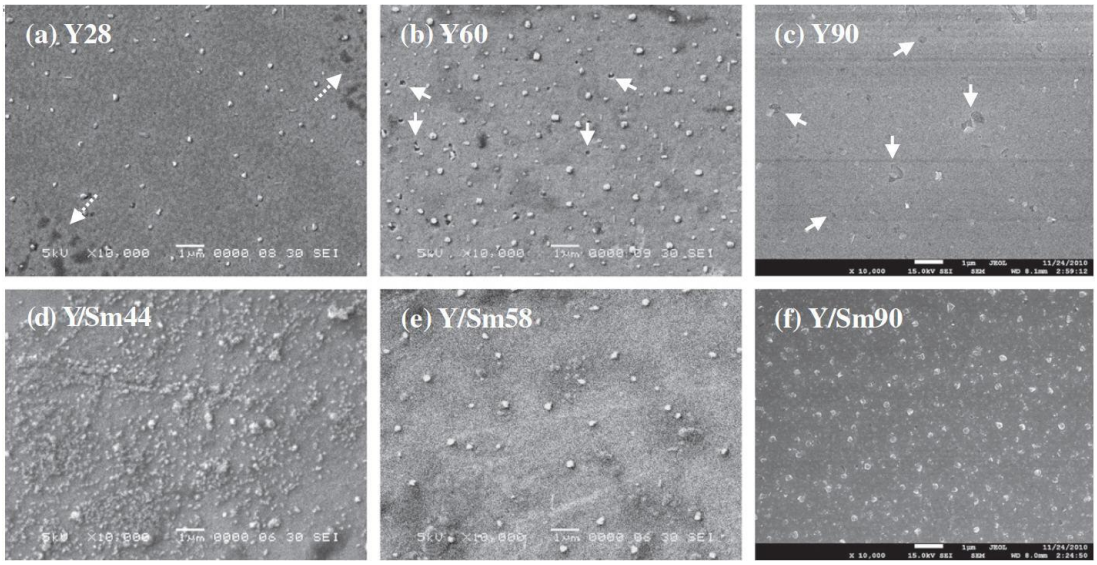

Figure 4.10 Morphology of the thin films studied. Images (a–c) and (d–f) correspond to the different thickness of monolayer and multilayered films, respectively. Broken arrows in (a) point to areas with large cavities. Solid arrows in (b) and (c) show some voids formed in 60 nm and 90 nm thick YBCO structures.

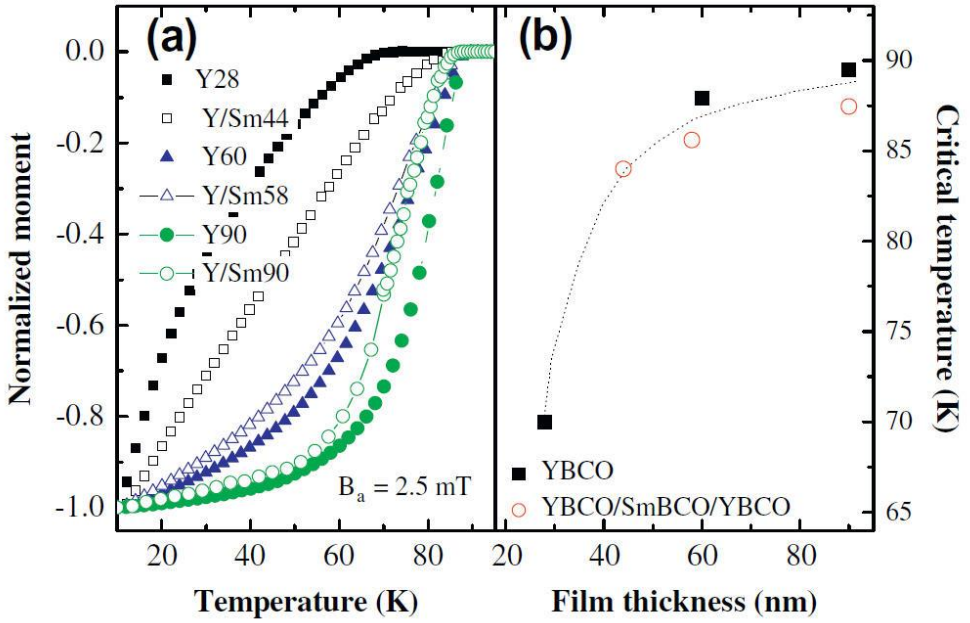

Figure 4.11 (a) Normalized magnetic moment as a function of temperature for the samples studied. (b) Critical temperature as a function of film thickness. (The line is a guide for eyes only).

broad T_c transition, which is consistent with highly inhomogeneous structure obtained in these films (Fig. 4.10a and b), and likely poor crystallinity of YBCO layers in these thin samples. Another factor which may significantly influence the broadness of a superconducting transition for very thin ReYBCO films is their larger strain. As the thickness of the films increases, the width of transition becomes narrow, and T_c values increase indicating improved homogeneity in structures formed in these thicker (≥ 60 nm) mono- and multilayered samples (Fig. 4.10b, c, e and f). It is not surprising that thicker YBCO and YBCO/SmBCO films have very close *M(T)* shapes. The improvement in *M(T)* dependence was not expected because different ReBCO superconductors demonstrate almost the same superconducting transition behavior. However (as it was shown in [15]) the multilayers have been shown the great improvement in terms of critical current density versus magnetic field dependence.

Fig. 4.11b demonstrates that there is a gradual reduction of T_c values for films with the thickness varying from 90 nm to 44 nm. After this point (44 nm) there is a dramatic decrease in T_c for the Y28 sample (down to 70 K). Although these results are limited in quantity, they show as the size of the films decreases there is a definite degradation of the superconducting properties, which is more pronounced for thicknesses below approximately 44 nm.

Direct analysis of T_c values suggests that multilayering causes reduction of the eventual superconducting properties for films with thickness less than 90 nm. However, this may not be the case. Indeed, each single layer building the multilayered structure has the thickness of 630 nm, which is comparable to thickness of Y28 sample. Thus, each of YBCO layers should have about the same level of structural inhomogeneity (Fig. 4.10a) and have broad width of T_c transition as observed for sample Y28 (Fig. 4.11a). In reality, the structural and superconducting properties of multilayered samples are gradually enhanced. We speculate that if we are able to find the way to improve crystallinity and continuity of the initial YBCO layer, we may benefit from multilayering approach for thinner (< 90 nm) samples in a similar way as we achieved for thicker films [44,46].

Figure 4.12 shows the zero-field magnetization per sample volume (M) for each film at 10 K, 50 K and 77 K. From this graph the trend in critical current density can be determined, because according to Bean model $J_c \sim M$ [51]. As can be

seen, increase of the film thickness results in enhancement of M (and hence J_c) of the film. The multilayered samples show lower magnetic moment values compared to the YBCO samples at the same thickness and temperature, which is in contradiction with previously studied thicker samples [44, 46]. This is believed to occur due to very thin thickness of the individual layers in the multilayered films which likely exhibit an island growth, creating more defects than compared to monolayer YBCO. This leads to a decrease in J_c and magnetic moment.

The electromagnetic homogeneity of the films was investigated by MOI (Fig. 4.13). From the flux distribution in the Y/Sm44 sample, multiple defects can be seen over the entire surface of the film, which allows the magnetic flux (bright areas in pictures) to penetrate the sample more readily. This shows that this sample has poor electromagnetic homogeneity and would explain the low value of magnetic moment obtained from the magnetic measurements. As the thickness of the film increases (Fig. 4.13b and c), dramatically less magnetic flux can penetrate in the sample, showing enhancement of the electromagnetic homogeneity. This reflects the magnetic moment trend, since the lower flux penetration leads to a higher magnetic moment and corresponding J_c.

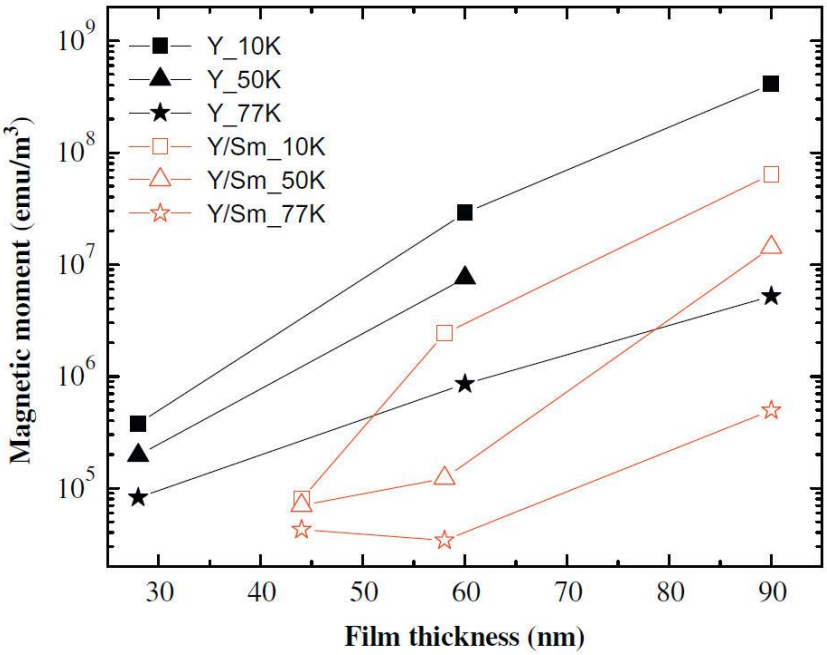

Figure 4.12 Magnetic moment of films studied at temperatures of 10 K, 50 K and 77 K. (Lines are guides for eyes only.)

4.4 Conclusions

Multilayered approach has been employed for fabrication of step-edge YBCO-based Josephson junction. The results of this work show that this approach advances performance of YBCO step-edge Josephson junctions prepared by pulsed laser deposition technique. This is achieved by tuning the microstructure of YBCO-based films, which becomes smooth and improves current- carrying ability of thin film and junctions. The transport properties of the junctions fabricated on multilayered (Y/Nd/YBCO) thin film have high values.

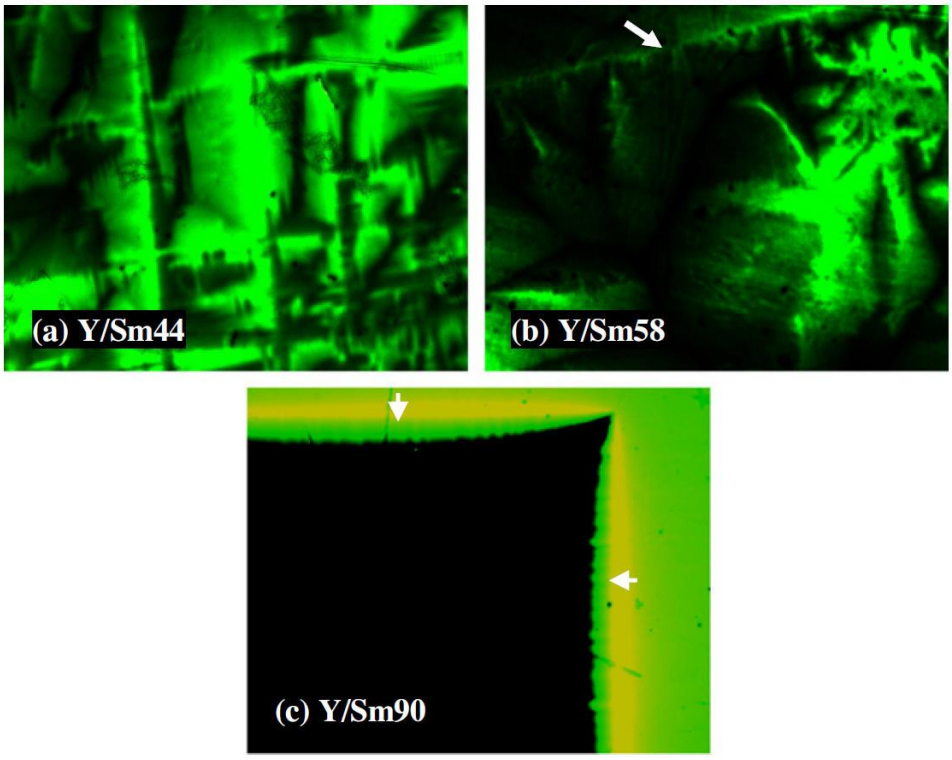

Figure 4.13 Magneto-optical images for multilayered YBCO/SmBCO/YBCO samples with different thicknesses. Arrows show the edge of the sample. The external magnetic field is 21 mT for (a) and 33 mT for (b and c).

On the other hand, the junctions fabricated on monolayer (YBCO) thin film suggest there is formation of small separated junctions or significant faceting effect along the width of the grain boundary compared with the multilayer counterparts. Work is currently conducted on optimization of multilayer type films in order to

further improve surface morphology and reduce the spread of and values. Once these goals are achieved, the multilayering approach by PLD technique is expected to advance functionality of HTS Josephson junctions over junctions fabricated by other techniques (e. g. EBE). Experiment is underway to investigate the faceting effect and grain boundary structure of multilayered films.

The HTS YBCO long film multichannel cables with 100 μm wide superconducting stripes have been deposited by PLD technique after modification of a standard PLD chamber. A long contact resistive heater has been identified to be the most accurate and robust design, providing the most homogeneous 8 cm to 10 cm long films during PLD process. The magnetic and resistance measurements exhibit high quality rather homogeneous films with properties comparable with best small samples obtained in our standard PLD setup and those available in the world for any type of application. The critical current density in self field and at 77 K is of 2.4×10^{10} A/m^2, the critical temperature onset $T_c \approx 90$ K over the entire length of the long sample, and the surface resistance $R_s \approx 4$ mΩ at 1 GHz and 77 K. These properties are sufficient for applications in electronics, providing effective reduction in transferred and generated heat.

The properties of monolayer YBCO and multilayered YBCO/SmBCO/YBCO thin films with thicknesses less than 90 nm were investigated. It was found that as the film's thickness decreased there was a decrease in superconducting characteristics (T_c, J_c) of the films. The properties obtained were rationalized using SEM and MOI visualization techniques. We demonstrated that the thinner samples had very poor structural homogeneity, and thus magnetic flux could easily penetrate the sample along many defects. For thicker samples (58–90 nm), the homogeneity increased dramatically, which is confirmed by enhanced T_c and J_c values and MOI study of the samples. It was also found that multilayering of thin films with thickness 90 nm results in degradation of their overall superconducting properties. However, there is a qualitative difference in homogeneity between two types of films studied, which suggest better homogeneity of multilayered films taking into account the thickness of each individual layer. We speculate that if epitaxial growth of the initial layers of YBCO and SmBCO is improved, the multilayering approach may enhance structural and electromagnetic properties of the films at very thin (tens of nm) thickness.

References

[1] K. E. Leslie, R. A. Binks, C. P. Foley, R. G. Thorn, M. J. Roberts, J. Du, E. E. Mitchell, S. K. H. Lam, C. J. Lewis, C. Millar, and R. Osmond. *IEEE Trans. Appl. Supercond*, **13**, 759–762, (2003)

[2] J. Du, D. L. Tilbrook, J. C. Macfarlane, K. E. Leslie, and D. S. Ore. *Physica C*, **411**, 18–24, (2004)

[3] M. Bick, K. E. Leslie, R. A. Binks, D. L. Tilbrook, S. K. H. Lam, R. Gnanarajan, J. Du, and C. P. Foley. *Appl. Phys. Lett.*, **84**, 5347–5349, (2004)

[4] D. Drung, E. Dantsker, F. Ludwig, H. Koch, R. Kleiner, J. Clarke, S. Krey, D. Reimer, B. David, and O. Doessel. *Appl. Phys. Lett.*, **68**, 1856–1858, (1996)

[5] J. Du, A. D. Hellicar, L. Li, S. M. Hanham, J. C. Macfarlane, K. E. Leslie, N. Nikolic, C. P. Foley, and K. J. Greene. *Supercond. Sci. Technol.*, **22**, 114001, (2009)

[6] J. Clarke and F. Wilhelm. *Nature*, **458**, 1031–1042, (2008)

[7] H. Hilgenkamp and J. Mannhart. *Rev. Mod. Phys*. **74**, 485–549, (2002)

[8] E. Sarnelli, G. Testa, D. Crimaldi, A. Monaco, and M. A. Navacerrada, *Supercond. Sci. Technol.*, **18**, L35–L39, (2005)

[9] M. V. Liatti, U. Poppe, and Y. Y. Divin. *Appl. Phys. Lett.*, **88**, 152504-3, (2006)

[10] A. J. Pauza, D. F. Moore, A. M. Campbell, A. N. Broers, and K. Char. *IEEE Trans. Appl Supercond.*, **5**, 3410–3413, (1995)

[11] H.-J. H. Smilde, H. Hilgenkamp, G. Rijnders, H. Rogalla, and D. H. A. Blank, *Appl. Phy. Lett.* **80**, 4579–4581, (2002)

[12] E. E. Mitchell and C. P. Foley. *Supercond. Sci. Technol.*, **23**, 065007, (2010)

[13] D. Koelle, R. Kleiner, F. Ludwig, E. Dantsker, and J. Clarke, *Pev. Mod. Phys.* **71**, 631–686, (1999)

[14] C. P. Foley, E. E. Mitchell, S. K. H. Lam, B. Sankrithyan, Y. M.Wilson, D. L. Tilbrook, and S. J. Morris. *IEEE Trans. Appl. Supercond.*, **9**, 4281–4284, (1999)

[15] A. V. Pan, S. Pysarenko, and S. X. Dou. *Appl. Phys. Lett.*, **88**, 232506, (2006)

[16] B. Dam, J. M. Huijbregtse, F. C. Klaassen, R. C. F. van der Geest, G. Doornbos, J. H. Rector, A. M. Testa, at al. *Nature*, **399**, 439–442, (1999)

[17] C. M. Gilmore and J. Kim. *Appl. Phys. A*, **75**, 565–571, (2002)

[18] D. Marre, A. Diaspro, C. Ferdeghini, G. Grassano, I. Pallecchi, and A. S. Siri. *Supercond, Sci. Technol.* **11**, 737–743, (1998)

[19] T. Frey, C. C. Chi, C. C. Tsuei, T. Shaw, and F. Bozso.*Phys. Rev. B,* **49**, 3483–3491, (1996)

[20] H.-U. Habermeier, *Iranian J. Phys. Res.* **6**, 117–128, (2006)

[21] M. Tinkham, *Introduction to Supercondcutivity*. : McGraw-Hill, Inc., (1996)

[22] M. V. Costache and J. S. Moodera. *Appl. Phys. Lett.*, **96**, 082508, (2010)

[23] C. A. Copetti, F. Ruders, B. Oelze, C. Buchal, B. Kabius, and J. W. Seo. *Physica C*, **253**, 63–70, (1995)

[24] S. K. H. Lam and S. Gnanarajan. *Phys. Rev. B*, vol. **78**, 094521, (2008)

[25] Kogge P. *IEEE Spectrum.* **48**, 48-54, (2011)

[26] Mukhanov O. A. *IEEE Trans. Appl. Supercond.* **21**, 760, (2011)

[27] Mukhanov O.A, Kirichenko D., Vernik IV, et al. *IEICE Trans. Electron.* E91-C:306-17, (2008)

[28] Kadin, AM, et al., *IEEE Trans. on Appl. Supercond.* **17**, 975-8, (2002)

[29] Webber RJ, Delmas J, Moeckly BH. *IEEE Trans Appl Supercond.* **19**, 9991003, (2009)

[30] Merker M, Delmas J, Webber RJ. HTS tape-based multi-line current lead. In: Proceedings of CEC-ICMC, (2011)

[31] Yung SC, Moeckly BH. *IEEE Trans Appl Supercond.* **21**,107-10, (2011)

[32] V. Pan, S. A. Fedoseev, O. V. Shcherbakova, I. A. Golovchanskiy at all. Physics Procedia 00 1–6, (2011)

[33] S. Pysarenko, and S. X. Dou, *IEEE Trans. Appl. Supercond.* **21**, 3179, (2011)

[34] I. A. Golovchanskiy, A. V. Pan, O. V. Shcherbakova, S. A. Fedoseev, and S. X. Dou, *Supercond. Sci. Technol.* **24**, 105020, (2011)

[35] G.N. Gol'tsman et al., *Appl. Phys. Lett.* **79**, 705, (2001)

[36] H. Shibata et al., *Appl. Phys. Lett.* **97**, 212504, (2010)

[37] E. Reiger et al., *IEEE J. Sel. Top. Quant. Electron.* **13**, 934, (2007)

[38] F. Marsili et al., *Opt. Expr.* **16,** 3191, (2008)

[39] A. Korneev et al., Appl. Phys. Lett. **84,** 5338, (2004)

[40] T. Terashima et al., *Phys. Rev. Lett.* **65,** 2684,(1990)

[41] T. Terashima et al., *Phys. Rev. Lett.* **67** 1362, (1991)

[42] X.Y. Zheng et al., *Phys. Rev. B* **45,** 7584 (1992)

[43] J. Gao, T.C. Chui, W.H. Tang, *IEEE Trans. Appl. Supercond.* **9,** 1661, (1999)

[44] O. V. Shcherbakova, A. V. Pan, S. K. Gorman, S. A. Fedoseev, I. A. Golovchanskiy, S. X.Dou. *Physica C,* Volume 479, p. 102-105, (2012)

[45] O.V. Shcherbakova et al., IEEE Trans. Appl. Supercond. **21**, 156, (2011)

[46] A.V. Pan et al., IEEE Trans. Appl. Supercond. **17**, 3585(2007)

[47] Q.X. Jia et al., *Appl. Phys. Lett.* **80**, 1601, (2002)

[48] I. Bozovic, *IEEE Trans. Appl. Supercond.* **11,** 2686, (2001)

[49] R.T. Thew et al., *Nucl. Instrum. Methods Phys. Res. A* **610,** 16, (2009)

[50] N. Curtz et al., *Supercond. Sci. Technol.* **23** 045015, (2010)

[51] C.P. Bean, *Rev. Mod. Phys*. **36,** 31, (1964)

Chapter 5

Lanthanum Calcium manganite thin films deposition and investigation of their properties

Lantanum manganites, also known as CMR oxides, are in focus of modern materials research. From the applications perspective, interest in these materials arose initially from their unusually large magnetoresistance. However, CMR manganites have also promising potential for bolometric infrared detection in a wide range of temperatures. The operating temperatures can be tuned over a wide range by simple variations in chemistry. The bolometric application of CMR manganites is based on the steep drop in resistivity with temperature accompanying an insulator-metal transition [1]. The heterostructure based on manganite (such as LCMO) and ferroelectric thin films allow the electric-field control of magnetization and may have many potential applications in magnetic memory storage, sensors and spintronics [2]. All these applications require LCMO thin films and the device performance will mainly depend on the thin film quality. The optimization of the LCMO thin films is not straightforward, as different parameters exist which can be optimized, e.g. the magnetization and the electrical conductivity. In addition to these parameters, a smooth surface morphology is required for most applications [3].

5.1 LCMO films deposition procedure

All LCMO films were deposited in the automated PLD system, described in Chapter 3. STO, LAO, and YSZ 5×5 mm size (100) monocrystal were used as substrates after the standard cleaning procedure. The standard 1-inch diameter PLD target of LCMO from Super Conductor Materials Inc. was used in all experiments. The actual LCMO film growth procedure was similar to YBCO film. The details of this procedure are shown in the Table 5.1. The only difference between YBCO and LCMO film deposition procedure was a value of target-substrate distance because of shorter laser plum from LCMO target. After series of depositions and measurements of film properties we have conclude that the optimal target-substrate distance for LCMO films must be in the range d = 55 - 65 mm. All films were crystalline and epitaxial. The film thickness was in the range of 20-200 nm and its exact value for each sample was obtained from the direct measurement by Profile Meter.

Table 5.1 PLD parameters for high quality LCMO film deposition.

Substrate type	Laser fluence, Hz	Laser energy, mJ	Substrate heater temperature, ^{o}C	Distance target - substrate, mm	Oxygen pressure, mTorr	Annealing temperature and time, ^{o}C/min
STO, LAO,YSZ	1-5	430-450	780	55-65	300	400 /60

5.2 LCMO films chemical composition and surface quality

The surface chemical state of LCMO films was analysed by x-ray photoelectron spectroscopy (XPS). Figure 5.1 shows the wide-scan XPS spectrum of the LCMO thin film grown on YSZ (100) substrate in the binding energy range of 0-1260 eV. All of the binding energies at various peaks were calibrated by the binding of C 1s (284.70 eV). The LCMO film contains La, Ca, Mn, O and C elements near its surface, and no other impurity element was detected in the spectrum except carbon.

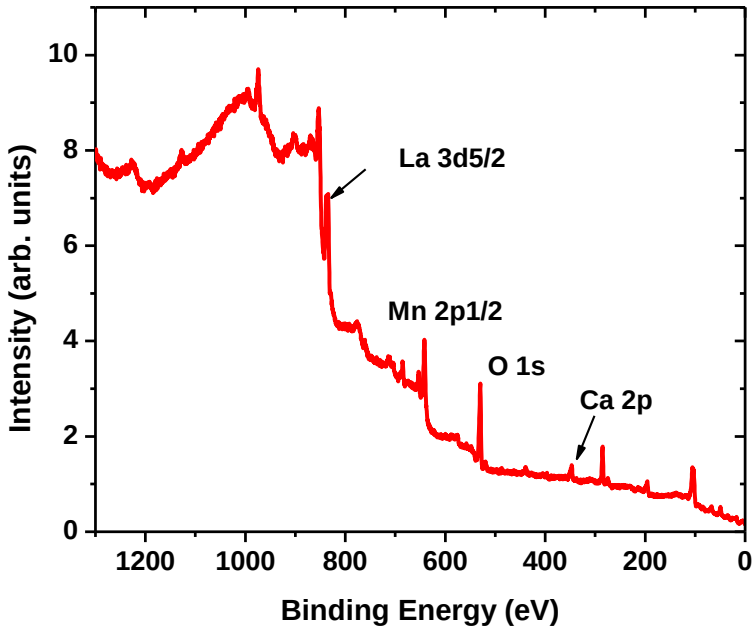

Figure 5.1 Wide-scan XPS spectrum of a of 200 nm thick LCMO film grown on YSZ substrate; main lines are annotated (La 3d, Mn 2p, O 1s, and Ca 2p).

The carbon results from surface contamination. X-ray photoelectron spectroscopy analysis did not show major differences between the surface composition of the sample without prior surface cleaning treatment of as deposited film (surface) and about 30 nm sputtered (bulk) material.

Table 5.2 Positions of characteristic XPS lines for LCMO film on YSZ.

Electron orbital	XPS Peak Position, eV	Reference Peak, eV [4, 5, 6]
Ca 2p	346.8	346.5
O 1s	531.0	531.5
Mn $2p_{3/2}$	641.6	642.2
Mn $2p_{1/2}$	653.2	653.5
La $3d_{3/2}$	852.8	851.8
La $3d_{5/2}$	834.3	833.7

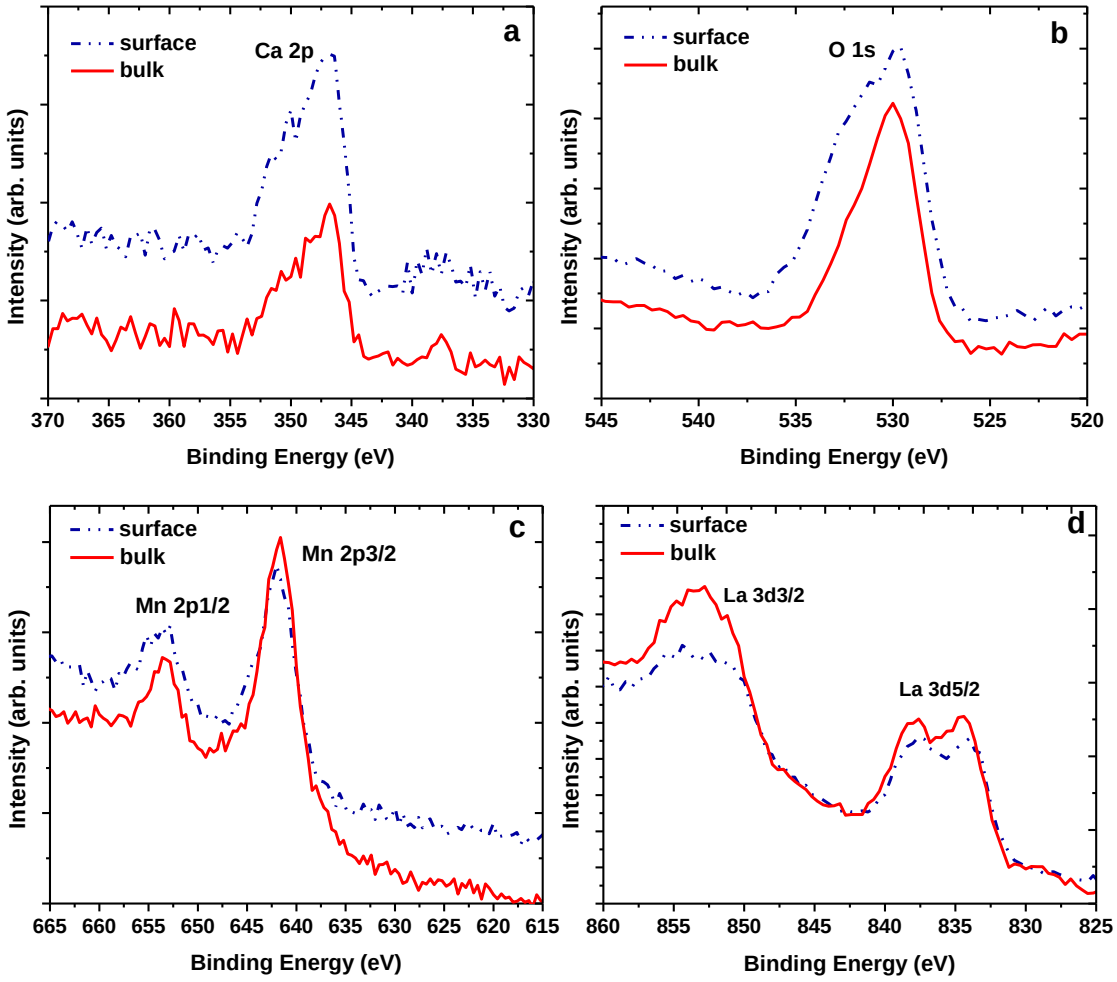

Figure 5.2 Narrow scan XPS spectra of the monitored emission lines of LCMO thin films grown on YSZ substrate: (a) Ca 2p; (b) O 1s; (c) Mn $2p_{3/2;1/2}$; (d) La $3d_{3/2;5/2}$.

The energy distribution curves for lines Ca 2p, O 1s, Mn 2p, and La 3d are reported in Figure 5.2. XPS signals from this sample (see Table 5.2) are in the good agreement with data reported in the literature for lanthanum manganite thin films deposited by PLD [4, 5, 6].

Figures 5.3a and 5.3b show SEM images of LCMO thin films deposited on (100) YSZ and LAO substrates. The films present a smooth surface with small amounts of tiny particles with a maximum size of 0.5 μm for all studied deposition conditions. After examination of XPS data and surface morphology of our samples we may conclude that PLD technique allows us to produce high quality epitaxial films of LCMO on different substrates.

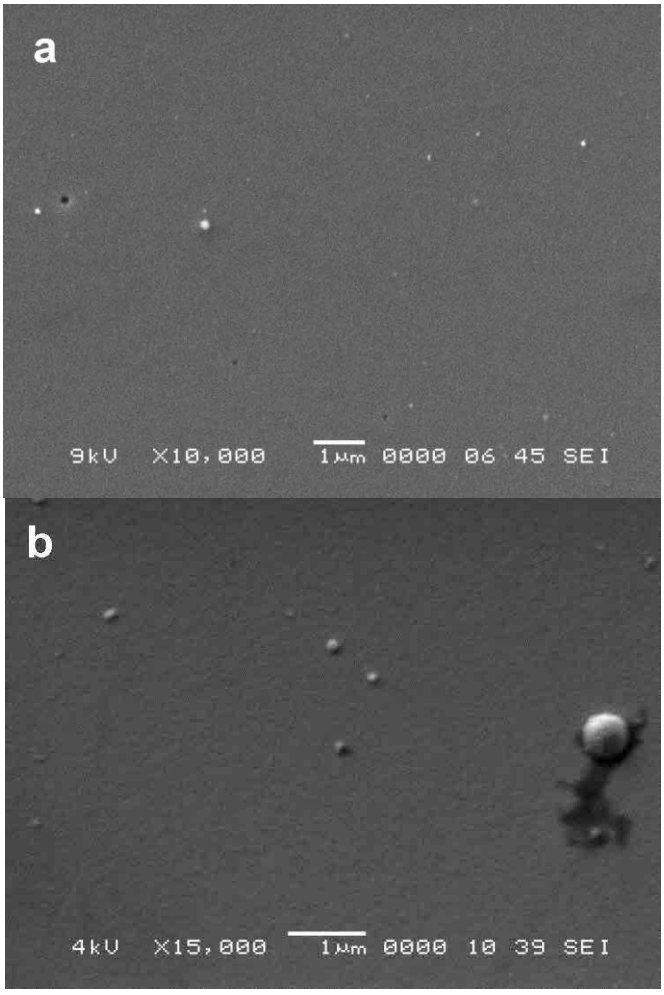

Figure 5.3 The SEM image of LCMO thin film deposited on YSZ (a) and LAO (b) substrates.

5.3 Magnetic properties of LCMO films

The magnetisation *M* of LCMO thin films was measured as a function of the applied field *B*. Figure 5.4 shows hysteresis loops for 200 nm thick LCMO/YSZ sample. The magnetic field was scanned from 3.0 T to – 3.0 T parallel to the film surface. All LCMO films were ferromagnetic at low temperatures. It is seen that the magnetic moment of the film saturates at a magnetic field of ~ 0.7 T and it decreases as temperature increases. The coercive field at 10 K is ~ 60 mT and it also decreases with increasing temperature.

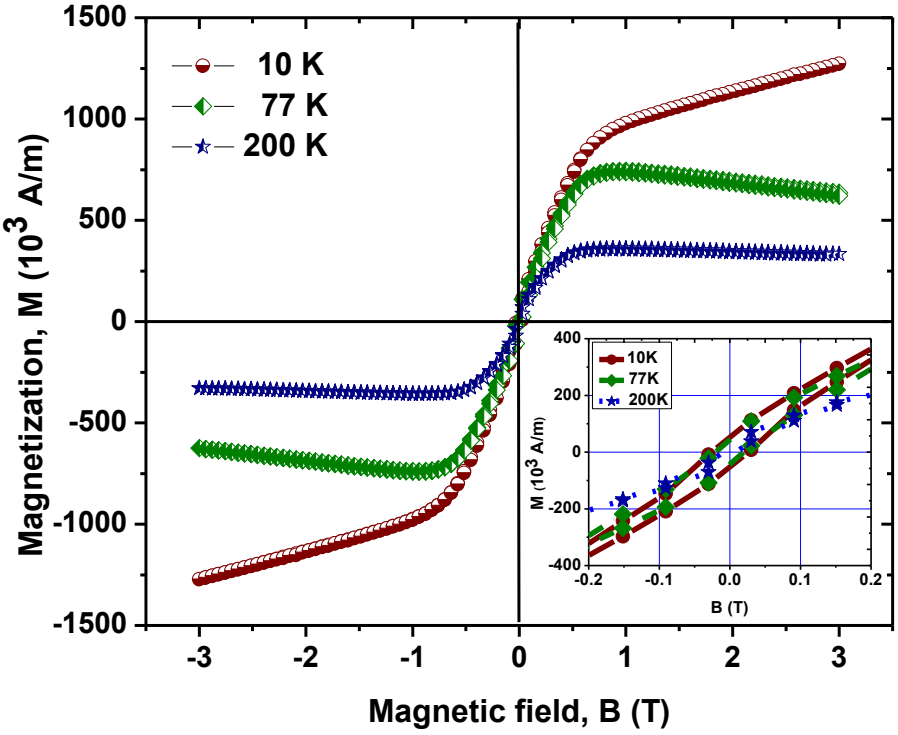

Figure 5.4 Hysteresis loops for LCMO film, measured at 10, 77, and 200 K and field applied parallel to the sample. Inset: zoom-in of the hysteresis loops at low fields.

Temperature dependence of magnetization of the same LCMO/YSZ film is presented in Figure 5.5 for two external field directions: parallel to the film (in plane) and perpendicular to the film surface (out of plane). Both, zero field cooling (ZFC) and field cooling (FC) curve are shown. The ferromagnetic Curie temperature (T_C) for all measured samples has been estimated by finding the steepest slope from the temperature derivative of magnetization (dM/dT) shown by arrows in Figures 5.5 and

5.6. It can be seen that the Curie temperature for both external field directions is almost the same ($T_C \approx 240$K) but the magnitude of magnetization in all our samples was much higher for the in plane magnetization which is related to the significant anisotropy.

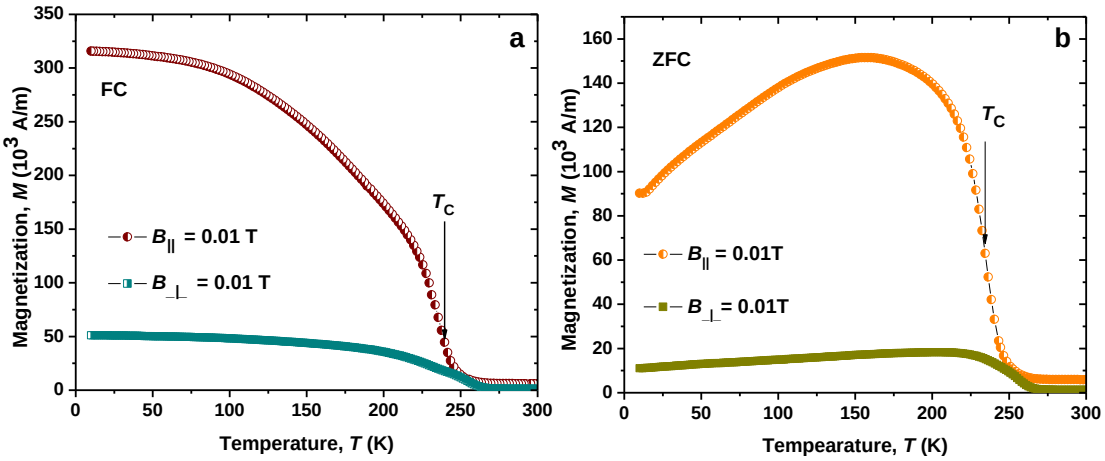

Figure 5.5 Magnetization versus temperature for 200 nm thick LCMO film on YSZ substrate showing the anisotropic behaviour for in plane and out of plane magnetic field with zero field cooling conditions (ZFC) (a); and field cooling (FC) conditions (b). The measurements were made in a magnetic field of 0.01 T.

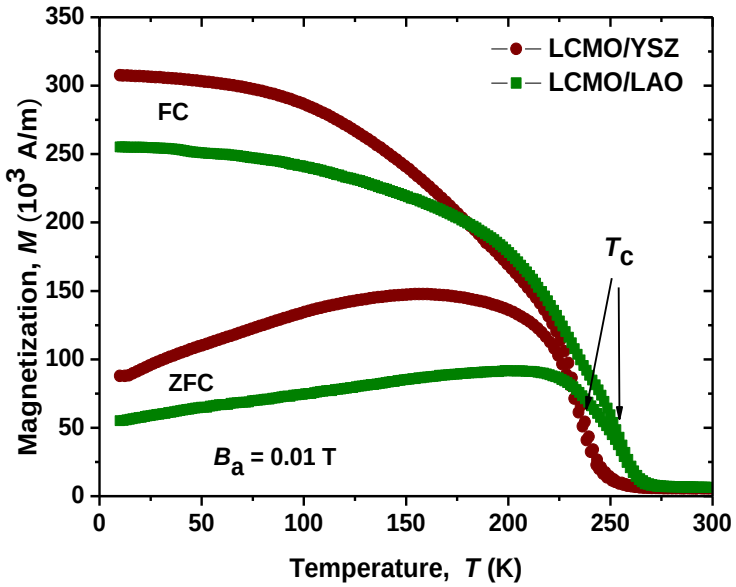

Figure 5.6 Temperature dependence of magnetization for two 200 nm thick LCMO films grown on YSZ and LAO substrates showing Curie temperature $T_C \approx 237$ K and 255 K correspondingly.

Figure 5.6 demonstrates *M (T)* curves for two LCMO films with the same thickness grown on different substrates. T_C value for the films on LAO was close to 260K and for film on YSZ was about 20 K lower. This phenomenon can be explained by the degree of strain relaxation in the LCMO films [7]. Compressive and tensile stresses lead to a reduction of the T_C. A relaxed film gives the highest T_C [8], remembering that the lattice mismatch between LCMO and LAO is a much smaller, then between LCMO and YSZ.

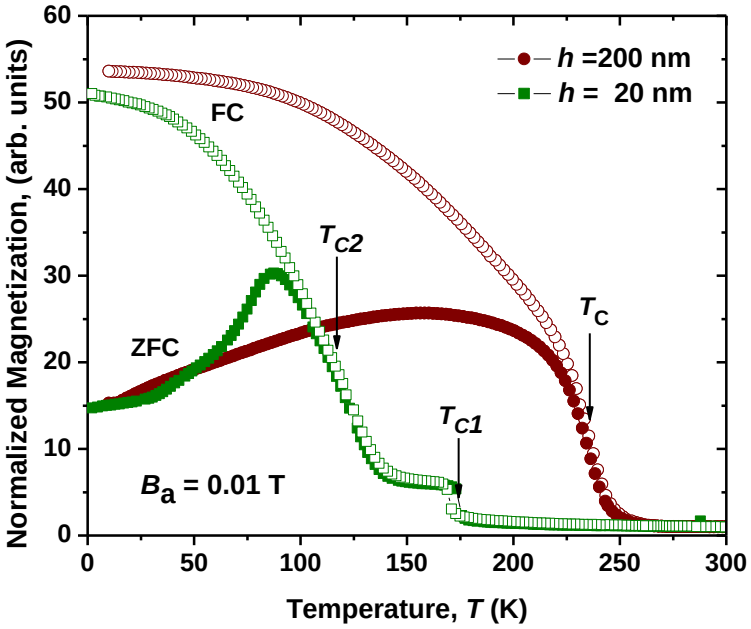

Figure 5.7 Normalized magnetization versus temperature for two LCMO/YSZ samples with different film thickness. The thinnest film demonstrates two metal-insulator transitions at around 175 K and 120 K.

The temperature dependence of the ZFC and FC magnetization for LCMO/YSZ heterostructures is shown in Fig. 5.7 for two thicknesses: 200 nm and 20 nm. The Curie temperature for the 200 nm thick film is 237 K and is decreased to175 K when the thickness is decreased to 20 nm, revealing a strong dependence of the Curie temperature on the thickness of the film. Moreover this film demonstrates one more low temperature transition at 120 K. This is a very large reduction in T_C, which could be related to interfacial strains. Really, in [9] the magnetic and magneto-transport properties of LCMO thin films as a function of the thickness were investigated. It was found that the reduction of the film thickness leads to a

systematic decrease of the Curie temperature and of the metal-insulator transition temperature values. This effect was attributed to the different strain state: fully relaxed above 100 nm and coherently strained with 70 nm thickness. They claim that the substrate-induced strain might lead to a weakening of the double exchange interaction and therefore a reduction of the conductivity which we will observe in next section. Similar T_C thickness dependence was also observed in [10]. This reduction of T_C and the increase of resistivity are believed to be due to the in-plane tension in films and to the thickness of films. The thinner the film, the stronger the in plane strain and the more closely it approaches a 2D system. Moreover, a large difference between FC and ZFC magnetization for $T < T_C$ (see Fig. 5.6 and 5.7) was observed, indicating a cluster glass magnetic behaviour [11].

In order to better illustrate the magnetic ordering in very thin LCMO film (h = 20 nm), the temperature dependence of ZFC and FC magnetization is presented in Fig. 5.8 in different fields. For B = 0.01 T, the FC and ZFC curves separate at around 100 K accompanied by a remarkable thermomagnetic hysteresis (or irreversibility) with $M_{ZFC} \neq M_{FC}$ at the irreversibility temperature, and M_{FC} - M_{ZFC} increases as temperature decreases. However, for B = 0.1 T, T_{irr} decreases remarkably up to 60 K and at the magnetic field of 1 T the irreversibility disappears almost completely.

This type of irreversibility in magnetization is generally indicative of antiferromagnetic (AF) ordering; however, for a simple AF no thermomagnetic hysteresis is expected. This latter effect is traditionally accepted as a hallmark of cluster-spin-glass systems with a characteristic spin-glass transition temperature T_g. This may be attributed to the presence of Mn–Mn clusters [12] in the interface region which are anti-ferromagnetically coupled, and such coupling is stronger at low temperature. However, as in the case of many other manganites, the charge ordering coexists with ferromagnetism in the low-temperature phase.

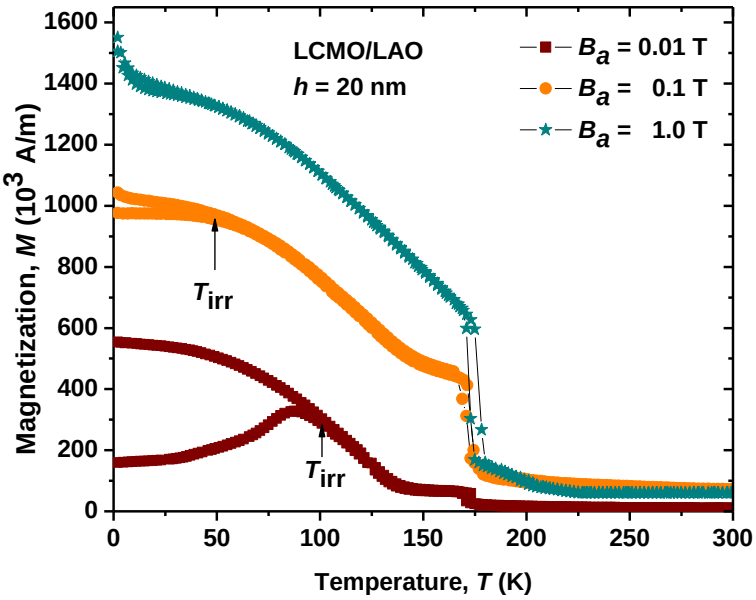

Figure 5.8 Temperature dependence of FC and ZFC magnetization of 20 nm thick LCMO/YSZ sample at various field values showing the shift of T_{irr} to lower temperatures with increasing field values.

5.4 Transport properties of LCMO films

The DC electrical resistivity of the LCMO films deposited on YSZ and LAO substrates was measured along the (100) film direction as a function of temperature in zero magnetic field. Typical temperature dependence of the resistivity of a thick (h ≈ 200 nm) LCMO film is presented in Fig. 5.9. It may be seen that there are three regions with substantially different $R(T)$ dependences [13]: (I) the region of a ferromagnetic metallic phase, which lies below 220 K; (II) the region of the magnetic phase transition in the range from 220 to 260 K; and (III) the region of a paramagnetic semiconductor phase at T > 260 K. At T < 150 K, the resistivity has nearly parabolic temperature dependence and it is described satisfactorily by the expression $\rho(T) = \rho(0) + AT^2$, where $\rho(0) = 2.3 \times 10^{-2}$ mΩ·cm and $A = 4.2 \times 10^{-4}$ mΩ·cm/K^2. At 150 < T < 220 K, the resistivity grows somewhat more rapidly, reaching 0.38 mΩ·cm at T = 220 K. The metal-insulator transition (MIT) accomplishes at T = 260 K and above this temperature the sample is in the insulating paramagnetic phase. However the resistivity vs temperature dependence was changed dramatically when the film thickness was reduced up to 50 nm. We may distinguish similar three regions with different $\rho(T)$ dependences, but with much

lower peak temperature (T_P) values and a small valley at low temperature (~ 30K). Figure 5.10 shows the resistivity traces for a LCMO film in a magnetic fields of B_a = 0, 0.1 T, and 1.0 T. The resistivity decreased with increasing magnetic field. This reduction in ρ was most significant close to the resistivity peak and there was comparatively insignificant change above 230 K. The maximum in $\rho(T)$ on warming also showed a field dependence, increasing from 176 K (at B_a = 0) to 184 K (at B_a = 1.0 T).

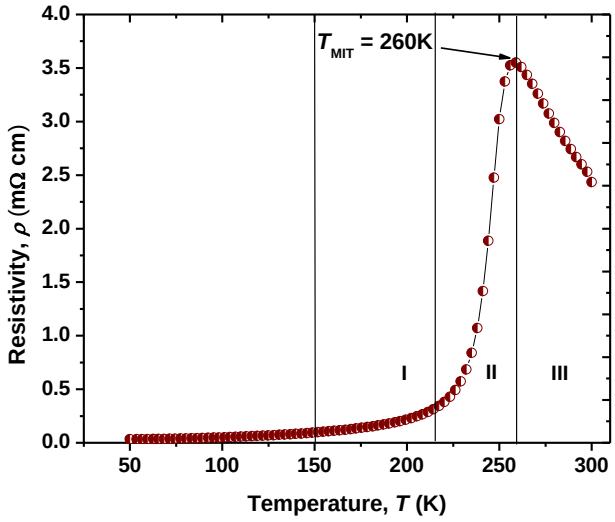

Figure 5.9 Temperature dependence of the resistivity for 200 nm thick LCMO film grown on LAO substrate showing regions with: ferromagnetic phase (I), phase transition (II), and paramagnetic phase (III).

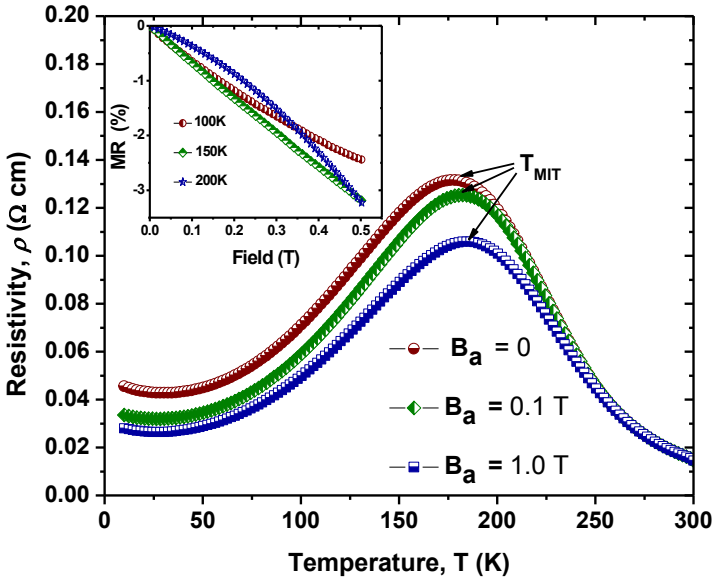

Figure 5.10 Resistivity vs. temperature for a 50 nm LCMO/YSZ film in three different in plane magnetic fields of B = 0; 0.1; and 1.0 T respectively. Inset: Low field magnetoresistance of LCMO film vs. applied in plane magnetic field.

The low-field magnetoresistance (*MR*) of the same LCMO film at three various temperatures in an in plane applied field is shown in Inset of Fig. 5.10. This confirms the increase in resistivity with increasing of an external magnetic field. It also indicates that the magnetoresistance curves in the temperature range around MIT point have nearly linear dependence and do not saturate in low magnetic fields (up to 0.5 T). Low-field *MR* has achieved value as high as 3.4 % at 150 K.

In Figure 5.11, the resistivity of the LCMO-50nm thin film is shown as a function of temperature at the applied magnetic field B_a = 0 T and 5 T. We can see a clear metal-to-insulator transition (MIT) at $T_P \approx$ 160 K and metallic-like behavior below T_P. For this film the transition temperature increased to 170 K in B = 5 T.

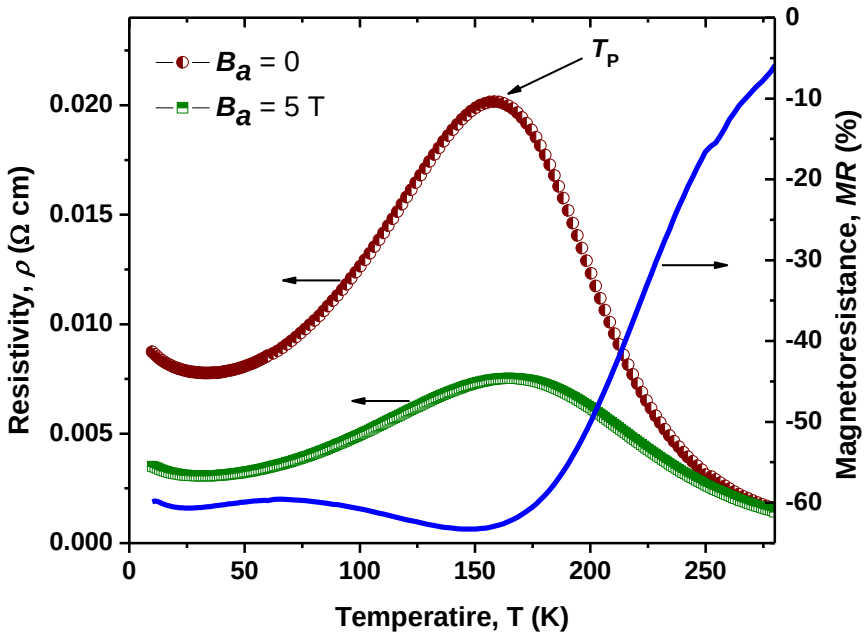

Figure 5.11 Resistivity in zero field (red) and 5T (green) as a function of temperature for a 50 nm LCMO film on LAO substrate (left panel). Magnetoresistance of this film vs temperature (right panel).

The temperature dependent high field magnetoresistance (*MR*) for the same LCMO film is also shown in Figure 5.11. The *MR* is defined as $MR = [(R(B_a) - R(0))/R(0)] \times 100\%$, where $R(0)$ and $R(B_a)$ are the resistances at the applied field B_a = 0 T and 5 T, respectively. The sample shows an *MR* minimum in the vicinity of the metal-insulator transition temperature. Both resistivity and *MR* behavior of the

LCMO films measured are typical for the samples with similar thickness and composition as described in [14, 15].

5.5 Summary

In this chapter we have demonstrated the ability of deposition of high quality epitaxial LCMO films on different substrates using PLD method. The quality of film surface was proven by XPS spectra analysis and SEM data. The magnetic and transport properties of epitaxial LCMO films with different thickness were investigated. It was shown that the Curie temperature for given LCMO samples is strongly dependent on film thickness and substrate in use which can be explained by the strain relaxation in epitaxial films. The transport measurements confirm the thickness dependence of a temperature of metal-insulator transition. It was found that $T_p \approx$ 250-260 K for LCMO film thickness h = 150-200 nm and $T_p \approx$ 150 K for h = 30-50 nm. All LCMO thin film samples demonstrated CMR behavior with negative magnetoresistance minimum in the vicinity of metal-insulator transition point.

Reference

[1] M. A. Todd, P. P. Donohue, P. J. Wright, M. J. Crosbie, P. A. Lane1, M.-H. Jo, B. S. H. Pang, and M. G. Blamire *Ann. Phys.* (Leipzig) 13, 1 – 2, **48 – 51** / DOI 10.1002/andp.200310042, (2004)

[2] S. M. Wu, Shane A. Cybart, P. Yu, M. D. Rossell, J. X. Zhang, R. Ramesh & R. C. Dynes *Nature Materials* **9**, 756–761, (2010)

[3] H Boschker, M Huijben, A Vailionis, J Verbeeck, S van Aert, M Luysberg, S Bals, G van Tendeloo, E P Houwman, G Koster, D H A Blank and G Rijnders *J. Phys. D: Appl. Phys.* **44,** 205001, (2011)

[4] P. R. Broussard, V. M. Browning, and V. C. Cestone *J. of Appl. Phys.* **85**, 8, (1999)

[5] Elke Beyreuther, Stefan Grafström, Lukas M. Eng, Christian Thiele, and Kathrin Dörr *Physical Review B* **73**, 155425, (2006)

[6] C.N. Borca, S. Canulescu, F. Loviat, T. Lippert, D. Grolimund, M. Do¨beli, J. Wambach, A. Wokaun *Applied Surface Science* **254**, 1352–1355, (2007)

[7] J. Elemans, J. *Solid St. Chem*, **3**, 328, (1971).

[8] Y.Y. Tse, R. I. Chakalov, I. P. Jones1, C. M. Muirhead, H. Huhtinen, and R. Palai *Journal of Physics*: Conference Series **126,** 012051, (2008)

[9] M. Ziese, H. Semmelhack, and K. H. Han *Physical Review B* **68,** 13444, (2003)

[10] H. Chou, S.J. Sun, M.N. Ou, T.C. Wu, H.L, Kao at all. *Thin Solid Films* **515,** 2567–2572, (2006)

[11] V. MOSHNYAGA, B. DAMASCHKE, O. SHAPOVAL, A. BELENCHUK, J. FAUPEL at all. *Nature Materials*, **2,** APRIL, (2003**)**

[12] A. K. Pradhan, D. Hunter, T. Williams, B. Lasley-Hunter, R. Bah, H. Mustafa at all *J. Appl. Phys.* **103**, 023914, (2008)

[13] N. G. Bebenin. *The Physics of Metals and Metallography,* **111**, 3, 236–252, (2011)

[14] Markovich, V.; Jung, G.; Yuzhelevskii, Y.; Gorodetsky, G.; Gao, *J. Phys. Rev. B*, **75**, 104419, (2007)

[15] Zhai, H.; Ma, J. X.; Gillaspie, D. T.; Zhang, X. G.; Ward, T. Z.; Plummer, E. W.; Shen, *J.Phys. Rev. Lett.*, **97**, 167201, (2006)

Chapter 6
YBCO-LCMO Hybrid Structures

6.1. Introduction to cuprate-manganite hybrids

Superconducting/ferromagnetic structures are under intense investigation due to their unusual properties and possible applications in various devices including spintronic. Heterostructures comprising cuprate and manganite layers offer the possibility to combine and interplay such effects as colossal magnetoresistance (CMR) and high-T_c superconductivity (HTS) in one system. Generally, the cuprate–manganite multilayered structures and superlattices can demonstrate the suppression of both superconducting and ferromagnetic properties due to the mutual influence, but under certain conditions superconductivity and magnetism are able to coexist which can lead to exotic behavior [1]. If an insulating layer is introduced between superconductor and ferromagnetic layers the proximity effect, strongly affecting short-range order parameters in superconductor and ferromagnet, should be attenuated or completely suppressed. However, long-range magnetic interaction can survive [2, 3]. On the other hand, depending on the thickness of the intermediate layer, tunneling effects should be considered, making the understanding of the behavior of such hybrid systems quite a complex task.

Recently, both experimental and theoretical studies have demonstrated the so-called nanoscale phase separation (PS) in manganite systems, which is likely to be responsible for the metal-insulating transition and moreover to be the key in understanding the CMR effect [4]. Oxygen-deficient $La_{2/3}Ca_{1/3}MnO_3$ (LCMO) is expected to contain a ferromagnetic conducting phase and antiferromagnetic charge ordered insulating phase [5]. It has been found that the application of electric current can lead to the melting of the insulating phase and the increase of the portion of the conducting phase in these materials.

The cuprate/manganite bilayers and multilayers investigated by many research groups [6, 7] have been grown on top of each other. This means they were coupled to each other electronically and magnetically. In order to control the electronic interaction between two layers, an insulating interlayer may be grown between superconductor and ferromagnet. This achieves an electronic decoupling. In

the last decade, a large effort has been devoted to the development of three terminal high-T_c superconductor devices, and one viable approach is the quasiparticle injection device [8, 9]. These devices are attractive because their speed, when limited by the effective quasiparticle relaxation time, may be the order of 100 GHz [8].

In this chapter, we investigate superconductor-ferromagnet hybrid structures with few active layers separated by a thin (10-30 nm) STO or CeO_2 insulating layer which makes it possible to keep properties of HTS $YBa_2Cu_3O_7$ (YBCO) cuprate in one layer and manganite (LCMO) in the other layer almost unaffected. Yet, the insulator allows their mutual influence via tunneling through its thin barrier. We focus on magnetic and transport measurements of such LCMO/Insulator/YBCO heterostructures with possible device applications.

6.2 Experimental details

The thin films of YBCO, LCMO and their heterostructures were epitaxially grown on (100) YSZ and LAO substrates using automated PLD system, described in Chapter 3. The deposition parameters for both cuprate and manganite films were kept in the ranges described in Chapters 3 and 5. The thickness of the epitaxial layers was controlled by the deposition rate pre-calibrated employing surface profile measurements. YBCO and LCMO layers were grown with the thickness of 100 - 250 nm, whereas the intermediate insulating layer of STO was fixed at about 30 nm. To ensure the properties are not pertained to STO properties of its growth, CeO_2 insulating layer of similar thickness was also used. The programmable target carrousel has been used to ensure the non-interrupting deposition process upon switching between the different targets for manufacturing of the multilayered hybrid architectures. For magneto-transport measurements, the samples were patterned using conventional photolithography and wet etching process. The micro-bridge width was in the range of 25 - 100 μm. The sample resistance as a function of temperature and current-voltage characteristics were measured in a temperature range from 10 K to 300 K by a *dc* four probe method.

6.3 Magnetic properties of LCMO/I/YBCO hybrid structures

A sketch of general geometry of the investigated samples of the F/I/S type is shown in Fig. 6.1. This type of samples consists of three epitaxial layers grown on a single crystalline substrate. First layer to grow denoted as (S) was YBCO with the thickness of about 200 nm. Then the insulating buffer layer (I) (h_{buff} ≈ 10-30 nm) was deposited on YBCO, and finally the LCMO epitaxial layer (F) was grown on the top of the structure.

Figure 6.1 Sketch of the F/I/S sample geometry. LCMO and YBCO are grown by pulsed laser deposition via insulating buffer layer onto YSZ (or LAO) (100) single crystalline substrates.

Figure 6.2 shows the field cooled (FC) as well as zero field cooled (ZFC) magnetization studies at 0.01 T applied along the film plane (B_a) and perpendicular to this plane (B_c) for the F/I/S heterostructure. Firstly, the FC magnetization curve of this sample shows a typical ferromagnetic-like behaviour below the irreversibility temperature T_{irr} ≈240 K which is consistent with the behaviour of the single LCMO film of nearly the same thickness grown under identical conditions and showing a Curie temperature of ~250 K (see Chapter 5, Fig. 5.6). The data in Fig. 6.2 also clearly demonstrates that at T_c ≈ 90 K a transition to superconductivity occurs. This can be seen from the diamagnetic signal that occurs below T ≈ 90 K in both in plane and out of plane magnetization measurements ad demonstrates that below T = 90 K both superconducting and magnetic ordering are present in the sample. This is consistent with data presented in [10] where was found that for LCMO/YBCO bilayers with YBCO layers thickness h > 30 nm T_c was almost equal to the value reached within pure YBCO films. The discrepancy between the ZFC and the FC

curves suggests the existence of spin glass or spin cluster like behaviour in the LCMO layer [11].

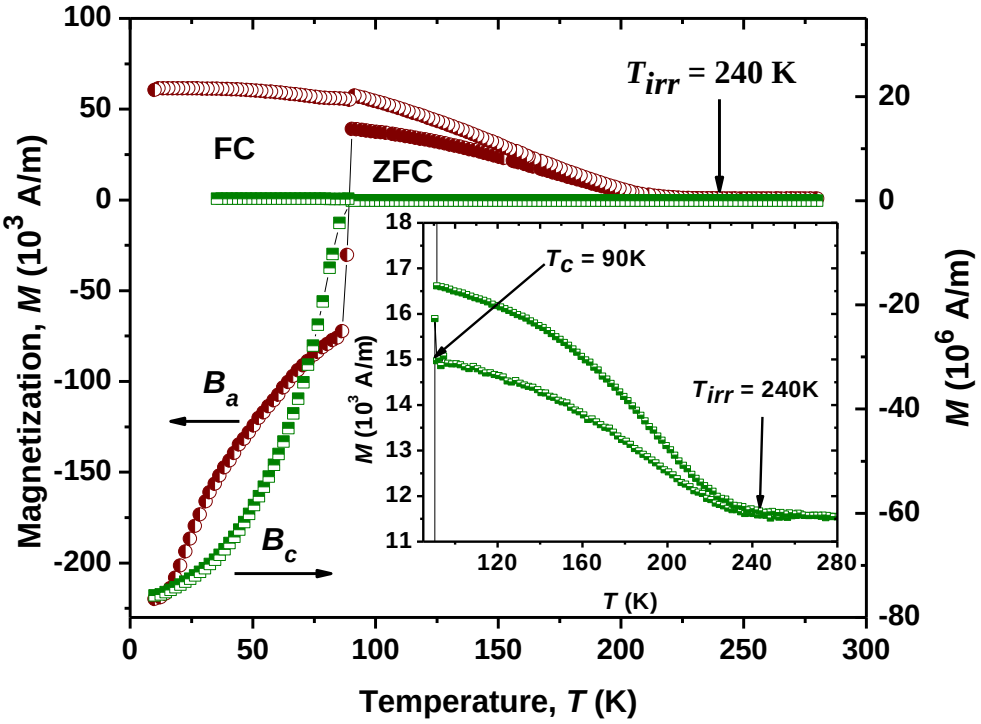

Figure 6.2 Temperature-dependent magnetization of a type F/I/S heterostructure ($LCMO_{200\ nm}/CeO_{2\ 30\ nm}/YBCO_{200\ nm}$) grown on LAO substrate and measured with in plane (left panel) and out of plane (right panel) field configuration under constant magnetic field of 0.01 T. The upper curve represents the field-cooled (FC) and the lover curve – zero field cooled (ZFC) measurements with metal-insulator transition at T_{irr} = 240 K. Inset: magnified part of out of plane field curves showing $T_C \approx 90$ K and $T_{irr} \approx 240$ K.

Figure 6.3 represents a sketch of general geometry of the S/I/F type samples. This type of samples also consists of three epitaxial layers grown on a single crystalline substrate. First layer to grow denoted as (F) was LCMO with the thickness *h* of about 200 nm. Then the insulating buffer layer of CeO_2 (I) ($d_i \approx 30$ nm) was deposited on LCMO, and finally YBCO epitaxial layer (S) was grown on the top of the structure. Figure 6.4 shows the FC and ZFC magnetization as a function of temperature for this type of samples for two external field orientations. As for F/I/S heterostructure curves display a sudden step in magnetization occurring just at the superconducting transition at $T_c \approx 89.5$ K (which is more pronounced for ZFC magnetization measurements) followed by a tendency to saturate at temperatures far below T_c. The metal-insulator transition point for S/I/F structure can

be also well identified at $T_{irr} \approx T_{Curie} = 250$ K. Compared with the F/I/S heterostructure the S/I/F sample demonstrates much bigger level of paramagnetic signal just above T_C making in plane field ZFC curve almost symmetric with respect to this temperature.

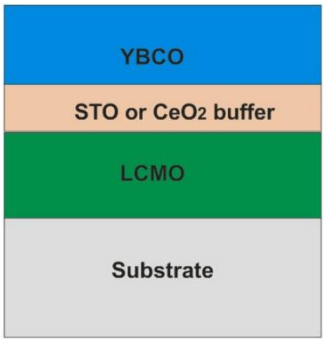

Figure 6.3 Sketch of the S/I/F sample geometry. LCMO and YBCO are grown by pulsed laser deposition via insulating buffer layer onto YSZ (or STO, LAO) (100) single crystalline substrates.

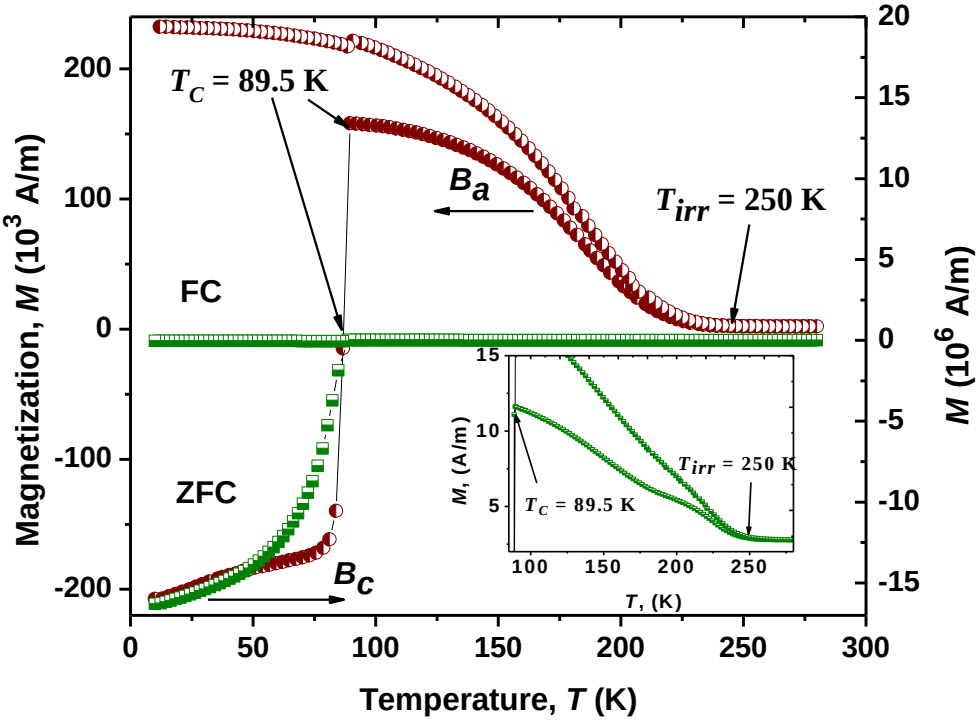

Figure 6.4 Temperature-dependent magnetization of a type S/I/F heterostructure ($YBCO_{200\ nm}/CeO_{2\ 30\ nm}/LCMO_{200\ nm}$) grown on a STO substrate and measured with in plane (left panel) and out of plane (right panel) magnetic field configuration under constant magnetic field of 0.01 T. The measurement was provided under ZFC and FC conditions and demonstrated the metal-insulator transition around $T_{irr} \approx 250$ K and a superconducting transition at $T_c \approx 89.5$ K. Inset: magnified part of out of plane field curve showing $T_c \approx 89.5$ K and $T_{irr} \approx 250$ K.

Investigation of magnetic properties of multilayered heterostructures such as F/I/S/I/F and S/I/F/I/S (see Fig. 6.5a and 6.5b correspondingly) shows in general the similar $M(T)$ curves behaviour. The metal-insulator transition occurs at the same temperature $T_{irr} \approx 250$ K but superconducting critical temperature $T_{c,}$ as well as ΔT_c show lower values compared to sole YBCO film (see Table 6.1). So the multilayered configuration has more degraded the superconducting properties of YBCO as observed through the decreasing of T_c and ΔT_c.

Table 6.1 Characteristics of multilayered hybrid structures.

Sample	T_c **, K**	ΔT_c**, K**	T_{irr}**, K**	J_c **(10K), A/m^2**	J_c **(77K) A/m^2**
YBCO	90	1.2		4.3×10^{11}	5.2×10^{10}
F/I/S	90	9.8	240	4.2×10^{11}	2.2×10^{10}
S/I/F	89.5	6.3	250	1.2×10^{11}	7.7×10^{9}
F/I/S/I/F	88	5.8	250	4.0×10^{10}	9.7×10^{9}
S/I/F/I/S	86	6.3	250	3.0×10^{11}	1.4×10^{9}

The $M(B)$ measurements of hybrid structures were performed with the applied magnetic field oriented in a direction parallel to the *c*-axis of the YBCO films (out of plane magnetization). Typical $M(B)$ curves of an F/I/S type hybrid structure in comparison with sole YBCO film for two different temperatures below the superconducting transition are shown in Figure 6.6. Such curves were used in the determination of the critical current densities [12], J_c (B) for all possible type of hybrid structures described in this section, which is shown in Figure 6.7 and 6.8 for 10, and 77 K, respectively. By comparing the J_c (B) curves for the YBCO film grown directly on YSZ and those for the different type of hybrid structures, two features may mainly be noted. First, at $B \approx 0$, the reference YBCO film has a slightly higher J_c with respect to the hybrid structures grown on the similar substrate. A diminishing critical current density of F/I/S hybrid structures with STO buffer layer deposited by PLD has been previously reported [13]. The decrease of J_c was explained by the circumstance that the superconducting correlations induced by the YBCO film are destroyed by the LCMO exchange field to a degree that depends on the transparency of the interface.

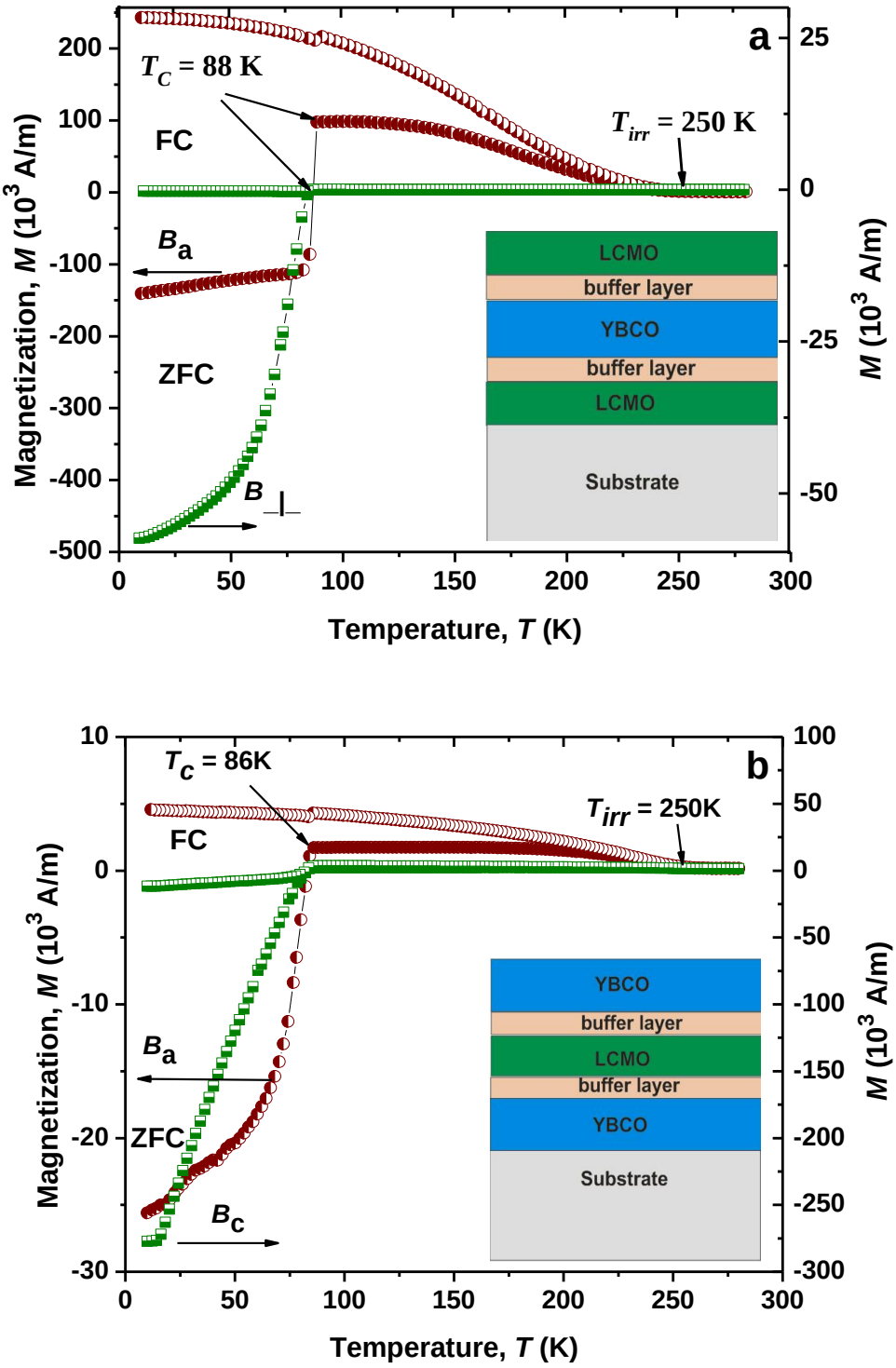

Figure 6.5 Temperature-dependent FC and ZFC magnetization of a type F/I/S/I/F heterostructure (a) and S/I/F/I/S heterostructure (b) measured with in plane (left panel) and out of plane (right panel) magnetic field configuration under constant magnetic field of 0.01 T. Inset: sketch of the sample geometry.

a)

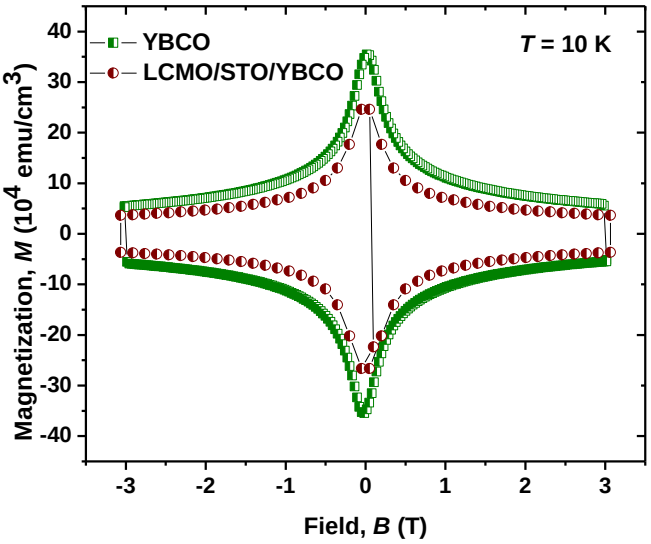

b)

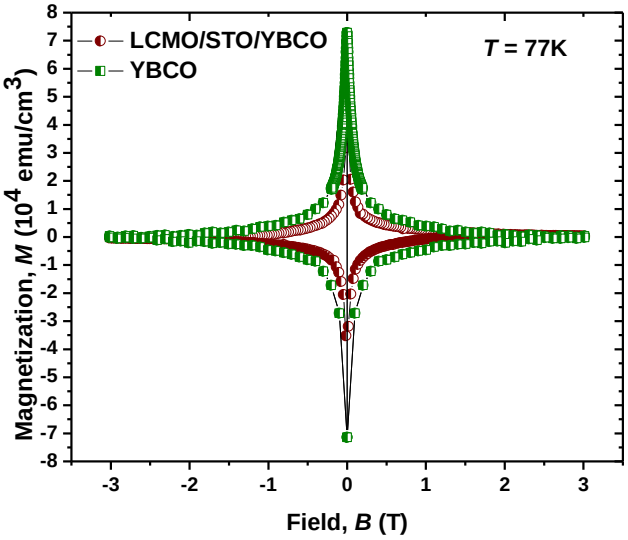

Figure 6.6 Magnetization curves of the single YBCO film and LCMO/STO/YBCO heterostructure measured at 10 K (a) and 77 K (b).

The second feature regards the magnetic field dependence of the critical currents. A closer examination of the $J_C(B)$ dependencies leads to the conclusion that at low temperatures, 10 K, all hybrid structures show a similar curve shape with the smallest J_C value for FISIF hybrid which would not be surprising as it contains only one superconducting layer surrounded by two ferromagnetic layers. So the

suppression of superconductivity here must be more pronounced. But at higher temperature, 77K (see Fig.6.8), the J_C (B) curve demonstrates better shape in the region of medium fields (B =1-3T) compared with S/I/F/I/S and S/I/F hybrids. Such J_c (B) curve behavior may be explained in terms of a competition of two effects [13]. Because of diffusion during PLD process, some of the LCMO molecules penetrated deeper into the YBCO film, creating additional pinning centers.

In thin YBCO films the critical current is determined by the pinning of the vortex structure. The LCMO exchange field leads to a partial destruction of the superconducting correlations induced by the YBCO film and hence to a decrease of J_c. At the same time, the appearance of strong new pinning centers because of the ferromagnetic inclusions that have diffused into the YBCO film should lead to an increase in J_c. The competition between these two effects probably may even enhance J_c (B) shape.

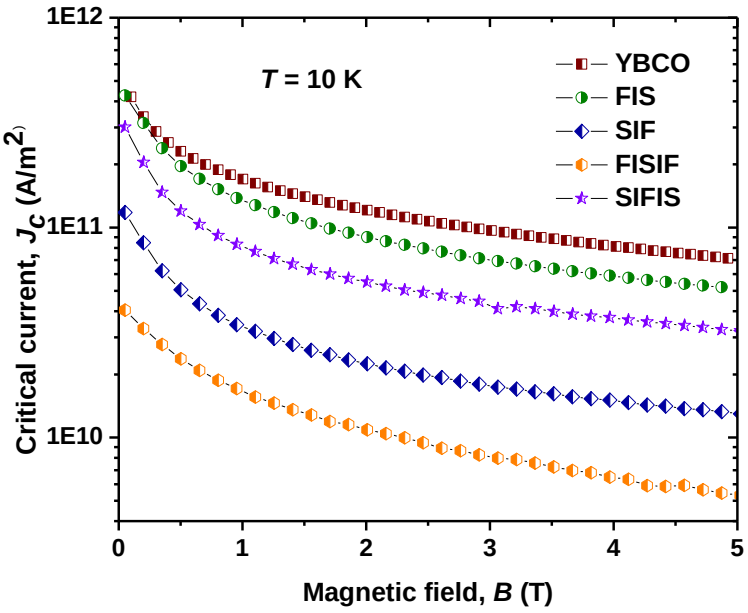

Figure 6.7 Magnetic field dependence of the critical current density, J_c, for different type of hybrid structures compared with single YBCO film at 10 K.

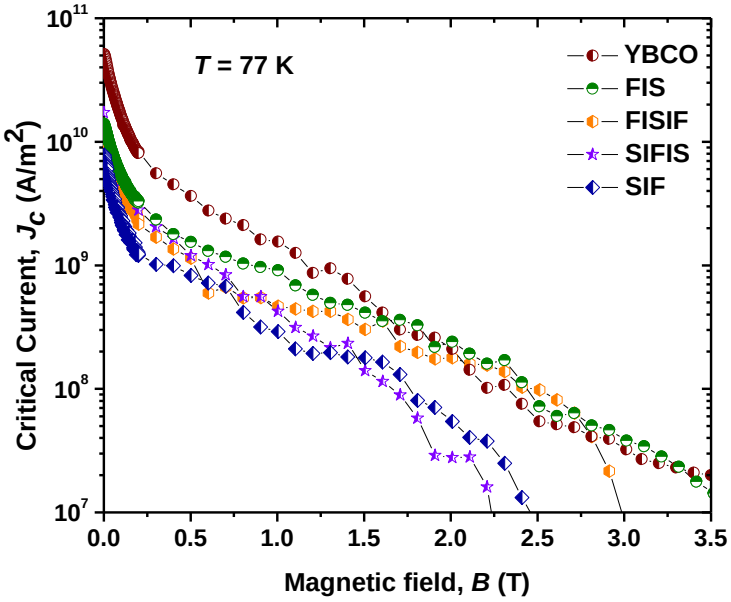

Figure 6.8 Magnetic field dependence of the critical current density, J_c, for different type of hybrid structures compared with single YBCO film at 77 K.

From Fig. 6.8 it may be observed that the critical current density corresponding to multilayered hybrid structures (F/I/S/I/F and S/I/F/I/S) starts to decrease more abruptly at high applied field, compared to single YBCO film and the difference between hybrid structures and YBCO is directly observed, as above 3.0 T, the J_c of the YBCO film is higher than that of hybrids. Only F/I/S structure demonstrates the behavior similar to YBCO in higher fields.

6.4 Transport properties of YBCO/STO/LCMO hybrid structures (YBCO on the top) under in-plane current injection through manganite layer

Figure 6.9 shows the typical behaviour of the resistivity versus temperature for our sole YBCO and LCMO films of a similar thickness grown by PLD on YSZ substrates. We can readily identify the superconducting transition for YBCO film at T_c = 89 K and the metal – insulator transition point (MIT) for LCMO film at T_p = 255 K. These are similar to bulk material parameters, demonstrating the ability of PLD method to grow high quality epitaxial films for both materials.

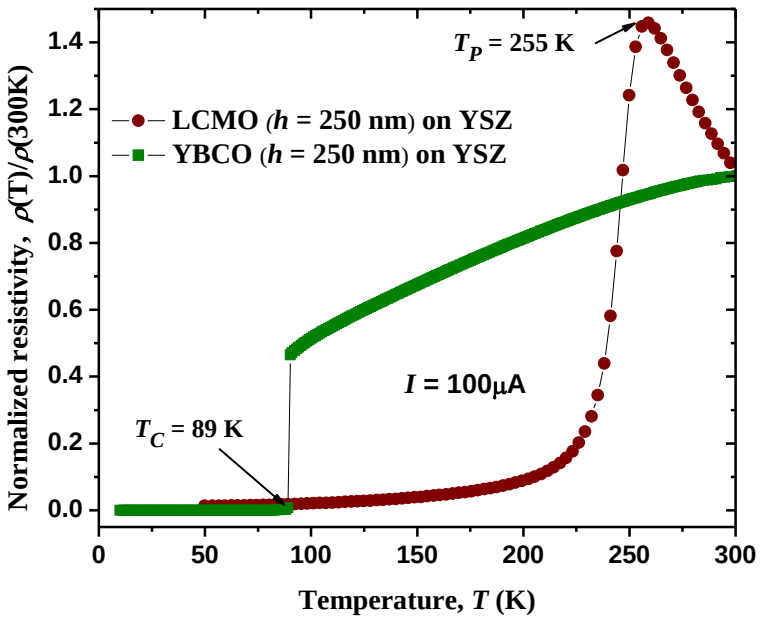

Figure 6.9 Temperature dependence of a normalized resistivity (warming curves) at 100 μA probing current for: 250 nm – thick YBCO/YSZ and 250 nm – thick LCMO/YSZ films.

The geometry for in-plane current injection is shown in Figure 6.10a. Injection and $R(T)$ measurement gold contacts pads (~100 nm thick) were deposited on both, the LCMO buffered by STO layers, and the YBCO micro bridge. Four contacts were placed on YBCO micro bridge for the resistance measurement (I_1) and two contacts for the injection current power source (I_{inj}).

The $R(T)$ measurement for zero external magnetic fields and 5 T field applied in plane is presented in Figure 6.10b. It is clearly seen that the structure demonstrates both superconducting-like behavior with T_c = 80 K and manganite-like behavior above this temperature. Resistance of a hybrid structure is not dependent on the applied magnetic field at the superconducting state and it significantly changes with applied field far above T_c. This means that in this state the electrical current passes through both the superconducting layer (YBCO) and the giant magneto-resistive LCMO layer. Above superconducting transition temperature T_c = 80K the curves demonstrate YBCO-like shape until $T \approx$ 160K where the resistance starts to rise faster and reaches its maximum at around T_P = 250K which is consistent with the metal-insulator transition point for sole LCMO film (see Fig.6.9).

Such *MR(T)* behavior was also observed in [14], and it was explained in terms of the spin-dependent interface scattering which together with thermally

activated flux flow takes account of the present giant positive *MR* in the mixed state region near the onset temperature of the superconducting transition. The magnetoresistance curve *MR*(*T*) at higher temperatures shows its minima point shifted for ~ 20 K to lover temperatures in comparison with T_P. Above this temperature *R*(*T*) curve demonstrates the semiconducting-like behavior similar to sole LCMO film.

a)

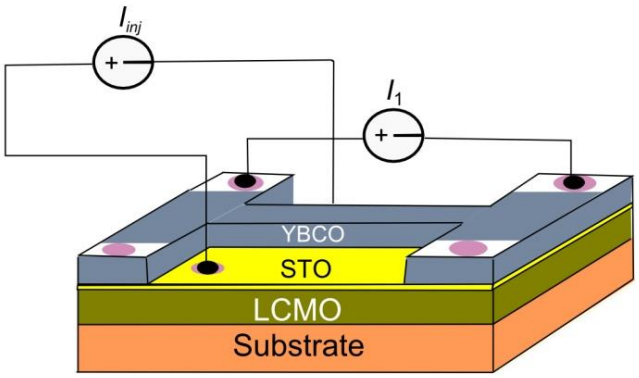

b)

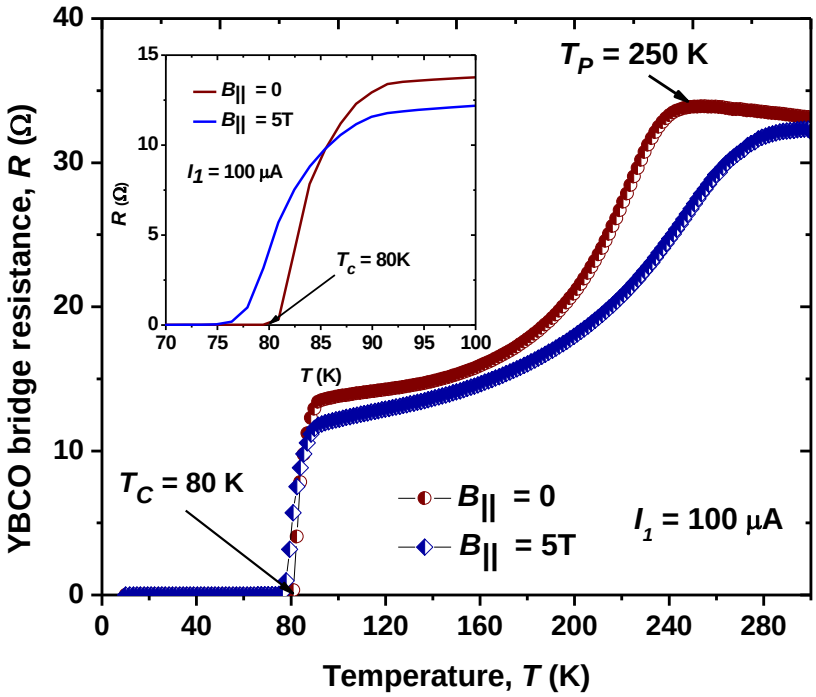

Figure 6.10 (a) Sketch of geometry for hybrid structure of S/I/F type representing YBCO micro bridge (w = 25μm) on the top of LCMO epitaxial layer buffered with STO thin layer (with injection current source connected to STO). (b) The in-plane resistance vs. temperature curves of a hybrid $YBCO_{200nm}/STO_{20nm}/LCMO_{200nm}$ for zero field and 5 T applied magnetic field showing superconducting transition at $T_c \approx$ 80K and metal-insulator transition at $T_P \approx$ 250K(b). Inset: an enlarged plot of *R* (*T*) curves around superconducting transition.

Application of an injection current as shown in Fig.6.10a will dramatically change the $R(T)$ curve behavior. Figure 6.11 demonstrate the trend of the $R(T)$ curve evolution when the different injection current is applied. Small injection current I_{inj} = 0.5 mA slightly increases the resistance just above T_c and it leads to the formation of a drop in resistance in the temperature region between T_c and T_p. This drop of the resistance becomes more pronounced for bigger injection currents with shifting of the minimum resistance point (T_d) to higher temperatures. The application of a high injection current (~ 5 mA) also leads to the reduction of T_c for about 4 K and significant reduction of a sample resistance at room temperature. Such behavior is very promising for bolometric applications.

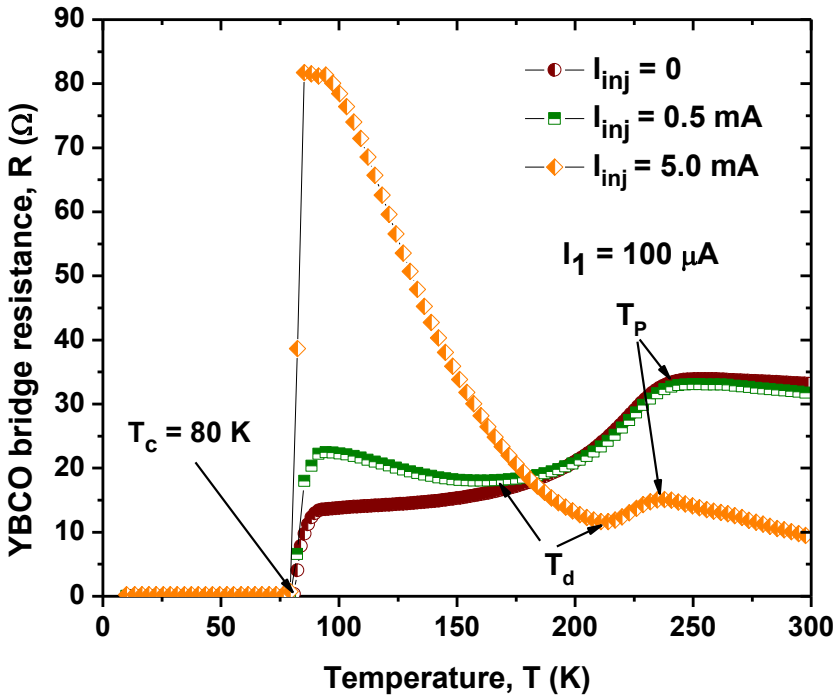

Figure 6.11 Temperature–dependent in-plane resistance $R(T)$ for the YBCO bridge in setup of Fig. 6.10a for different injection currents values. Notice that an increasing of the injection current causes a decrease in the resistance at room temperature, but a drop in resistance around the temperature T_d is shifted to higher temperatures. Additionally, a shift in the superconducting transition temperature T_c from 80 K to 76 K was detected.

6. 5 Electroresistance and magnetoresistance effects in LCMO/STO/YBCO hybrid structures (LCMO on the top)

In the Figure 6.12, the schematic of the $LCMO_{150\ nm}/STO_{20nm}/YBCO_{200nm}$ hybrid structure and its micro-photograph is shown. It comprises the YBCO micro-bridge (w = 100 μm) with LCMO pad grown across it on the top of a 20 nm thick STO insulator layer. The sample configuration allows the resistance measurement to carry out within different layers separately. The results of these measurements are presented in Figure 6.13. Clearly, the superconducting transition of YBCO micro bridge was not affected by the presence of the top LCMO layer. The shape of the YBCO $R(T)$ curve is quite similar (except for the slight rise around T_p = 255 K) to the resistance of the single YBCO layer shown in Fig.6.8. Moreover, the superconducting transition temperature (T_c = 90 K) is the same.

a)

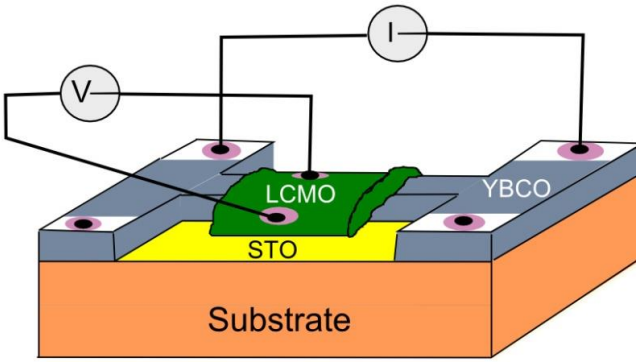

b)

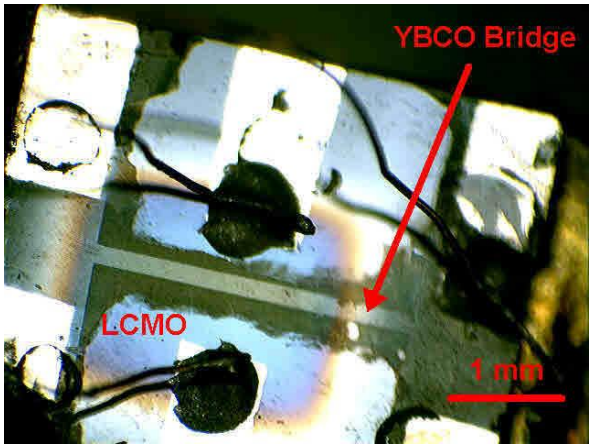

Figure 6.12 (a) Sketch and (b) micro-photograph of a LCMO/STO/YBCO hybrid structure representing epitaxial LCMO layer grown on the top of STO buffered YBCO micro-bridge (w = 100 μm).

In contrast, the superconductivity has considerably been affected in similar YBCO/LCMO heterostructures which is consistent with data presented in Refs. [1], and [15, 16] where the intermediate insulating layer has not been introduced.

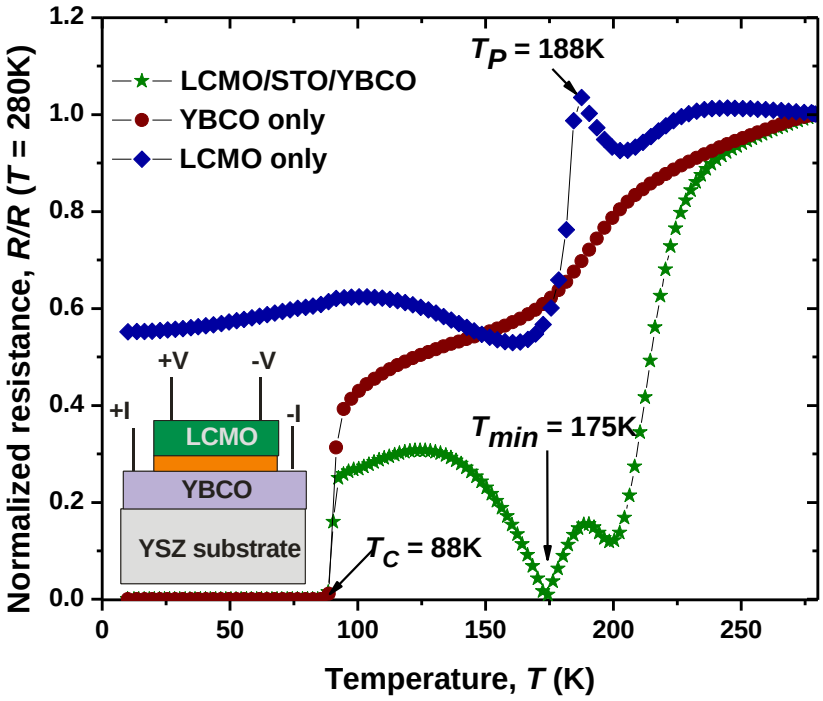

Figure 6.13 Temperature dependence of a normalized resistance (warming curves) for: 200 nm – thick LCMO film growing over YBCO-bridge via 20 nm STO buffer layer; 300 nm - thick YBCO bridge; LCMO/STO/YBCO hybrid trans-resistance. Inset: the cross section of a hybrid structure.

This confirms our expectation to suppress the proximity effect by the insulating buffer layer for YBCO/LCMO heterostructures with LCMO on top. The direct measurement of the critical current density of the YBCO bridge gives $J_c \approx 2\times10^9$ A/m^2 at 80 K, which is reasonably high value for the film at these conditions. On the other hand, we have found that the resistance behaviour of the LCMO layer (Fig.6.13) is significantly different from properties of a sole LCMO film shown in Fig.6.9. This is likely due to different growth conditions on the top of the YBCO/STO structure, which can also be affected by the intermediate optical lithography carried out before depositing the LCMO layer. Nevertheless, the LCMO

layer still demonstrate the metal-insulator transition, but now the MIT point is shifted to low temperatures showing $T_p \approx 188$ K.

In order to study the interplay between the superconductor and magnetic layers, we have carried out resistance measurements of the hybrid structure using the configuration of electrical terminals shown in the inset to Fig. 6.13. As it can be seen, the measured *R(T)* behavior of the hybrid structure exhibits several intriguing features as follows.

First of all, our hybrid structure still demonstrates superconducting properties below $T_c \approx 88$ K. Note, the voltage is measured over the LCMO layer which is separated from YBCO layer by the STO insulator. Another recognizable feature can be identified as the MIT point of the LCMO layer, which occurs at nearly the same temperature of about 190 K as it does for the LCMO layer measured directly. Above 200 K, the so-called trans-resistance is steeply rising to eventually reproduce the trend exhibited by the curve measured directly in the superconducting YBCO layer. The most unexpected behaviour of the trans-resistance is observed around $T_{Rmin} \approx$ 175 K, where the curve shows the sharp dip with a small minimum resistance of about 0.5 Ohms.

Somewhat similar behaviour of the *R*(*T*) curve with strong fluctuations in resistance below the MIT point was obtained in Ref. [1] for YBCO/LCMO superlattices but only under FC condition with small magnetic field applied. However, such fluctuations carried an unstable (likely even non-reproducible) character, unlike very reproducible and clear behaviour for both warming and cooling curves in our case.

These fluctuations have been explained in terms of current percolation effect within the LCMO material. The percolation is widely discussed for manganites [17, 18], which enables metastable transitions through its phases having various conductivities and magnetic properties. Naturally, this kind of transitions would lead to a change in resistance. Although this explanation does not provide a complete description of the observed drop in the resistance at 175 K, but indicates a possible direction in further exploration.

Another scenario for this behaviour can be inferred by involving the trance-resistance measurement setup shown in Fig. 6.13, where the current passes through YBCO bridge and the voltage is measured on the top LCMO layer. Indeed, the setup

can be considered as the circuit of parallel resistances. In the simplest case, we can consider YBCO layer as one resistor with rather linear behaviour above T_c (Fig. 6.13), and the LCMO layer is the second resistor with extremely nonlinear characteristics. In this scenario, one may try to explain the exotic $\rho(T)$ in terms of the current shunting model [17]. In this scenario, the current injected into the YBCO film re-distributes through parallel YBCO and LCMO layers. Note that the redistribution succeeds through the insulating layer, which is likely to complicate the picture with additional serial and parallel resistors (or tunnelling effects).

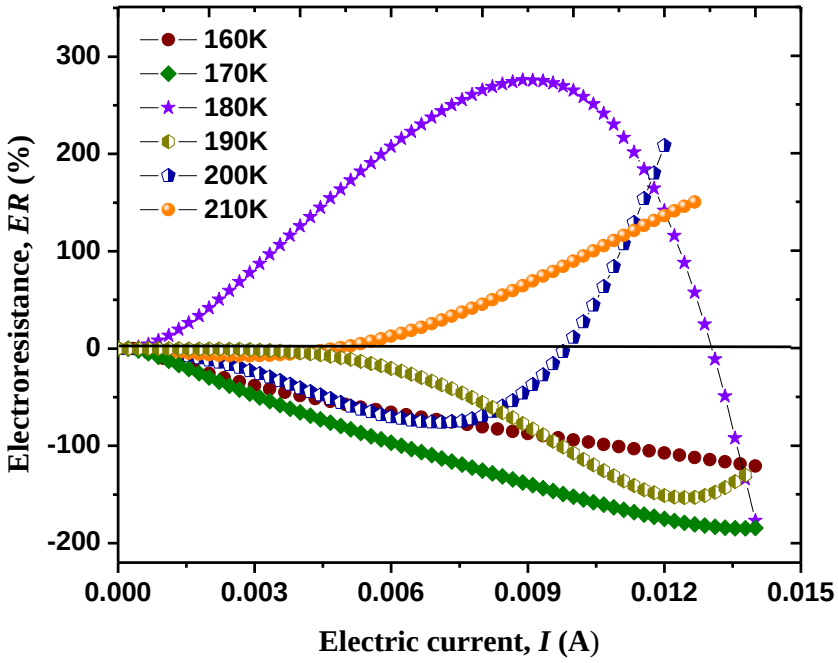

Figure 6.14 Electroresistance of LCMO/STO/YBCO structure as a function of applied current at different temperatures around minimal resistance point showing temperature depended transition from high negative to high positive electroresistance defined as: $ER = [(R - R_{min})/ R_{min}]\times 100\%$.

In any case, below the superconducting transition temperature almost all current is passing through the YBCO layer, whereas the LCMO layer is in a high resistance state. The combined resistance of this circuit is very small (~10^{-5} Ohms), and it is dominantly defined by the superconducting channel. In the vicinity of T_c, the situation changes dramatically. The resistances of two layers may become

comparable and the charge transfer through the circuit is redistributed. Again, it should be noted that the redistribution occurs through the thin insulating layer between the superconducting and ferromagnetic materials. The current redistribution results in much high rate of charge transfer through the LCMO layer, provoking the formation of the larger volume of the conducting phases, which eventually leads to the percolation mechanism of charge transfer with lowered resistance. The total circuit resistance goes down (as if it was in a re-entrant superconducting state) and reaches a finite minimum resistance value of $R_{min} \approx 0.5$ Ohms nearby the MIT point. Above T_p, the manganite returns to the high resistance state which rapidly increases the total circuit resistance. Notably, the single LCMO layer resistance above T_c shows the strong temperature dependence; hence expectedly the temperature dependence of the total network resistance is mostly determined by LCMO behaviour in this temperature range.

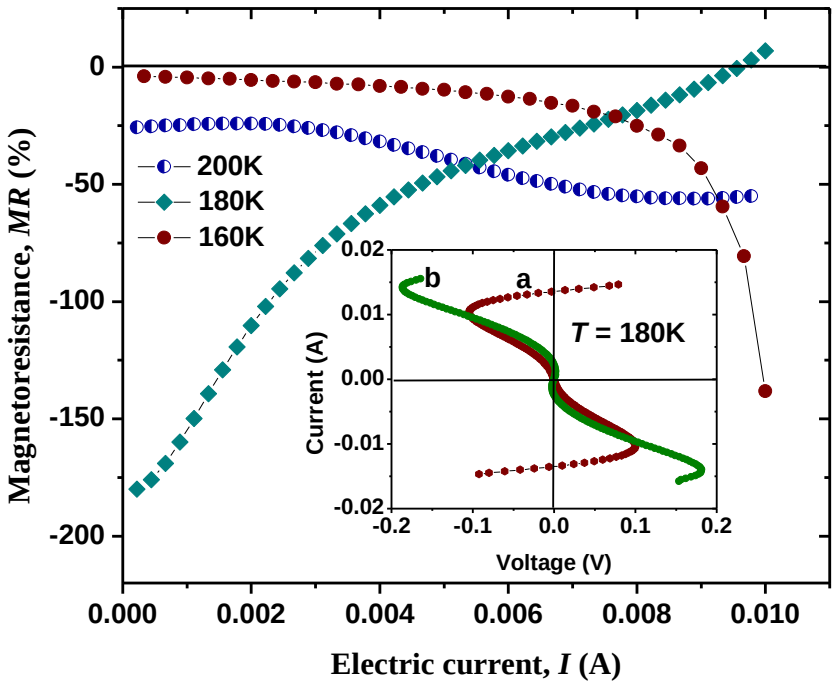

Figure 6.15 Magnetoresistance ($MR = (R_B - R_0)/R_0 \times 100\%$) of a hybrid structure as function of applied current for different temperatures around T_{Rmin}. Inset: *S* type *IV* characteristic of a sample at $T \approx 180$ K showing negative differential resistance with zero field condition (*a*) and $B = 1$ T (*b*).

The investigation of *I-V* characteristics of the hybrid structure shows: (i) their nonlinear character and (ii) giant electroresistance effect for a wide range of temperatures from 90 K to 220 K. The typical *I-V* is shown in the inset to Fig. 6.15. Figure 6.14 shows the electroresistance (*ER*) of LCMO/STO/YBCO hybrid structure as a function of applied current at different temperatures around the temperature exhibiting the lowest resistance (T_{Rmin}). The electroresistance was calculated from *I-V* measurements as follows: $ER = [(R - R_{min})/ R_{min}]\times 100\%$, where $R_{min} = R$(at $I = 1$ μA). As can be seen in Fig. 6.14, the electroresistance changes nonlinearly with the applied current, indicating that the effect is reversible [18, 19]. Below T_{Rmin}, the *ER* effect is negative and can be fitted exponentially. Above T_{Rmin}, the *ER*(*I*) behaviour becomes more complicate and shows upward curvature. It should also be noted that the value of the resistance comes back up again when the current is reduced, indicating the effect is reversible.

However at $T \approx 180$ K, which is very close to T_{Rmin} the electroresistance demonstrates unusual giant positive behavior, showing downward curvature with $ER_{max} \approx 270\%$ under 9 mA current. This behavior clearly indicates that the charge transfer through the heterostructure is strongly dependent on external parameters such as temperature and applied current.

Since the electric current has a strong influence on the total resistance of the hybrid structure, it is important to know whether the applied current affects the magnetoresistance (*MR*) of the sample. We have investigated the influence of the applied magnetic field ($B_a = 1$ T) on the current transport properties for three different temperatures around T_{Rmin} (Fig. 6.15). The applied magnetic field was parallel to the current.

The magnetoresistance was calculated as follows: $MR = [(R_B - R_0)/R_0]\times 100\%$, where R_0 denotes the zero field resistance. The most unusual behavior was detected at $T \approx 180$ K (which is at or just above the resistance minimum). At this temperature, the MR behavior experiences a crossover from large negative to positive values.

Obviously, the electric current has a strong influence on the *MR* behavior of the hybrid structure. This assumes the complex interplay between clusters with different magnetic and electric properties in the phase separated LCMO layer, presumably experiencing some sort of percolation for the charge transfer.

6.6 Conclusion

In this Chapter the magnetic and transport properties of multilayered hybrid structures based on YBCO-LCMO were investigated. All measurements show the coexistence of ferromagnetism at high temperatures ($T > T_c$) and superconductivity at low temperatures ($T < T_c$) in these structures. All hybrid structures demonstrate no enhancement in the critical current in comparison with pure YBCO films, although the hybrid structure of F/I/S type (LCMO on top) shows almost the same J_c *(B)* behaviour as the single YBCO film at 77K. The last may involve the importance of the first grown layer and it influence on the superconducting properties of the total multilayered structure.

The possibility of the control of YBCO bridge resistance by injection of an in plane current through LCMO layer was demonstrated in the hybrid structure of S/I/F type (YBCO bridge on top of buffered LCMO film). The application of injection current dramatically changes the shape of $R(T)$ curve. This leads to the decreasing in T_c, demonstrate the drop in resistance before T_p and the reduction in resistance at room temperature which may be interesting for bolometric applications.

We have also investigated the electrical transport properties of a tri-layers hybrid structure of F/I/S type (LCMO on top of buffered YBCO bridge). The resistance measurement data show features consistent with both superconducting and ferromagnetic behaviors, yet having minimal direct influence through, for example, the proximity effects. On the other hand, the hybrid structure demonstrates the unusual $R(T)$ behavior, with a sharp dip in resistance below T_c. It was also found that electroresistance and magnetoresistance around T_{Rmin} can be tuned by electric current, which may have applications in controlling the properties of such hybrid devices. This behavior may be explained in terms of the current shunting model and phase transition effect in LCMO triggered by electrical current. We may conclude that in such hybrid structures the superconductivity and ferromagnetism can easily coexist, showing some new current dependences with steep characteristics which may be useful for potential applications.

References

[1] P. P. Deen, F. Yokaichiya, A. de Santis, F. Bobba, A. R. Wildes, and A. M. Cucolo, *Phys. Rev. B* **74,** 224414, (2006)

[2] A. I. Buzdin, *Rev. Mod. Phys.* **77**, 935–976, (2005)

[3] A Yu Aladyshkin, A V Silhanek, W Gillijns, and V V Moshchalkov, *Supercond. Sci. Technol.* **22,** 053001, **(**2009)

[4] **J. Tao, D. Niebieskikwiat, M. Varela, W. Luo, M. Schofield, et al.** *Phys. Rev. Lett.* **103,** 097202, (2009)

[5] C. Şen, G. Alvarez, and E. Dagotto, *Phys. Rev. Lett.* **105**, 097203, (2010)

[6] S Piano, A De Santis, F Bobba, F Giubileo, M Longobardi, A Di Bartolomeo, at al. *J. Phys.: Condens. Matter* **21,** (2009)

[7] C. Z. Chen, C. B. Cai,L. Peng, B. Gao, F. Fan, Z. Y. Liu, Y. M. Lu, R. Zeng, and S. X. Dou. *Journal of Applied Physics* **106**, 093902, (2009)

[8] Z. W. Dong, R. Ramesh, and T. Venkatesan, Mark Johnson, Z. Y. Chen, S. P. Pai, V. Talyansky, at al. *Appple.Phys. Lett.* **71**, 1718, (1997)

[9]C.-C. Fu, Z. Huang, N.-C. Yeh. *Phys. Rev. B* **65**, 224516, (2002)

[10] R. Werner, C. Raisch, A. Ruosi, B. A. Davidson, P. Nagel, M. Merz, *at all Physical Review B*, **82**, Issue 22, 224509, (2010)

[11] X. Guo, S. Dai, Y. Zhou, Z. Chen, G. Yang, F. Liu, K. I˙brahim, H. Qian, *Mater. Sci. Eng. B.* **76** ,18, (2000).

[12] T. Petrisor, Jr. M. S. Gabor, C. Tiusan, V. Galluzzi, G. Celentano, S. Popa, A. Boulle, and T. Petrisor. *Journal of Applied Physics* **112**, 053919, (2012)

[13] V. A. Khokhlov, A. Yu. Prokhorov, V. F. Drobotko, G. G. Levchenko, P. N. Mikheenko, R. Chakalov, and C. Muirhead. *Low Temperature Physics*, **29**, N 2, (2003)

[14] C B Cai, L Peng, B Holzapfel, X M Xie, Z Y Liu, Y M Lu and C Z Chen *Supercond. Sci. Technol.* **23,** 034010, (2010)

[15] S. Soltan, J. Albrecht, H.-U. Habermeier, *Materials Science and Engineering B*, **144**, 15–18, (2007)

[16] R. Werner, C. Raisch, A. Ruosi, B.A. Davidson, P. Nagel *et all*, *Phys. Rev B*, **82,** 224509, (2010)

[17] S. F. Chen, P. I. Lin, J. Y. Juang, T. M. Uen et al. *Appl. Phys. Lett.* **82** N8, 2003

[18] V. Markovich, G. Jung, Y. Yuzhelevskii, G. Gorodetsky, and J. Gao, *Phys. Rev. B*, **75** 104419, (2007)
[19] X. P. Zhang, B. T. Xie, Y. S. Xiao, B. Yang, P. L. Lang, and Y. G. Zhao. *Appl. Phys. Lett.* **87,** 072506, **(**2005)

Chapter 7
Investigation of STO/LCMO superlattices

7.1 Introduction to STO/LCMO superlattices

The manganites of type $La_{1-x}Ca_xMnO_3$ demonstrate the colossal magnetoresistance (CMR) and could be possibly the base for for magnetic sensors, recording memory devices [1, 2] and emerging spintronic applications in the form of epitaxial films and heterostructures [3, 4]. The key feature responsible for the CMR effect in this compound is the dynamic coexistence of phases with different properties, known as phase separation (PS) [5, 6]. The coexistence of insulating and metallic phases in $La_{2/3}Ca_{1/3}MnO_3$ (LCMO) was directly observed at temperatures below the Curie temperature (T_{Curie}) [7]. In [8] the direct imaging of clusters with the size of around 3-4 nm was reported in lanthanum manganite and attributed to as the evidence of the nanoscale phase separation. Moreover, manganite thin films exhibit unusual properties such as nonlinear resistance and resistance metastability [9, 10]. However, the successful development of manganite-based devices requires certain magnetic and transport properties, in particular at surfaces and interfaces if hybrid heterostructures comprising of cuprate and manganite components are used for spintronic applications employing CMR and high temperature superconductivity [11]. Unfortunately, the lanthanum manganites usually demonstrate their relevant magnetic properties well above the superconducting critical temperature of the cuprates, which impairs the development of these hybrid applications.

Lower temperatures of the metal-insulator transition and the magnetoresistance enhancement at low temperatures were obtained by reducing the manganite film thickness [12] or by creating manganite-insulator superlattices with periods of $n < 10$ [13, 14]. However, no observations of unusual CMR behaviour in these superlattices were reported below 90 K, the range of interest for combination with HTS materials. In this work, we have grown $(LCMO/STO)_n$ superlattices (with n = 20-30 periods) on LAO and YSZ substrates by pulsed laser deposition (PLD). To enhance effects observed, the thickness of individual LCMO layers (~ 3 nm) is chosen to be comparable with diameter of nano-clusters formed as a result of phase

separation. We have investigated magnetic and transport properties of such superlattices, and compared them with properties of LCMO films grown on similar substrates under the same technological conditions.

7.2 Experimental details

Thin films of $La_{2/3}Ca_{1/3}MnO_3$ (LCMO), $SrTiO_3$ (STO) and their heterosructures were epitaxially deposited on 5×5 mm^2 (100) YSZ and LAO substrates with STO buffer by standard PLD technique described in Chapter 3. Only the laser fluence was changed to 2 Hz. The programmable target carousel was used to facilitate the non-interrupting deposition process for manufacturing multilayered structures and superlattices. The surface morphology of thin film was investigated using field emission scanning electron microscope (SEM) equipped with a through the lens (TTL) detector. The interfaces between layers and microstructure of the superlattices were observed by transmission electron microscopy (TEM), as well as energy-filtering transmission electron microscopy (EFTEM). Cross-sectional TEM samples were prepared using lift-off focused ion beam technique. For magneto-transport measurements, golden contact pads were deposited by laser ablation. The sample resistance as a function of temperature was measured by DC four probe method at different applied magnetic fields.

7. 3 Results of SEM and TEM investigation

The transmission electron microscopy confirms epitaxial grow, sharp interfaces and continuous layers in both single LCMO films and superlattices $(LCMO/STO)_n$, where the subscript denotes the superlattice (SL) period number. Figure 7.1 demonstrates the color map of a TEM cross-section image for such superlattice showing: LAO substrate (red), STO layers (green, including buffer layer), and LCMO sub-layers (dark red). This picture allows the appreciation of sub-layer average thickness as: 3-nm for LCMO and 7-nm for STO with STO buffer layer of 25-30 nm thick. In this superlattice a perfectly smooth layers of uniform thickness for both STO and LCMO can be observed. Figure 7.2 shows the example of

individual EFTEM jump ratio image of the same superlattice using the Lanthanum ionization edges (Fig.7.2a) and Strontium ionization edges (Fig.7.2c) together with the corresponding line profiles (Fig.7.2b) and (Fig.7.2c) correspondingly. The line profile across the image on Fig.7.2b shows (from left to right): the high intensity area related to LAO substrate, the valley associated with STO buffer layer, and the series of peaks for every single LCMO sub-layer with the same spatial separation and similar intensity. The similar behavior but with inversed valley (LAO) and peaks (STO) is demonstrated on Fig.7.2c.

However after the detailed analysis of TEM and SEM images we have detected the columnar grains grown with the grain size ~50 nm (see Fig.7.3). It is well known that the grain boundaries will disrupt the crystal structure and act as accumulative pinning centers for structural defects. So the crystallized film can be seen as a scenario of mixed phase coexistence, containing high conductive crystalline grains and low-conductive grain boundaries [10].

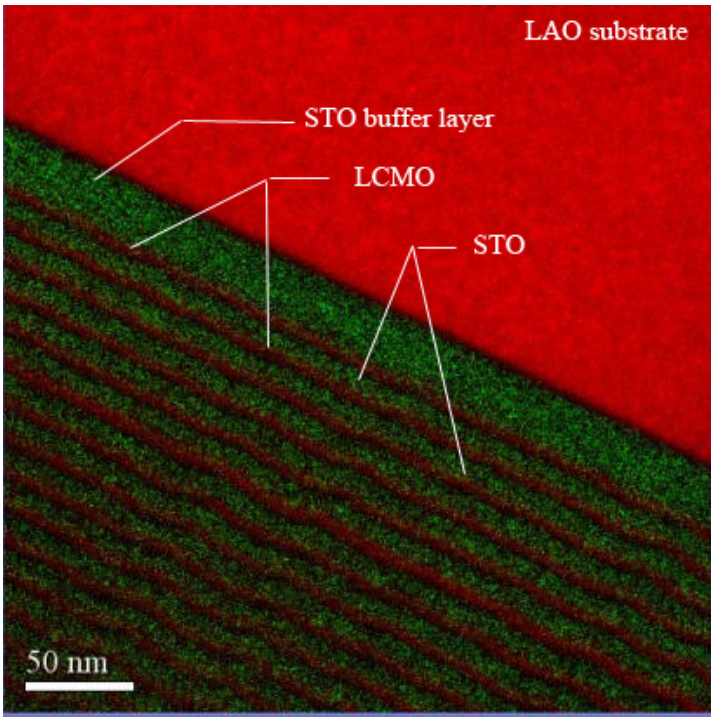

Figure 7.1 Color map of the cross-section TEM image of SL1 (LCMO-3 nm/STO-7 nm)$_{20}$ superlattice grown on LAO substrate via STO-25 nm buffer layer.

Transmission electron microscopy shows sharp interfaces between LCMO and STO sub-layers in LCMO/STO superlattices. In Figure 7.4, the superlattice of type (LCMO - 3 nm/STO - 3 nm)$_{30}$, hereafter denoted as SL4, is shown. The region in the vicinity of the substrate buffered by a 35 nm thick STO layer exhibits a high density of columnar defects, which evolve into a presumably more relaxed structure with 25 to 60 nm wide columnar domains characteristic to PLD epitaxial films. A similar structure has been observed for REBa2Cu3O superconducting films and multilayers (RE denotes a rare earth element, such as Y or Nd) [15].

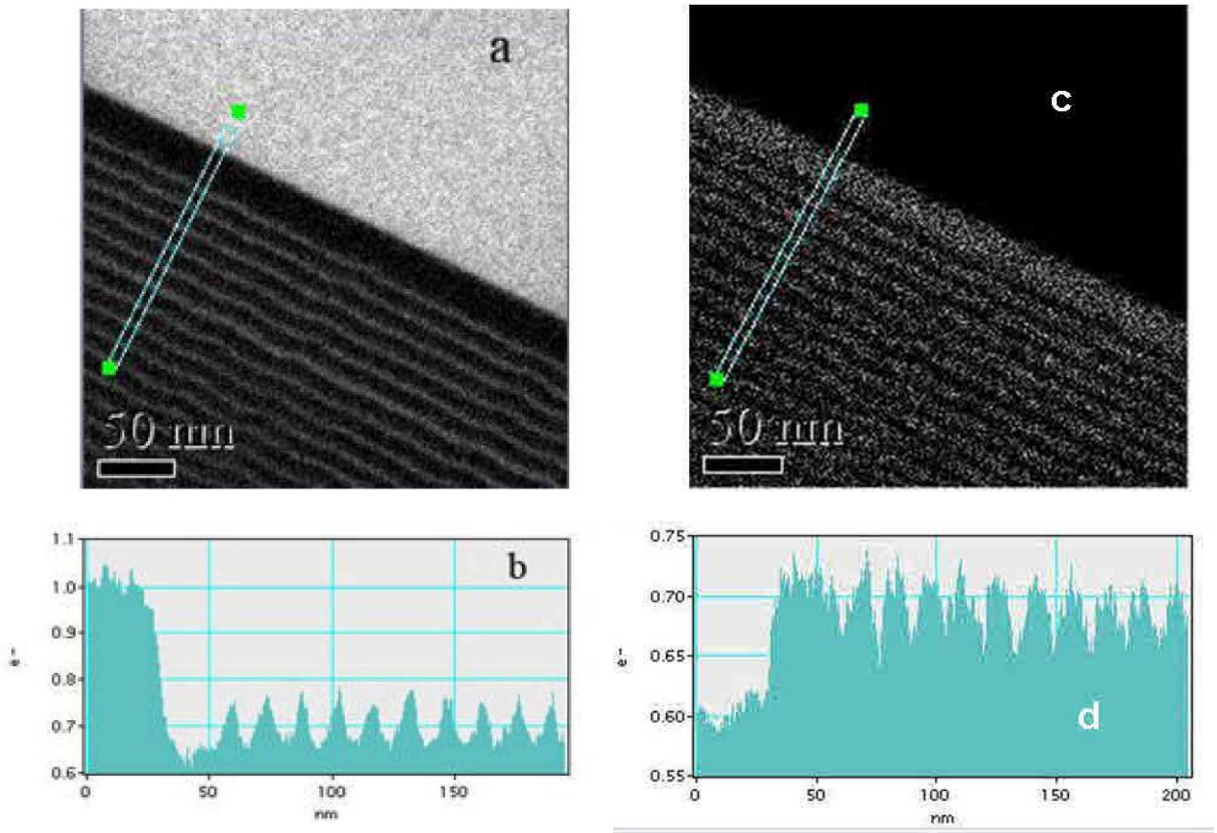

Figure 7.2 Lanthanum jump-ratio image (a), and corresponded line profile of Lanthanum jump-ratio (b). Strontium jump-ratio image (c), and corresponded line profile of Strontium jump-ratio (d).

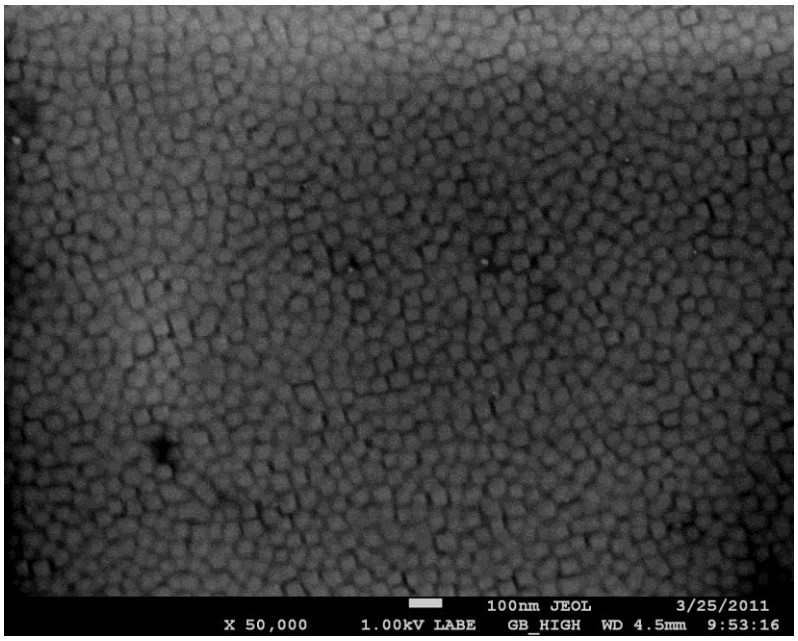

Figure 7.3 SEM image of SL1 (LCMO-3 nm/STO-7 nm)$_{20}$ sample.

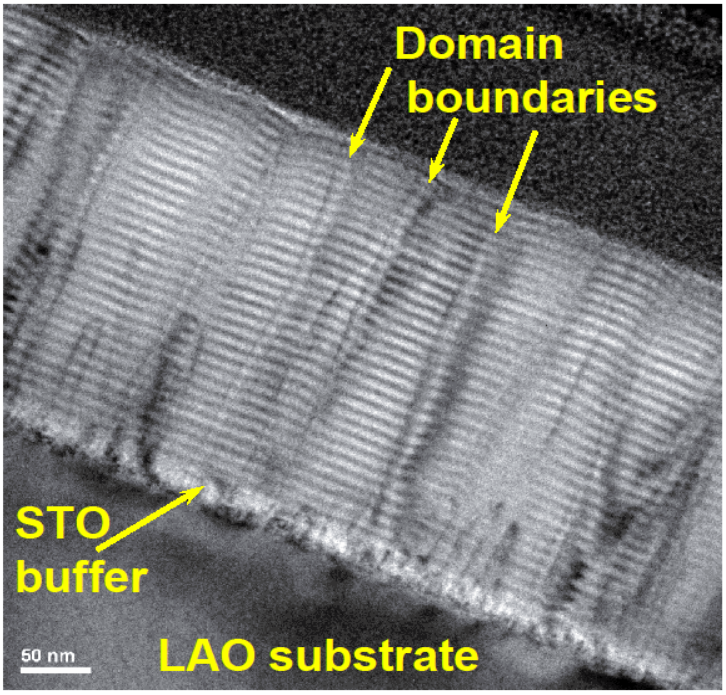

Figure 7.4 A transmission electron microscopy image of the cross-section of SL4 (LCMO -3 nm/STO - 3 nm)$_{30}$ superlattice grown on LAO substrate buffered with a 35 nm thick STO layer. Alternating bright and dark layers are STO and LCMO layers, respectively.

The analysis of SEM images of the SL surfaces shows various rectangular patterns, from clearly separated rectangular islands of about 50 nm (see Fig.7.3) to the mosaics of interconnected chains of rectangular islands (as shown for SL4 in Fig.7.5) formed on the surface of the LCMO/STO superlattice depending on the structure, deposition conditions, and substrate selected. These rectangular surface features indicate the dimension (~ 50 nm) of the columnar domains. The columnar domains exhibit enhanced deformation (slightly enhanced upward layer curvature within domains) in the upper half of the structure (Fig. 7.4), which can result in rougher interfaces between the layers and eventually the surface itself. In the case of the SL4 shown in Fig. 7.5, the surface is rather smooth with the roughness on the surface of about 10 nm as can be estimated from its lowest points at the boundaries to the highest points in the middle of the domains in Fig.7.4.

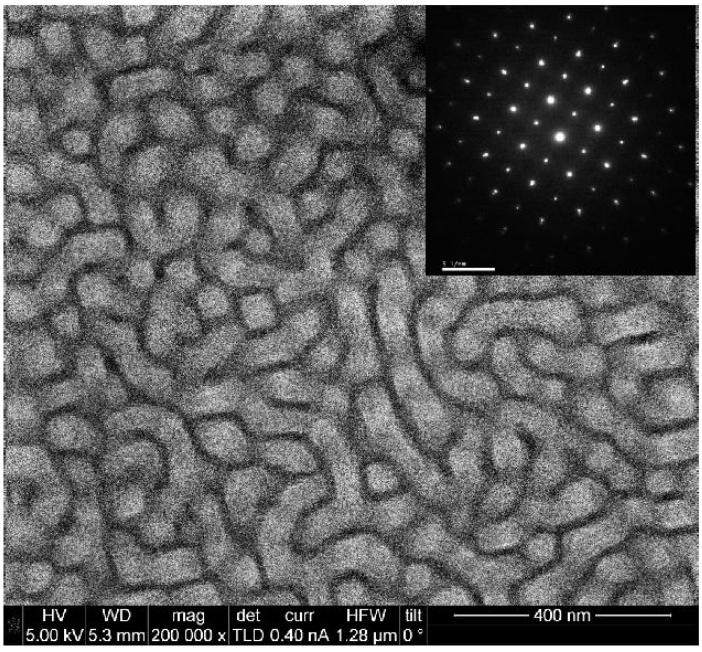

Figure 7.5 Field emission scanning electron microscopy (SEM) of the surface of SL4 (LCMO -3 nm/STO - 3 nm)$_{30}$ superlattice, exhibiting the mosaic of interconnected chains of rectangular islands formed as a result of columnar growth. The diffraction pattern in the top right corner shows the cubic crystal structure of the epitaxially grown superlattice.

It is well known that the boundaries between the columnar domains, traversing the entire thickness of SL, disrupt the crystal structure and act as cumulative pinning centres for structural defects, such as edge dislocations [16, 17]. These boundaries, marked by arrows in Figure 7.4, are usually 2-4 nm thick. On the other hand, the epitaxial growth of the cubic crystal structure in the superlattice is confirmed by the diffraction pattern in the inset to Figure 7.5. The sharp electron diffraction spots show no satellites or broadening indicating that the multilayers have good single crystallinity. The similar electron diffraction patterns were found for different samples and in different points of a sample. This result together with TEM pictures allow us to use the term *superlattice* for multilayered superstructures discussed here.

Thus, such columnar superlattices exhibit alternating sections of LCMO and STO with the average dimensions of $50\times50\times3$ nm^3 each (or whatever the thickness of the layers is). This structure represents a 3D well-ordered mixed phase (or defined phase separation). Indeed, we consider presence of two clearly defined, transversally alternating phases of LCMO and STO, as well as one or two minor in-plane phases serving as the domain boundaries. Obviously, we obtain a unique, well-organised 3D structure of alternating in plane regions possessing high conductivity (crystalline LCMO) and low conductivity (STO and boundaries between columnar domains [21]). This structure can be well controlled by selecting layer thickness and/or using various PLD deposition parameters and conditions, allowing the obtaining of controllable structural properties of phase separation which governs the CMR effect.

7.4 Magnetic properties of STO/LCMO superlattices

The temperature dependence of magnetization [*M(T)*] for the zero-field cooled (ZFC) and field cooled (FC) samples of type SL4 with the in-plane field geometry is shown in Fig.7.6. The ferromagnetic Curie temperature for all measured samples has been estimated by finding the steepest slope from the temperature derivative of FC magnetization (*dM/dT*) [18, 19] shown in the Inset of Fig.7.6. It has been observed that for single layer LCMO films grown on LAO substrates, T_{Curie} is decreased with decreasing thickness of the layer (see Chapter 5).

The same trend was observed for STO/LCMO superlattices. For the superlattice of type SL1 (LCMO -3 nm/STO - 7 nm)$_{20}$ the Curie temperature was

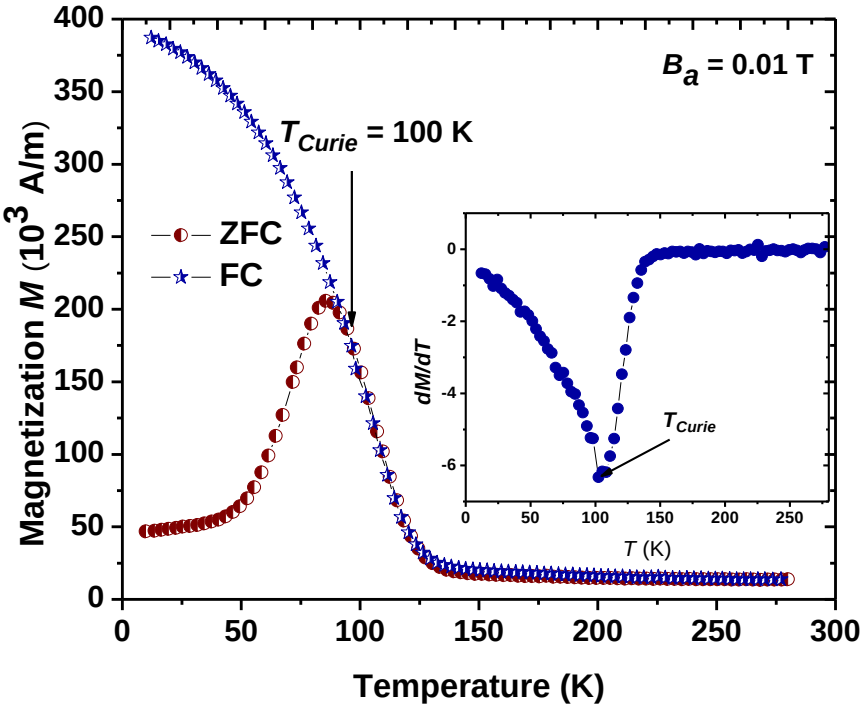

Figure 7.6 Magnetic properties of SL4 type STO/LCMO superlattice. Inset: *dM/dT* curve as a function of temperature for the Curie temperature determination.

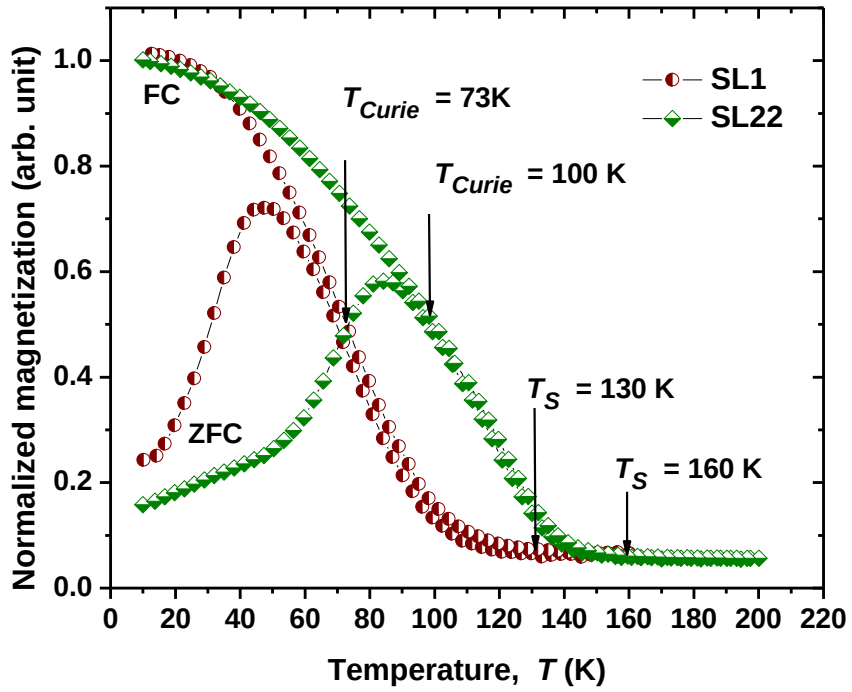

Figure 7.7 Temperature dependence of ZFC and FC magnetizations for SL1 (LCMO -3 nm/STO - 7 nm)$_{20}$ and SL22 (LCMO -3 nm/STO - 3 nm)$_{30}$ superlattices showing Curie temperatures T_{Curie} and saturation of magnetisation temperatures T_S.

found to be in the range of 75-105 K and for the type SL4 (LCMO -3 nm/STO - 3 nm)$_{30}$ – in the range of 95-110 K (see Table 7.1 and Fig. 7.7). This result is consistent with data presented in [12] which reported a similar trend for similar thickness reductions. More than 30 samples with different STO/LCMO composition and periods (mostly of type SL1 and SL4) were manufactured and investigated. Their magnetic properties are presented in Table 7.1.

Table 7.1 Magnetic properties of selected STO/LCMO superlattices.

Sample #	SL composition and period	T_{Curie} (K)	T_S (K)	Substrate type
SL1	$[LCMO_{3\ nm}/STO_{7\ nm}]_{20}$	≈ 73	130	YSZ
SL2	$[LCMO_{3\ nm}/STO_{7\ nm}]_{20}$	≈ 93	150	LAO
SL4	$[LCMO_{3\ nm}/STO_{3\ nm}]_{30}$	≈ 115	180	LAO
SL8	$[LCMO_{3\ nm}/STO_{7\ nm}]_{20}$	≈ 75	140	YSZ
SL5	$[LCMO_{3\ nm}/STO_{7\ nm}]_{20}$	≈ 95	130	LAO
SL6	$[LCMO_{3\ nm}/STO_{7\ nm}]_{20}$	≈ 58	120	YSZ
SL8	$[LCMO_{3\ nm}/STO_{7\ nm}]_{20}$	≈ 80	150	LAO
SL10	$[LCMO_{3\ nm}/STO_{7\ nm}]_{20}$	≈ 105	150	LAO
SL11	$[LCMO_{3\ nm}/STO_{7\ nm}]_{20}$	≈ 100	150	LAO
SL12	$[LCMO_{3\ nm}/STO_{7\ nm}]_{20}$	≈ 97	150	LAO
SL13	$[LCMO_{3\ nm}/STO_{6\ nm}]_{20}$	≈ 79	125	YSZ
SL18	$[LCMO_{3\ nm}/STO_{6\ nm}]_{20}$	≈ 63	120	LAO
SL19	$[LCMO_{3\ nm}/STO_{6\ nm}]_{20}$	≈ 95	150	LAO
SL20	$[LCMO_{3\ nm}/STO_{7\ nm}]_{30}$	≈ 85	140	LAO
SL21	$[LCMO_{3\ nm}/STO_{4\ nm}]_{30}$	≈ 88	130	LAO
SL22	$[LCMO_{3\ nm}/STO_{3\ nm}]_{30}$	≈ 100	160	STO
SL23	$[LCMO_{3\ nm}/STO_{6\ nm}]_{20}$	≈ 76	130	LAO
SL27	$[LCMO_{3\ nm}/STO_{3\ nm}]_{20}$	≈ 100	150	STO
SL35	$[LCMO_{3\ nm}/STO_{2nm}]_{40}$	≈ 120	170	LAO
SL41	$[LCMO_{3\ nm}/STO_{3\ nm}]_{30}$	≈ 95	160	LAO
SL42	$[LCMO_{3\ nm}/STO_{3\ nm}]_{30}$	≈ 96	160	LAO
SL43	$[LCMO_{3\ nm}/STO_{6\ nm}]_{25}$	≈ 88	150	LAO

The analysis of collected data shows superlattices common features as follow:

- saturation magnetization temperature T_S for superlatices of the same type grown on the same type of substrate is perfectly reproduced (see for example SL8-SL12 series);
- Curie temperature for superlattices of SL1 type is always less for about 10-15 K than Curie temperature of type SL4 independent of the used substrate, which may be explained by lower LCMO content in SL1 type superlattice;
- Curie temperature for superlattices grown on YSZ substrate is always less for about 20 K in comparison with superlattices grown on LAO substrate because the biggest lattice mismatch between YSZ and LCMO makes such structure more strained which also leads to the reduction of T_{Curie}.

So we may propose to effectively and dramatically control the T_{Curie} shift to lower temperatures by introducing a certain LCMO/STO superlattice structure grown on the same type of substrates. The SL2, which has the total LCMO thickness of ~ 60 nm shows $T_{Curie} \approx 93$ K (see Table 7.1). The SL4 superlattice with the total LCMO thickness of about 90 nm exhibits a correspondingly higher $T_{Curie} \approx 115$ K. Notably, as also follows from other measured samples, the thickness of STO sub-layers may significantly affect the T_{Curie} trend (see Fig.7.8). This change in properties of separated phases by the thickness of the STO sub-layer is likely to support the phase separation as the mechanism responsible for the reduction of T_{Curie} with increasing insulating domains [7]. We should note that some differences in the paramagnetic signals for our samples above T_{Curie} is most likely due to different amount LCMO material, its architecture, and its possibly varying paramagnetic properties dependent on oxygen content [19,20].

7.5 Transport properties of STO/LCMO superlattices

The transport measurements show significant differences between the temperature dependence of resistivity for single LCMO films and LCMO/STO superlattices. As it was discussed in Chaper 5 the single LCMO-50nm thick film shows a clear metal-to-insulator transition (MIT) at $T_p \approx 160$ K and metallic-like behaviour below T_p (see Fig. 5.11, which demonstrates the resistivity (ρ) as a

function of temperature at the applied magnetic field B_a = 0 T and 5 T). This graph also shows the temperature dependence of magnetoresistance (*MR*) which can reach the significant negative value (~ 60%) in the vicinity of MIT point. Both resistivity and *MR* behaviour of the LCMO films measured are typical for samples with similar thickness and composition as described in [9, 10].

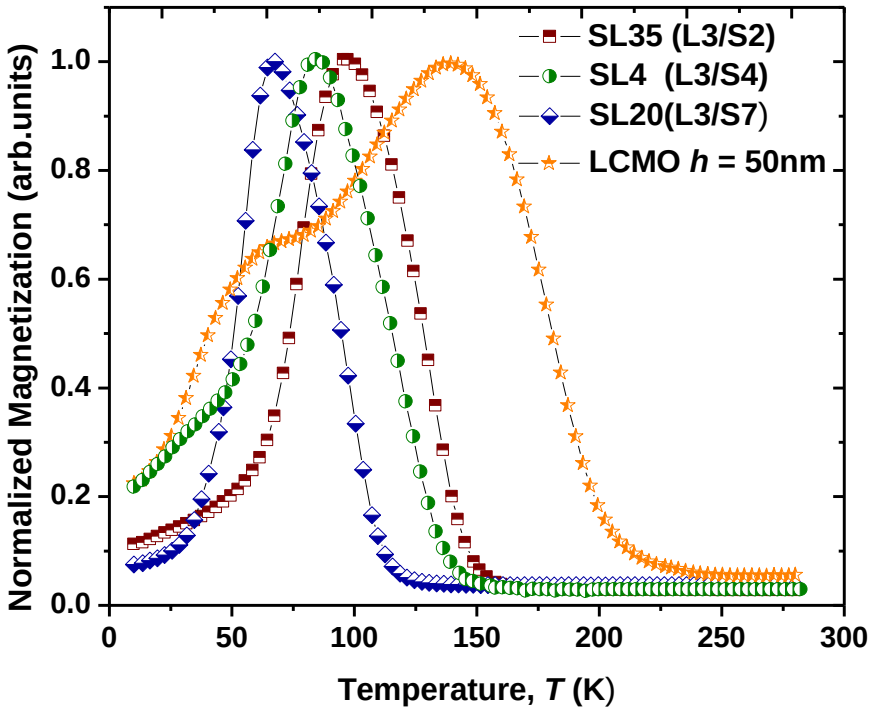

Figure 7.8 Temperature dependence of magnetization for three superlattices having the same LCMO sub-layer thickness (L = 3nm) and different STO sub-layer thickness (S = 2, 4, and 7 nm) compared with single 50 nm thick LCMO film showing the trend of T_{Curie} reduction with increasing of STO sub-layer thickness.

In the LCMO/STO superlattices of type SL1 (Figure 7.9), the *ρ(T)* behaviour of the high temperature paramagnetic part at $T > T_{p1}$, is rather similar to the LCMO single layer films with approximately the same thickness except of very low magneto resistance in STO/LCMO superlattice (less than 2%). However below T_{p1}, the transport characteristic of SL1 is different compared to the LCMO films of comparable thickness. It may be clearly seen the appearance of the second MIT point around $T_{p2} \approx 70$K.

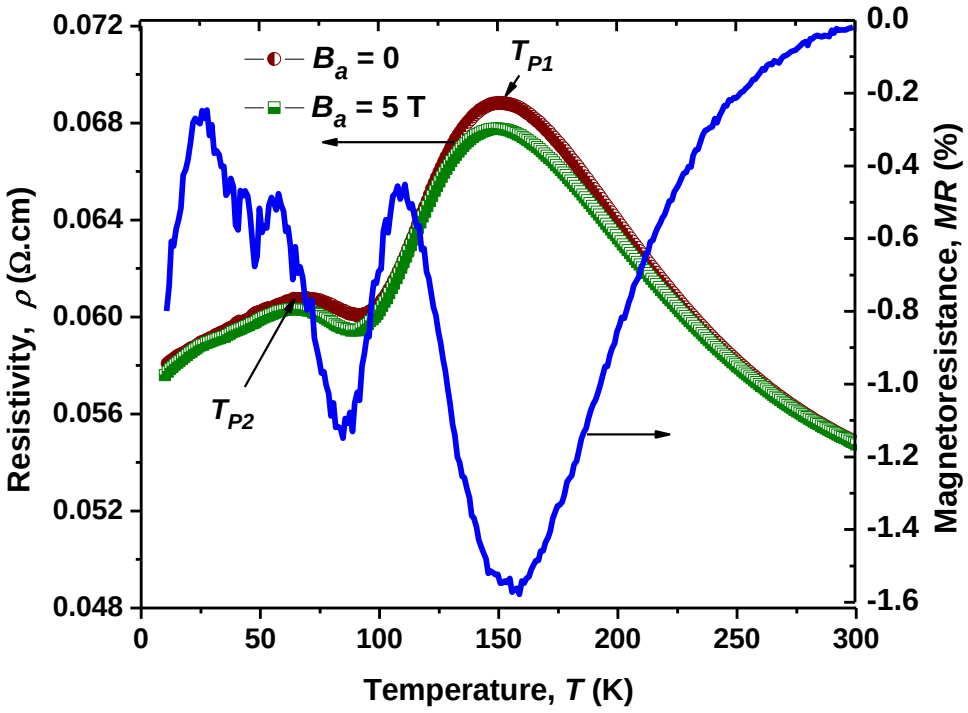

Figure 7.9 Temperature dependence of the resistivity for the SL1 type superlattice showing two MIT points (denoted by T_{P1} and T_{P2}) at about 150 K and 70 K correspondingly, for zero and 5 T applied magnetic fields (left panel). The magnetoresistance vs temperature for the same structure (blue curve) demonstrating the minimum at around T_{p1} (right panel).

The $\rho(T)$ curves for SL4 type superlattice below T_p shows much more difference in comparison with single LCMO film (see Fig.7.10a). The corresponding magnetoresistance curve is shown in Figure 7.10b for this superlattice. Above MIT temperature, the *MR(T)* demonstrates the behaviour similar to single layer LCMO films with negative *MR* values as high as ~90% (see Inset in Fig.7.10b). Whereas below T_P, the magnetoresistance of the superlattice shows two sharp positive peaks with the highest value of more than 1800% at $T \approx 75$ K, which corresponds to the lowest resistivity point for the zero-field resistance dependence on temperature.

Note that $\rho(T)$ curves are highly reproducible for every sample and do not have any dependence on cycles of cooling and heating. However, the behaviour of spikes depends on the layer architecture and deposition parameters (including substrate selection). For example, for thicker STO interlayers (SL1 type) and fewer number of layers in the SL with very straight interfaces even at the domain boundaries, no spikes have been observed (see Figure 7.9); a slight variation of the STO sub-layer thickness ($h_{STO} < 3$ nm) the spikes position can be adjusted;

importantly, the identical deposition conditions and layer architecture for different samples lead to identical behaviour (verified during the refereeing process).

The discussion of exact parameters allowing us to control the resistance drop behaviour is outside the scope of this work and will be detailed elsewhere. In this work, we report this new phenomenon and its most pronounced behaviour obtained for SL4 type superlattices, as well as focus on its possible explanation. The explanation of such unusual behaviour can be proposed within the framework of phase separation model, arising as a result of the well-ordered 3D alternating structure of ferromagnetic (FM) and insulating domains in our hybrid multilayered system (explained above).

7.6 Model of LCMO/STO superlattice as the 3D RC-network

According to the models of phase separation [5, 6] the concentration of carriers in various clusters (or system domains) affects the local and global magnetic properties due to effective spin exchange through various mechanisms including double exchange, carriers (electron) hoping, crystal lattice distortions, etc. [23].

In the paramagnetic state above the MIT temperature, spin-charge-ordered insulating phases create potential barriers between clusters (or domains) of ferromagnetic phase. The mutual phase charging due to raising concentration of carriers leads to increasing Coulomb fields. This increase would expand conducting regions eventually leading to setting up presumably percolative conduction between them below the MIT at T_p. This does not destroy the phase separation, but changes its topology [6], most likely also within the LCMO domains.

Furthermore, below the MIT (Figure 7.10a), two negative spikes in the resistivity curves have been observed in the superlattices for zero magnetic field and B_a = 5 T. The lower temperature spike (at 27 K) is usually broader than the high temperature spike (at 75 K). In addition, the spikes measured in the applied fields are shifted relative to their zero-fields temperatures, so that the low temperature spikes is observed at even lower temperatures, while the high temperature spike is shifted tohigher temperatures. It is also important to notice that the “background” resistivity

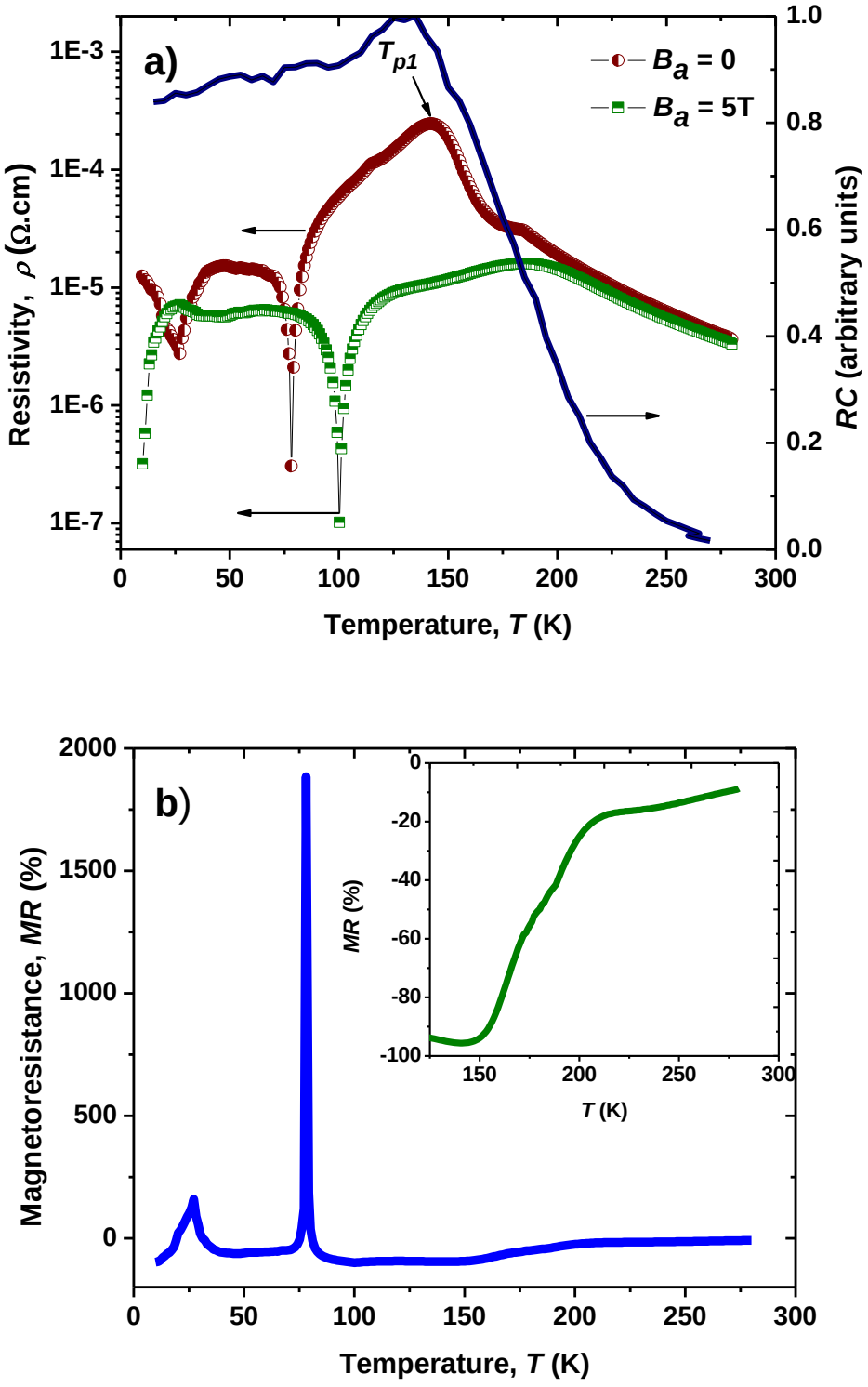

Figure 7.10 (a) Temperature dependence of resistivity of the SL4 superlattice measured at B_a = 0 T and 5 T. The solid line exhibits the temperature dependence of *RC* product (right axis) for LCMO/STO interface with *C(T)* is taken from Ref.26 and *R(T)* from Figure 5.11. (b) Magnetoresistance as a function of temperature shows two maxima at $T \approx 27$ and 75 K. Inset: The part of *MR(T)* curve with negative magnetoresistance and the curve shape similar to single layered LCMO films.

does not drop substantially, remaining at the same level and likely indicating a similar mechanism of conductivity outside of the spike ranges. We presume that a certain degree of “tunnelling" through structural barriers with high resistances between LCMO domains shown in Figure 7.3 is involved with marginal variations outside the spikes. Within the spike temperature range, the Coulomb potentials experience a progressive breakdown as the temperature of the sample is changed. The properties of multiple potential barriers created by the superlattices are expected to be temperature and magnetic field dependent, which plays an important role in the progressive breakdown. This would mean that instead of tunnelling, the neighbouring ferromagnetic regions become electrically connected and hence progressively lower resistivity is measured. As the Coulomb potentials discharge throughout the entire sample, the insulating barriers are again progressively reinstated, leading to reinstating resistivity and eventually to the “background” tunnelling-driven percolative conductivity level. Both negative spikes may have very similar scenario. However, the high temperature spike at 75 K may have additional contribution of the out-of-plane tunnelling barrier breakdown because of conducting filaments formation (through the STO layers) [24]. Thus, these two negative spikes may reflect characteristic behaviour of the well-ordered domain structure (well-ordered PS) for in-plane (2D-like) and out-of-plane (3D-like) conductivity.

To illustrate the scenario described above, we propose the dimensional RC-network model as follows. Taking into account that in our superlattice the LCMO semiconductor layers are separated by the insulating STO layers, a certain capacitance is created across each insulating layer. Thus, we can analyse a *RC*-network in our superlattice with nonlinear, temperature dependent resistors being represented by LCMO layers (Figure 7.11). The capacitors characteristics would depend on dielectric properties of STO layers, which in turn can also vary as function of temperature and electric field strength. In Figure 7.10a, we reproduce the *RC* curve (solid line) obtained for a hybrid temperature dependence of a LCMO/STO interface capacitance (from Ref.26) and a resistance of LCMO single film (from Figure 5.11). Indeed, the curve indicates substantial influence of the capacitance on the behaviour observed in the superlattice. This approach should be reasonable for the STO interlayer thicknesses used in our SL, because it was shown that even 0.8 nm thick STO layers can display good insulating properties [25]. However, the

application of threshold voltages is likely to lead to the formation and rupture of filamentary conducting paths inside insulating sub-layers [24] (lightning bolt-like thin lines in STO layers in Figure 7.11), which respectively results in short-circuiting and re-opening the capacitors.

In the situation when all the in-plane capacitors (across the LCMO domain boundaries) are short-circuited presumably at the low-temperature negative spike, the *RC*-network behaves as a set of 2D capacitively coupled resistors with the resistance *R* being determined by the in-plane LCMO resistance. The equivalent diagram of the *RC*-network model is simplified in this case to the one shown in Figure 7.12.

At low temperatures (well below the low-temperature spike), the capacitance of the STO insulating layers is the highest [26], hence the total resistance is likely defined by the 2D *RC*-network of only one upper LCMO layer (an ideal case) that is *R1* ~ 1 kOhm (measured at 10 K). As temperature rises, the relatively small capacitances across the LCMO domain boundaries breakdown expanding electrically connected ferromagnetic clusters and decreasing the total 2D-like in-plane LCMO resistance. At the minimum of the low-temperature spike at $T_{m1} \approx 27$ K (for zero field), the superlattice possesses the minimum resistance of $R_{1min} \approx 80$ Ohm at $I = 100$ μA applied only to the upper manganite layer.

At the minimum, the electric field strength between the voltage terminals has its minimal value $E \approx 0.2$ V/m, which is too small for the connectivity filament formation and the inverse process of filament rupture is triggered. Note that the local electric field strength between the LCMO domains across domain boundaries can be as high as hundreds of kV/m, if we consider the width of the boundaries which is of the order of a few nanometres [15–17]. It is sufficient to facilitate the capacitive domain boundary rapture.

Upon further rising temperature, we are expecting three processes to occur. (i) The capacitance of STO interlayers keeps degrading, which lowers the Schottky like barrier and enables the formation of conducting filaments through STO layers [26, 27]; (ii) a similar degradation process would be valid for the capacitance of the domain boundaries (reducing local electric field strengths); (iii) whereas the resistance of the LCMO film within the domains keeps rising due to MIT (Figure 5.11), which redistributes *E* more evenly over the LCMO layers reducing the chance

of the rupturing. This three-fold process can result in the behaviour observed experimentally as follows.

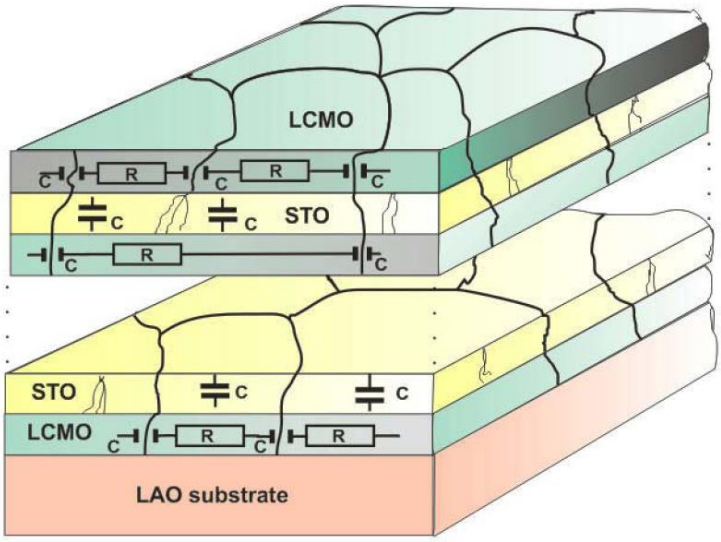

Figure 7.11 Model of LCMO/STO superlattice as the 3D *RC*-network, where the formation of the filamentary conducting paths in the STO interlayers are shown as thin lightning bolt-like lines.

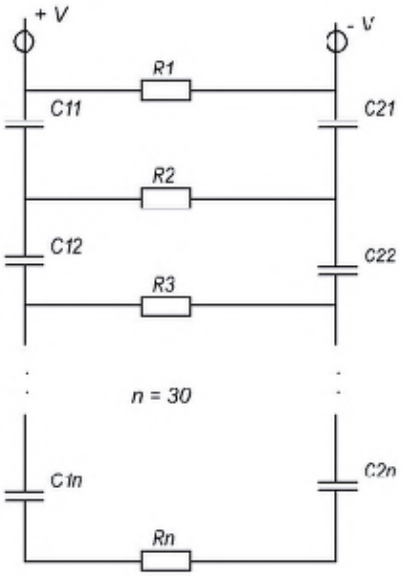

Figure 7.12 The simplified equivalent diagram of a superlattice with the assumption that all the 2D-like in plane resistance is within the LCMO layers with the in plane capacitors across the LCMO domains being short-circuited, while the out of plane capacitors (across STO layers) effectively decouple the LCMO layers at and below the low-temperature negative spike where the capacitance would still be large to form conductive filament [24] (or breakdown) across the STO sub-layers.

The resistivity is rather constant between the two negative spikes, being the result of counteraction of rising resistivity within the LCMO domains, on one hand, and lowering capacitance of the domain boundaries, hence gradually enhancing the tunnelling, on the other hand.

At a certain point the capacitance across STO layer drops below a threshold level (the onset of 3D-like behaviour), so that it becomes favourable for carriers to tunnel through (or to rupture) the STO layers. As a result, a similar process to the 2D process described above for a single LCMO layer is initiated, but now it is likely to engage not only one LCMO layers but all LCMO layers for 2D in-plane conductance as well as tunnelling or rupture of STO layers enabling the 3D-like participation of all LCMO layers. Again, a rough estimation of electric field across one ~ 3-6 nm thick STO sub-layers reaches E ~ 2-4 MV/m, which corresponds to the field strength necessary to rupture STO layer of up to 1 μm thick [27]. According to our model, at the minimum of the spike at T_{m2} = 78 K, all capacitors across STO interlayers in Figure 7.12 have to be replaced by conducting filaments. This allows us to verify our model by a simple check of the total resistance expected at the minimum. It can be found by dividing the resistance of the single LCMO layer *R1* ≈ 80 Ohm measured at T_{m1} by the number of the deposited LCMO layers in the SL4 (n = 30). Hence, the total network resistance expected at the minima of the spike is ~ 3 Ohm. This value can be considered to agree well with the measured value of ≈ 15 Ohm, in particular if we recall that the resistance within LCMO domains rises with the temperature, while our estimation is based on the *R1* value obtained at T_{m1} =27 K. Furthermore, the disagreement may also be due to structural imperfections and short-circuiting between layers, which could also mean that *R1* was measured as a parallel resistance of two (or even a few) LCMO layers, whereas we initially considered an ideal case. Additionally, the resistance of the LCMO layers near the substrate may be quite different to the upper layers due to the larger amount of defects in initial layers near the substrate as can be seen in TEM image (Figure 7.4).

At temperatures higher than T_{m2}, the reverse process commences due to the low averaged E value, in a similar fashion described above for the low-temperature spike. Eventually, the total superlattice resistance rises with temperature up to the MIT point.

Yet another confirmation of the dimensional mechanism proposed comes from the field dependence of the spike behaviour. The first 2D low temperature spike is proposed to be governed by in-plane FM domains. By applying an in-plane magnetic field, it forces the domains to align along the field, so that some neighbouring domains are likely to merge decreasing their number and increasing their size. This would lead to (i) a more rapid rupturing (and inverse) process (fewer domains), (ii) which is likely to happen at lower temperature, and (iii) resulting in a lower resistance at the minimum (fewer domain boundaries to rupture). Indeed, we observe these three features in our experiments (Figure 7.10a).

Furthermore, the second 3D high-temperature spike, on the contrary, shifts to a higher temperature at the applied field, which may confirm its different dimensionality as follows. Indeed, the dielectric properties of materials can be changed in materials in general and systems alike the STO structure in particular [28, 29]. In our case, during PLD process STO interlayers in the superlattice, may become doped (contaminated) with Mn or LCMO due to remnant plasma after switching targets from LCMO to STO, or/and the secondary ablation of LCMO upon STO deposition, or/and interdiffusion between layers at the deposition temperature of 780^{o}C. STO doped with Mn and LCMO itself have been both shown to exhibit magnetodielectric effects [30]. This means that the dielectric constant of the STO interlayers would increase in the magnetic field applied, leading to the rupture process occurring at higher temperatures, as indeed was observed in our experiment at B_a = 5 T. Similarly to the first spike, because of the in plane larger FM clusters, the rupture process would be more rapid exhibiting lower resistance. These peculiarities are observed in our measurements (Figure 7.10a).

It is important to note that the resistivity of single layer LCMO films in Figure 5.11 is higher than in the SL by two orders of magnitude, which is consistently observed for these type of SL. Intuitively, the resistance trend should have been reversed simply because the thicker conducting LCMO film had lower resistance than in the 2D LCMO layers of the SL separated by insulating STO. Indeed, although the total thickness of LCMO in the SL was kept equal to the corresponding single layer LCMO films, the current was applied to the upper layers only. The explanation of this seemingly unexpected effect is in fact in line within the RC model we propose as follows. The current applied, which would flow through the

entire 3D LCMO single layer film, flows through one (or a few) upper 2D layers in the SL, implying higher *E* in each of them across all possible barriers, such as domain boundaries, phase separation within domains, *etc*. Higher *E* suggests easier mutual phase charging followed by the corresponding easier discharging and formation of additional conducting filaments between phases, domains, *etc*. This obviously leads to lower resistivity in the SL than in the LCMO films with tunnelling-driven conductivity across all possible barriers. In general, this process is likely to be responsible for the presence (controllability) of the sharp resistivity drops. However, we should mention that the difference in resistivity can also be influenced by (i) the oxygen content in LCMO [18, 19], which (ii) may not be reproduced by PLD without the due attention, which (iii) may be affected by the proximity of the interlayers and interfaces (also reducing surface conductivity noticed upon SEM studies), and (iv) by the loss of oxygen during gold contact deposition, which (v) may be different for the films and SL.

The recent theoretical study has demonstrated [23] that in the vicinity of region of competition between the ferromagnetic metallic and spin-charge-ordered insulating phases, the CMR phenomenon may be observed with MR of up to 10000% with the resistivity behaviour becoming metallic via an abrupt discontinuity. We indeed observe large MR in excess of ~ 1800% in the form of discontinuities, likely representing the dimensional or a first-order transition. It is the sharpest, strongest and, importantly, controlled MR behaviour reported in LCMO films and superlattices [31].

7.7 Conclusion

In summary, we have manufactured LCMO/STO superlattices by PLD and investigated their properties by means of magnetic and transport measurements. We have managed to establish an acceptable technology for combination of LCMO films exhibiting the CMR effect with HTS REBCO films for novel hybrid functionalities and devices, so that the relevant magnetic properties of LCMO at $T < T_c$ would be exhibited below the superconducting transition temperature. This can be achieved by reducing thickness of LCMO single layer films, but more *effectively and controllably* by introducing LCMO/STO superlattices with the period of $n > 20$ and 3-7 nm thick

layers. We have obtained $T_{Curie} \approx 75$ K which is even below liquid nitrogen temperature (and $T_c = 91$ K of HTS REBCO films), enabling an easier cooling approach for potential applications. A shift of the metal-insulator transition to lower temperatures in $\rho(T)$ curves has been also observed for the films and superlattices. Importantly, the $\rho(T)$ curves of the superlattices below the MIT have remarkable sharp features exhibiting about two order of magnitude drops of resistivity, which result in the positive peak of magnetoresistance in excess of 1800% at 75 K. We have explained this behaviour in the framework of the phase separation theory for manganites for the well-organised 3D structures, which experience dimensional transitions of their spin-charge transport properties. The significant result is that because the structure of the superlattices can be easily controlled, it can enable the prescribed tuning of the magnetoresistance properties required for applications. Moreover, the dimensionality dependent behaviour observed and its magnetic field dependence indicate the presence of magnetodielectric properties in STO layers. The variety of the new technological and fundamental results obtained in this work is applicable to a broad range of adjoining scientific areas.

References

[1] Helmholt, R. von.;Wecker, J.; Holzapfel, B.; Schultz,L.; Samwer, K. Giant. *Phys. Rev. Lett.* **71**, 2331, (1993)

[2] Jin, S.; Tiefel, T. H.; McCormack, M.; Fastnacht, R. A.; Ramesh R.; Chen, L. H. *Science* **264**, 413, (1994)

[3] Hoppler, J.; Stahn, J.; Niedermayer, Ch.; Malik, V. K.; Bouyanfif, H.; Drew, A. J.; Rossle, M.; Buzdin, A.; Cristiani, G.; Habermeier, H. U. et al. *Nat Mater.* **8**, 315, (2009)

[4] Fedoseev, S. A.; Pan, A. V.; Shcherbakova, O. V.; Dou, S.X. *Physica C,* **479**, 143-146, (2012)

[5] Dörr, K.; De Teresa, J. M.; Müller, K-H.; Eckert, D.; Walter, T.; Vlakhov, E.; Nenkov K.; Schultz, L. J. *Phys.: Condens. Matter.* **12**, 7099-7109, (2000)

[6] Nagaev, E. L. *Physics of the Solid State.* **40**, 1873-1877, (1998)

[7] Chen, S. F.; Lin, P. I.; Juang, J. Y.; Uen, T. M.; Wu, K. H.; Gou, Y. S.; Lin, J. Y. *Appl. Phys. Lett.* **82**, N8, (2003)

[8] Tao, J.; Niebieskikwiat, D.; Varela, M.; Luo, W.; Schofield, M.; Zhu, Y.; Salamon, M. B.; Zuo, J. M.; Pantelides, S. T.; Pennycook, S. J. *Phys. Rev. Lett*. **103**, 097202, (2009)

[9] Markovich, V.; Jung, G.; Yuzhelevskii, Y.; Gorodetsky, G.; Gao, J. *Phys. Rev. B* **75**, 104419, (2007)

[10] Zhai, H.; Ma, J. X.; Gillaspie, D. T.; Zhang, X. G.; Ward, T. Z.; Plummer, E. W.; Shen, *J. Phys. Rev. Lett*. **97**, 167201, (2006)

[11] Deen, P. P.; Yokaichiya, F.; de Santis, A.; Bobba, F.; Wildes, A. R.; Cucolo, A. M. *Phys. Rev. B* **74**, 224414, (2006)

[12] Dvorak, J.; Idzerda, Y. U.; Ogale, S. B.; Shinde, S.; Wu, T.; Venkatesan, T.; Godfrey, R.; Ramesh, R. *J. Appl. Phys.* **97**, 10, (2005)

[13] Kwon, C.; Kim, K. C.; Robson, M.C.; Gu, J. Y.; Rajeshwari, M.; Venkatesan, T.; Ramesh, R. *J. Appl Phys.* **81**, 4950-4952, (1997)

[14] Jo, M.; Mathur, N. D.; Evetts, J. E.; Blamire, M. G. *Res. Soc. Symp. Proc.* **602**, 3, (1999)

[15] Pan, A. V.; Pysarenko, S. V.; Wexler, D.; Rubanov, S.; Dou, S. X . *IEEE Trans. Appl. Supercond.* **17**, 3585, (2007)

[16] Pan, V. M.; Pan, A. V. *Fiz. Niz. Temp.* (Rus.) 2001, 27, 991. [*Low Temp. Phys*. **27**, 732, (2001)].

[17] Pan, V. M.; Cherpak, Y.; Komashko, V.; Pozigun, S.; Tretiatchenko, C.; Semenov, A.; Pashitskii, E.; Pan, A. V. *Phys. Rev. B* **73**, 054508, (2006)

[18] Ziese, M.; Semmelhack, H. C.; Han, K. H. *Phys. Rev. B* **68**, 134444, (2003)

[19] Guo, H. Z.; Gupta, A. J.; Zhang, Jiandi; Varela, M.; Pennycook, S. J. *Appl. Phys. Lett.*
91, 202509, (2007)

[20] Lee, Y. P.; Park, S. Y.; Park, J. S.; Prokhorov, V. G.; Komashko, V. A.; Svetchnikov, V. L.; Kang, J.-H. *J.Appl .Phys.* **101,** 053708, (2007)

[21] Shang, D. S.; Chen, L. D.; Wang, Q.; Yu, W. D.; Li, X. M.; Sun, J. R.; Shen, B. G. *J. Appl. Phys.* **105**, 063511, (2009)

[22] Nigam, R.; Pan, A. V.; Dou, S. X. *Phys. Rev. B.* **77**, 134509, (2008)

[23] Sen, C.; Alvarez, G.; Dagotto, E. *Phys. Rev. Lett.* **105**, 097203, (2010)

[24] Sawa, A. *Materials Today* **11**, Issue 6, (2008)

[25] Infante, I. C.; Sanchez, F.; Fontcuberta, J.; Fusil, S.; Bouzehouane, K.; Herranz, G.;
Barthelemy, A.; Estrade, S.; Arbiol, J.; Peiro, F. et al. *J.Appl. Phys.* **101**, 093902, (2007)
[26] Boikov Yu. A.; Danilov, V. A Zh. Tekh. Fiz. 2005, 31, 73 [*Tech. Phys. Lett*. **31**, 36, (2005)].
[27] Boikov Yu. A.; Danilov, V. A. *Physics of the Solid State* **52**, No. 7, 1439-1443, (2010)
[28] Kolodiazhnyi, T.; Fujita, K.; Wang, L.; Zong, Y.; Tanaka, K.; Sakka, Y.; Takayama-
Muromachi, E. *Appl. Phys. Lett.* **96**, 252901, (2010)
[29] Choudhury, D.; Mukherjee, S.; Mandal, P.; Sundaresan, A.; Waghmare, U. V.; Bhattacharjee, S.; Mathieu, R.; Lazor, P.; Eriksson, O.; Sanyal, B. et al. *Phys. Rev. B* **84**, 125124, (2011)
[30] Rivas, J.; Mira, J.; Rivas-Murias. B.; Fondado, A.; Dec, J.; Kleemann, W.; Señarís-Rodríguez, M. A. *Appl. Phys. Lett.* **88**, 242906, (2006)
[31] Fei, L.; Zhu, L.; Cheng, X.; Wang, H.; Baber, S. M.; Hill, J.; Lin, Q.; Xu, Y.; Deng, S., Luo, H. *Appl. Phys. Lett.* **100**, 082403, (2012)
[32] Pan, A. V.; Pysarenko, S.; Dou, S. X. *Appl. Phys.Lett.* **88**, 232506, (2006)

Chapter 8
Magnetic and transport properties of cuprate/manganite superlattices with insulating interlayer

8.1 Introduction to cuprate/manganite superlattices

Artificial superlattice (SL) structures offer a possibility of combining antagonistic order parameters such as superconductivity (SC) and ferromagnetism (FM). The motivation to study the interrelation of superconductivity and ferromagnetism in oxide systems arises from the fundamental interest of the common aspects and potential differences of the physical properties of artificially layered FM/SC systems [1]. In the last years, artificially grown superlattices consisting of high-T_c superconductors and manganese oxides have attracted increasing interests for various reasons. On one hand, SL's were developed as an important tool to explore the interplay between the two antagonistic SC and FM ground states [2], and on the other hand it is a very popular approach to obtain novel materials with modified or even with entirely new physical properties [3]. These properties can be readily tuned with external parameters like strain, electric or magnetic fields. Additionally, introducing insulating spacers in between the SC and FM layers opens possibilities for the investigation of interface and tunneling phenomena [1]. The most commonly investigated systems are heterostructures where the cuprate high temperature superconductor $YBa_2Cu_3O_7$ (YBCO) is combined with the ferromagnetic manganites $La_{2/3}Ca_{1/3}MnO_3$ (LCMO) or $La_{2/3}Sr_{1/3}MnO_3$ (LSMO) [4-10]. The high degree of spin polarization of the LCMO conduction band additionally makes this system a good candidate for the search of novel spin dependent effects, which could lead to the creation of a spintronic devices based on magnetoresistance (MR) effects associated with the accumulation and transport of spin polarized electrons. In an interface with high transparency (high conductance) the superconducting pair correlations can penetrate into a ferromagnetic metal and give rise to a proximity effect. The proximity effect extends to a distance determined by the exchange field energy ξ_F =

$(hD/k_BT_C)^{1/2}$ [10]. Here T_C is the Curie temperature of the ferromagnetic system. The study of the superconducting properties of series of heterostructures with varying thicknesses of either the LCMO or YBCO layers, proximity effects were detected evidenced by a depression of the superconductivity [1-6]. It was also shown in [5, 6] that the reduction of superconducting transition temperature for SL's with decreasing YBCO layer thickness is due to the electronic reconstruction at the YBCO/LCMO interface. When insulating layers intervene between the oxides superconducting layers (low transparency interface) the proximity effect should be suppressed [10].

This chapter deals with SL's with oxide ferromagnets such as LCMO and the oxide superconductor YBCO both having a highly anisotropic Fermi surface and the SC part is regarded as anisotropic *d*-wave. The advantages of the combination cuprate/manganite SL's is seen in their all oxide nature, crystal structure compatibility and partially adjustable lattice parameters of manganite part. It is known that the YBCO/LCMO superlattice composition influences its superconducting properties very much [1-4]. The superconductivity even disappears when the LCMO sub-layer thickness becomes much larger than YBCO one. In this Chapter we will discuss the superlattices where the superconductivity was not completely suppressed because of manganite sub-layer thickness was less or equal to the thickness of a cuprate sub-layer. The crystal structure (including HRTEM measurements) of cuprate/manganite superlattices manufactured by PLD was well investigated earlier [1, 3, 10]. Here we will focus on magnetic and transport properties of such SL's, where LCMO and YBCO sub-layers are separated by very thin insulating spacer ($SrTiO_3$, $PrBa_2Cu_3O_7$, or CeO_2) as it is seen from Figure 8.1. The introduction of an insulating spacer layer in between of YBCO and LCMO may at least reduce the interaction between them and thus, the intrinsic behaviour of individual layers can be restored.

8.2 Experimental details

The automated PLD system described in Chapter 3 was used for the fabrication of investigated SL's with deposition conditions already applied for YBCO/LCMO hybrid structure manufacturing (see Chapter 5). All superlattices were grown on LAO 5×5 mm^2 (100) substrates with STO buffer layer ($h_{STO} \approx 30$ nm). The growth of the superlattices was usually started with the YBCO layer and finished

with a LCMO layer (except the special samples described separately). Three different types of superlattices were manufactured: $(YBCO/STO/LCMO)_n$, $(YBCO/PBCO/LCMO)_n$, and $YBCO/CeO_2/LCMO)_n$ denoted as YSL, YPL, and YCL. YBCO sub-layer thickness was fixed to be 20 nm. This choice is dictated by optimization of PLD process for high reproducibility and good superconducting properties of YBCO films. One more reason to choose such thickness is that it must be sufficiently large that the critical temperature is unaffected by dimensionality or epitaxial strain effects. The number of periods for all superlattices was chosen to be n = 20 in order to have the configuration different from multilayered hybrid structures described in Chapter 6. For transport measurements the samples where patterned using standard optical photolithography with Ion Beam Milling in order to form few micro-bridges each having width of 25 nm. Au/Pd or Au/Pt contact pads were deposited by laser ablation in high vacuum and at room temperature to prevent the de-oxygenation of samples.

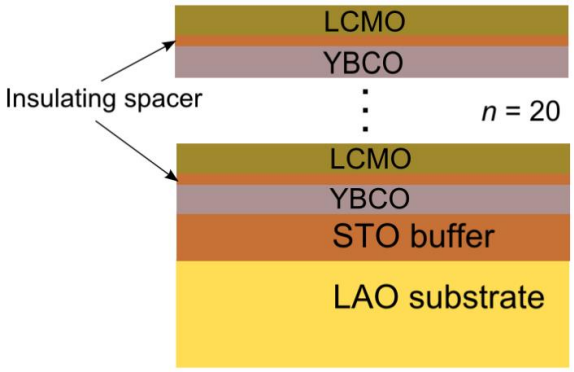

Figure 8.1 Configuration of superlattice type $(YBCO/Insulator/LCMO)_n$.

8.3 YBCO/STO/LCMO superlattices

8.3.1 Superlattices of type YBCO/STO/LCM – $[20nm/d_i\ nm/10nm]_{20}$

This series of non-symmetrical superlattices YBCO/STO/LCMO – $[20nm/d_i$ $nm/10nm]_{20}$ includes four samples with STO interlayer insulator thickness of 0, 1, 1.5 and 3 nm. For all samples the measurements of magnetization (both in plane and out of plane) as well as the transport measurements were performed. From magnetic

measurements the critical temperature of superconducting transition T_c (at zero field cooling conditions), the transition width ΔT_c and the critical current density J_c were found using methods described in Chapter 2. The superconducting properties of all samples from Set 1 are presented in Table 8.1.

Figure 8.2 shows results of magnetization measurements for the first sample of this series YSL1. Having zero STO spacer between YBCO and LCMO it may be used as reference for all other samples in this series. Its *M(T)* curve demonstrates the behavior similar to YBCO film with reduced T_c and the enlarged transition width that is usual for cuprate/manganite superlattices of such configuration [1-3]. This reduction of T_c is due to the presence of ferromagnetic LCMO layers, which reduce the layer coupling of YBCO sub-layers in this SL. However we did not detected any significant trace of the metal/insulator transition above T_c (see Inset in Fig.8.2). This experimental result can be explained by too small LCMO sub-layer thickness ($h_{\mathrm{LCMO}} \approx 10$ nm) which does not allow the displaying of ferromagnetic properties of manganite in this structure.

Figure 8.3 shows a zero-field cooling ZFC magnetic moment versus temperature for all SL's from given series. The superconducting critical temperature T_c of superlattices YBCO/STO/LCMO –[20nm/d_i nm/10nm]$_{20}$ with d_i = 0, 1.0, 1.5, and 3.0 nm STO spacer thickness is found to be dramatically increased with increasing of STO interlayer thickness (see the Inset in Fig.6.2). The introduction of very thin STO interlayer (d_i > 1 nm) will increase the T_c for about 8 K.

Table 8.1 Superconducting properties of superlattices from [20nm/d_i nm/10nm]$_{20}$ series: thickness of STO interlayer d_i, critical temperature T_c from magnetization measurements at zero field cooling, superconducting transition width ΔT_c, onset of superconducting transition from transport measurements T_{c_on}, transition width $T_{c\_off} - T_{c\_on}$ from transport measurements, and critical current density J_c.

Sample	**STO thickness d_i (nm)**	**T_c (K)**	**ΔT_c (K)**	**T_{c_on} (K)**	**$T_{c\_off} - T_{c\_on}$ (K)**	**J_c (10K) A/m^2**
YL1	**0**	**72**	**9.5**	**75**	**15**	**3.5×10^{10}**
YSL2	**~ 1**	**72.4**	**8.6**	**75**	**15**	**2.5×10^{10}**
YSL3	**1.5**	**79.6**	**8.4**	**76**	**14**	**6.9×10^{10}**
YSL4	**3**	**83**	**10.3**	**86**	**4**	**5.1×10^{10}**
YBCO	**-**	**88**	**2**	**89**	**2**	**8.2×10^{11}**

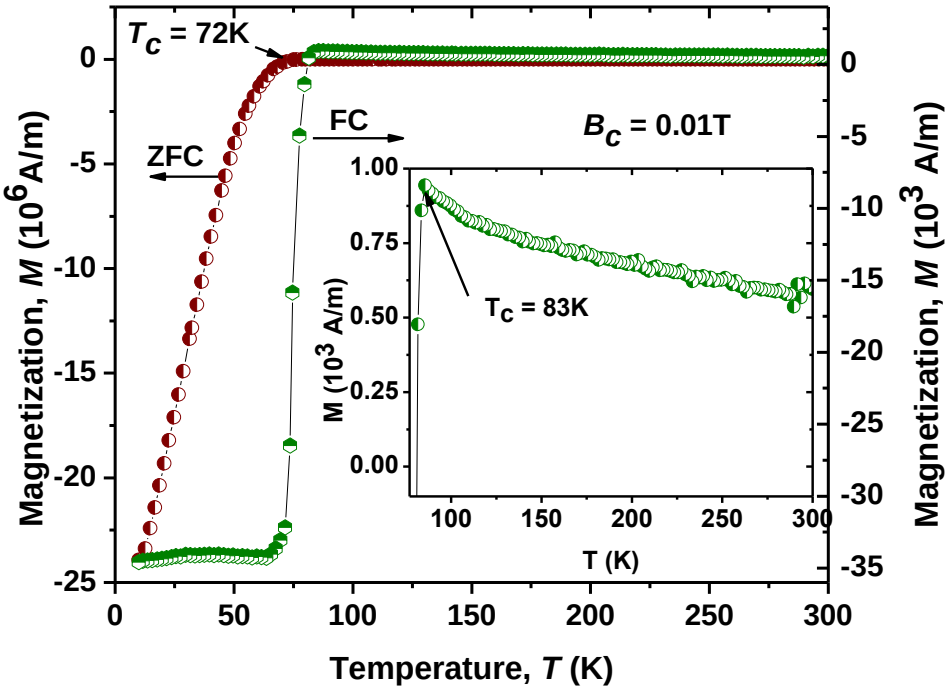

Figure 8.2 Zero field cooling (left panel) and field cooling (right panel) magnetization of YL1 sample (without STO interlayer) under out of plane applied field B_a = 0.01 T showing superconducting transition temperature $T_c \approx$ 72K (at ZFC). No traces of metal/insulator transition around T_{Curie} of LCMO are detected.

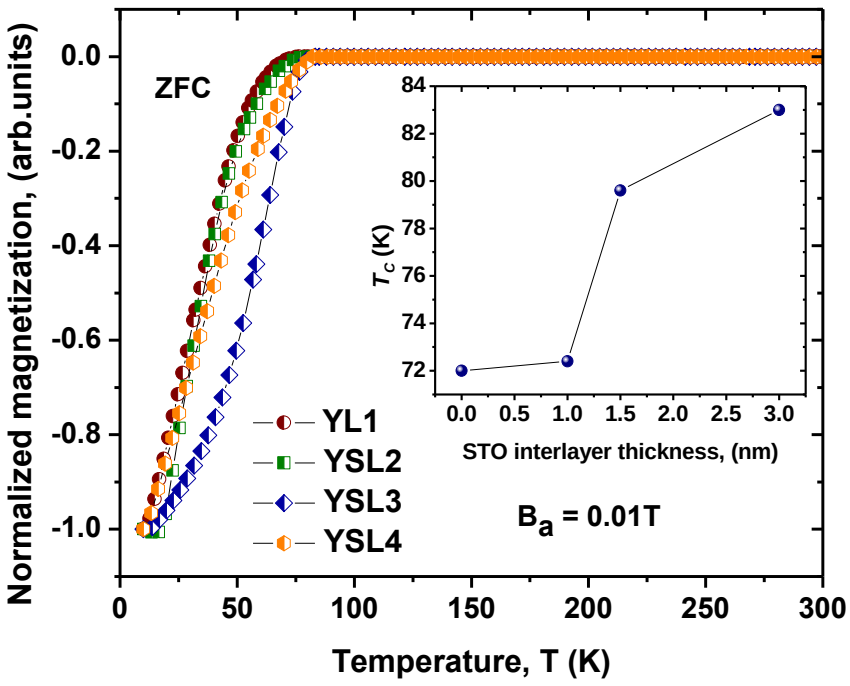

Figure 8.3 Normalized magnetization vs temperature for [20nm/d_i nm/10nm]$_{20}$ series of SL's (out of plane field configuration) at ZFC conditions. Inset: Critical current T_c vs STO spacer thickness for all samples from this series showing drastic improvement in T_c with STO thickness d_i > 1.0 nm.

Having $d_i \approx 3$ nm the superconducting critical temperature of YSL4 becomes comparable to the T_c of a single layered YBCO film deposited on LAO substrate under similar PLD conditions. Such improvement in T_c has the similar effect when the ferromagnetic layers become thinner or the YBCO layers get thicker [9]. However, the transition width ΔT_c for all SL's in the Set 1 has a weak trend of improvement and it is much larger in comparison with single layered YBCO film (see Table 8.1).

The critical current density $J_c(B)$ curves of SL's demonstrate the shape similar to YBCO film but with much lower critical current density value (see Table 8.1). The sample YL1 shows the worst J_c (in comparison with single layered YBCO film). When the STO interlayer thickness increases the critical current density increases too but it still has much lower values compared to YBCO film.

The electric transport properties of a series of samples from this series of SL's confirm the trend of T_c improvement when increasing the STO interlayer thickness that was derived from magnetic measurements. The corresponding temperature dependent resistance curves are shown in Figure 8.4. Here we define T_{c_on} $(R \rightarrow 0)$ as an onset of the superconducting transition and the transition width $\Delta T = T_{c\_off} - T_{c\_on}$. It can be clearly seen from Inset in Figure 8.4 that the critical temperature rises rapidly when d_i > 1nm. The comparison of T_c and ΔT_c values defined by magnetic and transport measurements (see Table 8.1) shows that generally speaking two different methods do not produce the same data. Such a discrepancy (sometimes very large) between the superconducting transition temperature as derived from resistance and magnetization measurements was previously observed, but its origin remains to be understood. It may well be the signature of an inhomogeneous superconducting state that arises from the magnetic pair breaking due to the proximity coupling with the ferromagnetic order in the LCMO layers [9].

8.3.2 Superlattice of type YBCO/STO/LCMO –[20nm/d_i nm/20nm]$_{20}$

The series of symmetrical superlattices YBCO/STO/LCMO – [20nm/d_i nm/20nm]$_{20}$ includes four samples with the thickness of STO interlayer d_i = 0, 1, 2 and 4 nm and YBCO as the first grown layer (indexed as: YL5, YSL6, YSL7, and YSL8) and one

sample LSY22 where the first grown layer was LCMO. The superconducting properties of all samples from this series compared with the single layered YBCO film are presented in Table 8.2. It is remarkable that opposite to the previous series all SL's from given series demonstrate ferromagnetic properties with the metal/insulator transition in the range of 200-250 K. But only YL5 has sufficiently high negative magnetoresistance (*MR* ≈ -94%) in this temperature range.

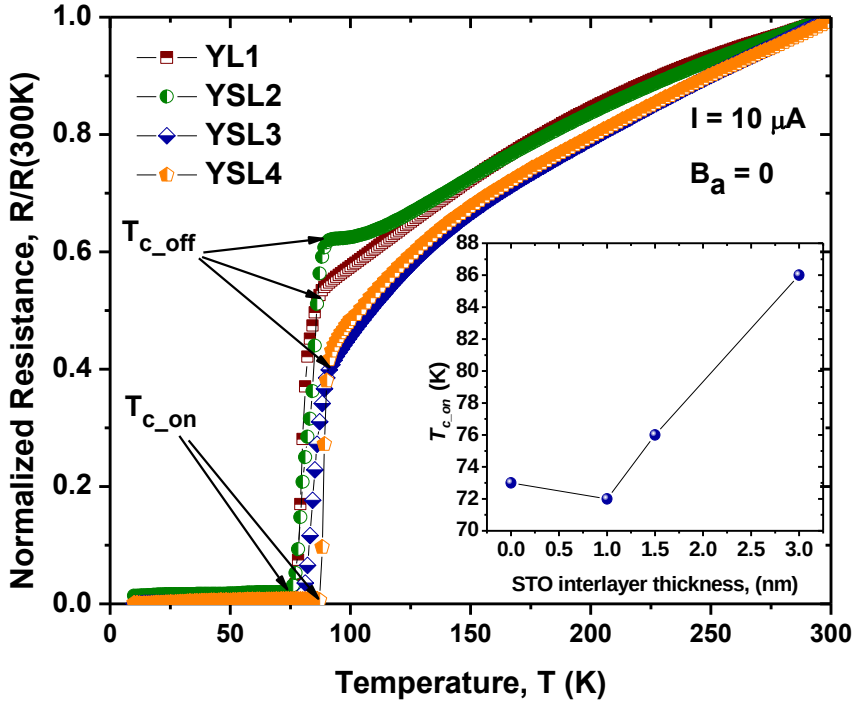

Figure 8.4 Normalized resistances as a function of temperature at zero magnetic fields for [20nm/d_i nm/10nm]$_{20}$ series of samples. Inset: Onset of superconducting transition vs STO spacer thickness showing drastic improvement in T_{c_on} with the increase of STO interlayer thickness.

It is also evident the significant reduction of the critical temperature T_c in the second series of SL's (especially derived from transport measurements as it is seen from Table 8.2 and Fig.8.5). Figure 8.5 shows normalized *R(T)* curves of YL1 and YL5 compared to the single layered YBCO film. The only one difference between two samples is the LCMO sub-layer thickness which is twice bigger in YL5. However it leads to the reduction of T_c for about 10K and almost twice bigger transition width in this sample (see Table 8.2 and Inset in Fig.8.5).

Table 8.2 Superconducting and magnetic properties of superlattices from [20nm/d_i nm/20nm]$_{20}$ series: thickness of STO interlayer d_i, critical temperature T_c from magnetization measurements with zero field cooling, superconducting transition width ΔT_c, onset of superconducting transition from transport measurements T_{c_on}, transition width $T_{c\_off} - T_{c\_on}$ from transport measurements, magnetoresistance at 250 K, and metal/insulator transition temperature T_{irr}.

Sample	STO thickness d_i, (nm)	T_c (K)	ΔT_c (K)	T_{c_on} (K)	$T_{c\_on} - T_{c\_off}$ (K)	MR(250 K) (%)	T_{irr} (K)
YL5	0	79	9	64	25	-94	220
YSL6	1	76	8	80	10	0	220
YSL7	2	79	9	74	16	0	200
YSL8	4	85	7	81	9	0	250
LSY22	4	80	6	85	5	0	250
YBCO	-	88	2	89	2	-	-

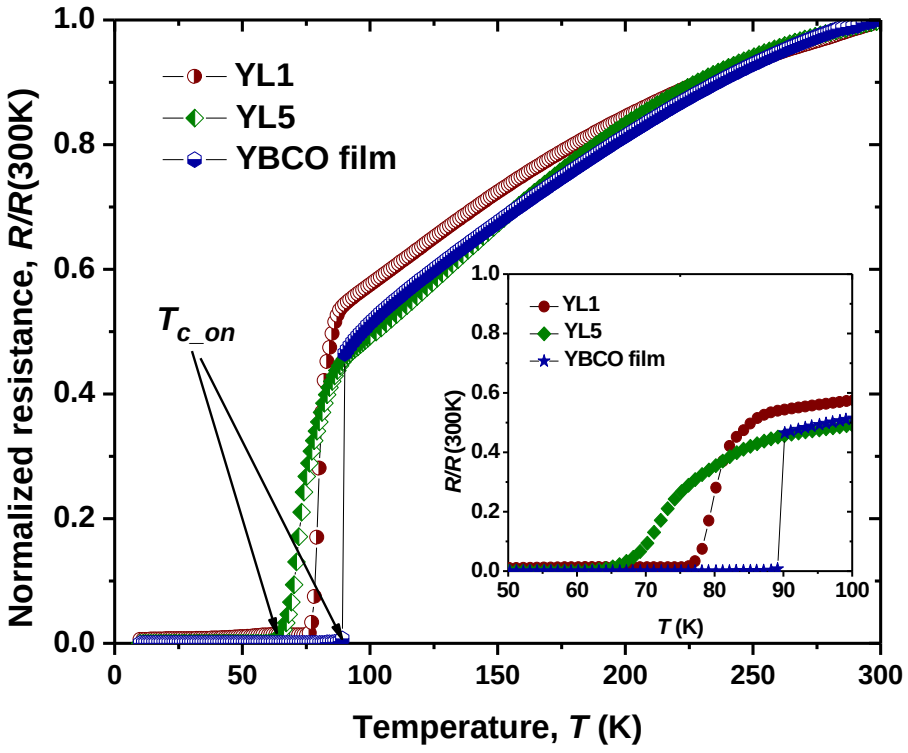

Figure 8.5 Normalized resistance vs temperature for two samples from two different series: YL1 ($YBCO_{20nm}/LCMO_{10nm})_{20}$ and YL5 ($YBCO_{20nm}/LCMO_{20nm})_{20}$ compared with single layered YBCO film. Inset: Close view of superconducting transition region showing the degradation of superconducting properties with increasing of LCMO sub-layer thickness.

Figure 8.7 shows the temperature dependence of ZFC and FC measurements where an external magnetic field of 0.01 T was applied parallel to the layers of the YL5 superlattice (right panel). It reveals the onset of a spontaneous ferromagnetic order below $T_{irr} \approx 220$ K. This value agrees well with the estimate from the temperature dependence of the resistance data that are shown in the same figure (left panel). Few features of YL5 sample can be derived if observing Fig.8.6 and analyzing Table 8.2. First we may note the greater discrepancy between magnetic and transport estimations of the critical temperature and the transition width compared to Set 1 samples. As usual, the transport measurement shows lower T_c and larger transition width ΔT_c.

The second remarkable feature of this series of samples is that their magnetization curves have a shape more similar to the shape of YBCO/LCMO bi-layered hybrid structures described in Chapter 6. It may be explained by the fact that this series of superlattices has the similar symmetrical structure (20nm-YBCO/20nm-LCMO)×20 as in the case of (200 nm-YBCO/200nm-LCMO) bilayers.

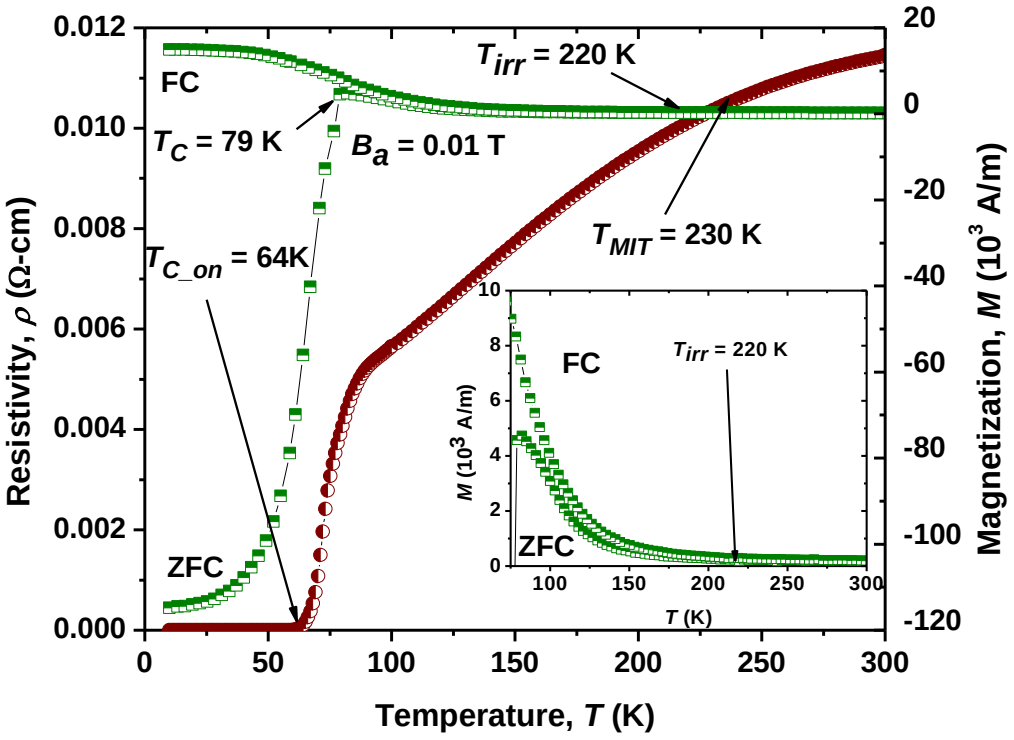

Figure 8.6 In plane magnetization of a YL5 sample (right panel) showing superconducting transition at $T_c \approx 79$K and its $\rho(T)$ curve (left panel) with $T_{c\_on} \approx$ 64K. Inset: Close view of the in plane magnetization above T_c showing the metal-insulator transition at $T_{irr} \approx 220$K.

The introduction of the thin insulating spacer (d_i > 1 nm) between YBCO and LCMO sub-layers will enhance both T_c and ΔT_c as it was already observed for previous series of samples. Figure 8.7 is an example of this improvement. It shows both magnetization and resistivity as a function of temperature for the sample YSL8 with STO interlayer thickness of about 4 nm. It also demonstrates the shift of MIT point to 250 K which is more consistent with LCMO films properties.

The measurements of a critical current density show that this series of sample with doubled LCMO layer thickness demonstrates even worse behavior than previous series with significant reduction of J_c compared to YBCO. However an introduction of STO interlayer may improve a little J_c *(B)* curve compared to the sample YL5 without insulting interlayer.

The systematic enhancement of superconducting properties for all samples of [20nm/d_i nm/20nm]$_{20}$ series is evident from transport measurements shown in Figure 8.8. We can observe the *R(T)* curves evolution with STO interlayer thickness increasing from 0 to 4 nm. Thicker STO will produce bigger T_c, less transition width, and the curve shape which is more similar to YBCO without any traces of metal/insulator transition around Curie temperature. This effect was already observed for previous SL's series [20nm/d_i nm/10nm]$_{20}$ and it is comparable to the increase of YBCO sub-layer thickness or to the decrease of thickness of LCMO. It may be also note that the room temperature resistance *R*(300K) is dramatically decreased (for about one order of magnitude) with STO spacer increasing from 0 to 4 nm. Its value (~70 Ω) is now comparable with usual resistance of a single layered YBCO sample at room temperature.

All these observations make us suggest that the introduction of a thin insulator between cuprate and manganite sub-layers leads to the change in current distribution along the superlattice. The observed effect of the resistance reduction with the increasing of STO spacer for YBCO/STO/LCMO superlatices could be explained in terms of the *RC* network model we have already discussed in Chapter 7 for STO/LCMO superlattices where the SL was examined as a complex combination of resistances and capacitors.

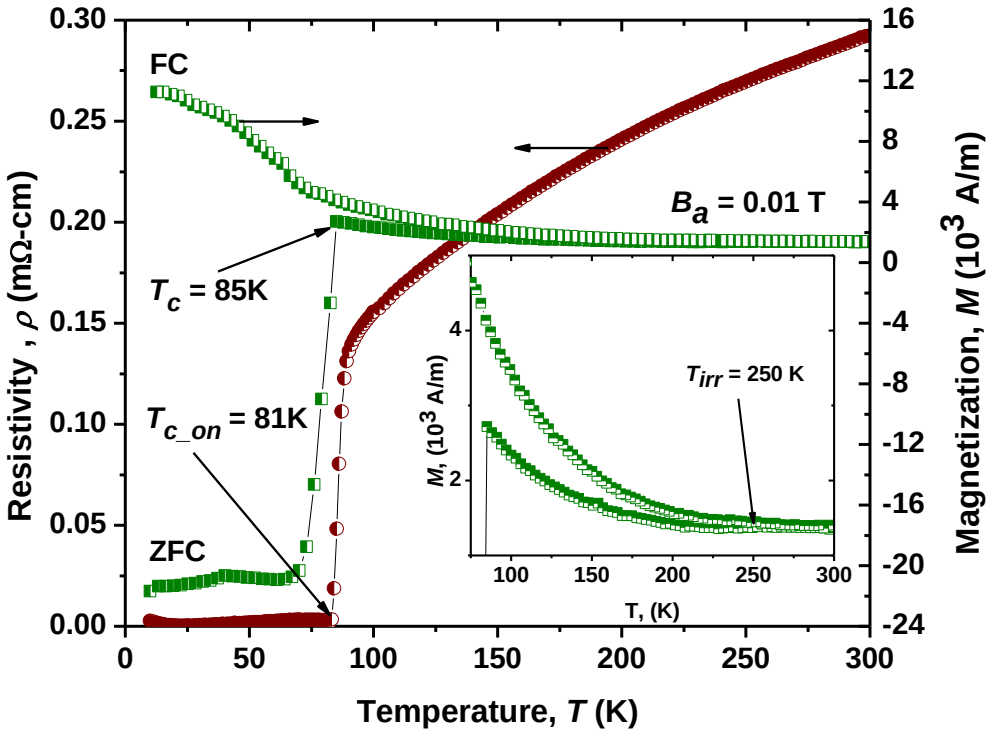

Figure 8.7 In plane magnetization of a sample YSL8 (right panel) showing superconducting transition at $T_c \approx 85$ K and its $\rho(T)$ curve (left panel) with $T_{c\_on} \approx$ 81K. Inset: Close view of the in plane magnetization above T_c showing metal-insulator transition at $T_{irr} \approx 250$K.

We may suggest that the thicker STO insulator will reduce the probability of the electrical punch-through and it will make the LCMO and YBCO sub-layers more electrically isolated. This leads to the network where the parallel combination of sub-layers dominates and thereafter, to the reduction of the total resistance. The resistivity of LCMO sub-layers is much larger than that of YBCO sub-layers, hence the transport current above T_c primarily flows along YBCO sub-layers making the $R(T)$ curve more similar to YBCO.

It may be also noted by the comparison of almost similar superconducting properties for two samples YSL8 and its mirror version LSY22 (with LCMO as the first grown layer) that the first grown layer does not define the behavior of whole superlattice.

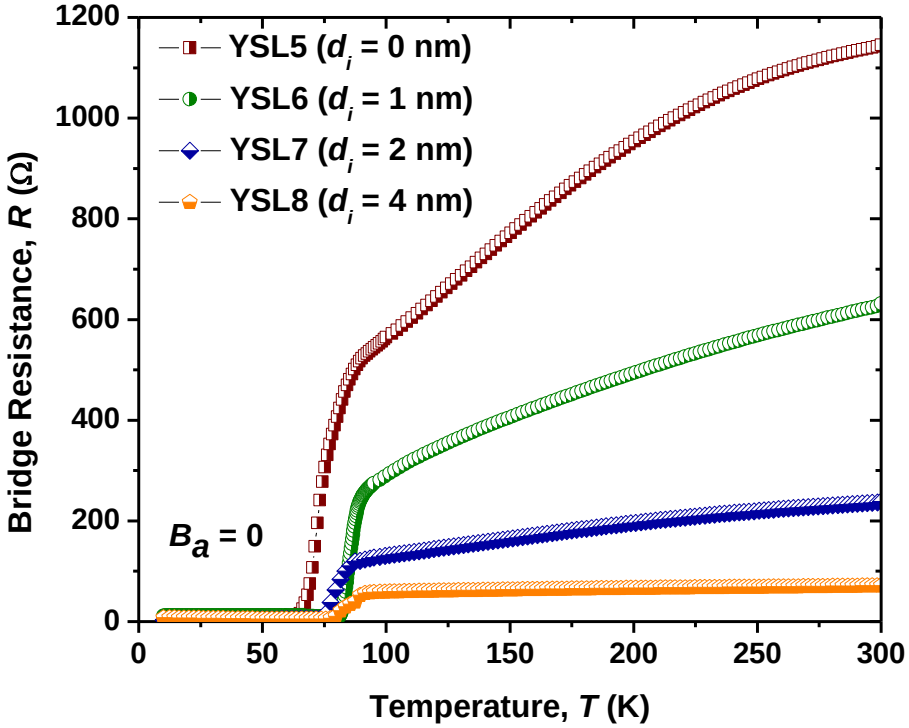

Figure 8.8 Resistance of a micro-bridges vs temperature for SL's of [20nm/d_i nm/20nm]$_{20}$ series showing the enhancement in T_c and the reduction of a room temperature resistance R (300K) with increasing of STO interlayer thickness.

8.4 Superlattices of type YBCO/PBCO/LCMO –[20nm/d_i nm/20nm]

The series of superlattices YBCO/PBCO/LCMO – [20nm/d_i nm/20nm]$_{20}$ includes five samples with $PrBa_2Cu_3O_7$ (PBCO) interlayer spacer thickness of 0, 1.5, 3, 6, and 20 nm with YBCO as the first grown layer (indexed as: YL5, YPL12, YPL10, YPL11, and YPL16) and one sample LPY20 where the first grown sub-layer was LCMO. The superconducting and magnetic properties of this series of SL's are presented in the Table 8.3.

One can readily see from the Table 8.3 and Figure 8.9 that both the superconducting critical temperature and the transition width have an articulate trend of gradually improvement with increasing of the thickness of insulating interlayer d_i as it was already noted for (YBCO/STO/LCMO) superlattices. Only 1.5 nm - thick PBCO interlayer (sample YPL12) radically improves superconductivity in this SL's and when the thickness of PBCO spacer reaches $d_i \approx 20$ nm (sample YPL16) the superconducting parameters of a superlattice trend to be very close to the single layered YBCO film. It is not surprizing because PBCO is known as a good Mott

insulator that exhibits high electrical resistivity at low temperatures and acts as good insulating spacer between YBCO and LCMO sub-layers.

Table 8.3 Superconducting and magnetic properties of SL's from (YBCO/PBCO/LCMO) series: thickness of PBCO interlayer d_i, onset of superconducting transition from transport measurements T_{c_on}, transition width $T_{c\_off} - T_{c\_on}$, magnetoresistance at 250 K, and metal/insulator transition temperature T_{irr}.

Sample	PBCO thickness d_i (nm)	T_{c_on} (K)	$T_{c\_off} - T_{c\_on}$ (K)	MR(250K) (%)	T_{irr} (K)
YL5	0	64	25	-94	220
YPL12	1.5	82	7	< 1	250
YPL10	3	85	5	< 1	220
YPL11	6	86	4	< 1	200
YPL16	20	88	2	< 1	190
LPY20	6	40	49	-2	180
YBCO	-	89	2	-	-

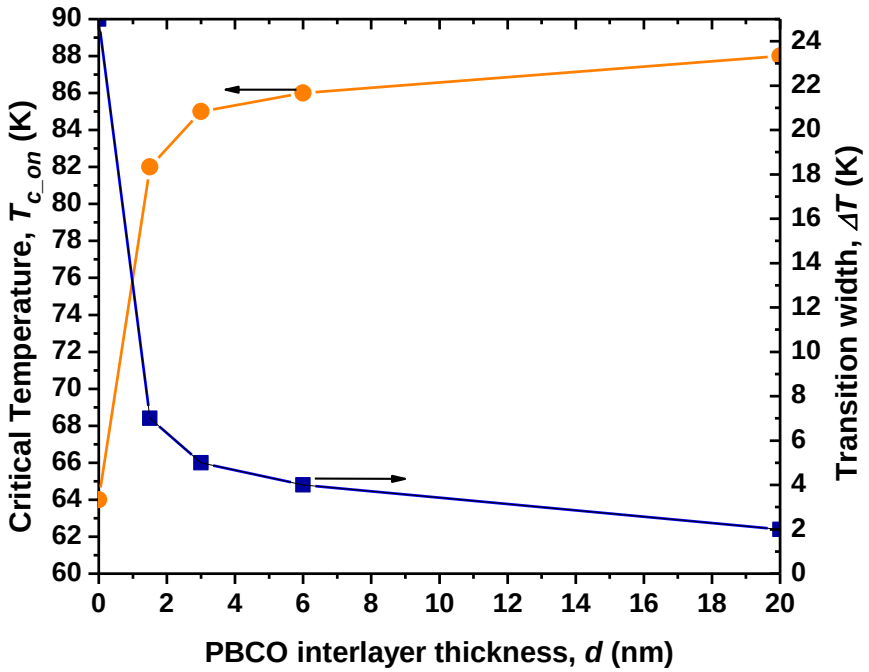

Figure 8.9 Critical temperature (left panel) and superconducting transition width (right panel) vs PBCO interlayer thickness for SL's of type $(YBCO/PBCO/LCMO)_{20}$.

Figure 8.11 shows normalized resistance curves of superlattices for different thicknesses of the PBCO interlayer. Log scale plots (not shown) display sharp and well-behaved superconducting transitions for all supperlattices with PBCO spacer. The superconducting transition width ΔT_c was found to decrease down to a saturation value when the thickness of the insulating PBCO spacer was increased (see also Fig.8.9).

Something similar behaviour of *R(T)* curves was observed in [12] for YBCO/LCMO superlattice when the thickness of YBCO sub-layer was fixed and the thickness of LCMO sub-layer was changed demonstrating the trend of T_c improvement with decreasing in LCMO thickness. This result suggests that the interplay between magnetism and superconductivity in such structures may be controlled by the thickness of insulating spacer.

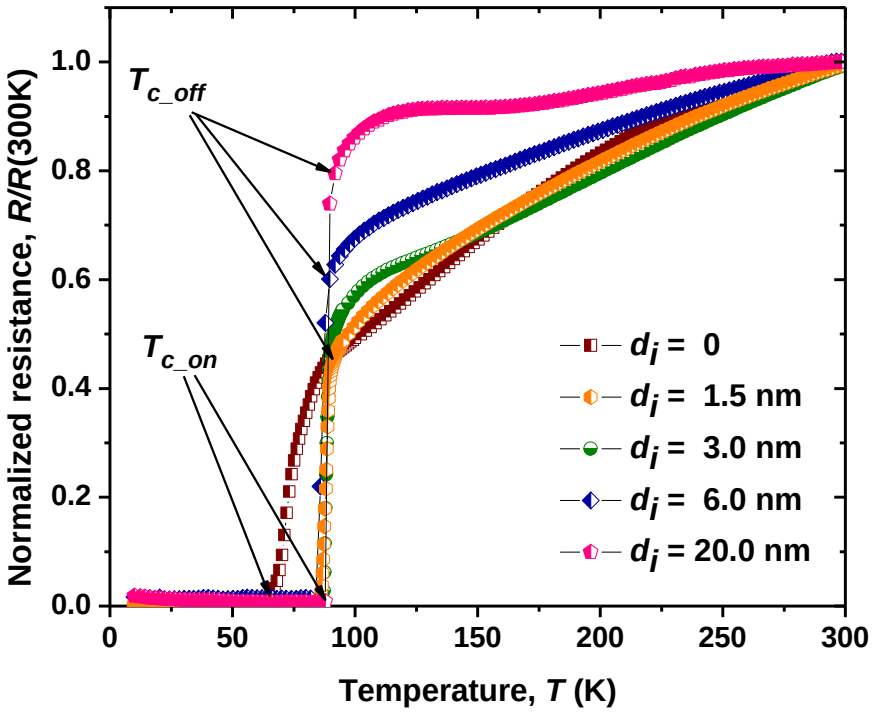

Figure 8.10 Normalized resistance vs temperature for superlattices of type (YBCO/PBCO/LCMO) with different thickness of PBCO interlayer d_i demonstrating the trend of superconducting properties improvement and the increase of normalized resistance just above T_c with increasing of PBCO interlayer thickness.

One more feature of (YBCO/PBCO/LCMO) SL's derived from Figure 8.10 is a fact that their resistance just above T_c was found to increase gradually when the thickness of the insulating PBCO layer was increased. It is absolutely different from the series of (YBCO/STO/LCMO) SL's where the increasing of STO interlayer decreases the resistance above T_c. One reason of the resistance increasing if PBCO interlayer becomes thicker is very trivial and it is related to the simple increasing of the total thickness of a sample.

However we obviously observe the increasing of the normalized resistance too. In order to investigate the contribution of PBCO/LCMO multilayers to the total resistance of a SL the separate sample representing (PBCO-20 nm/LCMO-20 nm)$_{20}$ super-structure was deposited under the same technological conditions adapted for (YBCO/PBCO/LCMO) SL's series. Figure 8.11 demonstrates the temperature dependence of a resistivity for such SL. It has the shape similar to *R(T)* curves measured for STO/LCMO superlattices described in Chapter 7. One can see that the resistivity has a maximum at very low temperature ($T_p \approx 20$ K) and then it gradually decreases. The PBCO/LCMO system has a week dependence on the external magnetic field with low negative magnetoresistance *MR* (see inset in Figure 8.11). So this sub-lattice definitely cannot be the reason of the resistance increasing above $T \approx 90$ K. The similar behavior of *R(T)* curve above T_c (see Fig.8.10) was observed in [13] and it was shown that the resistivity increased systematically in YBCO/PBCO superlattices with a fixed thickness of YBCO layers and increased thickness of PBCO layers. So we may conclude that in our case (superlattices of YBCO/PBCO/LCMO series) the contribution of YBCO/PBCO complex into the total resistance of a superlattice is predominant. Really, remembering that PBCO has the semiconductor nature, so if its thickness increases the probability of a formation of conducting filaments in it does not decrease. This behaviour does not lead to the formation of an *RC* network where the parallel combination of sub-layers is predominant and hence the reduction of total resistance is not observed.

All SL's from (YBCO/PBCO/LCMO) series demonstrate the magnetic proprieties in the temperature range of 180-250 K defined by magnetization measurements (see Table 8.3). It may be note that in this series of SL's there is a trend of T_{irr} decreasing with thicker PBCO spacer. Figure 8.12 shows the temperature dependence of both the resistivity and the magnetization for the sample

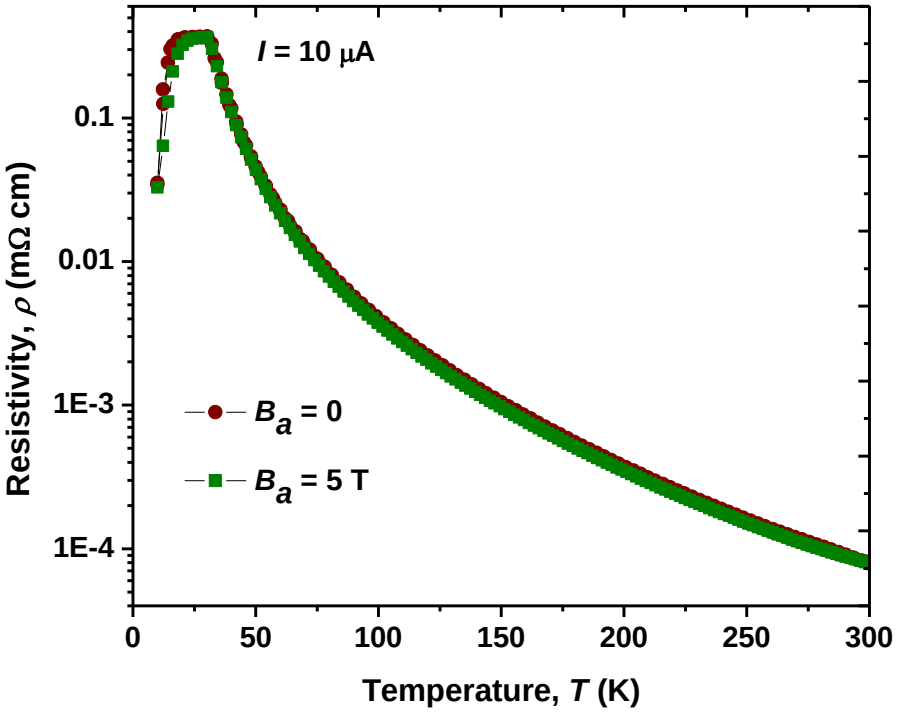

Figure 8.11 Temperature dependence of the resistivity for (PBCO-20 nm/LCMO-20 nm)$_{20}$ superlattice measured under zero magnetic fields and 5 T field and 10 μA current.

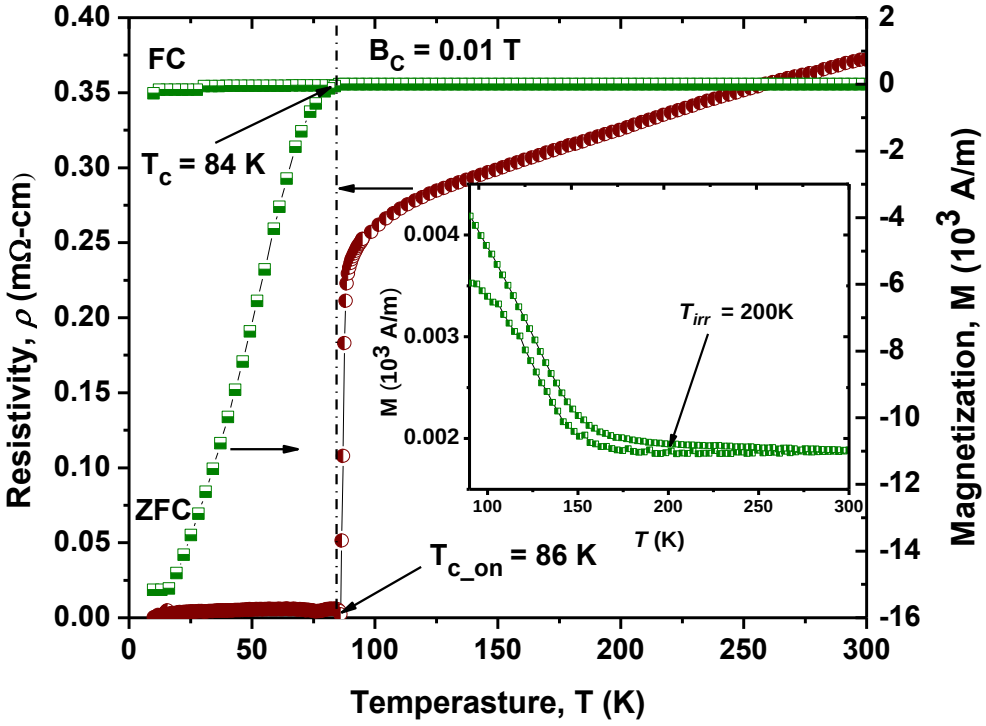

Figure 8.12 In plane magnetization under ZFC and FC conditions (right panel) and temperature dependent of resistivity (left panel) for the sample YPL11**.** Inset: Close view of magnetization above $T_c \approx$ 84K showing the metal/insulator transition at $T_{irr} \approx$ 200 K.

YPL11. The metal/insulator transition is clearly seen from Inset in Fig.8.12 with T_{irr} ≈ 200 K. One more note derived from Figure 8.12 is related to the much low discrepancy between values of T_c ≈ 84 K (derived from the magnetization measurement) and T_{c_on} ≈ 86 K (from the transport measurement) for this series of samples compared with SL's of (YBCO/PBCO/LCMO) type. Really the difference between these two values was not more than 2 K for all samples in this series (see for example Fig. 8.12).

We have also studied the magnetoresistance $MR = [(R(B) - R(0))/R(0)]\times 100\%$ of a sample YPL11. In Figure 8.13 the magnetic field dependence of the *MR* for this sample at different temperatures close to superconducting transition T_c ≈ 86 K is presented. Figure 8.13a shows the in-plane *MR* data for the magnetic field parallel to the current and the temperature range 65-83 K. We may note that the sign of magnetoresistance has a trend to oscillate with the temperature increasing. At temperatures below 75 K the high field magnetoresistance is negative and close to zero but at $T \approx 75$ K it changes its sign to positive keeping this sign up to $T \approx 82$ K where *MR* suddenly becomes negative again. The *MR* reaches its maximum negative value (≈ 60%) at $T \approx 83$ K. Figure 8.13b demonstrates the *MR (B)* curves evolution with temperature. For $T \approx 85$ K we may observe the abrupt change of *MR (B)* curve shape at $B \approx 1.5$ T. It becomes giant positive for $B > 1.5$ T. Low field giant positive magnetoresistance (PMR) effects are observed around superconducting transition which is interesting for practical applications. Magnetoresistance reaches its giant positive maximum at $T \approx 86$ K and just at $T \approx 87$ K its value drops down for about one order of magnitude keeping the positive sign and showing the low field magnetoresistance (see Figure 8.13b and 8.13c). The PMR reaches its maximum value of ~ 300% at $B_a = 0.2$ T (at $T = 76$K) while PMR value sharply decreases to 25% at 77 K. Further increase in temperature leads to the change of *MR* sign to negative one with the value close to zero. As it was shown in previous sections the giant positive magnetoresistance manifests the superconducting transition. So, after examination of data presented in Figure 8.13, we may conclude that superconducting transition occurs at $T_c \approx$ 86-87 K which is perfectly matched with T_{c_on} value derived from the transport curve of YPL11 (see Fig.8.12).

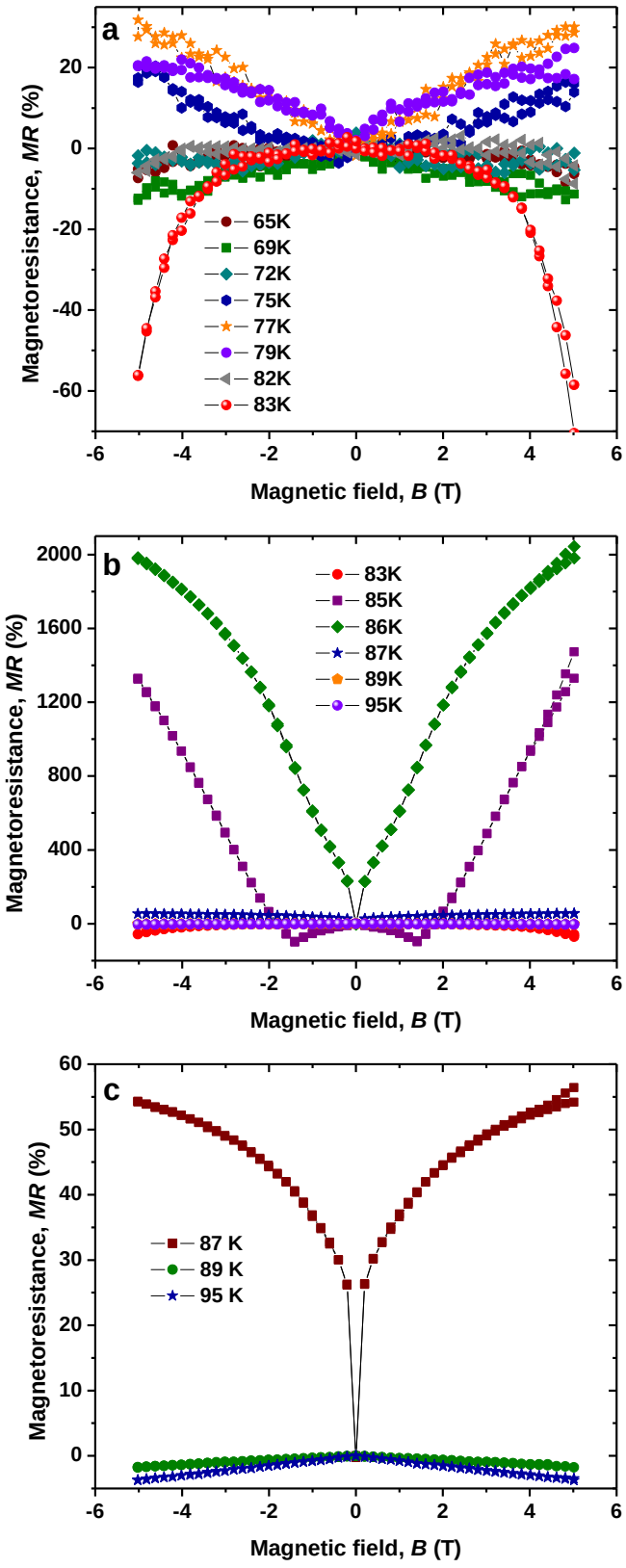

Figure 8.13 High field magnetoresistance, $MR = [(R(B) - R(0))/R(0)]\times 100\%$ vs in plane magnetic field B_a for the sample YPL11: (a) the small negative MR below $T_c \approx$ 86 K is converting to positive one at $T \approx 75$ K; (b) $MR(B)$ at T_c and above, showing the change of MR sign and its giant behavior at temperatures around T_c, (c) close view of $MR(B)$ curves just above the superconducting transition.

One more remarkable feature of (YBCO/PBCO/LCMO) series of superlattices was detected by investigating the sample LPY20 which is a mirror version of a sample YPL11 (see Table 8.3) where LCMO sub-layer was the first grown layer (with YBCO on top of the structure). Figure 8.14 shows normalized resistance as a function of a temperature for both LPY20 and YPL11 samples. It may be seen that two samples have very different behaviors. The LPY20 has an extremely low $T_{c\_on} \approx 40$ K and very large transition width $\Delta T_c \approx 49$ K compared with YPL11 ($T_{c_on} \approx 86$K and $\Delta T_c \approx 4$ K). LPY20 also demonstrates a well pronounced metal/insulator transition around $T_p \approx 200$ K which we already observed only in LCMO/YBCO hybrids described in Chapter 6.

Figure 8.15 shows the temperature dependence of a resistivity of LPY20 for two values of external magnetic field. It may be seen that the application of a field reduces the resistivity and shifts its maximum at T_p to higher temperatures. Although the negative magnetoresistance around Curie temperature is not very high (see Inset in Fig.8.15) the presence of the first grown manganite layer in this SL and its influence on the transport properties of whole structure is evident.

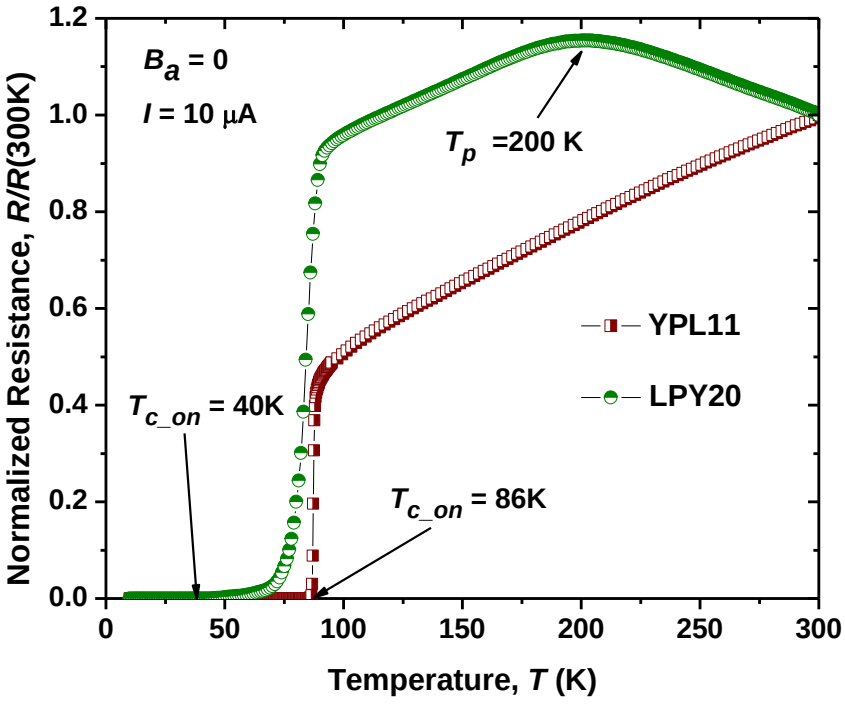

Figure 8.14 Temperature dependence of normalized resistance for the sample YPL11 $(YBCO/PBCO/LCMO)_{20}$ compared with its mirror sample LPY20 $(LCMO/PBCO/YBCO)_{20}$ demonstrating the influence of the first grown layer on whole structure transport properties.

The detailed study of the transport curves of LPY20 around and below T_c produces some more interesting results (see Fig.8.16). First of all we may note that the temperature of the on-set superconducting transition $T_{c\_on} \approx 40$ K, derived from the transport curve, is matched perfectly with the positive peak of the magnetoresistance. We already know that the giant positive magnetoresistance in our SL's is associated with a superconducting transition (see Section 8.3 of this Chapter). So we may suggest that the low temperature ($T \approx 26$ K) giant magnetoresistance peak may manifest probably the re-entrant resistance.

The more pronounced magnetic properties of this sample in comparison with a mirror sample YPL11 (see Fig.8.14) may be also associated with the structure mirror symmetry. Really, it was found in [15] that at the LCMO/YBCO interface the magnetization of LCMO has suppressed likely due to the charge transfer across the interface. This effect would influence the bottom LCMO layer less, as it is grown

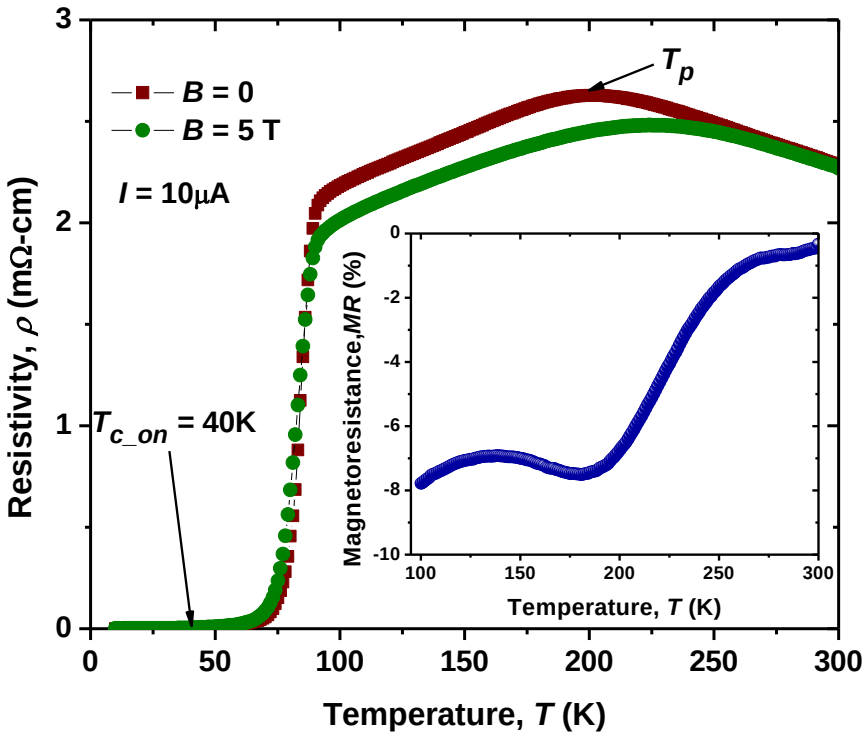

Figure 8.15 Temperature dependence of the resistivity for the sample LPY20 $(LCMO/PBCO/YBCO)_{20}$ at zero field and 5 T magnetic field. Inset: Temperature dependence of a magnetoresistance above T_c demonstrating the metal/insulator transition around 180 K.

directly on the substrate, therefore retains a magnetization that is close to that of the bulk material. In other words, this first LCMO sub-layer defines the behaviour of the whole structure suppressing the superconductivity and improving its magnetoresistance.

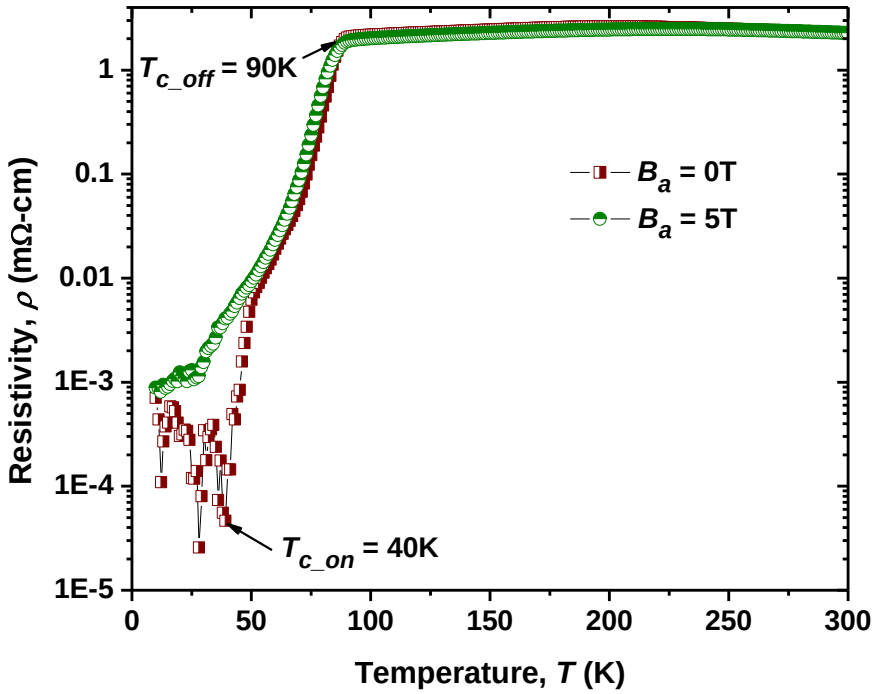

Figure 8.16 Logarithmic plot of the transport curves for the sample LPY20 $(LCMO/PBCO/YBCO)_{20}$ showing the value of $T_{c\_on} \approx 40$ K, the unstable resistivity below this temperature and very large transition width.

8.5 Superlattices of type YBCO/ CeO_2 /LCMO –[20nm/d_i nm/20nm]

This series of SL's includes three samples with the thickness of CeO_2 interlayer spacer of 0, 4, and 8 nm and YBCO as a first grown layer and LCMO as a termination layer (indexed as: YL5, YCL9, and YCL13) and one sample LCY21 which is a mirror version of YCL13 where the first grown layer was LCMO and the termination layer was YBCO. The characteristics of this series of SL's are collected in the Table 8.4.One can see from this table and Figure 8.17 that the superconducting properties of all SL's from given series have the same trend of improvement when the thickness of insulating interlayer increases as it was observed for previous series. All samples also demonstrate a weak magnetic field dependence of the resistance with the metal/insulator transition in the temperature range of 180-220 K.

Table 8.4 Superconducting and magnetic properties of superlattices from YBCO/CeO_2/LCMO series: thickness of CeO_2 interlayer d_i; onset of superconducting transition from transport measurements T_{c_on}; transition width T_{c_off} –T_{c_on}; and metal/insulator transition temperature T_{irr}.

Sample	CeO_2 thickness, d_i (nm)	T_{c_on} (K)	$T_{c\_on}-T_{c\_off}$ (K)	T_{irr} (K)
YSL5	0	64	25	220
YCL9	4	77	13	210
YCL13	8	84	6	180
LCY21	8	69	21	200

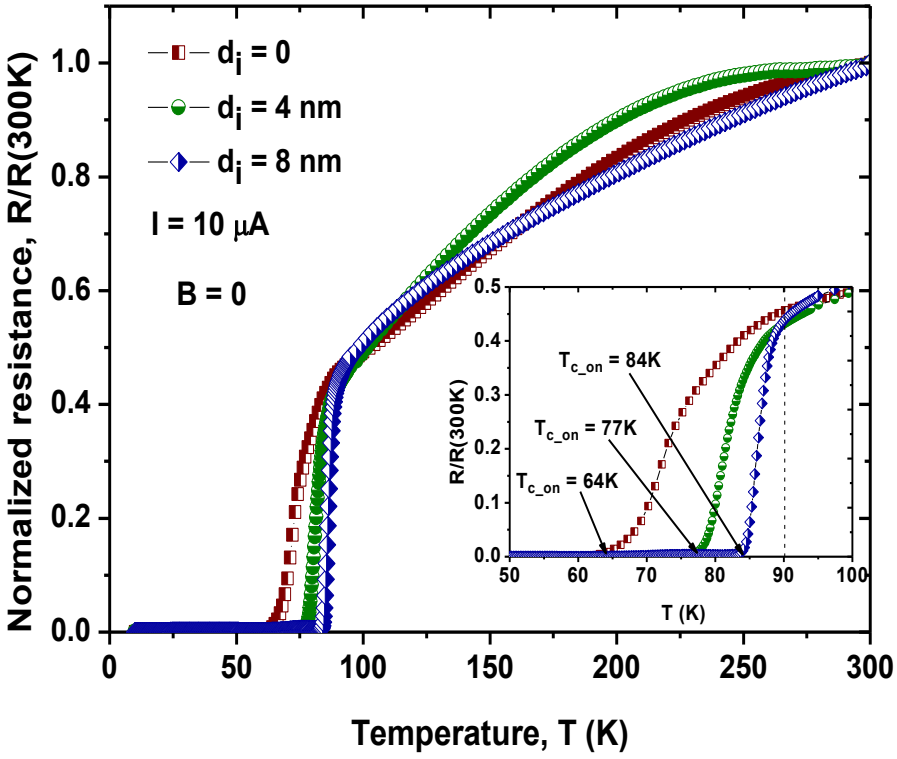

Figure 8.17 Normalized resistance vs temperature for three superlattices YSL5, YCL9, and YCL13 of type $(YBCO/CeO_2/LCMO)_{20}$ with different thickness of CeO_2 interlayer demonstrating the trend of superconducting properties improvement with the increase of CeO_2 interlayer thickness. Inset: Close view of the superconducting transition region for same three samples.

The data presented in Table 8.4 and Figure 8.17 is very similar to our results already found for other series of superlattices. However it is necessary to pay attention to the quite unusual behavior of the fourth sample LCY21 from given

series. Being the mirror version of YCL13 with 8 nm CeO_2 spacer and LCMO as a first grown layer, the sample LCY21 demonstrates much less $T_c \approx 69$ K and very broad superconducting transition compared to its mirror sample (see Figure 8.18 and Table 8.4). It also shows the resistance upturns below T_c with the peak of the re-entrant resistance at the temperature $T_{re} \approx 46$ K (for 10 μA applied current). This upturn is reversible and it exists for all applied electrical current and magnetic field values. Figure 8.19 shows the logarithmic plot of the temperature dependence of resistivity for LCY21 at zero and 5 T external magnetic fields. The resistance upturn below $T_{c2} \approx 69$ K is clearly observed. At this temperature the resistivity which was dropped to almost zero at the superconducting transition point, again starts to show some finite values which is approximately 50 time higher at T_{re} than ρ ($T \approx 69$ K). Then the resistivity demonstrates the downturn and it reaches its second minima at $T_{c1} \approx 15$ K. At this temperature we may observe the small upturn of the resistivity on the zero fields *R(T)* curve. The application of an in plane magnetic field $B_a = 5$ T shifts T_{c2} to low temperatures for about 5 K without any appearance of the low temperature upturn. Inset in Figure 8.19 shows the magnetoresistance of this sample with two giant positive *MR* peaks at T_{c1} and T_{c2} which is perfectly matched with the superconducting transitions temperatures found from *R(T)* plot. This behavior is quiet similar to the *MR* behavior of the superlattice LPY20 described in previous section. Comparing the configuration of two SL's LPY20 and LCY21 we may note that they both have the first grown LCMO layer. Remembering that such behaviour never was detected for superlattices with YBCO as the first grown layer, we may conclude that the re-entrant resistance behaviour is associated with the sub-layers order in given superlattice.

It should be noted that the position of the re-entrant peaks has the current dependence similar to the magnetic field dependence and they increase with the current increasing. Figure 8.20 shows the resistivity vs temperature plot for three different currents applied on LCY21. The shift of T_{re} for about 10 K to low temperatures with the current change from 10 μA to 100 μA can be clearly seen. For higher applied currents the maximum of the re-entrant resistance even cannot be measured because of its extremely low T_{re}.

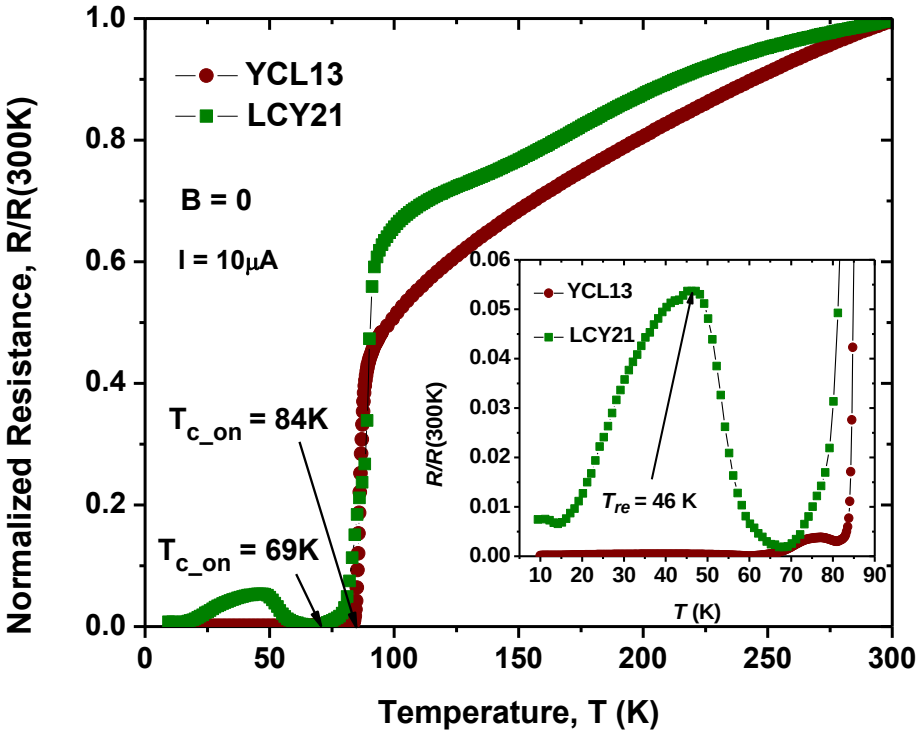

Figure 8.18 Normalized resistance vs temperature for superlattice YCL13 (with YBCO as the first grown layer) compared with the mirror sample LCY21 (with LCMO as a first grown layer). Inset: Close view of normalized resistance curves below the temperature of superconducting transition showing the re-entrant resistance behavior for LCY21 sample with the re-entrant resistance maximum at T_{re} ≈ 46 K.

The re-entrant resistance behaviour in LCMO/YBCO superlattices was observed for the first time by *H.-U Habermeier and G. Cristiani* in [1]. In [16, 17] this phenomena was experimentally investigated in more details for the superlattice $[YBCO_{7.5\ nm}/LCMO_{5\ nm}/]_{20}$ with LCMO as a first grown layer on STO substrate. The similar shift of the up-turn temperature with the increase of applied current was detected. However the pronounced low temperature downturn of resistance there was not observed. Authors have performed the attempt to explain this phenomenon by sophisticated *inverse*-proximity effects of the spin-polarized quasiparticles. But in our case, if the introduction of an insulating interlayer blocks the proximity effect in YBCO/LCMO system, such explanation is not seems to be quite satisfied. We rather try to explain such phenomena qualitatively in the frame of the model of complex *RC* network described in Chapter 7.

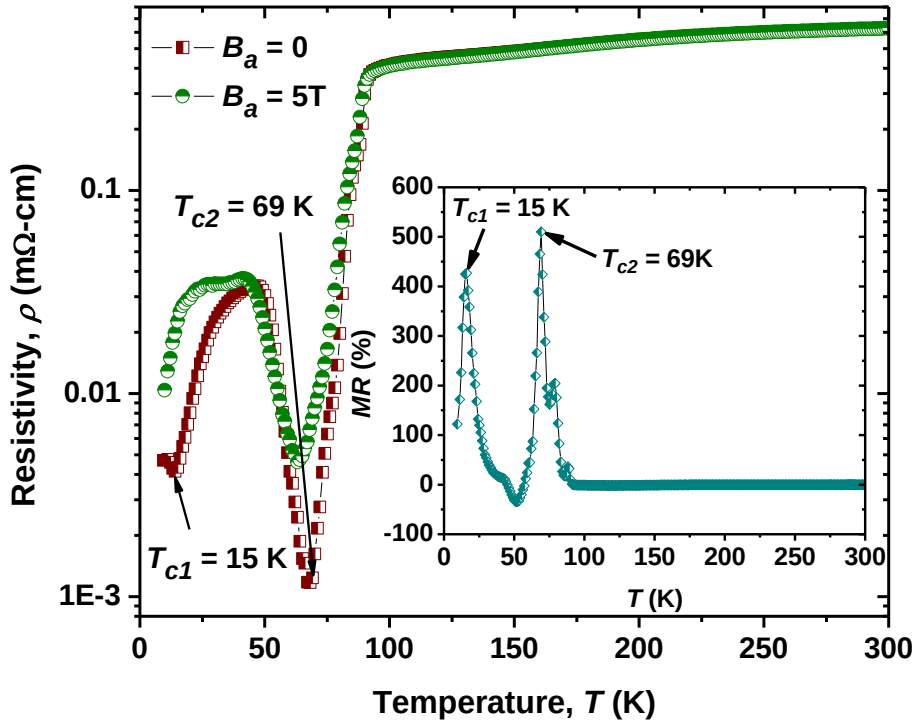

Figure 8.19 Logarithmic plot of transport curves at two external field values for the sample LCY21 $(LCMO/CeO_2/YBCO)_{20}$ showing the oscillation of superconducting transition with value of $T_{c1} \approx 15$ K and $T_{c2} \approx 69$ K and very large transition width. Inset: Magnetoresistance curve of LCY21 showing two positive peaks associated with superconducting transitions and the close to zero negative *MR* above T_{c2}.

It is well known from our previous experiments with LCMO and YBCO thin films deposition by PLD (see Ch.3 and Ch.5) that LCMO film with even small thickness (~ 20 nm in our case) is much less porous and it has higher epitaxial quality than YBCO film of the same thickness. We also know (from TEM data in Ch.7) that the number of defects is rising rapidly with increasing number of sub-layers in a superlative. So the sample LCY21 (and probably LPY20 as well) which demonstrates re-entrant resistance may be considered as the superstructure with two main parts: high quality solid epitaxial film of LCMO on the bottom and the defected $YBCO/CeO_2/LCMO$ superlative on the top. The prime LCMO layer directly grown on the substrate may significantly suppress the superconductivity of the superlattice LCY21 which was already shown in Fig.8.18 and Fig.8.19. The position of LCMO as a first grown layer also defines the resistivity of a whole SL below T_c. It can be seen from the Inset in Fig.8.18 that the resistance of LCY21 at low temperatures is

about two orders of magnitude higher than YCL13 with YBCO as a first grown layer.

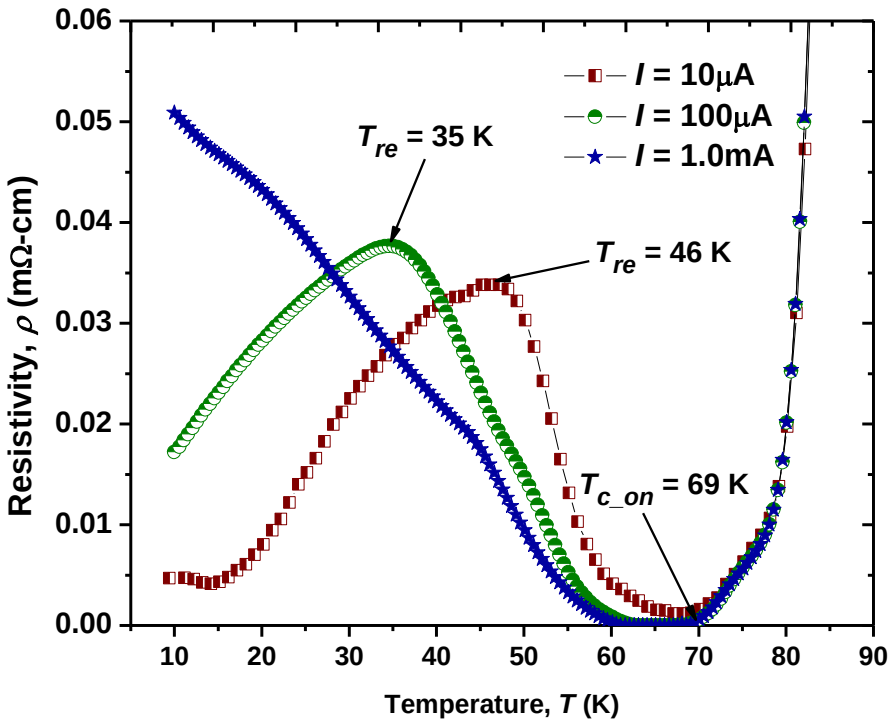

Figure 8.20 Resistivity vs temperature plot for LCY21 below T_{c_off} at zero magnetic field and three different currents. The re-entrant resistance peak is shifted to lower temperatures with increasing current. The on-set temperature of the main superconducting transition T_{c_on} has weak dependence on the applied current values.

Taking into account that in our superlattice the LCMO and YBCO semiconductor layers are separated by the insulating layers of CeO_2 (with dielectric properties even much better compared to STO [18]) a certain capacitance is created across each interface. Thus, we can analyse our superlattice as an *RC*-network with nonlinear, temperature dependent resistors and capacitors. This network represents a very complex serial/parallel combination of *RC* elements composed from YBCO/CeO_2, and LCMO/CeO_2 interfaces. The last one probably governs the shape of *R(T)* curve below T_c that leads to the re-entrant resistance behaviour. In order to verify this assumption we have deposited the structure containing the 200 nm thick YBCO film with LCMO/CeO_2 superlattice on top where we may observe the separate contribution of the SL to the resistance of a whole structure. Figure 8.21

shows the temperature dependence of a normalized resistance of such type of superlattice CL33 compared to samples YCL13 and LCY21. It may be clearly seen that the shape of *R(T)* curve of CL33 is very similar to the shape of LCY21with almost the same position of T_{re}. This confirms our suggestion about the importance of the influence of LCMO/CeO_2 sub-system on the *R(T)* curve shape of $(LCMO/CeO_2/YBCO)_n$ type superlattices. Although the nature of the re-entrant resistance behaviour in cuprate/manganite superlattices is not so clear it may have some practical applications because of possibility to control by an external magnetic field or an electrical current.

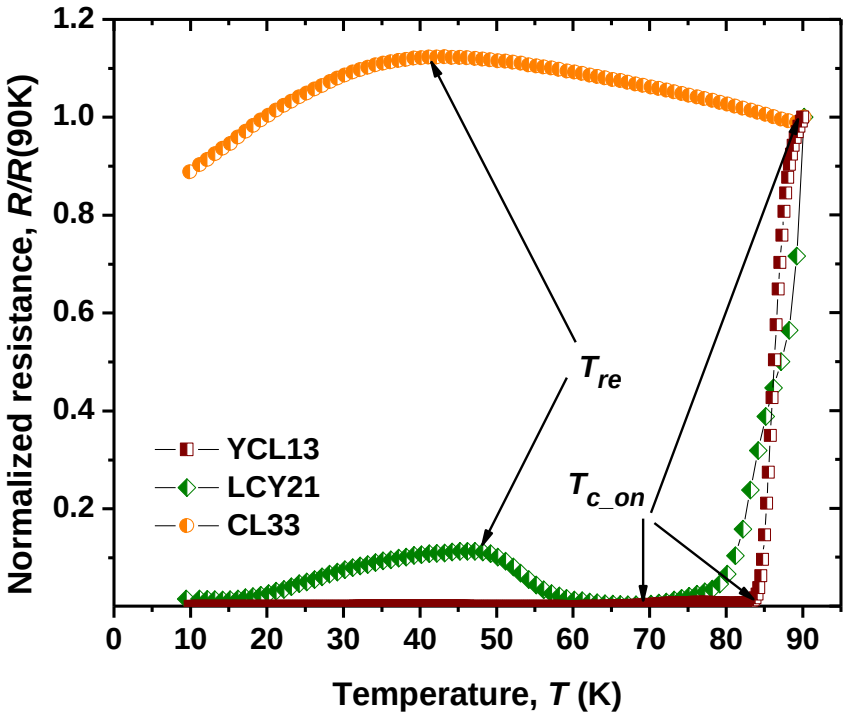

Figure 8.21 Comparison of normalized resistances as function of temperature below T_c for three different structures: superlattice YCL13, superlattice LCY21, superlattice CL33 (CeO_2 -4nm/LCMO-4nm)$_{40}$ grown on YBCO film with superconducting transition at $T_c \approx 90$K (not shown).

8.6 Conclusion

We have fabricated by PLD and investigated magnetic and transport properties of four series of cuprate/insulator/manganite superlattices with STO, PBCO, and CeO_2 as insulating spacers between YBCO and LCMO sub-layers.

The investigation of SL's of type $(YBCO\text{-}20nm/STO/LCMO\text{-}10\ nm)_{20}$ shows that superconducting properties of such type of SL's may be significantly improved by the introduction of STO spacer with thickness $d_i > 1$ nm. However this series of samples did not demonstrate any expected magnetic properties above T_c but very low negative magnetoresistance around T_{Curie} of LCMO, which is probably related to very small thickness of LCMO sub-layer compared to YBCO thickness. All samples in this series have demonstrated $J_c(T)$ behavior which is not consistent with the single layered YBCO film of the same thickness. Sao we may conclude that the presence of manganite ultimately suppress the superconductivity in cuprate/insulator/manganite multilayered structures.

In the second series of superlattices YBCO/STO/LCMO the thickness of LCMO sublayer was increased twice and this immediately produced the result demonstrating ferromagnetic properties with metal/insulator transition in the range of 200-250 K. As for previous series the improvement in T_c and ΔT_c with increasing of the thickness of STO interlayer was evident, however the magnetoresistance around T_{Curie} of LCMO has greatly suppressed in all samples with STO insulating spacer. Investigation of $J_c(T)$ curves for this series of sample shows even worse behavior with significant reduction of J_c compared to YBCO which is predictable because of higher thickness of LCMO sub-layer. This series of superlattices demonstrates the interesting feature of the decreasing of a room temperature resistance (for about one order of magnitude) with STO spacer increasing from 0 to 4 nm. This could be explained by current redistribution between superconducting sub-layers if the thickness of insulator spacer increases.

Besides the same trend of the enhancement of superconducting properties with increasing of the thickness of insulator spacer, the main feature of superlattices of type YBCO/PBCO/LCMO was a quite different shape of $R(T)$ curves for two mirror samples with LCMO or YBCO as the first grown layer. It was shown that the sample with LCMO on bottom has worse superconducting properties ($T_c \approx 40$ K) and

better magnetoresistance (~ 10%) around metal/insulator transition point. It was also shown that positive magnetoresistance peaks coincided with superconducting transitions in such sample. This was also confirmed by series of *MR(B)* measurements for different temperatures around T_c.

The similar behaviour of the mirror sample with LCMO as a first grown layer and even more pronounced re-entrant resistance at $T_{re} \approx 46$ K (for $I = 10\mu A$) was observed in YBCO/CeO_2/LCMO series of SL's with CeO_2 as the insulating spacer. It is shown that the re-entrant resistance is stable and it can be controlled by the external magnetic field and applied current which is interesting for possible practical applications.

References

[1] H.-U Habermeier and G. Cristiani. *Egypt. J. Sol.*, **26**, No. (1), (2003)

[2]Chen, F; Gorshunov, B; Cristiani, G; Habermeier, H.-U; Dressel, M. *Solid State Communications*, **131**, No 5, 295 – 299, (2004)

[3] V. K. Malik, I. Marozau, S. Das, B. Doggett, D. K. Satapathy, M. A. Uribe-Laverde *at al*. *Phys. Rev. B.* **85**, 054514, (2012)

[4] N. Driza, S. Blanco-Canosa, M. Bakr, S. Soltan, M. Khalid, L. Mustafa at all. *Nature Materials* 11, 675–681, (2012)

[5] J. Chakhalian, J. W. Freeland, H.-U. Habermeier, G. Cristiani, G. Khaliullin, M. van Veenendaal, B. Keimer. *Science* **318**, 1114, (2007)

[6] Kazuhiro Kawashima, Soltan Soltan, Gennady Logvenov, and Hanns-Ulrich Habermeier *Appl. Phys. Let*. **103**, 122603, (2013)

[7] Chien, Te Yu; Kourkoutis, Lena F; Chakhalian, Jak; Gray, Benjamin; Kareev, Michael; Guisinger, Nathan P . *Nature communications*, ISSN 2041-1723, **4**, 2336, (2013)

[8] N. Driza, S. Blanco-Canosa, M. Bakr, S. Soltan, M. Khalid, L. Mustafa *at al. Nature Materials*. ISSN 1476-1122, **11**, Issue 8, 675 – 681, (2012)

[9] Todd Holden, H.-U. Habermeier, G. Cristiani, A. Golnik, A. Boris, A. Pimenov at all. *Phys. Rev. B*. **69**, 064505, (2004)

[10] P. Przyslupski, I. Komissarov, W. Paszkowicz, P. Dluzewski, M. Sawicki, and R. Minikayev. *J. Appl. Phys.* **95**, 2906, (2004)

[11] C B Cai, L. Peng, B Holzapfel, X M Xie, Z Y Liu, Y M Lu, and X Z Chen. *Supercond. Sci. Technol.* **23**, 034010, (2010)

[12] V. Peña, Z. Sefrioui, D. Arias, C. Leon, J. Santamaria, M. Varela, S. J. Pennycook, J. L. Martinez . *Physical Review B* **69**, 224502 (2004)

[13] L. M. Wang and H. C. Yang, H. E. Horng. *Physical Review B* **56**, 10 (1997)

[15] A. Hoffmann, S. G. E. te Velthuis, Z. Sefrioui, J. Santamaría, M. R. Fitzsimmons, S. Park and M. Varela. *Phys. Rev. B* **72,** 140407 (R), (2005)

[16] S. Soltan, J. Albrecht, H.-U. Habermeier *Materials Science and Engineering B.* **144,** 15–18, (2007)

[17] Soltan Soltan *Physica C,* **470** (2010)

[18] V Grosse, R Bechstein, F Schmidt and P Seidel *J. Phys. D: Appl. Phys*. **40,** 1146–1149, (2007)

Chapter 9
Summary

During last few decades the most important and unexpected discoveries in the field of a solid state physics were made in oxide systems. The discovery of high-temperature superconductivity and colossal magnetoresistance has demonstrated that oxides and their interfaces can provide practically all physical phenomena typical for solid state materials. Sometimes these phenomena go well beyond those exhibited by conventional semiconductor interfaces because new and largely unexplored physics becomes relevant, enabling novel electronic phases. So the study of oxide systems, interfaces, and heterostructures, as well as the development of processes for the formation, growth, and phase stability of oxide thin films, remain the important and actual field of scientific research.

All samples in this work are grown by pulsed laser deposition. So a lot of attention was drawn to this technique optimization and improvement. After PLD system was automated with LabView and optimized which was described in Chapter 3 of this thesis, the best grown conditions were found for proven high quality YBCO films and superconducting multilayered structures on different substrates. It was shown that the PLD technique can be successfully implemented for the manufacturing of superconducting device prototypes such as: Josephson junctions with advance functionality; YBCO long film multichannel cables with effective reduction in transferred and generated heat for superconducting electronic applications; multilayered YBCO/SmBCO/YBCO thin films (with thicknesses less than 90 nm) for possible future applications as single photon detectors.

High quality perovskite manganites, $La_{1-x}A_xMnO_3$ (A = Ca, Sr, Ba) are very interesting materials due to their great application potential for magnetic memory and spintronics devices. We have demonstrated the ability to grow of high quality epitaxial $La_{1-x}Ca_xMnO_3$ (LCMO) films with different thickness on different substrates using PLD technique. The quality of manganite thin films was confirmed by XPS and SEM measurements, as well as by electromagnetic properties of LCMO samples. All LCMO thin films demonstrated CMR behavior with the negative

magnetoresistance minimum at the metal-insulator transition temperature T_p which has the trend of reduction if the LCMO film becomes thinner.

We have manufactured by PLD and investigated magnetic and transport properties of multilayered hybrid structures consisting of superconductor (YBCO as S) and ferromagnetic (LCMO as F) layers separated by thin insulator (STO or CeO_2 as I). Measurements show the coexistence of ferromagnetism at high temperatures ($T > T_c$) and superconductivity at low temperatures ($T < T_c$) in these heterostructures with the suppression of both superconductivity and magnetism. The possibility to control of YBCO micro-bridge resistance above superconducting transition by current injection through LCMO bottom layer was demonstrated in the hybrid structure of S/I/F type (YBCO on top). We have also investigated the electrical transport properties of a hybrid structure of F/I/S type (LCMO on top). This hybrid structure demonstrated the unusual $R(T)$ behavior, with a sharp dip in resistance below T_c. It was also found that electroresistance and magnetoresistance around T_{Rmin} can be tuned by electric current, which may have applications in controlling the properties of such hybrid devices. This behavior may be explained in terms of the current shunting model and phase transition effect in LCMO triggered by electrical current.

We have managed to establish an acceptable technology for combination of LCMO films exhibiting the CMR effect with HTS REBCO films for novel hybrid functionalities and devices, so that the relevant magnetic properties of LCMO at $T < T_c$ would be exhibited below the superconducting transition temperature. We have manufactured by PLD a series of LCMO/STO superlattices with more than 20 periods of 3-7 nm thick sub-layers and investigated their properties by means of EFTEM, SEM, magnetic, and transport measurements. The superlattices have demonstrated CMR behaviour with a strongly reduced Curie temperature, enabling an easier cooling approach for potential applications. Importantly, the $\rho(T)$ curves of the superlattices below the MIT have remarkable sharp features exhibiting about two order of magnitude drops of resistivity, which result in the positive peak of magnetoresistance in excess of 1800% at 75 K. This behaviour was explained in the framework of the phase separation theory for manganites for the well-organised 3D structures, which experience dimensional transitions of their spin-charge transport properties. The significant result is that because the structure of the superlattices can

be easily controlled, it can enable the prescribed tuning of the magnetoresistance properties required for applications. Moreover, the dimensionality dependent behaviour observed and its magnetic field dependence indicate the presence of magnetodielectric properties in STO layers.

Artificial superlattice (SL) structures offer a possibility of combining antagonistic order parameters such as superconductivity (HTS cuprates) and ferromagnetism (CMR manganites) in order to obtain novel materials with modified or even with entirely new physical properties. We have fabricated by PLD and investigated magnetic and transport properties of four series of cuprate/insulator/manganite superlattices with STO, PBCO, and CeO_2 as insulating interlayer between YBCO and LCMO sub-layers. As a rule the superconductivity is suppressed by proximity effect in YBCO/LCMO superlattices. The investigation of SL's with LCMO sub-layer twice thinner than YBCO sub-layer shows that superconducting properties of such SL's may be significantly improved by the introduction of STO interlayer with thickness $d_i > 1$ nm. However this series of SL's does not demonstrate any expected magnetic properties above T_c. In the second series of superlattices YBCO/STO/LCMO the thickness of LCMO sublayer was increased twice and this immediately produced the result demonstrating ferromagnetic properties with metal/insulator transition in the range of 200-250 K. Although a very thin STO interlayer can significantly improve the superconductivity in this type of SL's it is also leads to the depression of the magnetoresistance around T_{Curie} of LCMO in all samples with STO insulating layer compared to YBCO/LCMO superlattice. The investigation of superlattices type YBCO/PBCO/LCMO has shown completely different $\rho(T)$ curves behavior for two mirror samples with LCMO or YBCO as the first grown layer. It was shown that the SL (YBCO-20nm/PBCO/LCMO-20nm)$_{20}$ with LCMO on bottom has worse superconducting properties ($T_c \approx 40$ K) and better magnetoresistance ($MR \approx -10\%$) compared to the mirror sample (YBCO on bottom). The positive magnetoresistance peak of this sample is perfectly coincided with the superconducting transition. This was also confirmed by series of $MR(B)$ measurements for different temperatures around T_c. The similar behaviour of the mirror sample with LCMO as a first grown layer and even more pronounced re-entrant resistance at $T_{re} \approx 46$ K (for $I = 10\mu A$) was observed in YBCO/CeO_2/LCMO series of SL's with CeO_2 as the insulating

interlayer. It is shown that the re-entrant resistance is stable and it can be controlled by the external magnetic field and applied current that is interesting for possible practical applications.

PUBLICATIONS

1. I.A. Golovchanskiy, Alexey V. Pan, **Sergey A. Fedoseev**, Michael Higgins Significant tunability of thin film functionalities enabled by manipulating magnetic and structural nano-domains. *Applied Surface Science* **08**, 549–557 (2014)
2. A. V. Pan, O. V. Shcherbakova, **S. A. Fedoseev**, I. A. Golovchanskiy, D. Attard, S. K. H. Lam, J. Du, C. P. Foley, S. Rubanov, A. Suvorova. Enhancing properties of high temperature superconducting step-edge Josephson junctions by nano-multilayers with a small mismatch. *Advanced Materials Interfaces.* Volume 1, Issue 3, (2014).
3. A. V. Pan, I. A. Golovchanskiy and **S. A. Fedoseev** Critical current density: Measurements vs. reality**.** *EPL*, **103** 17006, (2013)
4. Igor A Golovchanskiy, **Sergey A Fedoseev** and Alexey V Pan Quantitative model for tunable microstructure in magnetic FePt thin films by pulsed laser deposition. *J. Phys. D: Appl. Phys*. **46,** 215502, (2013)
5. **Sergey A. Fedoseev,** Alexey V. Pan, Sergey Rubanov, Igor A. Golovchanskiy, and Olga V. Shcherbakova. Large, Controllable Spikes of Magnetoresistance in La2/3Ca1/3MnO3/SrTiO3 Superlattices. *ACS Nano*, **7**, 286-293, (2013)
6. Golovchanskiy, I. A., Pan, A. V., **Fedoseev S. A.**, Shcherbakova, O. V. & Dou, S. Xue. Critical current behaviour of YBCO thin films described by vortex pinning on low-angle domain boundaries and vortex creep. *Physica C: Superconductivity and its Applications*, ***479,*** 151-153 (2012).
7. O. V. Shcherbakova, A. V. Pan, S. K. Gorman, **S. A. Fedoseev,** I. A. Golovchanskiy, S. X.Dou. Inhomogeneities in YBa2Cu3O7 thin films with reduced thickness *Physica C,* Volume 479, p. 102-105, (2012)
8. **S.A. Fedoseev,** A.V. Pan, O.V. Shcherbakova, S.X. Dou. Electroresistance and magnetoresistance effects in superconductor–insulator–ferromagnet hybrid structures**.** *Physica C,* Volume 479, p. 143-146, (2012)
9. A. V. Pan, **S. A. Fedoseev,** O. V. Shcherbakova, I. A. Golovchanskiy at all. Development of Energy-Effcient Cryogenic Leads with High Temperature

Superconducting Films on Ceramic Substrates**.** *Physics Procedia,* 00 1–6, (2011)

10. I A Golovchanskiy, A V Pan, O V Shcherbakova, **S A Fedoseev,** and S X Dou. An all-field-range description of the critical current density in superconducting YBCO films. *Supercond. Sci. Technol.* **24,** 105020, (2011)
11. Shcherbakova, O. V., Lam, S. KH., Pan, A. V., **Fedoseev, S**., Dou, S. Xue., Du, J. & Foley, C. P. Step-edge Josephson junctions on multilayered high temperature superconducting thin film. *IEEE Transactions on Applied Superconductivity, **21 (3),*** 156-159 (2011).
12. Olga V. Shcherbakova, Alexey V. Pan, **S.A. Fedoseev**, Shi X. Dou, Simon K. H. Lam, Jia Du, and Cathy P. Foley. Multilayered approach to step-edge Josephson junctions. *Materials Science Forum* Vols. 654-656 (2010) pp. 1836-1839 © (2010) Trans Tech Publications, Switzerland.